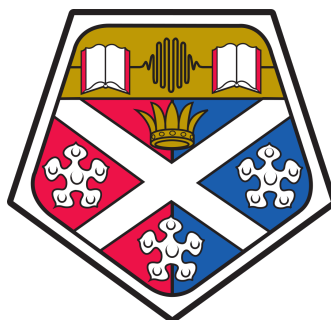


Prediction and control of organic xerogel microstructure: Experiments and modelling



Martin Prostredny

Department of Chemical and Process Engineering
University of Strathclyde

This dissertation is submitted for the degree of
Doctor of Philosophy

September 2019

Declaration

This thesis is the result of the author's original research. It has been composed by the author and has not been previously submitted for examination which has led to the award of a degree.

The copyright of this thesis belongs to the author under the terms of the United Kingdom Copyright Acts as qualified by University of Strathclyde Regulation 3.50. Due acknowledgement must always be made of the use of any material contained in, or derived from, this thesis.

Martin Prostredny
September 2019

Acknowledgements

The completion of this thesis would not be possible without the support of a number of people and I would like to express my gratitude to all of them.

First, I would like to extend my sincere thanks to both of my supervisors, Paul Mulheran and Ashleigh Fletcher, for their guidance and mentorship but also for providing a friendly atmosphere in our meetings and encouragement throughout my PhD.

I would like to thank all the friends I have made here in Glasgow, with special thanks to Carla, Dasha, David, Sofia, Alexandra, Ruben, Rab, Andrew, Gary, Fiona, Scott, Craig, Ivan, and Hrvojka. You have all made my time in Scotland enjoyable and it wouldn't be the same without you.

Thank you to Fletcher and Mulheran research groups, especially to Elisha for working with me and continuing my work further, to lab technicians, academics, and admin staff within the department, who have all been very helpful and friendly during this journey.

I would also like to thank Baxter and Brackenreid (and Ross for bringing them) for being my motivation for submitting chapters.

Last, but not least, I would like to thank all my family and friends in Slovakia for supporting me from afar and making me look forward to every visit back home. A special thank you to my mum, without her this would not have been possible.

Abstract

Resorcinol-formaldehyde (RF) gels are a fairly new addition to the variety of porous materials used by current industry. However, a better understanding of their formation processes is crucial for efficient structure tailoring, leading to high-performance materials for a range of applications. The usual RF gel manufacture process involves gelation of an RF sol at elevated temperatures, followed by exchanging water within the structure for another liquid, in order to limit shrinkage during the final drying step. Yet, despite significant research efforts, the RF growth processes are still not fully understood and there is no accepted model describing these processes.

Therefore, this study combines experimental and simulation approaches to better understand the gel growth process, and how the resulting structure depends on the growth conditions. The experimentally investigated areas include the influence of sodium carbonate catalyst concentration, processing temperature, solvent exchange and drying methods, as well as the presence of different anions within the reaction solution. Discussion on optimal processing parameters is included, in order to preserve the majority of the porous structure of RF xerogel materials, taking process economics into account, and the diversity of textural properties for obtained materials is examined.

In order to model the growth processes in RF gels, and investigate how they impact the structural properties of final materials, a two-dimensional lattice-based computational model, using kinetic Monte Carlo, was developed in this work. The presented model is developed to capture growth from monomeric species present in the initial stages of the gelation composition. Experimentally, gel growth is primarily controlled through catalyst concentration, which determines the density of species that are activated for rapid growth, and solids concentration; the model captures both of these dependencies.

Generated cluster structures were analysed for textural properties, such as accessible porosity and accessible surface area, as well as fractal properties, in the form of the correlation dimension and the Hurst exponent. Increasing both solids content and percentage of activated monomers led to an observed increase in complexity of cluster arrangement and tortuosity of pore structure, both reflected in the values of evaluated fractal properties.

In order to allow comparison of generated cluster structures with trends observed for experimental samples, gas sorption was modelled here using a lattice gas in a mean field approximation. The observations for model pores with varying dimensions agree with the background theory and the trends observed for the cluster structures were in line with those obtained experimentally. This helps to close the loop from growth processes to textural properties, providing the possibility to tailor materials for specific application.

Table of Contents

List of Abbreviations	ix
1 Introduction	1
1.1 Porous materials	1
1.1.1 Natural materials	1
1.1.2 Synthetic materials	2
1.1.3 Porous polymers	4
1.2 Resorcinol-formaldehyde gels	6
1.2.1 Reagents	6
Resorcinol	6
Formaldehyde	7
Sodium carbonate	7
1.2.2 Reaction	8
1.2.3 Hofmeister series	11
1.2.4 Structure control	11
Catalyst concentration	12
Catalyst species	12
Resorcinol to formaldehyde ratio	13
Solids content	14
Processing temperature	14
Solvent exchange	15
Drying method	16
Pyrolysis	17
1.2.5 Applications	18
Catalyst support materials	18
Gas separation and storage	19
Insulation	19
Electrode material	20
Water purification	20
1.3 Aims and Objectives	21
1.4 Thesis structure	22

2	Background theory	23
2.1	Textural characterisation	23
2.1.1	Gas adsorption	23
2.1.2	Surface area determination	28
	Langmuir theory	28
	Brunauer-Emmett-Teller theory	29
2.1.3	Porosity analysis	31
	Barrett-Joyner-Halenda theory	31
	t-plot method	32
2.1.4	Mercury porosimetry	32
2.1.5	Gas pycnometry	32
2.2	Modelling techniques	33
2.2.1	Kinetic Monte Carlo	34
2.2.2	Modelling of porous materials	35
2.2.3	Fractal analysis	35
	Fractal dimensions	36
	Hurst exponent	38
2.2.4	Gas adsorption modelling	39
3	Experimental study	41
3.1	Methodology	41
3.1.1	Gel synthesis	41
3.1.2	Solvent exchange	43
3.1.3	Drying	43
3.1.4	Nitrogen sorption measurements	44
	Degas procedure	44
	Sorption measurement	46
3.1.5	Nitrogen sorption data analysis	48
	Accessible surface area calculation	48
	Total pore volume	50
	Micropore volume	51
	Pore size distribution	52
3.2	Results and discussion - experimental study	55
3.2.1	Effect of sodium carbonate concentration	56
3.2.2	Improved solvent exchange	58
3.2.3	Effect of processing temperature	61
3.2.4	Vacuum vs ambient pressure drying	64
3.2.5	Different sources of sodium ions	65
3.3	Summary	72
4	Modelling porous xerogels	74

4.1	Cluster growth model	74
4.1.1	Code algorithm	76
	Run initialisation	80
	Drawing clusters	81
	Diffusion	85
	Cluster links	91
	Time increment	94
	Data output	95
4.1.2	Static clusters	98
4.1.3	Diffusing clusters	101
4.2	Textural characterisation	104
4.3	Fractal analysis	105
4.3.1	Correlation dimension	105
4.3.2	Hurst exponent	108
4.4	Solvent exchange modelling	112
4.5	Summary	116
5	Gas sorption modelling	119
5.1	Model gas and liquid	120
5.2	Calculation algorithm	123
5.3	Textural analysis	126
5.3.1	Accessible surface area	126
5.3.2	Pore size distribution	126
5.4	Effect of temperature and interaction parameter	127
5.5	Pores with both ends open	129
5.5.1	Filling and emptying of pores	130
5.5.2	Hysteresis	132
5.5.3	Pore length	133
5.5.4	Pore width	134
5.6	Pores with one end open	136
5.7	Pores with constant aspect ratio	138
5.8	Multiple pores	139
5.8.1	Varying pore width	139
5.8.2	Varying pore length	140
5.9	Conical pores	141
5.10	Model cluster structures	143
5.10.1	Textural properties	144
	Accessible surface area	144
	Pore size distribution	146
5.11	Summary	147

6	Conclusions	150
7	Future work	153
	References	155
	Appendix A Reaction solution compositions	169
	Appendix B Nitrogen sorption measurement validation	171
	B.1 Free space correction	171
	B.2 Silica alumina standard measurement	172
	Appendix C Preliminary results	174
	C.1 Titration study	174
	C.2 Gradual addition of formaldehyde	175
	C.3 Gelation time	177
	Appendix D Publications	179
	D.1 Published	179
	D.1.1	180
	D.1.2	194
	D.2 Submitted	202
	Appendix E Computational codes	212
	E.1 Visual Basic for Application macros used for nitrogen sorption data analysis	212
	E.1.1 BET surface area calculation	212
	E.1.2 t-plot method calculation	215
	E.2 Fortran codes	219
	E.2.1 Cluster growth code	219
	E.2.2 Percolation module	233
	E.2.3 Surface area analysis code	236
	E.2.4 Correlation dimension analysis	239
	E.2.5 Hurst exponent analysis	241
	E.2.6 Solvent exchange simulation	249
	E.2.7 Gas sorption simulation	254

List of Abbreviations

BET	Brunauer-Emmett-Teller
BJH	Barrett-Joyner-Halenda
C_C	percentage of activated monomers
D_B	box-counting dimension
D_C	correlation dimension
D_I	information dimension
H	Hurst exponent
kMC	kinetic Monte Carlo
λ/λ_0	relative activity
MIP	mercury intrusion porosimetry
MOF	metal-organic framework
NMR	nuclear magnetic resonance
p/p_0	relative pressure
PSD	pore size distribution
R/C	resorcinol/catalyst molar ratio
RF	resorcinol-formaldehyde
S_C	solids content

Chapter 1

Introduction

1.1 Porous materials

Porous materials differ from their bulk counterparts in characteristics such as high surface to volume ratio and low density, which determine their distinct applications, such as thermal and acoustic insulation, separation media, and as construction materials.

There are a number of naturally occurring porous materials, some of which will be discussed in the following section (1.1.1). Taking inspiration from natural materials, synthetic materials with enhanced characteristics and tunable structure have been developed and have subsequently replaced some of the natural materials in selected applications, as explored in Section 1.1.2, with focus on polymer materials in Section 1.1.3.

1.1.1 Natural materials

Pumice, an inorganic material found in nature, is a porous volcanic rock that can have various compositions depending on its source. Its relatively high porosity leads to low densities of these minerals, which allows them to even float on water [1]. A photograph showing the porous character of pumice is presented in Figure 1.1a. It can be used as a basis for lightweight construction material, as an abrasive, a growing substrate for plants, and to make materials for water filtration and spill containment [2].



(a) pumice [3]



(b) cork [4]

Figure 1.1 Natural porous materials

Cork, a natural organic material harvested from the outer bark of the cork oak tree, is mostly used to manufacture wine bottle stoppers [5] (Figure 1.1b). However, this sustainable material has found other uses as well, such as insulation, flooring, and sorption [6]. The applications of this material are a consequence of its low thermal coefficient, elasticity, and durability [7].

Other natural materials, such as wood, plant fibres and mineral materials, have been used in applications including as sorbents for chemical spills and as insulation materials [8, 9]. One of the advantages of natural materials is their availability in a form that is often ready for application and environmentally sustainable, however, they lack the tunability of properties offered by synthetic materials.

1.1.2 Synthetic materials

Porous metals can be obtained via different methods, leading to varying morphology, e.g. by sintering powders (Figure 1.2a) or fibres (Figure 1.2b), melt foaming (Figure 1.2c), metal deposition (Figure 1.2d), and directional solidification (Figure 1.2e) [10]. As can be seen from Figure 1.2, the different techniques lead to materials with varying structure. The advantage of metal-based materials is their electrical conductivity and high thermal stability, compared to e.g. organic materials. As a result of combination of properties of metals and porous solids, these materials have been previously used for separation, acoustic and thermal insulation, catalysis, and in medicine [10].

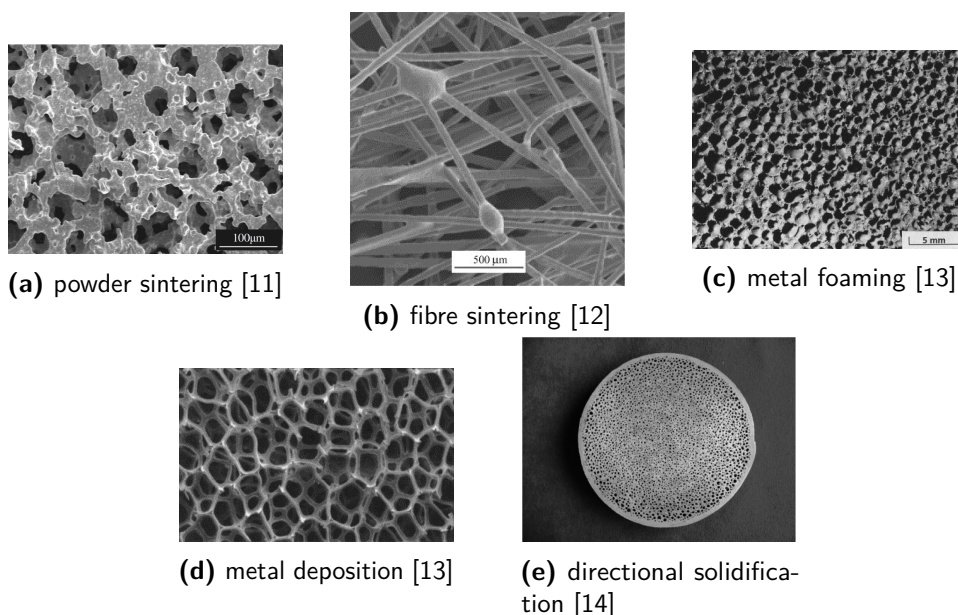


Figure 1.2 Structure of porous metal materials produced by different methods

Metal-organic frameworks (MOFs) are materials composed of units containing metal and organic linkers. There is a wide range of potential combinations of these building blocks, both for the organic and inorganic components, allowing adjustment of textural properties as

well as interactions with other substances, e.g. for gas storage, catalysis, or separation [15]. The diversity of these structures has led to over 20 000 different structures being reported by 2013 [16]. MOFs exhibit extraordinary properties, such as high values of accessible surface area ($\geq 7000 \text{ m}^2/\text{g}$ [17]), pore volume (up to $4.4 \text{ cm}^3/\text{g}$ [17]), and very low density (down to $0.126 \text{ g}/\text{cm}^3$ [18]). These remarkable properties, along with tunable chemical composition, allow high uptakes for gases of interest, such as hydrogen, methane, and carbon dioxide [15]. However, manufacture of these materials at industrial scale, and subsequent widespread application, are currently limited due to high fabrication costs [19] and insufficient chemical stability [16].

Zeolites, porous aluminosilicate materials, are found naturally but, for industrial applications, are usually prepared synthetically, in order to control their morphology and purity. Depending on their structure, there are materials with micropores (e.g. ZSM-5) or mesopores (e.g. MCM-41) [20]. Due to their regular pore structure, which results from their crystalline nature, zeolites have been used for water purification [21, 22], in separation processes [23–25], and as catalytic materials [20] and sorbents [26]. As with any material, there are some limitations related to their use, such as sensitivity to deactivation and limited pore size, which can be unsuitable for applications involving large molecules [27].

Porous ceramics encompass inorganic materials such as alumina (Al_2O_3), silica (SiO_2), zirconia (ZrO_2), magnesium oxide (MgO), titania (TiO_2), and silicon carbide (SiC) [28]. Depending on the production method, different morphologies can be obtained. Using extrusion moulding, two-dimensional honeycomb ceramics can be prepared. However, more common types of ceramics are three-dimensional materials, made by methods similar to those presented above for porous metals (e.g. particle sintering and foaming), as well as other methods, such as adding a pore-forming agent, sol-gel processes, and freeze-drying [28]. Due to their chemical composition, porous ceramics exhibit extraordinary thermal stability, finding use at extreme conditions, in particular within processes involving high temperatures, corrosive environments, and radiation. Applications of porous ceramics include filtration and separation (including molten metals), insulation, heat exchange, catalyst support, electrode and membrane materials [29]. One of the disadvantages of these materials is their inherent brittleness, which limits their use in certain applications.

Apart from ceramics, porous silica materials can also be obtained through a sol-gel process, as mentioned above. Depending on the synthesis conditions, materials with different sizes of primary particles can be obtained. In the 1930s, Kistler found out that by performing supercritical drying of silica gels, prepared via sol-gel reaction in an aqueous solution with subsequent exchange of the pore liquid for supercritical CO_2 , a highly porous material can be obtained [30]. This led to the discovery of a new type of materials; aerogels. Since their discovery, silica aerogels have attracted a significant amount of research interest and have been applied in various commercial applications, including as radiation detectors, and as thermal and acoustic insulation [31]. These materials exhibit unique textural properties,

including high surface area (up to 1200 m²/g), high porosity (up to 99 %), low density (down to ~0.003 g/cm³), low thermal conductivity (down to 0.005 Wm⁻¹K⁻¹), low dielectric constant, and low refraction index [32]. However, for some applications the porous nature is insufficient and the chemical composition, or other properties such as electrical conductivity, limit the use of porous silica materials.

Activated carbon is an amorphous porous material that can be obtained from various precursors, mostly organic waste materials, such as wood, nut shells, husks, and worn tyres [33–35]. The textural properties, and surface chemistry of the final product, are determined by the type of raw material used, as well as the processing conditions, e.g. temperature, carbonisation atmosphere, and activation time [33, 34]. Relatively high values of surface area (up to ~2500 m²/g) make them a suitable material for various sorption processes, in particular purification of gases and liquids, and as catalyst support materials [34].

1.1.3 Porous polymers

Synthetic polymers are used widely for various applications by today's industry. Apart from the traditional bulk material, porous alternatives have been used mainly for thermal and acoustic insulation, especially in the form of foams.

Polystyrene (PS) is used, as a porous material, in two distinct forms of closed-cell foams: expanded and extruded polystyrene. Despite a different process of manufacture, both forms share the same monomeric building blocks, as presented in Figure 1.3. Expanded polystyrene (EPS) is produced by expanding small polystyrene beads, partially swollen by a blowing agent (e.g. pentane), which are subsequently sintered together, allowing the material to be moulded to a desired shape. This makes EPS a common material used for packaging and construction [36]. On the other hand, extruded polystyrene (XPS) is produced in the form of sheets; as a result of the manufacture process, the outer surfaces are non-porous and thus have better vapour barrier properties compared to EPS. The porous structure of XPS is achieved by expansion of a blowing agent (e.g. cyclopentane, CO₂, or hydrofluorocarbons) immediately after the extruder die, due to the pressure difference. The aforementioned properties of both materials are a result of relatively low values of density (18–50 kg/m³ for EPS and 20–80 kg/m³ for XPS) and thermal conductivity (0.029–0.041 Wm⁻¹K⁻¹ for EPS and 0.025–0.035 Wm⁻¹K⁻¹ for XPS) [36]. Both materials have been widely used in insulation applications [37], due to their relatively low cost of manufacture and favourable properties.

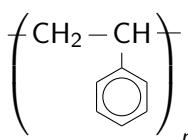


Figure 1.3 Polystyrene repeating unit

Polyurethanes (PU) are a group of polymers made by reacting polyfunctional alcohols with isocyanates, forming a urethane link ($-\text{NH}-\text{CO}-\text{O}-$). A typical monomeric unit of a polyurethane (ethylene glycol and methylene diphenyl diisocyanate) is presented in Figure 1.4. However, various polyols and isocyanates can be used for the reaction, adjusting the final material properties, and resulting in materials with varying mechanical properties (e.g. rigid or flexible materials). PU foams are used as a common insulation material, with the option of introducing the porous structure during the formation reaction of PUs, providing materials with low values of thermal conductivity, down to $\sim 0.02 \text{ Wm}^{-1}\text{K}^{-1}$ [38].

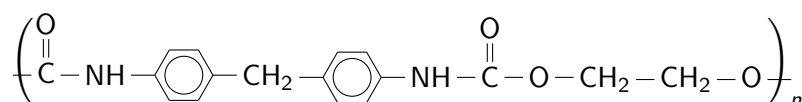


Figure 1.4 Typical repeating unit in polyurethanes

The first ever commercially used synthetic polymer material was bakelite, a phenol-formaldehyde (PF) resin developed by Baekeland, at the beginning of the 20th century [39]. Phenolic resins are usually produced in two varieties: novolaks and resoles. Novolaks are synthesised under acidic conditions with a higher phenol/formaldehyde (P/F) ratio and thus, require the addition of a curing agent (e.g. hexamethylenetetramine) to form a three-dimensional cross-linked material [40]. On the other hand, resoles are manufactured with a higher formaldehyde content ($\text{P/F} < 1$) with the addition of a base [40, 41]. Since the discovery of PF resins, phenol has been replaced by other substances that react with formaldehyde in a similar manner, such as resorcinol [41, 42], melamine [43], urea [44], and their combinations with phenol [45, 46]. The chemical structures of common reagents used for resin manufacture are presented in Figure 1.5.

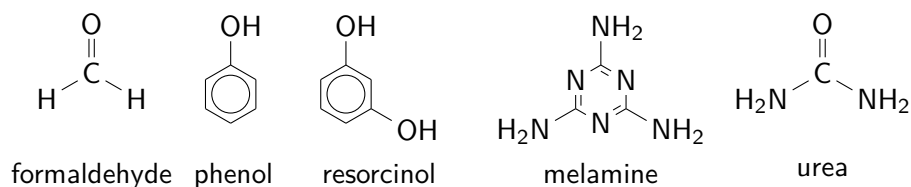


Figure 1.5 Substances used for resin manufacture

Much later, after the discovery of supercritical drying for silica gels by Kistler [30], Pekala utilised the process for resorcinol-formaldehyde (RF) gels, in 1989 [47]. He observed that, if the reaction between resorcinol and formaldehyde was performed in an aqueous solution in presence of sodium carbonate, acting as a base, porous hydrogel materials are obtained. Exchanging the water present in the organic hydrogel pores using supercritical CO_2 leads to an organic aerogel. This discovery opened up the new research field of organic aerogels, which has attracted significant interest amongst the scientific community [48–58]. While the materials have found use in their organic form, for some applications it is desirable to transform them into carbonaceous materials, usually via pyrolysis [50, 55, 57, 59–66].

1.2 Resorcinol-formaldehyde gels

Due to the broad research interest surrounding the manufacture and applications of resorcinol-formaldehyde (RF) gels, this work focusses on the study of these materials. This section introduces the reagent substances in Section 1.2.1, followed by discussion about the processes occurring during the sol-gel process in Section 1.2.2. Due to the observed effect of ions present in the solution, the Hofmeister series is presented in Section 1.2.3, while Section 1.2.4 discusses different ways to control the structure of the final RF gel materials, with their applications reviewed in Section 1.2.5.

1.2.1 Reagents

The original work by Pekala [47], as well as the majority of current research utilises a base-catalysed synthetic route. The three main reagents used in the base-catalysed RF gel manufacture are: resorcinol, formaldehyde, and an inorganic base, usually in form of a hydrolysing salt. In this work, sodium carbonate (Na_2CO_3) is used as the base, and will be referred to, as is the convention of nomenclature within the field, as a catalyst in this work. However, this is not technically accurate, since the salt is not recoverable after the reaction.

Resorcinol

Resorcinol (systematic name *m*-dihydroxybenzene or benzene-1,3-diol, $\text{C}_6\text{H}_6\text{O}_2$) is a white solid substance, readily soluble in water. Hydroxyl groups present on the benzene ring of a resorcinol molecule contain acidic hydrogen atoms, leading to a resorcinol anion with nucleophilic character (donates an electron pair when forming a bond with an electrophile) under basic conditions. Due to the positive mesomeric effect (charge distribution in a molecule with a system of conjugated π bonds due to the presence of electron-donating groups) on the aromatic benzene ring, the negative charge generated on the oxygen atom is distributed around the molecule. The electron density is increased in positions 2, 4, and 6 (ortho and para positions) with regards to the negatively charged oxygen atom. This process is shown in Figure 1.6, along with the resulting resonance forms of the resorcinol anion.

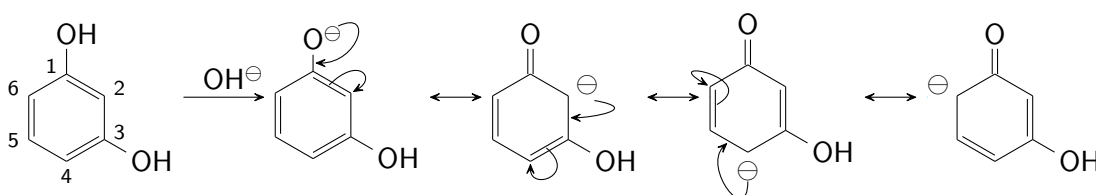


Figure 1.6 Formation of a resorcinol anion under basic conditions along with the resonance forms of the resorcinol anion

Even though all three positions mentioned above (two ortho and one para) contain a higher electron density, the reactivity of the ortho position found between the hydroxyl groups (carbon atom labelled 2 in Figure 1.6) may be slightly hindered due to steric effects of the adjacent hydroxyl groups.

Formaldehyde

Formaldehyde (systematic name methanal, CH₂O) is a colourless, irritant gas with a pungent odour at ambient conditions [67] and is the simplest of the aldehydes. It occurs naturally, in very small quantities, in the environment and in living organisms, as a metabolic product [67]; however, at higher concentrations it is classified as an irritant, toxic and carcinogenic to humans [68]. Due to these harmful properties, there has been misinformation in the media about banning formaldehyde use in the European Union [69]. However, formaldehyde is not listed in the current version of the Regulation (EU) No 649/2012 [70] that is concerned with the export and import of dangerous chemicals and is not expected to be added in the near future.

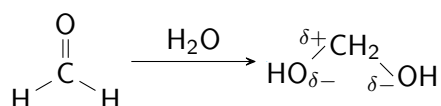


Figure 1.7 Hydration of formaldehyde (left) to methanediol (right) in an aqueous solution with partial charges shown on the carbon and oxygen atoms of methanediol

Formaldehyde gas is readily soluble in water and is usually used in the form of an aqueous solution, called formalin. It reacts with water to form a hydrated form, methanediol, as shown in Figure 1.7. Methanediol has a partial positive charge on the carbon atom, due to the higher electronegativity of the bonded oxygen atoms, as presented in Figure 1.7. This partial positive charge is the reason for methanediol to react with the resorcinol anion as an electrophile, as is described in more detail below.

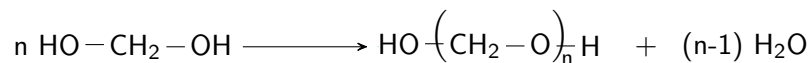
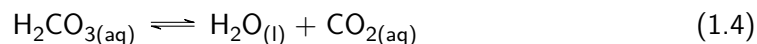
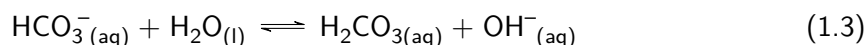
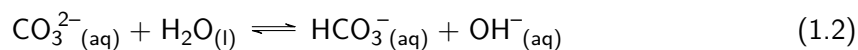
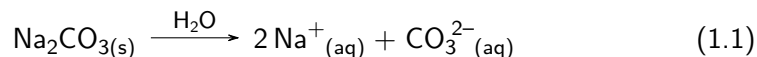


Figure 1.8 Polymerisation of methanediol in an aqueous solution forming oligomers

In an aqueous solution, methanediol forms oligomers (Figure 1.8), as has been observed experimentally, e.g. by NMR studies [71, 72]. The number of monomeric units in these oligomers, denoted *n* in Figure 1.8, is usually within the range 1 to 8, with lower oligomers present in higher concentrations compared to their larger counterparts [67]. In order to limit the extent of polymerisation, commercially available formalin solution usually contains methanol as a polymerisation inhibitor. With usually 10–15 wt% of methanol in the solution, some of the hydroxyl end groups of methanediol react with methanol instead of another methanediol molecule, thus limiting the length of the oligomers formed.

Sodium carbonate

Sodium carbonate (Na₂CO₃) is a sodium salt of carbonic acid (H₂CO₃), a weak acid with an experimental value of pK_a(H₂CO₃) = 6.36 [73]. This leads to hydrolysis of carbonates and hydrogencarbonates in aqueous solutions, since they are conjugated bases of a weak acid. Sodium carbonate can hydrolyse, after dissociation (Equation 1.1), in two steps, as presented in Equations 1.2 and 1.3, leading to increased pH of sodium carbonate solutions.



A useful measure of the strength of acids and bases are the dissociation constants K_a and K_b , and the logarithmic versions $\text{p}K_a$ and $\text{p}K_b$ ($\text{p}K_a = -\log(K_a)$). These constants are taken as the equilibrium constants for the reaction between the corresponding acid, or base, and water. From the reaction presented in Equation 1.2, $K_b(\text{CO}_3^{2-}) = \frac{[\text{HCO}_3^-][\text{OH}^-]}{[\text{CO}_3^{2-}]}$, with the concentration of water omitted from the equation by convention. The acid and base dissociation constants are related to each other via the logarithmic form of the water self-dissociation constant $\text{p}K_w$ as $\text{p}K_a + \text{p}K_b = \text{p}K_w$.

The values of $\text{p}K_a$ for the carbonate (CO_3^{2-}) and bicarbonate (HCO_3^-) anions are 6.35 and 10.33, respectively [74]. Using the relation between $\text{p}K_a$ and $\text{p}K_b$ gives the corresponding values of $\text{p}K_b$ constants (taking the value of $\text{p}K_w = 14$) for the carbonate and bicarbonate anions as 7.65 and 3.67, respectively, showing that carbonate is a stronger base than bicarbonate. Carbonic acid is not stable and most of it dissociates into H_2O and CO_2 , as shown in Equation 1.4, with the ratio between dissolved CO_2 and H_2CO_3 at 25 °C being $\frac{[\text{H}_2\text{CO}_3]}{[\text{CO}_2]} \approx 1.7 \times 10^{-3}$ [75]. Due to decreased solubility of gases in aqueous solutions at elevated temperatures, the equilibrium of the aforementioned reactions will be shifted towards the products during RF gelation processes. Furthermore, the self-ionisation of water is higher at elevated temperatures, leading to a higher concentration of both H^+ and OH^- ions at RF reaction conditions, compared to ambient temperatures.

1.2.2 Reaction

The first step, in the RF gel reaction, is the formation of hydroxymethyl monomeric species from resorcinol anions and methanediol (hydrated form of formaldehyde) by electrophilic substitution under basic conditions, as shown in Figure 1.9. The most commonly used resorcinol to formaldehyde molar ratio (R/F) is 1:2 [55], resulting, on average, in two hydroxymethyl groups ($-\text{CH}_2\text{OH}$) on each benzene ring, as in Figure 1.9. However, the reaction solution contains a variety of different derivatives, as observed previously by NMR [76], some of which are presented in Figure 1.10. The number and type of the derivatives present in the solution depends on the solution pH, which is related to the amount of catalyst salt added, usually expressed as resorcinol to catalyst molar ratio (R/C). Methanol present in the formalin solution, as described above, is less reactive towards electrophilic substitution (Figure 1.9) due to the lower partial charge found on the carbon

atom with only one hydroxyl group present. These monomeric species then undergo condensation reactions, forming larger structures, as discussed below.

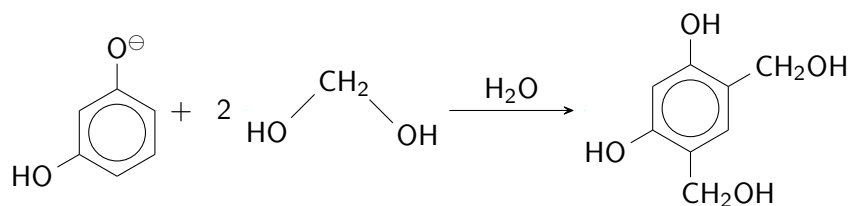


Figure 1.9 Formation of a hydroxymethyl monomer species in a basic aqueous solution

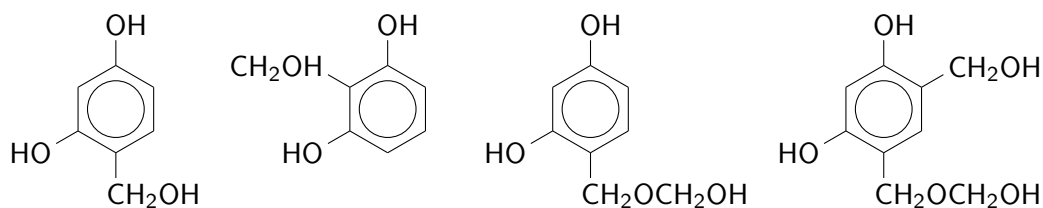


Figure 1.10 Variety of derivatives present in the RF reaction solution

It has been proposed that a metal ion, coming from the catalyst salt, creates a transition complex with a phenol anion and a formaldehyde molecule [77] in solution during the phenol-formaldehyde gel reaction. This is likely to occur for a solution containing resorcinol as well, due to its very similar structure compared to phenol. The potential formation of another 6-membered ring presumably stabilises this arrangement, possibly promoting the subsequent reaction between resorcinol and methanediol.

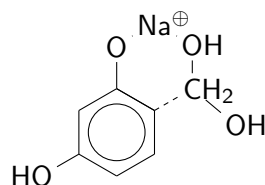


Figure 1.11 Proposed transition complex of a resorcinol anion, methanediol, and a sodium ion

Two types of links between the benzene rings are formed as a result of the condensation reactions in RF gel solution. The first one involves the reaction of a hydroxymethyl group on one benzene ring with another benzene ring, as shown in Figure 1.12, resulting in a methylene ($-\text{CH}_2-$) bridge. However, if two hydroxymethyl groups react together, as in Figure 1.13, a methylene ether bridge ($-\text{CH}_2-\text{O}-\text{CH}_2-$) is formed. The ether bridges are more flexible compared to the methylene bridges, leading to a variation in mechanical properties of the final material based on the ratio of the bridge types present.

Deprotonation of hydroxymethyl derivatives leads to transformation into a very reactive *o*-quinone methide in the basic reaction solution [78], as presented in Figure 1.14. This leads to an increased rate of condensation reaction and bridge formation.

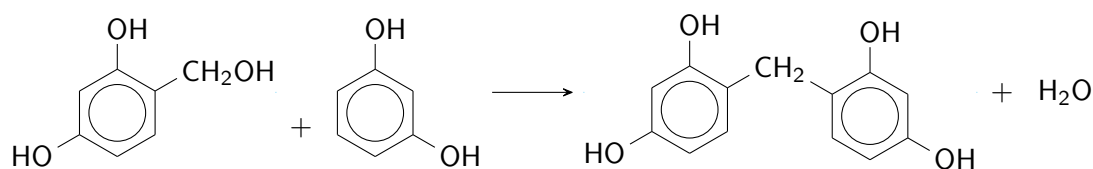


Figure 1.12 Condensation reaction leading to formation of a methylene bridge

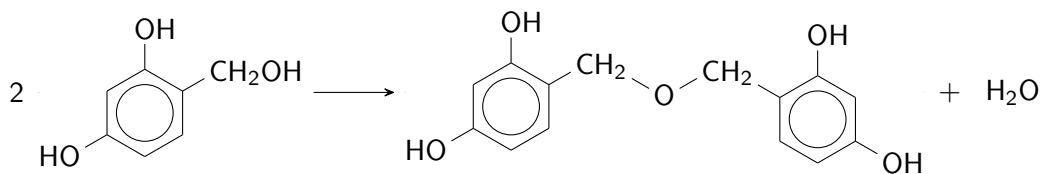


Figure 1.13 Condensation reaction leading to formation of a methylene ether bridge

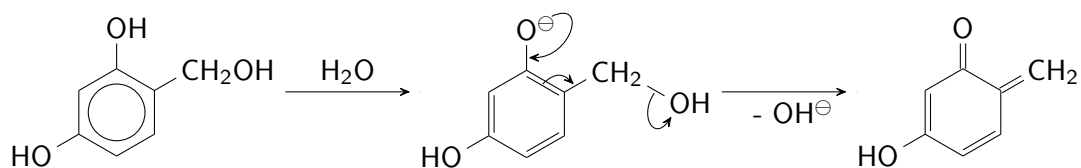


Figure 1.14 Formation of *o*-quinone methide from a hydroxymethyl species in a basic solution

The dimers created by bridge formation, as described above, continue growing in the reaction solution by analogous reactions. However, there is experimental evidence that these growth reactions occur significantly only above $\sim 55^\circ\text{C}$ [79], with no condensation products observed at ambient temperature, determined using liquid phase NMR [76]. Thus, during the stirring period, at ambient temperature, after all reagents have been added and dissolved, only the formation of the small species, most likely hydroxymethyl monomers, occurs with subsequent growth starting once the solution reaches a sufficiently high temperature.

During the sol-gel process, clusters not only grow in the reaction solution but can adhere to each other, forming larger structures. These will eventually span the reaction space when the gel point is reached. At higher catalyst concentration (lower R/C ratio), there will be a high number of activated monomer species, leading to a higher number of small clusters present in the final material. The small clusters are able to fill the space more efficiently, leading to smaller gaps between them, hence, smaller pore sizes observed in the final materials. On the other hand, at higher R/C ratios (lower catalyst content), there will be fewer clusters growing in the solution, and, therefore, these will grow to larger sizes with the same amount of material present in the reaction solution. These larger particles will create larger gaps between them, compared with the smaller ones, resulting in larger pore sizes as determined from textural characterisation [79].

The sol-gel process starts with all reagents and growing oligomers dissolved in the solution, forming a homogeneous system. However, as the reaction proceeds, the clusters grow in size, increasing their molecular weight, as well as the extent of cross-linking within the

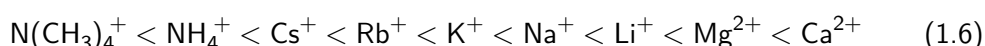
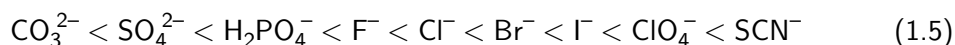
clusters, leading to a decrease in cluster solubility, and resulting in phase separation at the nano/micro-scale. As a consequence of phase separation, an interface on the cluster surface is formed, leading to potential adsorption of unreacted species from the solution. This increased concentration of reagents on the cluster surface may lead to a change in the reaction kinetics of the growing cluster. Yet, this hypothesis is yet to be confirmed experimentally.

1.2.3 Hofmeister series

As mentioned above, the metal cation appears to play a role in the process of RF gel formation. However, the presence of ions in a reaction solution does not only have an impact on the chemical reactions taking place in the solution but potentially affects other processes as well. In the case of RF gel formation, as the clusters grow and their solubility decreases, as mentioned above, the point at which the clusters are no longer soluble in the solution is dependent on the concentration and type of ions as well as the cluster properties. In 1888 Hofmeister studied the effect of salts, with different anions and cations, on salting-out of proteins from aqueous solutions [80].

Since then, the effect of different ions on the solubility of macromolecules in solution has been studied by various techniques [81–84]. Several theories explaining this phenomenon have been proposed, one of them describing the influence of the ion presence on water structures, leading to more (kosmotropic effect) or less (chaotropic effect) stable and organised structures, strengthening or weakening hydrogen bonds [81]. However, this theory was not confirmed by experimental data [82]. Work by Bostrom *et al.* [83] studied the effect of ions on calculated dispersion forces within the system, while another theory proposed the ions ability to penetrate into the structures formed by the aggregating molecules [84], agreeing with the effect observed for dispersion forces [83].

The currently accepted Hofmeister series for anions and cations [85, 86] are shown in Equations 1.5 and 1.6, respectively. The ions on the left in Equations 1.5 and 1.6 promote salting-out of proteins in solution, while the ones on the right stabilise proteins in solution, salting them in. However, it has been found that for hydrophilic surfaces, such as the surface of growing RF clusters, the anion series effect is reversed [87] due to the ion-surface interactions, which affect the long-range forces stabilising macromolecules in solution.



1.2.4 Structure control

Properties of the final RF gel material can be controlled in all of the stages of manufacture, including reaction solution preparation, gelation and curing, solvent exchange, and drying.

The main variables influencing the final properties of RF gels, that are discussed in this work, are concentration and type of catalyst used, molar ratios of reagents, total amount of solids in the reaction solution, gelation and curing temperature, solvent exchange method, drying method, and potential pyrolysis into a porous carbon material.

Catalyst concentration

Catalyst concentration, usually expressed as resorcinol to catalyst molar ratio (R/C), is one of the most commonly changed variables in the RF gel manufacture process [55, 57]. As discussed above, the presence of catalyst adjusts the solution pH, determining the extent and kinetics of cluster formation and growth. As mentioned above, it has been observed experimentally that increasing the amount of catalyst in the reaction solution leads to a higher number of smaller clusters formed [58, 79, 88], and subsequently, smaller pore size in the final material [57, 65, 89]. The increased particle, and pore, size for RF gels prepared using higher R/C ratios, leads to lower values of accessible surface area [52, 55, 79]. The total pore volume, determined from gas sorption measurements, generally increases with increasing R/C ratio, up to R/C \sim 300–400, for xerogels [79]. At high R/C ratios, the xerogel total pore volume, determined from gas sorption measurements, decreases due to a weak gel structure formed at these conditions, resulting in significant shrinkage. Measured micropore volume also tends to decrease with increasing R/C ratio [63].

Catalyst species

In order to obtain a viable porous RF gel structure, the solution pH needs to be adjusted to a value within an appropriate region. This can be achieved using either a base or an acid, and the most commonly used pH value window in the literature is 5.4 to 7.6 [55, 57]. A work by Rey-Raap *et al.* suggested a wider range of pH values (approximately 3–8), using HCl and NaOH [90], but this work will focus on the narrower pH range, more common in the literature. The more frequently used synthesis method, from a study of the literature, is the base catalysed route using mostly inorganic bases, such as hydrolysing salts of weak acids or hydroxides. The most widely used hydrolysing salts are carbonates and bicarbonates of alkali metals (Group 1) and alkaline earth metals (Group 2), with sodium carbonate being most prevalent [55, 57]. Irrespective of the cation, Group 1 carbonates produce materials with very similar textural properties [79], whereas their Group 2 counterparts produce larger clusters, accompanied by larger pore sizes in the final materials [91]. The difference between Group 1 and 2 carbonates could result from the difference in the charge density on the metal cation, with higher charges present on the alkali earth metal cations. This leads to a larger hydration shell for ions with greater charge density, potentially influencing the size of structures grown in the reaction solution.

Another group of base catalysts, used for RF gel manufacture, are hydroxides, again with either Group 1 or 2 metals [92, 93]. The same observations are made as for carbonates, for the cation type impact on textural properties [92], suggesting that the metal ion plays a role

in the synthesis process. Comparing samples prepared under the same synthesis conditions (solution pH, dilution ratio, and R/F ratio) and using either a carbonate or hydroxide catalyst salt results in larger pore size and pore volume for the carbonate samples [93]. Calvo *et al.* [93] suggested that the final pore size might be influenced by the anion size, with carbonate anions being larger than hydroxide.

It has been proposed previously, in the work by Reuß and Ratke [94], that it is possible to obtain viable gel structures without the metal ion present in the solution, using ammonium carbonate ($(\text{NH}_4)_2\text{CO}_3$) as a catalyst, however, materials obtained this way, using high solids contents, exhibit very low surface areas compared to RF gels made using a catalyst containing a metal ion.

An alternative route for RF gel formation is using an acidic catalyst species rather than a base. Acid catalysed RF gels can be produced with a variety of acids, e.g. nitric acid (HNO_3) [95], perchloric acid (HClO_4) [96, 97], hydrochloric acid (HCl) [98, 99], acetic acid ($\text{CH}_3\text{-COOH}$) [100, 101], *para*-toluenesulfonic acid ($\text{CH}_3\text{-C}_6\text{H}_4\text{-SO}_3\text{H}$) [102], and oxalic acid (HOOC-COOH) [102]. In general, the gelation process occurs during a much shorter time period for acid-catalysed RF gels, compared to their base-catalysed counterparts, e.g. as observed in the work by Mulik *et al.* [98]. However, the majority of research within the field focusses on base-catalysed RF gels [55, 57], mainly due to their superior mechanical properties [56], which makes them suitable for most applications.

Due to the addition reaction being base-catalysed and the subsequent condensation reactions being acid-catalysed, some researchers have used a combination of both methods in their syntheses [49, 103, 104]. This involves starting the reaction with a basic catalyst, most commonly Na_2CO_3 , and adding an acidic species at a later stage to promote condensation and cross-linking reactions. Lambert *et al.* [49] have added benzoic acid to speed up the gelation process, reducing the time needed for gel formation from hours to minutes. Xu *et al.* [103] have used HCl to produce mesoporous RF gels at room temperature. Laskowski *et al.* [104] have used citric acid to obtain xerogels after gelation at 40 °C. It can be seen from the presented examples from literature, that the addition of an acid after initial base-catalysed reaction period can reduce both the gelation time and temperature needed to form an RF gel. However, for the study of the formation process of RF gels, it adds another variable into the process.

Resorcinol to formaldehyde ratio

Resorcinol to formaldehyde molar ratio (R/F) has an influence on the amount and type of bridges formed between the benzene rings of resorcinol molecules (described in more detail above). At lower R/F ratios (higher formaldehyde content), more cross-links are formed in the material, leading to more dense structures with lower pore volumes and smaller pore sizes [50]. There seems to be a limiting value of R/F ratio (approximately $\text{R/F} \sim 1$), above which the gelation is unsuccessful due to a lack of formaldehyde present for the bridge

formation [50], similar to novolaks mentioned above (where a curing agent is added to form a three-dimensionally cross-linked structure, as discussed in Section 1.1.3).

Solids content

Solids content can be expressed in the literature in a few different ways, the common ways are w/v%, dilution ratio, and resorcinol to water ratio (R/W). Weight per volume percent (w/v%) is calculated as mass of all the solids per 100 ml of the reaction solution (e.g. 20 w/v% is 20 g solids per 100 ml solution), as used e.g. in the work by Taylor *et al.* [79, 91]. Dilution ratio, usually labelled D in the literature, is defined as the molar ratio between the total solvents (water and methanol) and reactants (resorcinol and formaldehyde), as used e.g. in the work by Job *et al.* [63, 65, 92]. Similar to R/C ratio mentioned above, the amount of solids is sometimes expressed as resorcinol to water ratio (R/W), either as a molar ratio, e.g. in the work by Awadallah-F *et al.* [105], or as mass to volume ratio, e.g. in the work by Yamamoto *et al.* [54, 62].

An increase in dilution ratio was reported to increase gelation time and decrease mechanical properties, leading to a higher degree of shrinkage during drying [90]. A study by Job *et al.* [64] has compared the effect of dilution ratio on textural properties of aerogels (supercritically dried), cryogels (freeze-dried), and xerogels (subcritically dried). For aerogels, increasing the dilution ratio (decreasing solids content) has resulted in increased values of total pore volume (V_T), average pore size ($\bar{\phi}$), skeletal density (ρ_{skeletal}), slightly increased accessible area (S_{BET}) for lower R/C ratios, and decreased bulk density (ρ_{bulk}). Cryogel samples exhibited decreased values of S_{BET} , ρ_{bulk} and increased V_T , $\bar{\phi}$, and ρ_{skeletal} . Except for a decrease in S_{BET} for xerogel samples with increased dilution ratio, it had very little effect on the final properties of xerogels, with high degrees of shrinkage for these materials masking the effect of solids content. For all the studied samples in the aforementioned work, dilution ratio had an insignificant effect on the micropore volume and lower solids content, generally, led to a more pronounced shrinkage of the materials. Apart from the observed effects of the solids content on the properties of the dried material, there seems to be an upper limit for a successful gelation of the system for higher R/C ratios and lower solids contents (higher dilution ratios) [64, 90]. Tamon *et al.* [50] reported no significant impact of solids content on S_{BET} and $\bar{\phi}$ of RF aerogels, but an increase in mesopore volume with increased solids content.

Processing temperature

It is well known that, in general, temperature has a significant effect on the kinetics of chemical reactions, as well as their extent. Although, for the formation of RF gels, temperature could have an influence on the solubility of the growing clusters, as well as the extent of cross-linking within and between the clusters. The work by Taylor *et al.* [79] has shown, that the RF clusters start to grow in the aqueous reaction solution only at $\sim 55^\circ\text{C}$ and above. Tamon and Ishizaka [52] have looked at the effect of gelation temperature on

the textural properties of RF aerogels, concluding that temperature has no influence on the final gel structure. However, in their experiments, the gelation step (performed at 25 and 50 °C) was followed by a five day curing period at 90 °C. Thus, the influence of the lower temperature gelation step would have been masked by the subsequent exposure to the same higher temperature during the curing stage.

Job *et al.* [56] have compared the effect of different gelation temperatures (namely 50, 70, and 90 °C), concluding that the final properties of RF gels are significantly affected by the processing temperature. They stated that the increased temperature not only reduces the gelation time needed, by increasing the reaction kinetics, but also has an impact on the final pore size of the materials. At lower R/C ratios, the temperature increase led to increased values of both S_{BET} and average pore size, while at higher R/C ratios the effect was less clear. The authors hypothesised that the cause for these changes could be due to the effect of temperature on the dissociation of species present in the reaction solution, as well as the influence on the ratio of addition and condensation reactions taking place.

Wiener *et al.* [106] have made a similar observation with the average pore size increased for samples exposed to higher temperatures (and for longer times), along with a lower degree of shrinkage. This suggests that the materials prepared at higher temperatures are better able to withstand the drying process, preserving more of the porous structure after the gelation step.

In some work, base-catalysed gels are placed in an acid solution bath after gelation to promote cross-linking within the structure [53, 107], improving their mechanical properties and enhancing structure preservation during drying. However, conditions used for this extra step lead to an additional variable potentially influencing the final structure of the materials. Thus, while investigating the formation processes during RF gelation, and their impact on the final properties, it is favourable to omit this additional step and limit the number of factors influencing the end material.

Solvent exchange

Solvent exchange involves the replacement of water present in hydrogel pore structure, after the gelation and curing steps, with another solvent, preferably with a lower boiling point and/or surface tension than water. Naturally, the solvent used for exchange has to be miscible with water, otherwise it would not replace the liquid within the pores. The most common solvent used for this purpose in the literature is acetone ($(\text{CH}_3)_2\text{CO}$) due to its relatively low price, boiling point, and surface tension (Table 1.1) [47, 55, 57, 59, 64, 105]. Other solvents previously used for solvent exchange include methanol (CH_3OH) [47], ethanol ($\text{CH}_3\text{CH}_2\text{OH}$) [104, 108, 109], isopropanol ($(\text{CH}_3)_2\text{CHOH}$) [47, 49], *tert*-butanol ($(\text{CH}_3)_3\text{COH}$) [110, 111], and amyl acetate ($\text{CH}_3\text{COO}(\text{CH}_2)_4\text{CH}_3$) [47]. Comparison of boiling points and values of surface tension at 50 °C for the aforementioned solvents and water are presented in Table 1.1. It can be seen that all the presented organic solvents, that

have been previously used for solvent exchange of RF gels, have a similar value of surface tension at 50 °C (~17–23 mN/m) that is significantly lower than the value obtained for water. Even though amyl acetate exhibits a lower value of surface tension than water, its boiling point is higher, which would lead to increased costs associated with the subsequent drying process.

Table 1.1 Values of boiling point and surface tension for water and selected solvents used for solvent exchange

Substance	Boiling point [°C]	Surface tension [112] at 50 °C [mN/m]
Water	100 [113]	68.45
Acetone	56.2 [114]	20.66
Methanol	64.5 [113]	20.18
Ethanol	78.3 [114]	19.89
Isopropanol	82.2 [115]	18.95
<i>tert</i> -butanol	82.4 [114]	17.71
Amyl acetate	149.2 [116]	22.69

Drying method

Drying method has a significant impact on the final structure of RF gel materials, and the dried materials are named according to the drying technique used. The first method used for drying RF gels was supercritical drying, using supercritical CO₂, since the technique was previously developed for silica materials [47], as mentioned in the previous section. Supercritically dried materials, aerogels, exhibit the lowest degree of shrinkage out of all drying methods used [55, 57]. However, this method requires the use of relatively high pressures (critical point for CO₂ is ~31 °C and ~7.4 MPa [117]), making it more expensive compared to other methods. Schematically, the process of supercritical drying is shown in Figure 1.15 in blue. Pressure, followed by temperature, is increased above the critical point for the pore fluid with subsequent decrease in pressure. This leads to bypassing the critical point, removing the pore fluid without a vapour-liquid interface, eliminating the capillary forces exerted onto the pore walls during drying. Another disadvantage of this method, along with the increased cost, is the necessity of first exchanging water from the hydrogel with another solvent, most commonly acetone, that is miscible with both water and CO₂.

Another method used for drying RF gels, that preserves the majority of the porosity, is freeze drying (lyophilisation), producing cryogels. This involves freezing the liquid found within the pore structure, by lowering the temperature, followed by sublimation under reduced pressure, as shown in Figure 1.15 in green. Due to not crossing the vapour-liquid boundary in the phase diagram, a vapour-liquid interface is not formed, minimising shrinkage of the dried material. However, water within the pores has to be replaced with another solvent, due to the expansion of water during ice formation, to prevent the resulting destruction of the

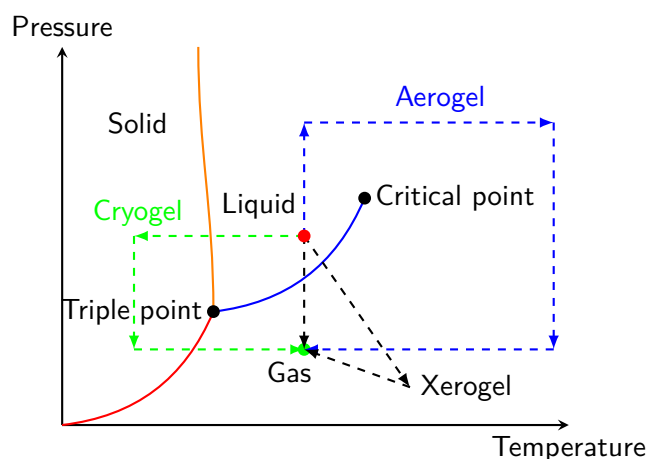


Figure 1.15 Schematic diagram showing different drying methods for RF gels with a phase diagram of the liquid within the pore structure

porous gel structure. A common solvent used for freeze drying is *tert*-butanol [110, 111] due to its relatively high melting point (25 °C) and vapour pressure (41.25 mmHg at 25 °C) [118], compared to e.g. water (melting point 0 °C and vapour pressure 23.78 mmHg at 25 °C [118]).

A very common, and industrially more viable [64, 119], option of drying RF gels is subcritical drying, yielding xerogels. This involves solvent removal below its critical point, resulting in a more pronounced degree of shrinkage during drying [64]. Therefore, it is important to ensure a thorough exchange of water with a selected solvent, with a lower value of surface tension than water, to minimise the capillary forces causing the collapse of the porous structure during drying. Drying can be performed either under an inert atmosphere [110] or under vacuum [79], as shown in Figure 1.15 in black. Subcritical drying involves the removal of solvent with a vapour-liquid interface present, where the resulting capillary forces cause pore shrinkage. Instead of using a conventional (or vacuum) oven, microwave drying is sometimes used to obtain xerogels, where drying usually follows immediately after the gelation and curing steps, omitting solvent exchange [90, 120, 121].

Pyrolysis

For some applications, as described in more detail in the next section, it is desirable to obtain a porous carbon material, rather than an organic gel. Pyrolysis, a process involving high temperatures under an inert gas atmosphere, converts the organic gel into a carbon material, while preserving the porous character. Carbon gels exhibit increased values of accessible surface area, total pore volume, and micropore volume compared to their organic analogues [110]. Due to the changes in textural properties of RF gels after pyrolysis [64, 110], the conditions used are another variable in the process, and in order to better understand the process of formation of RF gels, it is more suitable to analyse them in their organic form, without introducing another factor into the process.

1.2.5 Applications

Due to their highly porous structure, RF gels in form of aerogels, cryogels, as well as xerogels, have found uses in many applications since their discovery. RF gels have been previously reported as materials for catalyst support, in gas separation and storage, fuel cells, thermal insulation, porous electrodes, and water purification. However, in order to manufacture materials suitable for a particular application, the textural properties of the RF gel based materials need to be tailored in order to maximise their potential. For this purpose, a deeper understanding of the structural property dependence on manufacture conditions is required.

Catalyst support materials

Catalysis is a crucial industrial process; however, catalytic materials tend to be expensive and their efficiency is determined by the surface area exposed to the reaction mixture. Therefore, a common approach is to use an inert material with high surface area as a catalyst support. This reduces the cost, since the bulk of the material consists of the cheaper support, as well as improving the efficiency of catalysis. RF gels have been previously shown as suitable materials for catalyst supports for chemical reactions [122, 123] and for fuel cell applications [65, 124, 125].

Rodrigues *et al.* [122] have tested two carbon xerogels, with different textural properties, as supports for a gold catalyst for glycerol oxidation. They have observed that the pore structure of the xerogel support has a significant impact on the catalytic process, with a change in pore size resulting in different reaction products. Job *et al.* [65] have compared a carbon aerogel with several carbon xerogels with regards to performance as platinum catalyst supports for polymer electrolyte membrane (PEM) fuel cell cathodes. They have concluded that the xerogels are a potential substitute for aerogels if their textural properties are tuned appropriately. Similarly, Smirnova *et al.* [124] stated that the pore structure of carbon aerogels is a major factor in performance enhancement for platinum catalyst support for PEM fuel cells. It was also suggested, in the work by Jin *et al.* [125], that RF based carbon xerogels can be a promising replacement for carbon black as a catalyst support for a typical Pt/C catalyst used in industry. Conversely, Marie *et al.* [123] observed no influence of pore size on the catalytic activity of a platinum catalyst with both samples showing suitable characteristics for catalyst support application; however, the authors noted that the small particle size of the platinum particles used may be detrimental. Additionally, the sample with higher surface area exhibited a higher degree of microporosity, which contributes to the accessible surface area of the support but the platinum particles entrained in the micropores may not be accessible for the catalytic process.

The high values of accessible surface area of RF gels, along with their inertness in the carbonised form and tunability of textural properties, make them a suitable candidate for catalyst support materials [65, 122–124].

Gas separation and storage

In order to mitigate the effects of global warming, especially due to high carbon emissions, and to develop sustainable materials for energy storage, materials with high selectivity towards selected gases and storage capacity of carbon dioxide (CO₂) and hydrogen (H₂) are required.

Robertson and Mokaya [126] have prepared highly microporous carbon xerogels, activated by potassium hydroxide at elevated temperatures, capable of significant CO₂ uptake at ambient conditions as well as high hydrogen storage capacity at -196 °C and 20 bar. Zubizarreta *et al.* [127] have developed a nickel-doped carbon xerogel material capable of high hydrogen storage capacity, also at -196 °C and 40 bar, with the textural properties of the xerogel support having a major influence on the final capacity of the material. Anas *et al.* [128] investigated RF aerogels as adsorbents for methane storage and they have noted that the micropore surface area had a major influence on the adsorption extent.

Vivo-Vilches *et al.* [66] have developed a carbon capture material based on RF carbon xerogel, catalysed by Cs₂CO₃. This highly microporous material was able to adsorb CO₂ from a mixture with methane with high selectivity, even at atmospheric pressure. Awadallah-F *et al.* [129] have tested a microporous RF carbon xerogel for affinity towards adsorption of CO₂, CH₄, and N₂, with the selectivity for the studied gases in the presented order. Successful separation of hexane isomers was performed by Vivo-Vilches *et al.* [101] using carbon aerogels and xerogels. Hollow fibre membranes made from a combination of RF xerogel particles and polysulfone were shown to have improved selectivity for CO₂/O₂ and CH₄/N₂ mixtures compared to unfilled polysulfone membranes [130]. Carbon cryogel and xerogel microspheres with a high level of microporosity, prepared by Yamamoto *et al.* [131], exhibited an amplified adsorption rate of nitrogen compared to oxygen at 25 °C. Dong *et al.* [132] have shown preferential adsorption of water from water/ethanol and water/isopropanol mixtures by applying microporous carbon membranes.

As can be seen from the presented literature, RF gel based materials seem to be a suitable candidate for carbon and hydrogen storage materials. It was also shown that a wide variety of gas mixtures that can be separated by using a RF gel based material, with textural properties tailored for a particular mixture.

Insulation

Minimising thermal losses to the environment is important in order to maximise process efficiency and save energy. An early study by Lu *et al.* [133] has reported RF aerogel monoliths with low values of thermal conductivity, superior to the values obtained for their silica counterparts at that time. The authors have argued that there is an optimal range of RF aerogel density that yields minimum values of thermal conductivity. Rey-Raap *et al.* [134] have successfully synthesised xerogel materials with thermal conductivity comparable to

commercial insulating materials. However, they have noted that the thermal conductivity of the material is determined by the textural properties. A composite material made from a carbon aerogel reinforced with polyacrylonitrile fibres, studied by Feng *et al.* [135], exhibited good mechanical properties, no cracking, and low values of thermal conductivity. The authors have suggested a more in-depth investigation into adjusting the properties of the aerogel matrix to further enhance the performance of these materials for thermal insulation. Ye *et al.* [109] have developed high-temperature thermal insulation materials from a composite comprising carbon aerogel with carbon fibres, that demonstrated remarkable mechanical properties and low values of thermal conductivity as well as density.

Electrode material

Development of electrode materials for batteries is important in order to meet the increasing demand for energy storage and other applications. Carbonised forms of RF gels are electrically conductive, making them potential candidates for electrode manufacture. Early work by Pekala *et al.* [61] reported carbon aerogel materials suitable for electrode manufacture, with performance dictated by structural characteristics. Carbon xerogel nanoparticles, prepared and analysed by Kakunuri *et al.* [136], were found to have satisfactory properties as lithium-ion battery anode materials, superior to graphite. Recently, Rey-Raap *et al.* [137] reported a more environmentally friendly procedure, using water instead of organic solvents, for porous carbon electrode manufacture; the authors stated that the electrode performance is related to the external surface area of the materials.

Water purification

Water contaminants pose a high risk to human health and aquatic wildlife, and a variety of pollutants come from industrial processes, pharmaceuticals, personal care products, as well as heavy metals. Removal of these substances is not a straightforward process, due to the range of contaminants present in the water supply.

One approach is to adsorb the harmful species from solution. Rodrigues *et al.* [138] have used pyrolysed carbon xerogels, prepared from Na_2CO_3 catalysed RF gels, for phenol adsorption from aqueous solution. They have observed a good level of phenol removal over a wide pH range with greater than 80 % recovery of the material after exposure to pure ethanol.

Yang *et al.* [139] have reported good adsorption capacities for heavy metals from aqueous solutions using nitrogen doped carbon xerogels, by adding melamine to the reaction mixture, with the adsorption capacity controlled by nitrogen content, rather than textural properties. A similar approach was used in the work of Veselá and Slovák [140], with nitrogen introduced from exposure to ammonia during pyrolysis, improving the adsorption capacity for Cu^{2+} and Pb^{2+} ions compared to undoped materials. Alternatively, gel materials have been used as catalysts for the degradation of organic pollutants. Fathy *et al.* [141] have developed a nitrogen and phosphorus doped carbon xerogel, achieved by adding melamine to the reaction

and exposing the gel to H_3PO_4 before pyrolysis, that acted as a metal-free catalyst for peroxide oxidation of 4-nitrophenol contaminant. Similar to previously mentioned studies, a dependence of catalytic performance on textural properties was observed.

A survey of the relevant literature, presented in this section, demonstrates the wide range of application for porous RF gels, potentially replacing some of the materials currently used by the industry. One of the important advantages of RF gels is the tailorability of their structures over a wide range of textural properties, which allows them to be adjusted for a given application, leading to an enhanced performance. However, in order to precisely control the structure of these materials, its formation needs to be understood in a better detail. Therefore, this work focusses on better understanding of the formation processes during RF gel manufacture and developing a computational model that could help optimise the material structure formed during the synthesis.

1.3 Aims and Objectives

Based on the review of relevant literature, discussed above, porous materials can find many uses in today's industries and RF gels are promising candidates for many of them. However, in order to make full use of their potential, and tailor their structure more precisely to a particular application, further investigation into how processing conditions affect the final properties of RF gels is required. Therefore, the aims of this work were set as follows:

- i) experimentally investigate the effects of the following processing parameters on the final textural properties of RF gels:
 - (a) sodium carbonate concentration
 - (b) solvent exchange method
 - (c) processing temperature
 - (d) drying method
 - (e) different sources of sodium ions
- ii) develop a computational model for aggregation and growth of RF clusters with a focus on:
 - (a) initial development of a code algorithm with static clusters, with subsequent implementation of cluster diffusion
 - (b) analysis of textural and fractal properties of generated structures
- iii) perform gas sorption modelling and textural analysis applied to:
 - (a) model pores

- (b) generated cluster structures
- iv) compare modelling results with experiments, to gain better insight into RF gel formation and step towards the ability to design manufacture routes for specific applications

1.4 Thesis structure

Chapter 2 covers background theory and review of literature related to this work, first introducing textural characterisation using gas sorption measurements, mercury porosimetry, and gas pycnometry, followed by a review of modelling techniques, such as kinetic Monte Carlo, previous work in modelling of porous materials, fractal analysis (including fractal dimensions and the Hurst exponent), and gas adsorption modelling.

Chapter 3 includes the experimental part of this study. The methodology used for sample preparation and analysis is described, and followed by discussion of results obtained for the investigation of the effects of sodium carbonate concentration, solvent exchange method, processing temperature, drying method, and addition of other sodium-containing salts on textural properties of dried RF xerogels.

Chapter 4 presents a computational model generating cluster structures in two dimensions, along with subsequent analysis of their textural and fractal properties. Solvent exchange within the model structures is explored as well, allowing evaluation of fractal properties of the pore space within the cluster structures.

Chapter 5 explores the application of gas sorption modelling. Firstly, gas sorption in model pores with well-defined shapes is explored, followed by extension to cluster structures from the previous chapter, allowing evaluation of trends in textural properties of these structures.

Chapter 6 summarises the main conclusions drawn from the previous chapters and Chapter 7 outlines potential future work, based on the findings of this work.

Chapter 2

Background theory

2.1 Textural characterisation

Most of the useful properties of porous materials are the result of their surface morphology; therefore, it is crucial to analyse the textural properties of these materials and understand the impact of processing conditions on the final materials. This section explores different techniques commonly used to evaluate textural properties of porous materials. First, the theory related to gas adsorption onto the surface of a porous material is discussed, along with the definition of related terms used within this work. This is followed by introducing Langmuir and Brunauer-Emmett-Teller theories, used for analysis of the accessible surface area. This chapter also presents Barrett-Joyner-Halenda theory and t-plot method utilised for porosity analysis and the principle of mercury intrusion porosimetry, allowing exploration of larger pores than gas sorption, is discussed. Finally, gas pycnometry, a technique that can be used to determine skeletal density of a porous material, is presented.

2.1.1 Gas adsorption

When a solid surface is exposed to a gas, some of the gas molecules will spontaneously adsorb onto the surface, leading to an increased concentration of gas molecules at the solid surface [142]. When adsorbed molecules penetrate into the bulk of an adsorbent material, it is classified as absorption. If the interactions between the gas molecules and surface sites are relatively weak and reversible, physisorption takes place. However, if chemical bonds are created, chemisorption occurs, which is not reversible and requires higher amount of energy for the molecules to desorb, compared to physisorption. Further differences between the two phenomena are the selectivity of chemisorption, due to a specific chemical bond being created, and that the extent of chemisorption is limited to monolayer coverage.

After adsorbing onto a surface, the adsorbed gas molecules differ from bulk gas molecules, particularly in their entropy, due to a lower degree of freedom. Figure 2.1 presents a diagram

of gas adsorption with adsorbate (gas molecules attached to the adsorbent surface) shown in blue and adsorptive (free gas molecules) shown in red.

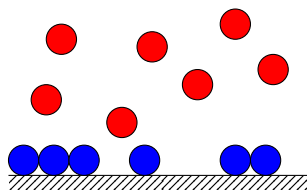


Figure 2.1 Schematic of gas adsorption on an adsorbent surface (hatched) with adsorbate particles in blue and adsorptive particles in red

Gas adsorption is a common technique used to obtain textural properties of porous materials. The International Union for Pure and Applied Chemistry (IUPAC) classifies pores [143], in the context of gas adsorption, into three ranges:

- i) *micropores* with widths approximately below 2 nm,
- ii) *mesopores* with widths in the range between 2 and 50 nm,
- iii) *macropores* with widths exceeding approximately 50 nm.

In addition to their size, pores can also be classified on the basis of their shape. Figure 2.2 presents a schematic drawing of a porous material particle. Pores that are completely encompassed within the solid material, such as the cavity labelled (a), are described as closed pores and do not contribute to gas adsorption, since they are not accessible to the gas from the outside. Pores that are open to the bulk gas, and are accessible to gas molecules, are classified as open pores, e.g. pores (b), (c), (d), (e), and (f) in Figure 2.2.

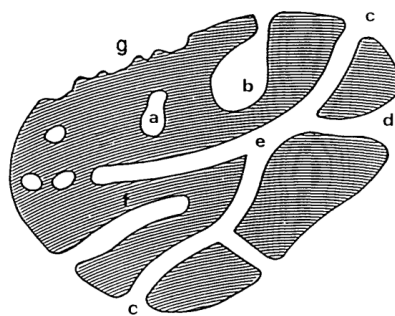


Figure 2.2 Schematic representation of a porous solid [144]

Open pores can be either open at one end (blind pores), like (b) and (f) in Figure 2.2, or open at both ends (through pores), e.g. (e) in the same figure. Based on their shape, different pores can be found in adsorbent materials, such as bottle-neck (ink-bottle) pores ((b) in Figure 2.2), conical (funnel shaped) pores ((d) in Figure 2.2), and cylindrical or slit pores [144]. Surface depressions that are wider than their depth, such as surface roughness, for example (g) in Figure 2.2, are not usually considered as pores [144].

Figure 2.3 presents a mechanism of gas adsorption onto a surface containing a micropore (left) and a mesopore (right) with increasing relative pressure of the adsorbing gas (p/p_0 , where p is the equilibrium pressure and p_0 is the saturation vapour pressure at the adsorption temperature) with gas molecules forming the first adsorbed layer are shown in blue, second layer in red, and subsequent layers in orange. Figure 2.3a presents the system at a low gas pressure, exhibiting sparsely distributed adsorbed gas molecules on the surface, with pore corner sites being preferential adsorption sites, due to higher energy of adsorption resulting from two pore walls interacting with gas adsorbed onto the sites. At a slightly increased gas pressure (Figure 2.3b), monolayer coverage occurs, where a single layer of adsorbed gas molecules is adsorbed on the whole surface and micropores are filled. This is followed by another layer adsorbing onto the first one, as presented in Figure 2.3c. At this point small mesopores may fill, while their larger counterparts do not contain enough adsorbed gas to fill them. Finally, at high relative pressures (Figure 2.3d), all pores up to the upper mesopore range limit are assumed to be filled with a condensed liquid.

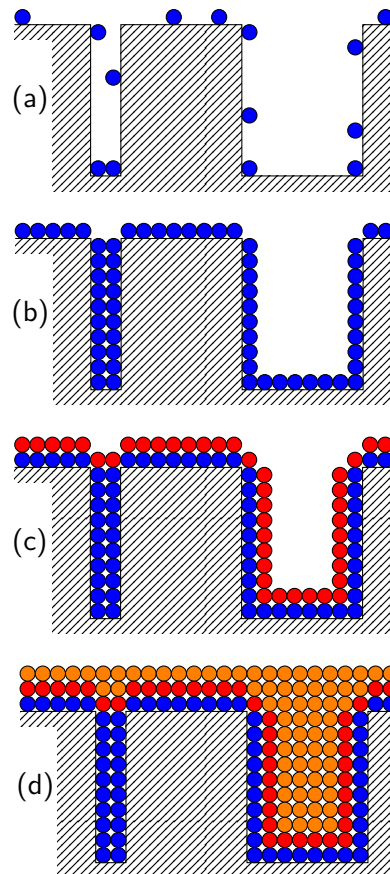


Figure 2.3 Schematic drawing of gas adsorption mechanism with increasing gas pressure (from (a) to (d)) for a system containing a micropore (left) and a mesopore (right); (a) gas molecules start to adsorb on the sorbent surface, (b) monolayer formation and micropore filling, (c) multilayer formation, and (d) further multilayer formation and mesopore filling

Experimental gas sorption data, collected below the critical point, is usually expressed in form of a sorption isotherm, plotting the relation between p/p_0 and the amount (or volume)

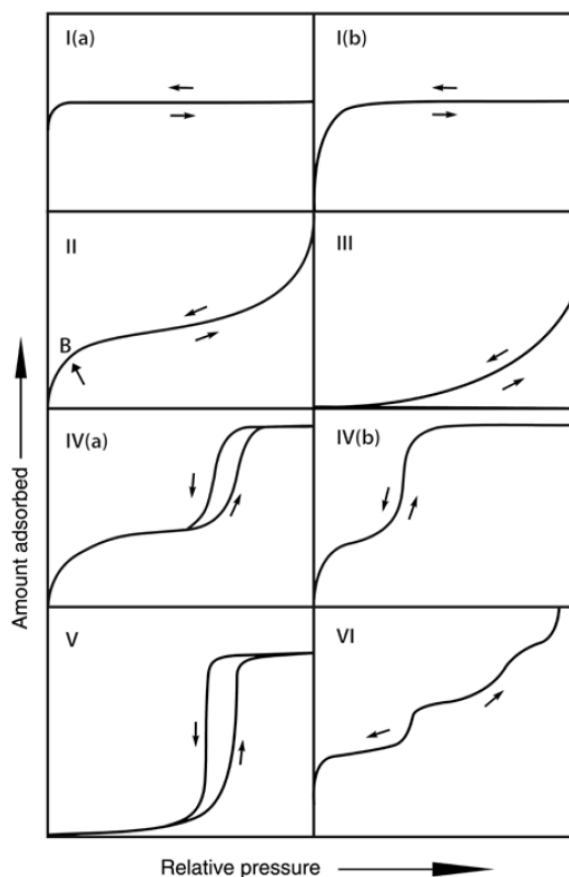


Figure 2.4 Classification of gas physisorption isotherms according to IUPAC recommendations [142]

adsorbed, at constant temperature. Adsorption data is obtained by gradually increasing p/p_0 , typically followed by decreasing p/p_0 in order to obtain desorption data. Based on the most recent report by IUPAC, regarding analysis of gas physisorption onto porous materials [142], there are six basic types of gas sorption isotherm shapes, with Type I and IV including two subtypes each, as presented in Figure 2.4. When adsorption and desorption branches of an isotherm do not overlap in a certain p/p_0 range, hysteresis is observed. Similar to isotherm shapes, hysteresis loops are classified using five types, with Type H2 comprising two subtypes, as presented in Figure 2.5.

Type I isotherms are associated with monolayer formation without subsequent multilayer adsorption, typical for microporous materials, where the external surface area is small, compared to the micropore surface area. The plateau at higher values of p/p_0 is equivalent to adsorption capacity of the material, and can be used to determine total pore volume and accessible surface area. Materials with a narrow distribution of small micropores exhibit a steep uptake at low values of p/p_0 (Type I(a)), while a more gradual increase, and a less pronounced shoulder, suggests a material containing a wider distribution of micropores, possibly with narrow mesopores present (Type I(b)). Type II isotherms, exhibiting a shoulder (point B in Figure 2.4) at lower values of p/p_0 and increasing gas uptake at higher values

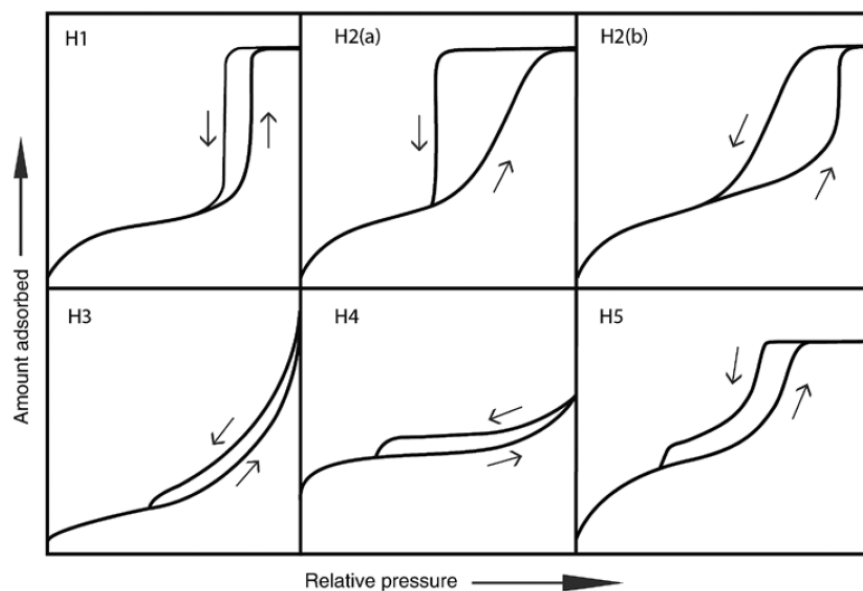


Figure 2.5 Classification of hysteresis loops for gas physisorption isotherms according to IUPAC recommendations [142]

of p/p_0 , without a plateau, correspond to monolayer formation followed by unrestricted multilayer adsorption, common for macroporous and non-porous materials [142]. In this case, the gas uptake at the highest value of p/p_0 is not equal to the total pore volume, because of the lack of a plateau, the pores present on the surface are not filled at this pressure. Weak interactions between the adsorbent and adsorbate lead to a Type III isotherm shape. At low values of p/p_0 , adsorption is limited and only when enough adsorbed species are present on the surface, multilayer adsorption occurs, without completing monolayer coverage, and condensation preferred to adsorption. This shape is usually obtained for macroporous or non-porous solids exhibiting weak interactions with the adsorbing gas [142], e.g. water vapour adsorption onto carbon black. Mesoporous adsorbents, such as porous organic and inorganic gels, give Type IV isotherms and with a monolayer-multilayer transition at lower pressures and a plateau at high p/p_0 . The difference between Type IV(a) and Type IV(b) is the presence of a hysteresis loop for the former, associated with capillary condensation. Similar to Type III, for a system with weak adsorbent-adsorbate interactions and a microporous or a mesoporous material, Type V isotherm is obtained. The hysteresis loop observed is attributed to condensation of adsorbing gas in mesopores and the plateau at high values of p/p_0 is related to the adsorption capacity of the adsorbent material. Type VI isotherms are given by adsorption on a highly uniform non-porous surface, such as a graphite-like surface [142] with the steps in gas uptake attributed to stepwise layer-by-layer adsorption.

While the isotherm type, as discussed above, is mostly related to the size of the pores present within the material, the hysteresis loop shape (Figure 2.5) is linked to pore structure. A narrow mesopore distribution of uniform shape leads to steep changes in amount of adsorbed

gas in a narrow range of p/p_0 , typical for a Type H1 loop, which is observed e.g. for templated silica and mesoporous carbon materials [142]. More complex pore structures, with important effects due to the pore network present, give Type H2 loops. While Type H2(a), with a steep section of the desorption branch, is attributed either to percolation (or pore-blocking) of narrowly distributed pores or to cavitation-induced evaporation, the more gradual decrease in the desorption branch for Type H2(b) is caused by a wider distribution of the pore necks. Both types of H2 loops can be observed for some types of porous silica materials or porous glasses [142]. If the macropores present within the pore structure are not completely filled or the material consists of non-rigid aggregates of plate-like particles, such as for some clays, a Type H3 loop is observed. The Type H3 loop can be distinguished by the shape of the adsorption branch resembling a Type II isotherm, described in more detail above, and a cavitation-induced closing of the loop at the lower end. If the isotherm exhibits higher uptake at low p/p_0 values, as typical for a Type I isotherm, while demonstrating a shape similar to a Type II isotherm at higher p/p_0 , the presence of micropores leads to a Type H4 loop, common for some mesoporous zeolites, aggregated zeolite crystals, or micro-mesoporous carbons [142]. The Type H5 loop, the least commonly observed amongst the types discussed here, is obtained for certain specific pore structures, e.g. plugged hexagonal templated silicas, with both open and partially blocked mesopores [142]. While the isotherm shape, and hysteresis loop, if present, gives an indication of the approximate shape and size of the pores present in the material, various theories were developed in order to quantify accessible surface area and porosity, as discussed in the following sections.

2.1.2 Surface area determination

Assuming that the adsorbing gas forms a monolayer on the accessible surface of the adsorbent, the value of surface area can be calculated, using the cross-sectional area of the adsorbing molecules and assuming ideal packing. Over the years, various theories, attempting to extract the value of accessible surface area from a gas sorption isotherm, have been developed. In this section, the two most commonly used theories, namely Langmuir and BET, are discussed.

Langmuir theory

In 1918, Langmuir developed a theory for gas adsorption isotherm analysis based on monolayer formation on a flat solid surface [145]. Langmuir theory is based on the following assumptions:

- i) All surface sites are energetically identical and each site can contain only one adsorbate molecule at a time.
- ii) Only monolayer coverage can occur, without subsequent multilayer formation.
- iii) There are no interactions between neighbouring adsorbing sites or adsorbate molecules.

The rate of adsorption is proportional to the adsorption rate constant (k_a), the gas pressure (p), and the amount of remaining unoccupied surface sites (Equation 2.1), while the rate of desorption depends only on the amount of surface sites occupied by the adsorbate molecules (θ) and the desorption rate constant (k_d), as presented in Equation 2.2.

$$\text{rate of adsorption} = k_a p(1 - \theta) \quad (2.1)$$

$$\text{rate of desorption} = k_d \theta \quad (2.2)$$

At dynamic equilibrium, the rates of adsorption and desorption are equal; thus, Equation 2.3 can be derived from Equations 2.1 and 2.2.

$$k_a p(1 - \theta) = k_d \theta \quad (2.3)$$

Since both k_a and k_d are constants for a given system, they can be merged into a single constant, $K = k_a/k_d$. This leads to the Langmuir equation, relating surface coverage to gas pressure, as presented in Equation 2.4.

$$\theta = \frac{k_a p}{k_d + k_a p} = \frac{K p}{1 + K p} \quad (2.4)$$

Substituting volumes for surface coverage ($\theta = V/V_m$), and rearranging Equation 2.4, provides a linearised version of the Langmuir equation (Equation 2.5), where V is the volume of gas adsorbed on the sample surface and V_m is the volume of gas at complete monolayer coverage.

$$\frac{p}{V} = \frac{1}{K V_m} + \frac{p}{V_m} \quad (2.5)$$

The Langmuir theory, especially in its linear form, as presented in Equation 2.5, is still commonly used for microporous adsorbents, where subsequent multilayer adsorption is restricted by pore dimensions. The isotherms for these materials, classified as Type I [142] (Figure 2.4), are usually described well using this theory, allowing surface area evaluation. Specific surface area (S_A in m^2/g) of a sample can be obtained using the aforementioned V_m in Equation 2.6, where A is the cross-sectional area of the adsorbate molecules (taken as $1.62 \times 10^{-19} \text{ m}^2/\text{molecule}$ for nitrogen), N_A is Avogadro's constant ($6.022 \times 10^{23} \text{ molecule/mol}$), and m is the mass of the adsorbent sample, in grams.

$$S_A = \frac{V_m A N_A}{m} \quad (2.6)$$

Brunauer-Emmett-Teller theory

Expanding on Langmuir's theory, Brunauer, Emmett, and Teller (BET) accounted for multilayer formation in their theory, developed in 1938 [146]. Similar to the hypothesis made by Langmuir, BET theory is based on the following assumptions:

- i) Adsorption takes place on surface sites that can contain only one adsorbate molecule at a time and the energy associated with the formation of the first layer is the heat of adsorption.
- ii) Multilayer formation, due to interactions of adsorbate molecules with the adsorptive, can occur, and the energy associated with the additional layers is the heat of liquefaction.
- iii) Multilayer formation is unlimited and the amount adsorbed tends to infinity at saturated vapour pressure ($p/p_0 = 1$).

The linear form of the BET equation, commonly used to obtain the value of BET accessible area, is presented in Equation 2.7, where p/p_0 is the relative pressure, V is the volume of gas adsorbed, V_m is the monolayer coverage gas volume, and C is the BET constant.

$$\frac{p/p_0}{V(1 - p/p_0)} = \frac{C - 1}{V_m C} \times p/p_0 + \frac{1}{V_m C} \quad (2.7)$$

The C constant reflects the difference between the heats of adsorption (E_A) and liquefaction (E_L) as $C = \exp\left(\frac{E_A - E_L}{RT}\right)$. Therefore, a very low value of C is related to very weak adsorbate-adsorbent interactions, such as for a polar gas adsorbing onto a non-polar surface (e.g. water vapour and carbonaceous adsorbent). On the other hand, a high value of the constant suggests very strong interactions, more similar to chemisorption rather than physisorption, where the assumptions of BET theory are not valid.

To obtain the value of accessible surface area, the values of slope ($\frac{C-1}{V_m C}$) and intercept ($\frac{1}{V_m C}$) from Equation 2.7 are used to calculate V_m , which is subsequently converted to BET surface area using Equation 2.6.

One of the shortcomings of BET theory is its limited applicability to materials containing micropores. However, Rouquerol, Llewellyn, and Rouquerol [147] published a set of recommendations in order to obtain objective and reproducible information when applying BET theory to a given isotherm, especially in case of Type I, combined Type I and II, or I and IV isotherms. Their suggested set of recommendations is as follows:

- i) The value of C constant should be positive, a negative value indicates that the BET theory is not applicable in the used p/p_0 range.
- ii) Only data within the range where the term $n(1 - p/p_0)$ continuously increases with p/p_0 should be used.
- iii) The value of p/p_0 corresponding to monolayer coverage (V_m) should be within the p/p_0 range used to determine C and V_m .

However, even though BET theory is one of the most commonly applied analyses to obtain surface area of experimental adsorbent samples, often not all of the assumptions postulated

in the theory are met. Therefore, the surface area obtained using BET theory should be treated as an indication of the accessible surface area but not necessarily as the actual value. The calculation algorithm used in this work to obtain values of accessible surface area, based on BET theory, is discussed in more detail in Section 3.1.5.

2.1.3 Porosity analysis

Accessible surface area is a very useful measure of the performance of porous materials; however, for some applications, such as thermal insulation, drug delivery, and in catalyst supports, it is crucial to assess information about the porosity of the material as well. For this purpose, researchers developed the BJH theory, used to obtain pore size distribution within the mesopore region, and the t-plot method, used to calculate the micropore volume and surface area; these are presented within this section.

Barrett-Joyner-Halenda theory

In 1951, Barrett, Joyner, and Halenda (BJH) developed a theory in order to obtain mesopore size distributions and pore volumes from experimental gas sorption isotherms [148]. The theory uses the Kelvin equation, presented in Equation 2.8, where p/p_0 is the relative pressure, γ is the liquid-vapour surface tension, V_m is the liquid molar volume, r is the radius of curvature, R is the universal gas constant, and T is the absolute temperature.

$$\ln \left(\frac{p}{p_0} \right) = -\frac{2\gamma V_m}{rRT} \quad (2.8)$$

The theory assumes that when the relative pressure is reduced, the core liquid of cylindrical pores with radius larger than the corresponding value of r from the Kelvin equation evaporates. After evaporation of the core, there is some adsorptive remaining on the pore walls and the thickness of the residual adsorbed layer is assumed to depend on the adsorptive-adsorbate combination. There are empirical equations relating the adsorbed layer thickness and relative pressure for several types of adsorbent surfaces, e.g. the so-called carbon black equation reported in the ASTM standard D-6556-17 [149]. However, for all relations, the thickness of the remaining layer of adsorbed gas decreases with decreasing pressure.

The calculation is usually based on the desorption branch of an isotherm; although, it can be applied to the adsorption branch, with some adjustments, as well. The theory assumes that the amount of gas desorbed within a given pressure interval can be attributed to only gas desorbed from the walls of previously opened pores, or core evaporation as well. If the amount of gas desorbed in a particular p/p_0 interval is higher than the calculated amount desorbed from previously opened pores, it is assumed that this difference is due to new pores opening, and an average pore is used to represent these pores. The algorithm for evaluating pore size distributions in this work is presented in more detail in Section 3.1.5.

t-plot method

A method based on the work by Lippens and Boer [150], also called the t-plot method, compares an isotherm to a standard Type II isotherm and can be used to calculate micropore volume and surface area of an adsorbent sample. A statistical thickness of adsorbed gas layer (t), discussed in more detail in the previous section, is used to convert the isotherm into a so-called t-curve, where t is used for the x-axis instead of p/p_0 .

For a sample with no micropores present, the t-curve is linear and its intercept is equal to zero, whereas a t-curve for a sample containing micropores deviates from linearity and its positive intercept is related to the micropore volume (V_μ) and the slope to the external surface area (S_{ext}). Micropore surface area (S_μ) can be obtained from $S_\mu = S_{\text{BET}} - S_{\text{ext}}$. Adsorption data analysis using the t-plot method is discussed in more detail in Section 3.1.5.

2.1.4 Mercury porosimetry

For materials containing macropores in their structure (pores above 50 nm per IUPAC classification [143]), other techniques, in addition to gas sorption measurements, can be used. A common technique for macropore analysis is mercury intrusion porosimetry (MIP), due to the high surface tension value of mercury, and the fact that it does not wet most surfaces. The measurement is performed by gradually increasing applied pressure and measuring the volume of mercury that enters the pores at a given pressure. Initially, large pores within the analysed sample are filled, subsequently filling smaller pores at increasing pressures (pressure and pore size are inversely proportional). The size of pores being filled at a particular pressure is calculated using the Washburn equation, shown in Equation 2.9, where L is the pore diameter, γ is the mercury surface tension (0.48 N/m), θ is the contact angle of mercury on the sample surface (usually taken as 140°), and P is the applied pressure [151].

$$L = -\frac{4\gamma \cos \theta}{P} \quad (2.9)$$

However, due to the high pressures required to force mercury into the pore structure, materials with insufficient mechanical strength can be compressed or even damaged in the process [152]. This may lead, not only, to inaccurate volume readings during an MIP measurement, due to contributions to the volume increase caused by structure collapse, but can also affect or even destroy smaller pores before they are explored by the measurement. Therefore, the applicability of this technique to softer materials, such as organic porous gels, is limited, due to the aforementioned effects.

2.1.5 Gas pycnometry

In order to obtain the solid skeleton density of a porous material, gas pycnometry measurements are usually performed. The density value is determined using a known mass of a

sample and measuring its volume with a pycnometer. A gas commonly used for this purpose is helium, due to its small atom size and inert character, but nitrogen can be utilised as well.

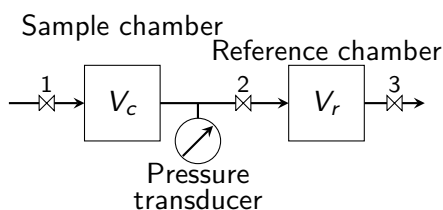


Figure 2.6 Schematic drawing of a gas pycnometer

The working principle of a gas pycnometer is based on the measurement of gas pressure difference after expansion from a chamber containing the sample to a reference chamber of known volume, allowing calculation of the volume excluded by the measured sample. A schematic drawing of a gas pycnometer is presented in Figure 2.6. After purging both chambers with the analysis gas, the sample chamber is pressurised to a selected pressure (closing valve 2 in Figure 2.6), followed by closing valve 1. Once the pressure reading within the sample chamber is stable, as measured using the pressure transducer, valve 2, between the sample chamber and the reference chamber, is opened, while valve 3 stays closed. This allows the gas from the sample chamber to expand into the reference chamber of known volume and the pressure is measured again. The gas volume displaced by the sample (V_s) is calculated using Equation 2.10, where V_c is the volume of the empty sample chamber, V_r is the volume of the reference chamber, P_1 is the first pressure value (before expansion), and P_2 is the second pressure value (after expansion). Values of V_c and V_r are known prior to measurement, via a calibration step.

$$V_s = V_c + \frac{V_r}{1 - \frac{P_1}{P_2}} \quad (2.10)$$

An important factor to take into account when selecting a gas to use in a measurement is its inertness with the analysed material, and that it exhibits no adsorption of the gas at measurement conditions and no absorption into the bulk of the material. Helium, due to its very small atomic size, might penetrate into some materials, causing an inaccurate volume reading; therefore, nitrogen is sometimes preferred.

2.2 Modelling techniques

This section provides a brief review of previous applications of the modelling techniques, and underpinning theory, used within this work. The Monte Carlo method, used to generate model cluster structures in this work, is presented, as well as previous studies involving models of porous materials. Fractal properties of porous materials can add useful information, in addition to e.g. textural characteristics; therefore, fractal analysis methods are explored,

including fractal dimensions and the Hurst exponent. As gas sorption is a widely used experimental technique for textural analysis of porous materials, and gas sorption calculations are used in this work to study generated cluster structures, this section also considers methods for gas sorption modelling previously reported in the literature.

2.2.1 Kinetic Monte Carlo

Monte Carlo simulation methods have been used for decades, allowing researchers to explore various physical and mathematical problems using random numbers. Kinetic Monte Carlo (kMC) introduces dynamic evolution of the system with the addition of time. One of the advantages of kMC methods is the ability to explore longer time scales compared to some other modelling methods, e.g. molecular dynamics [153].

There are two basic types of kMC methods, null-event and rejection-free algorithms [154]. In the null-event (also called rejection) kMC method, each move from one state to another is accepted or rejected with a selected probability and the transition rates are calculated at each simulation step. Moves that reduce the overall system energy are always accepted, while moves that lead to an energy increase are accepted with a lower probability (< 1). Conversely, in the rejection-free method all system moves are accepted, regardless of their impact on system energy; thus, making the algorithm more efficient in general, since every simulation step evolves the system further. However, transition rates are required to be known before the simulation, which can be an issue for some applications. In this work, the rejection-free kMC method is used and the diffusion rates scale inversely with species size.

In a kMC algorithm, each process has a corresponding rate constant (k_i), determining the probability of this process occurring during a move. Depending on the system, these rate constants are based on different conditions. The sum of all the rate constants adds up to the total kMC sum (k_{sum}), which can change throughout the simulation. The individual rates, presented as boxes of different height on the left in Figure 2.7, are translated into a cumulative sum for the computational algorithm (right in Figure 2.7). In each step, a number r is randomly drawn between 0 and 1 and is multiplied by the total kMC sum in order to determine the move, based on the cumulative sum of the rate constants. This

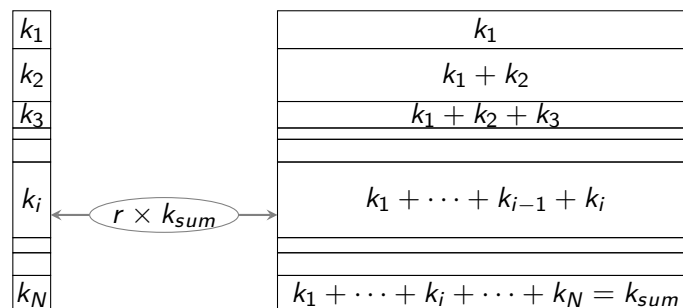


Figure 2.7 Schematic drawing of selecting a move during kinetic Monte Carlo algorithm

number ($r \times k_{sum}$) is used to select the move, as presented in Figure 2.7, where move k_i was selected due to the value being $k_1 + \dots + k_{i-1} > r \times k_{sum} > k_1 + \dots + k_i$ in this step.

2.2.2 Modelling of porous materials

Studies have previously focused on the generation of porous model gel structures that could be compared to those obtained experimentally. Early works by Meakin [155] and Kolb *et al.* [156] introduced a two-dimensional lattice model of diffusion-limited cluster-cluster aggregation. These models were developed with colloidal particle aggregation in mind, without the primary particles changing size, which is the case for agglomeration of metal or polymeric particle sols. Some other works included reordering of the initially formed structures to represent patterns observed in silica gel materials [157]. However, the bonds in silica gels are more likely to undergo hydrolysis, especially under acidic conditions, than their organic counterparts. In this work, the mechanism for base-catalysed RF gels is considered, where hydrolysis of the formed ether bonds is not favoured; therefore, it does not lead to structural reorganisation at the later stages of gelation [98].

Gavalda *et al.* [158, 159] modelled carbon aerogel structures using random close-packed, slightly overlapping, spheres with mesopores between the particles, and micropores incorporated within the particles. However, all particles were assumed to be equal in size, which is not always the case in a real system, where particles can vary over a range of sizes. Work by Morales-Flórez *et al.* [160, 161] used an algorithm with randomly-packed spheres in several hierarchically-ordered levels in order to simulate silica (SiO_2) and titania (TiO_2) porous materials. Even though the final structures obtained vary in shape, the primary spherical particles used to form the final clusters are all identical in size. A molecular dynamics study by Ferreiro-Rangel and Gelb [162] used a coarse-grained model for silica aerogel simulation; although again, using a uniform size of primary particles, which were allowed to diffuse and bond together to form the final structure. These examples from the literature show a trend of using monodisperse particles in order to model structures for porous xerogel and aerogel materials, which might not reflect all of the characteristics of these materials, since experimentally obtained aero- and xerogels are not formed by particles of identical size [163]. From a survey of the available literature, no study prior to this has tried to replicate the formation of gel structures starting from monomeric species, through nucleation and growth of primary particles, to the final aggregated state.

2.2.3 Fractal analysis

Fractal analysis of porous materials has been performed, in the past, using both simulations [162, 164] and experiments, through techniques including dynamic light scattering [96] and small angle X-ray scattering [51, 58, 96]. This section explores the basis of fractal dimensions and the Hurst exponent.

Fractal dimensions

The term fractal (fractional in the original paper) dimension was originally discussed by Mandelbrot as early as 1967 [165]. Fractal dimension is related to the complexity of a structure and how a pattern in the structure changes with analysis scale. One of the earliest examples of a well-defined mathematical fractal structure is a Koch curve, with its construction shown in Figure 2.8 [166]. The process of Koch curve generation begins with a line segment, initiator, denoted $n = 0$ in Figure 2.8. For a 60° indentation angle, the initiator line is divided into thirds and the middle segment is replaced with two lines, of length equal to each segment, at a 60° angle, forming a unilateral triangle ($n = 1$ in Figure 2.8). This process is repeated for all subsequent steps ($n = 2, 3, 4, \dots$), until a Koch curve is obtained for $n = \infty$. The fractal dimension of a Koch curve generated with indentation angle 60° is ~ 1.262 [166].

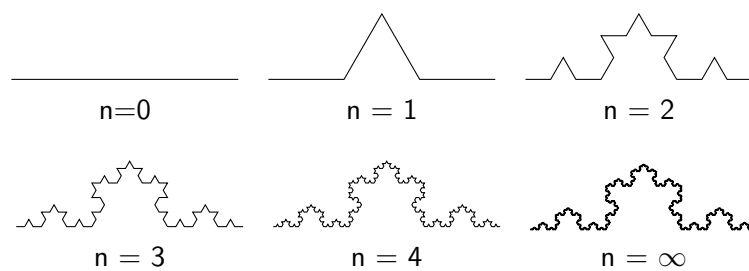


Figure 2.8 Construction of the Koch curve, where n is the number of construction steps

Two example Koch curves, generated with different indentation angles, are presented in Figure 2.9. The structure with a lower indentation angle (Figure 2.9a) exhibits a fractal dimension of 1.053, while the value for the higher angle counterpart (Figure 2.9b) is 1.404 [167]. The increased fractal dimension for the latter structure is due to its greater space-filling compared to the former.



Figure 2.9 Koch curves generated with indentation angle (a) 30° and (b) 70° [167]

For mathematical fractal structures, such as the Koch curves mentioned above, different ways of expressing the fractal dimension, introduced below, usually provide the same answer. This is due to the fact that for a mathematical fractal object, such as the Koch curves, each fragment is an identical to the original. However, real materials exhibit statistical self-similarity; therefore, their estimated fractal dimensions may vary, depending on the approach.

A number of methods can be used to characterize a structure in terms of a fractal dimension, including correlation dimension (D_C), box-counting dimension (D_B), and information dimension (D_I). These dimensions are related to each other dimensions through $D_C \leq D_I \leq D_B$ [168]. In this section, fractal dimensions in a two-dimensional space are discussed.

The box-counting dimension (D_B), defined in the simplest way from the dimensions discussed here, is determined by covering the studied object by a number (N) of boxes (squares) with varying side length r . The value of D_B is then obtained from Equation 2.11 [165].

$$D_B = \lim_{r \rightarrow 0} \frac{\log(N)}{\log(1/r)} \quad (2.11)$$

Figure 2.10 presents an example for box-counting dimension analysis method with another Koch curve, the fractal dimension of which is ~ 1.26 . Grids with boxes of varying side length (δ in Figure 2.10) are constructed and the number of boxes containing the studied structure are counted. The scaling of N with r is then used to evaluate D_B , using Equation 2.11.

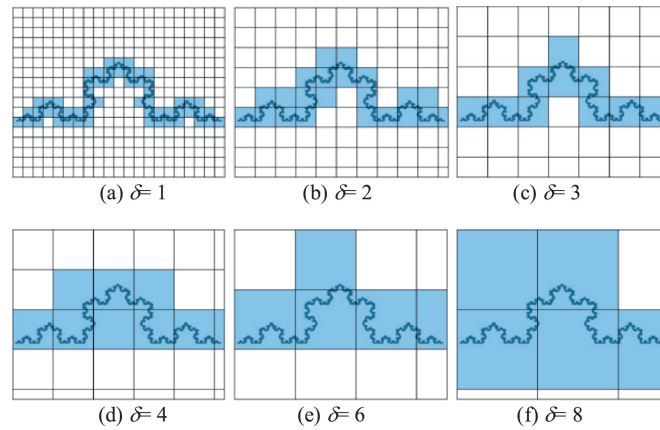


Figure 2.10 Example of box counting dimension analysis [169]

The information dimension (D_I), similar to the aforementioned box-counting dimension, is obtained by covering the analysed object by a set of boxes with different dimensions; however, in addition, it accounts for how much of the object is contained in each box [166]. Equation 2.12 is used to extract D_I of a system, where N is the number of boxes, P_i is the probability of a part of the object being within box i , and r is the box side length.

$$D_I = \lim_{r \rightarrow 0} \frac{-\sum_{i=1}^N P_i \log(P_i)}{\log(1/r)} \quad (2.12)$$

The correlation dimension (D_C), is related to scaling of the correlation integral ($C(r)$ in Equation 2.13) with distance (r) as $C(r) \sim r^{D_C}$ [168]. $x(i)$ and $x(j)$ in Equation 2.13 are

either coordinates or space vectors of two points contained within the analysed structure.

$$C(r) = \lim_{N \rightarrow \infty} \frac{1}{N^2} \sum_{i,j=1; i \neq j}^N \theta(r - |x(i) - x(j)|) \quad (2.13)$$

The Heaviside function (θ) in Equation 2.13 is a step function defined as in Equations 2.14 and 2.15.

$$\theta(r - |x(i) - x(j)|) = 0 \quad \text{if } (r - |x(i) - x(j)|) < 0 \quad (2.14)$$

$$\theta(r - |x(i) - x(j)|) = 1 \quad \text{if } (r - |x(i) - x(j)|) \geq 0 \quad (2.15)$$

Finally, the value of D_C can be obtained using Equation 2.16, or the slope of a log-log plot of correlation integral with r provides an estimate of D_C . For a finite number of data points, an estimate of the correlation integral, in form of a correlation sum, can be used, as discussed in Section 4.3.1.

$$D_C = \lim_{r \rightarrow 0} \frac{\log C(r)}{\log(r)} \quad (2.16)$$

Hurst exponent

The Hurst exponent (H) is related to fractal dimension [170] and can be used to describe the persistence of a time series [171]. Figure 2.11 presents time traces for walkers with

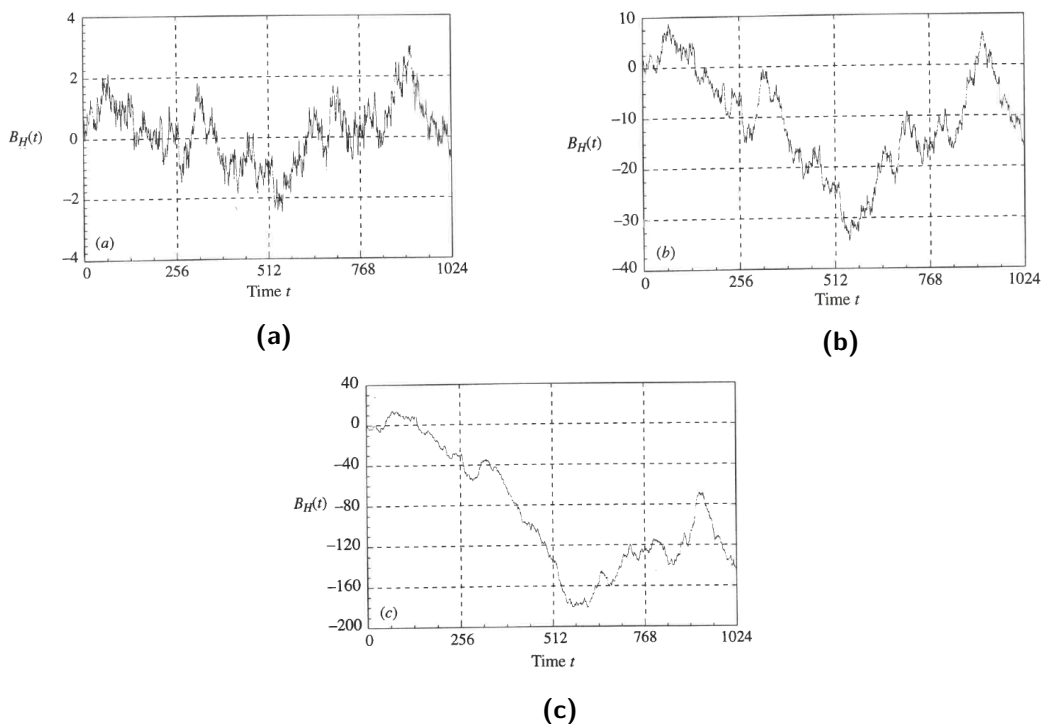


Figure 2.11 Time traces for walkers with the value of the Hurst exponent (a) 0.2, (b) 0.5, and (c) 0.8 [166]

varying values of the Hurst exponent, where $B_H(t)$ is the displacement from the origin at time t . Consider a random walker on a two-dimensional lattice; a particle exhibiting Brownian motion on an empty lattice, with no obstacles, has a value of $H = 1/2$. The Brownian particle exhibits an erratic trace (Figure 2.11b) and is equally likely to diffuse away from the origin (as around time 512 in Figure 2.11b) and return back to the origin (as around time 900 in Figure 2.11b). A random walker with a lower value $H < 1/2$ is described as antipersistent, which means that it is more likely to remain closer to the origin than a freely diffusing particle. This can be observed in Figure 2.11a, where the maximum displacement exhibits a lower value, compared to the Brownian particle in Figure 2.11b. A value of $H > 1/2$ is attributed to persistent walkers, meaning they are more likely to leave the origin with a smoother, less rugged trace. An example trace for a persistent walker is presented in Figure 2.11c and it can be seen that the maximum displacement is much higher, compared to both Brownian and antipersistent walkers, presented in Figures 2.11b and 2.11a, respectively. If one now considers a random walker on a plane with obstacles, its trace will become more antipersistent, tending to confine it to a smaller area. As the obstacle structures become more complex and the voids more tortuous, thereby restricting the movement of the walker, the value of H might be expected to approach $\sim 1/3$, the value found at the percolation threshold [172].

2.2.4 Gas adsorption modelling

Modelling gas sorption helps compare computational models of porous materials to experimental adsorbent samples and, in addition, also enhances the understanding of processes occurring during gas sorption experiments and their dependence on various parameters, such as the pore structure and experimental conditions. Therefore, a significant research interest has been put into studying gas sorption models, utilising various approaches in both simple pores with well-defined structures, as well as complex representations of real porous materials. Amongst the different approaches previously reported for studying gas sorption processes in the literature are molecular dynamics [173–175], Monte Carlo [173, 176], and mean field kinetic theory [177–184].

Studies by Leung, Luzar, and Bratko [173] and Sharma and Debenedetti [174] investigated water evaporation in capillaries with hydrophobic surfaces. The former paper utilised a combination of grand canonical ensemble Monte Carlo and molecular dynamics [173], while the latter combined molecular dynamics in conjunction with forward flux sampling technique [174]. Despite their different approaches, both studies reported similar observations for investigated capillary effects. Sarkisov and Monson investigated adsorption in pores with simple geometry using molecular dynamics, with the results agreeing with grand canonical Monte Carlo simulations [175]. However, the desorption processes in ink bottle pores observed within their work did not agree with the classical theory, due to the pore bulk emptying while the necks remained filled.

An early study by Kim and Landau investigated multilayer adsorption using a lattice gas model with Monte Carlo method, discussing discrepancies between their approach and that of mean field theory [185]. Page and Monson used Monte Carlo simulations in order to explore phase diagrams of a model system representing methane adsorption in a silica xerogel [176]. The authors have ascribed the two phase transitions observed in their system to a vapour-liquid bulk transition and a matrix wetting due to confinement effects.

In addition to the aforementioned gas sorption modelling approaches, Sarkisov and Harrison [186] developed a computational tool for a direct calculation of textural properties, such as accessible surface areas and pore size distributions, without modelling the gas sorption isotherm.

A model reported by Monson [177, 187], using mean field kinetic theory for lattice gas adsorption, has been recently applied to both model pores [178–183], as well as more complex simulated pore structures mimicking real materials [184]. Edison and Monson analysed gas sorption processes in model pore networks with varying pore sizes [178] and mesopores with fluid mixtures [179]; and Schneider, Valiullin, and Monson used simulations with the aforementioned model to study the impact of various pore structures on gas adsorption equilibration, observing pore filling and emptying for long pore systems with ink bottle structures [181]. Filling and emptying of slit pores, with associated liquid bridge formation, was reported in the work by Casselman, Desouza, and Monson [182]. The phenomena observed using the mean field theory were compared to other methods in order to confirm their observations. Edison and Monson compared capillary condensation during gas adsorption using dynamic mean field theory and dynamic Monte Carlo simulations, stating that the mean field theory provides qualitatively accurate results [180]. This was further verified by comparing to grand canonical molecular dynamics simulations [183]. A significant advantage of the mean field approach, compared to other models discussed above, is the applicability to larger pore structures and high precision [188].

Understanding gas sorption in simple model pores helps to, subsequently, interpret sorption data for more complex porous structures leading to a variety of methods and approaches for gas sorption modelling in the literature. However, due to the lattice-based nature of the aforementioned model by Monson [177], and its previous application to both simple model pores and simulated representations of porous materials, it was used in this work to assess the adsorption behaviour of the generated cluster structures in Chapter 5. However, in this work, only equilibrated sorption data is considered without analysing the dynamics, for comparison with experimental values obtained here.

As mentioned above, a variety of pore shapes and dimensions was investigated previously in the literature using various models. Therefore, pore structures likely to be found within RF gels and generated cluster structures are explored in this work using the same model and parameters in order to allow comparison between different model pores and cluster structures.

Chapter 3

Experimental study

3.1 Methodology

The following section describes methodology used in the experimental part of this work. First, the procedures used for resorcinol-formaldehyde (RF) gel manufacture are described, including the synthesis (sol preparation, gelation, and curing), solvent exchange, and drying. Subsequently, nitrogen sorption measurements and their analysis for textural properties of RF xerogel samples are discussed.

3.1.1 Gel synthesis

In order to investigate the effect of chosen process variables on the textural properties of subcritically dried resorcinol-formaldehyde (RF) xerogels, a series of gel samples was prepared. The total volume of liquids used in this study was kept constant at 60 ml, including water added to the solution along with water and methanol coming from the formalin solution. Resorcinol, formaldehyde, and catalyst salt were all considered as solids and the solids content was kept constant at 20 w/v% (20 g of total solids per 100 ml of total liquids). All chemicals were used as received from the supplying company, and deionised water was produced in-house (Millipore Elix[®] 5 with Progard[®] 2).

First, 50 ml of deionised water was added to a glass jar, shown in Figure 3.1 (diameter 9 cm). The appropriate amount of resorcinol (SigmaAldrich, ReagentPlus, 99%) was weighed out using a balance with accuracy to 10^{-5} g and the actual mass of added resorcinol was noted. The resorcinol was added to the jar and dissolved under stirring with a magnetic stirrer and a stirrer bar. The catalyst used for all the samples was sodium carbonate (Na_2CO_3 , SigmaAldrich, anhydrous, $\geq 99.5\%$), except for samples with different sources of sodium ions, studied in the last part of the experimental study, where sodium chloride (NaCl , SigmaAldrich, Redi-Dri[™], anhydrous, $\geq 99\%$) or sodium sulphate (Na_2SO_4 , SigmaAldrich, anhydrous, $\geq 99.0\%$) were used as well. The catalyst concentration is referred to here, as well as commonly in the literature, as molar resorcinol/catalyst ratio (R/C). The appropriate

amount of catalyst salt was weighed out, again using a balance with accuracy to 10^{-5} g, and the actual mass of added catalyst was noted. After all the resorcinol has dissolved, the catalyst was added to the solution and dissolved as well.



Figure 3.1 Glass jar used for gel synthesis

Formaldehyde was used in form of an aqueous solution, known as formalin, with methanol added as a polymerisation inhibitor (SigmaAldrich, 37 wt% formaldehyde, with 10–15 wt% methanol and 48–53 wt% water). The resorcinol to formaldehyde molar ratio (R/F) was kept constant at 0.5 in this work, which is the equivalent ratio for the addition reaction taking two active sites on each resorcinol molecule into account. The corresponding volume of formalin solution was calculated and, taking into account the water and methanol coming from the formalin solution, an additional amount of deionised water was added, so that the final volume of all liquids added up to 60 ml (as mentioned above). The formalin solution was added to the jar after all the solids have dissolved, and the jar was closed with a lid and left stirring at room temperature for ~ 30 minutes. It is important to keep this stirring period constant, since it has been reported before that addition reactions between activated resorcinol and formaldehyde take place even at room temperature [76].

After the stirring period, the magnetic stirrer bar was removed from the solution and if the pH of the RF sol was measured, it was done at this point. Before measuring the solution pH, the pH meter used (Hanna Instruments pH20 bench top pH meter with HI 1110-B pH probe) was calibrated using buffer solutions with pH 4 and 10 (Fluka Analytical). Afterwards, the lid was placed back on the jar, hand tightened, and the closed jar was moved to an oven (Mettmert ULE-500) preheated to 85 °C, except for samples used to study the effect of processing temperature, where an oven (Mettmert UFE400) was preheated to the chosen processing temperature. After 10–15 minutes in the oven, the jar lid was hand tightened again, due to the material dilation at elevated temperatures. The RF gel solution was left in the oven for 3 days, in order to allow enough time for the gelation and curing to take place. After 3 days, the jars containing the gels were removed from the oven, the lids were slightly loosened, and left to cool down to room temperature.

3.1.2 Solvent exchange

After the RF gel samples cooled to room temperature, following the gelation and curing step, the gel monolith was cut into smaller pieces (~ 1 cm) using a spatula in order to increase the surface area for solvent exchange. After cutting, 100 ml acetone (SigmaAldrich, $\geq 99.5\%$) was added to the jar, the lid was replaced and the jar was gently shaken for ~ 30 seconds to wash away water present on the surfaces of the hydrogel and the jar. The acetone was drained and for the standard solvent exchange, 180 ml or 240 ml of fresh acetone was added to the jar, the lid was resealed and wrapped with paraffin film in order to reduce acetone losses due to evaporation. The sealed jars were put on a shaker unit (VWR 3500 Analog Orbital Shaker) and agitated for 3 days with the shaking speed set to ~ 4 . For the improved solvent exchange method, 80 ml of acetone was added to the washed and drained gel and this was replaced with 80 ml of fresh acetone on each successive day for the 3 day period. If the gel structure seemed too weak (e.g. for higher R/C ratios), jars with these gel samples were not put on the shaker unit to prevent mechanical damage to the gel structure and were left on a bench top near the shaker unit. After the 3 day period of either solvent exchange method, the acetone was drained from the jars and the samples were ready for drying.

3.1.3 Drying

Jars with drained RF gel samples, after the solvent exchange step, were covered with a perforated aluminium foil and put into a vacuum oven (Towson and Mercer 1425 Digital Vacuum Oven). The perforated aluminium foil ensured that the samples could dry in the oven, but in case of a rapid acetone evaporation within the gel pieces, a flying piece of gel would not cross-contaminate other samples in the oven. After closing the vacuum oven door, the oven heating was turned on and the temperature was set to 110 °C, which corresponds to 85 ± 5 °C inside the oven (monitored using a thermometer placed inside the oven). For samples used for the temperature effect study, the drying temperature was set to match the curing temperature in order to eliminate a potential effect of a higher drying temperature, compared to the curing temperature. The vacuum pump (Vacuubrand MZ 2C NT) attached to the oven was turned on, with two solvent traps with water/ice mixture placed between the oven and the pump, to condense acetone evaporating from the gel samples. The solvent traps were used to preserve the vacuum pump, limiting the amount of solvent vapour that comes into contact with the membranes, as well as to monitor sample drying. For safety reasons, the oven and the pump were not left running overnight and were turned on the following working day to ensure thorough drying of the samples. After 2 days of drying, when there was no more acetone condensing in the solvent traps, the RF xerogel samples were deemed dried and transferred to labelled sample tubes for storage, indicating the catalyst used, R/C ratio, synthesis date, and any other conditions.

For samples dried at ambient pressure, jars covered with perforated aluminium foil were put into the oven used for gelation and curing, preheated to 85 °C. After 1 day of ambient

pressure drying, the samples contained only a small amount of residual solvent in their structure but to ensure a thorough drying, the samples were transferred to the vacuum oven for 1 day, dried and stored as described above.

3.1.4 Nitrogen sorption measurements

In order to characterise textural properties of the prepared RF xerogels, as described above, low temperature nitrogen sorption measurements were used. Before the measurement, volatiles present on sample surface had to be removed using a degas procedure described below. In this work, both degassing and gas sorption measurements were performed using a Micromeritics ASAP 2420 surface area and porosity analyser, shown in Figure 3.2. The bottom part of the instrument is used for sample degas and the top part for sorption measurements.

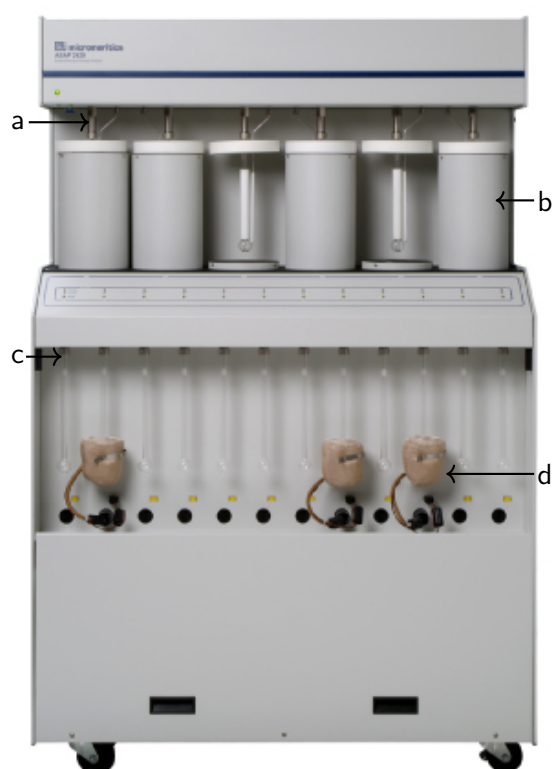


Figure 3.2 Micromeritics ASAP 2420 Accelerated Surface Area and Porosimetry System [189] with (a) analysis port, (b) liquid nitrogen dewar, (c) degas port, and (d) heating mantle

Degas procedure

In order to get accurate values of textural properties from gas sorption measurements, the sample surface has to be clean of any impurities adsorbed onto it which would mask some of the surface features present and affect the obtained sorption isotherm. Therefore, it is necessary to remove these impurities before the measurement and this is usually achieved

by exposing the sample to elevated temperatures and reduced pressure. The RF xerogel sample surface is most likely to contain water molecules that have adsorbed onto the surface after exposure to atmosphere and residual volatiles from the manufacturing process. For a complete removal of adsorbed molecules on sample surface, it is important to use appropriate combination of degas temperature, pressure, and time.

To begin with, approximately 0.5 g of xerogel sample was weighed out into a sample tube (shown in Figure 3.4), recording the sample mass with accuracy to 10^{-4} g. The sample tube with sample was attached to a degas port (c in Figure 3.2) on the instrument and a heating mantle (d in Figure 3.2) was slipped on the tube bulb and secured using a clip. It is important to make sure that the heating mantle is placed correctly, so that the mantle thermocouple is in touch with the glass. Otherwise, an inaccurate temperature reading could result in sample overheating, thus potentially damaging the sample and the instrument cutting off the degas procedure.

The first stage in the degas procedure involved heating the sample to 50 °C at 10 °C/min while reducing the pressure to 5 mmHg at 5 mmHg/s followed by unrestricted evacuation down to 10 µmHg. The sample was kept at 50 °C and below 10 µmHg for 30 minutes. Following the 30 minute period, the temperature was increased to 110 °C at 10 °C/min with continued unrestricted evacuation. After the temperature reached 110 °C, the sample was kept at 110 °C with unrestricted evacuation for 120 minutes. When the degas procedure has finished, the sample tube was left to cool down to room temperature and automatically backfilled with nitrogen to ~760 mmHg.

For samples used to study the effect of processing temperature, the degas temperature for the second stage (and the first stage for samples prepared at 45 °C) were set to the value of used processing temperature in the previous stages. However, due to the reduced temperature, a longer time period was used in order to allow sufficient outgassing of the sample surface. Readings from pressure transducers ensured that a sufficiently low value of pressure was maintained throughout the degas, providing thorough outgassing of the samples, even at lower temperatures. Times used for the last stage of the degas procedure for samples degassed at lower temperatures are presented in Table 3.1.

Table 3.1 Duration of last degas stage for samples degassed at different temperatures

Processing temperature [°C]	Last stage of degassing procedure [min]
45	840
55	720
65	720
75	600
85	360
95	240

After finishing the degas procedure, sample mass was recorded again and this value was used as the basis for the sorption measurement. The mass loss during the degas procedure also indicates how much material has desorbed during the degas process.

Sorption measurement

Degassed samples were analysed for textural properties using low temperature nitrogen sorption measurements performed at the nitrogen boiling point at atmospheric pressure ($-196\text{ }^{\circ}\text{C}$). If a sample was expected to exhibit a low value of surface area, a volume displacement insert (shown in Figure 3.3a) was used for the sorption measurement. This reduces the free volume in the sample tube, thus increasing the accuracy of the measurement. The equipment manufacturer recommends using a volume displacement insert for samples with less than 100 m^2 of total accessible surface area. If a volume displacement insert is used for samples above 100 m^2 of total accessible surface area, it does not significantly improve the accuracy of the measurement and prolongs the analysis time due to less free volume in the sample tube. Samples with larger surface area adsorb a higher amount of gas at each pressure point, thus requiring increased amount of times needed to adjust the gas volume in the sample tube at each pressure point.

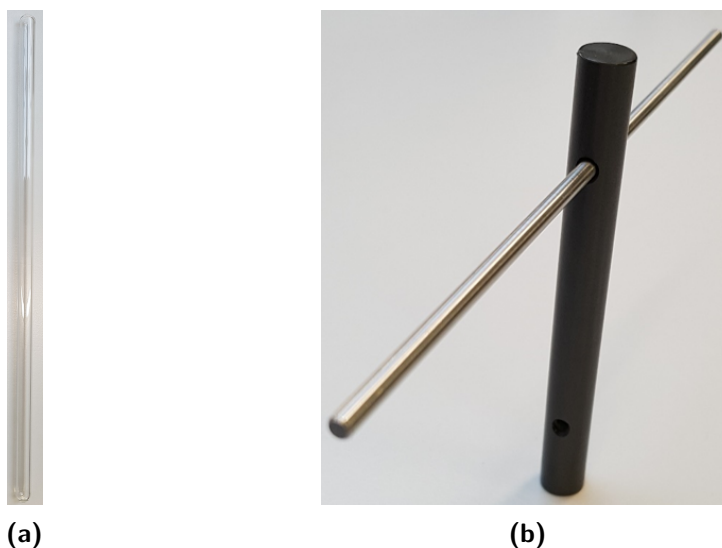


Figure 3.3 (a) volume displacement insert used for nitrogen sorption measurements and (b) dewar depth gauge used for measuring liquid nitrogen level

In order to maintain constant sample temperature throughout the measurement, a liquid nitrogen bath is used. Therefore, each analysis port of the equipment is fitted with a dewar (g in Figure 3.4) which needs to be filled with liquid nitrogen to an appropriate level, using a dewar depth gauge (shown in Figure 3.3b), prior to analysis. The required level of liquid nitrogen is between the bottom of the gauge and the hole near the bottom. However, as the analysis progresses, liquid nitrogen gradually evaporates from the dewar, which would lead to reduced contact area of liquid nitrogen and sample tube, thus causing changes in temperature profile within the tube. To minimise this effect, an isothermal jacket (d in

Figure 3.4) was slid onto the sample tube neck keeping a constant contact area between the liquid nitrogen and the sample tube due to capillary effects (a thin layer of liquid nitrogen between the isothermal jacket and the sample tube is maintained). If a sample was running for more than 24 hours, liquid nitrogen had to be topped up back to the appropriate level on each successive day. Care was taken not to interfere with the sample during data collection but rather during the equilibration period.

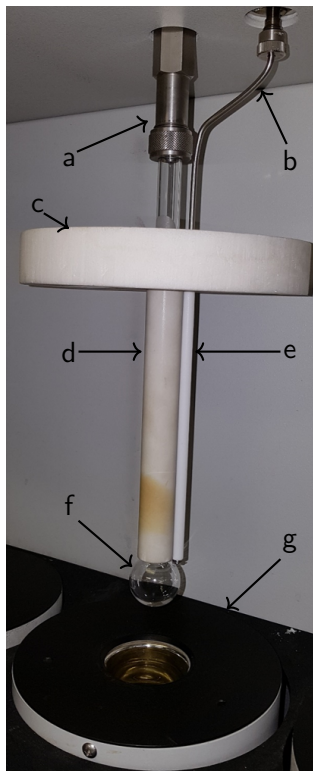


Figure 3.4 Sample tube set up for nitrogen sorption measurement with (a) analysis port, (b) saturation pressure tube, (c) dewar cover, (d) sample tube isothermal jacket, (e) saturation pressure tube isothermal jacket, (f) sample tube bulb, and (g) liquid nitrogen dewar

The sample tube with isothermal jacket was attached to an analysis port and a saturation pressure (p_0) tube (b in Figure 3.4) was positioned next to the sample tube. The top ends of isothermal jackets at both the sample tube and the p_0 tube (d and e in Figure 3.4, respectively) were aligned so that both tubes had the same temperature profile throughout the measurement. Finally, a dewar cover (c in Figure 3.4) was placed above the isothermal jackets and a splash guard was put in place. With a sample ready for analysis, as shown in Figure 3.4, the mass in the sample file was updated to the value after degas and if a filler rod was used, this option was selected in the measurement definition. All samples were analysed using a 40 pressure point adsorption and 30 pressure point desorption cycle with equilibration time set to 5 seconds. If an isotherm did not close during desorption below partial pressure p/p_0 0.4, the sample was analysed again, using an equilibration time value of 20 seconds.

3.1.5 Nitrogen sorption data analysis

In order to obtain useful textural properties of materials, the raw data collected from nitrogen sorption measurements, in the form of an isotherm, need to be analysed using various theories. This section will cover the methods of calculating BET accessible surface area, total pore volume, micropore volume, and pore size distribution. Data acquired for RF gel prepared with R/C 100 using a standard procedure, as described in the previous sections in this chapter, will be used here as an example. A nitrogen sorption isotherm for an RF gel prepared with R/C 100 is shown in Figure 3.5.

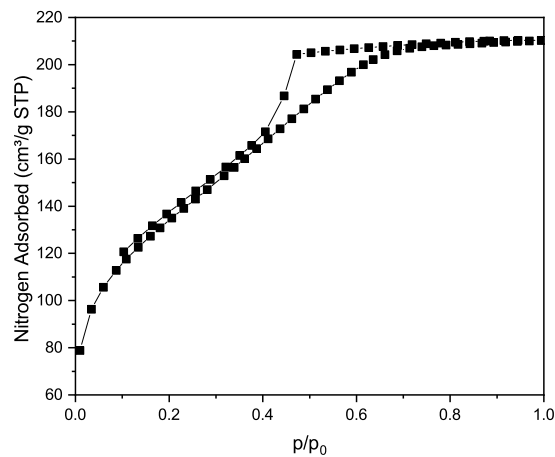


Figure 3.5 Nitrogen sorption isotherm for RF gel prepared with R/C 100

Additional information about the errors associated with the nitrogen sorption measurements, and the textural properties extracted from these, is described in more detail in Appendix B.

Accessible surface area calculation

In order to obtain accessible surface area of a mesoporous material, the theory of multilayer adsorption developed by Brunauer, Emmett, and Teller (BET) is most commonly used [146], described in more detail in Section 2.1.2. The linear version of the BET equation, used for monolayer volume calculation, is presented in equation 3.1.

$$\frac{\frac{p}{p_0}}{V \times \left(1 - \frac{p}{p_0}\right)} = \frac{1}{V_m C} + \frac{C-1}{V_m C} \left(\frac{p}{p_0}\right) \quad (3.1)$$

where $\frac{p}{p_0}$ is partial pressure of the nitrogen gas, V is the adsorbed volume of nitrogen, V_m is the adsorbed volume of nitrogen at monolayer coverage, and C is a constant related to the interaction energy between adsorbent and adsorbate, described in more detail in the theory section. Due to the assumptions made in the original theory, the maximum valid partial pressure range is 0.05 to 0.3. However, for some samples, especially if micropores are present, the full range is not applicable and a few criteria have been developed to help overcome this issue [142]. The value of C has to be positive since a negative value would

mean that the energy of adsorption is lower than that of liquefaction for the selected system, suggesting that the BET theory is not applicable for the selected pressure range. The term $V \times (1 - \frac{p}{p_0})$ should continuously increase with $\frac{p}{p_0}$ in the selected pressure range and the value of pressure corresponding to monolayer coverage (V_m) should be within the selected pressure range.

Dependence of the term $V \times (1 - \frac{p}{p_0})$ with $\frac{p}{p_0}$ in the pressure range 0.05 to 0.3 is shown in Figure 3.6. It can be seen that not all the data points in the $\frac{p}{p_0}$ range 0.05 to 0.3 fulfil the criterion of continuous increase with increasing $\frac{p}{p_0}$. Therefore, only the values for the $\frac{p}{p_0}$ range shown in black is used for further calculations of BET accessible surface area.

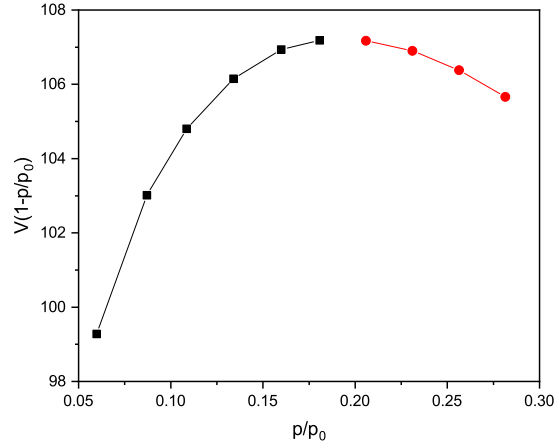


Figure 3.6 Dependence of term $V \times (1 - \frac{p}{p_0})$ with $\frac{p}{p_0}$ in the pressure range 0.05 to 0.3, as used for BET calculations for RF gel prepared with R/C 100. The data for range of continuously increasing values is shown with black squares and the data omitted from calculations is shown with red circles.

With the appropriate pressure range selected, a plot of $\frac{\frac{p}{p_0}}{V(1-\frac{p}{p_0})}$ versus $\frac{p}{p_0}$ is used to obtain the values of monolayer coverage volume (V_m) and C constant from the values of intercept and slope of a line of best fit. For the sample prepared with R/C 100, used as an example here, the plot along with data from linear regression is presented in Figure 3.7.

From equation 3.1, the value of C constant can be obtained as $C = 1 + \frac{\text{slope}}{\text{intercept}}$ and the value of monolayer coverage volume $V_m = \frac{1}{C \times \text{intercept}}$. For the example shown above, the value of the constants are $C = 139$ and $V_m = 110.9 \text{ cm}^3/\text{g}$. Considering the criteria described above, the value of C is positive, only data for pressure range where the term $V(1 - \frac{p}{p_0})$ increases is used, and the p/p_0 corresponding to monolayer formation (from interpolation) is approximately 0.08, which is within the selected range. The value of V_m is used to calculate accessible surface area using equation 3.2:

$$S_{BET} = n_m A N_A = \frac{V_m}{V_{mol}} A N_A \quad (3.2)$$

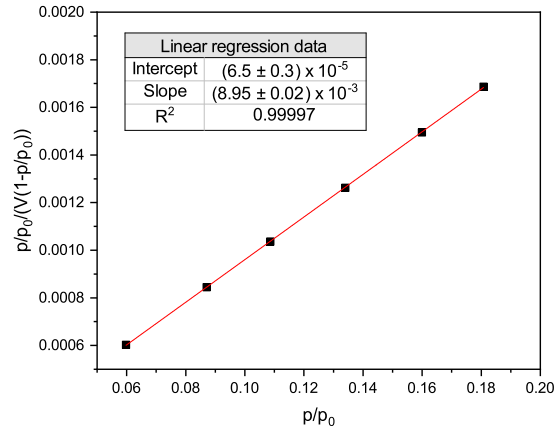


Figure 3.7 BET plot for RF gel prepared with R/C 100 used for calculation of BET accessible surface area with data from linear regression. Line of best fit is shown in red.

where S_{BET} is the BET surface area, n_m is the number of moles and V_m is the volume of nitrogen adsorbed at monolayer coverage, V_{mol} is the molar volume of nitrogen gas (ideal gas value $22.41 \text{ dm}^3/\text{mol}$ is used here), A is the cross-sectional area of a nitrogen molecule ($1.62 \times 10^{-19} \text{ m}^2$), and N_A is Avogadro's number ($6.022 \times 10^{23} \text{ mol}^{-1}$). The value of S_{BET} for the example used here is calculated as $482.8 \text{ m}^2/\text{g}$.

In order to automate this process, a macro in Microsoft Excel using Visual Basic for Applications has been developed and is attached in the appendices (E.1.1).

Total pore volume

The total pore volume obtained from nitrogen sorption corresponds to voids filled with nitrogen at the highest value of the relative pressure used, in proximity to $p/p_0 = 1$. Due to the experimental limitations, macropores within the sample are not taken into account, since partial pressures that close to 1 are currently not achievable within experimental errors for this technique.

For the example sample introduced above, the highest measured pressure point is at $p/p_0 = 0.994$ with corresponding volume of nitrogen gas adsorbed $210.32 \text{ cm}^3/\text{g}$ STP. This value of gas volume is converted into the volume of liquid nitrogen that fills the pore voids at the given pressure. A conversion factor provided within the software that is supplied with the ASAP equipment is used, as shown in equation 3.3.

$$V_{tot} = V_{ads} \times D \quad (3.3)$$

where V_{tot} is the total pore volume, V_{ads} is the nitrogen gas volume adsorbed at the highest value of p/p_0 , and D is the density conversion factor. A value of $D = 0.0015468$ is used in this work, with $D = M/(V_{mol}\rho)$, where $M = 28.0134 \text{ g/mol}$ is molar mass of nitrogen gas, $V_{mol} = 22.41 \text{ dm}^3/\text{mol}$ is the molar volume of an ideal gas at standard temperature and

pressure (STP), and $\rho = 0.809 \text{ g/cm}^3$ is the density of liquid nitrogen. For the sample used as an example in this section, the value of total pore volume is calculated as $0.33 \text{ cm}^3/\text{g}$.

Micropore volume

Micropore volume in a sample is the contribution to the total pore volume, described above, from pores with width below 2 nm, as classified by IUPAC [143]. In this work, the t-plot method, developed by Lippens and Boer [150], is used in order to calculate the micropore volume from nitrogen sorption isotherm data.

First, values of the standard multilayer thickness (t) on a reference non-porous material is calculated for the measured p/p_0 range. Due to the nature of the RF gel surface, the so-called carbon black equation, proposed in the ASTM standard D-6556-17 [149], is used here with the formula for calculation of t as shown in equation 3.4. The adsorption branch of the isotherm, for the example sample used in this section, converted into a so-called V-t curve is presented in Figure 3.8.

$$t = 0.88 \left(\frac{p}{p_0} \right)^2 + 6.45 \frac{p}{p_0} + 2.98 \quad (3.4)$$

The linear part of the adsorption branch of the isotherm is identified and linear regression is performed on the V-t curve data in this range. This allows for the value of the micropore volume to be calculated using the intercept value and equation 3.5 for the nitrogen adsorbate [150].

$$V_\mu = \text{intercept} \times 0.001547 \quad (3.5)$$

For the example sample analysed here, the value of the intercept is $20.69 \text{ cm}^3/\text{g}$ giving the value of $V_\mu = 0.032 \text{ cm}^3/\text{g}$.

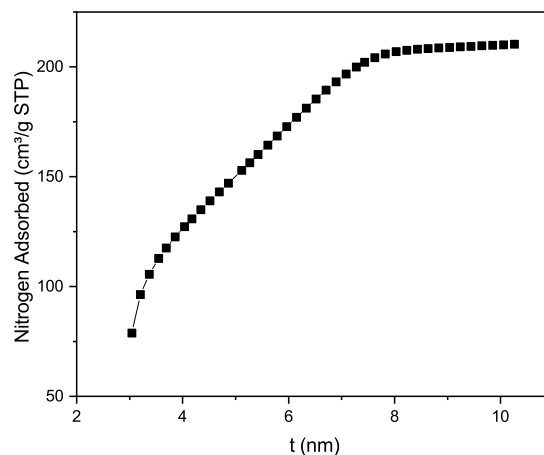


Figure 3.8 V-t curve for sample prepared with R/C 100, where t is the standard multilayer thickness

Value of the external surface area (S_{ext}) can be obtained from the slope of the linear part of the V-t curve as $S_{ext} = \text{slope} \times 15.47$, also providing the value of micropore surface area as $S_{\mu} = S_{BET} - S_{ext}$, but this is not explored in this work. Again, in order to automate this process a macro in Microsoft Excel using Visual Basic for Applications has been developed and is attached in the appendices (E.1.2)

Pore size distribution

A useful characteristic of porous materials is the distribution of pore sizes present in the material. The method developed by Barrett, Joyner, and Halenda [148] assumes that during desorption between two values of relative pressure (p/p_0), the amount desorbed in this pressure interval is equal to the sum of pore cores emptying, as per the Kelvin equation (discussed in Section 2.1.3), and desorption from the pore walls of previously opened pores. At the highest pressure, all the considered pores are filled with liquid, therefore, in the first desorption interval, the amount desorbed comes only from new pores opened without desorption from pore walls. The core liquid and adsorbed layers are schematically shown in Figure 3.9, where the core (□) empties at a given pressure, as per the Kelvin equation, and the subsequent layers gradually desorb, as the pressure decreases, until all the gas has desorbed. In Figure 3.9, the layers desorb in order 3 (■), 2 (■), and finally 1 (■).

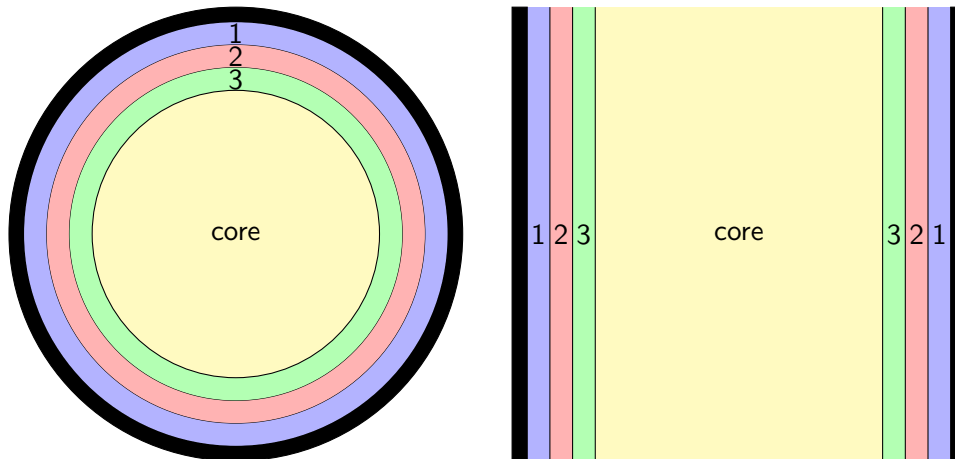


Figure 3.9 Schematic representation of a cylindrical pore emptying during desorption with top view (left) and side view (right)

The adsorbed volumes, from the desorption branch of the isotherm, are converted into liquid equivalent volumes for all relative pressure values measures (index x):

$$Vl_x = Va_x \times D \quad (3.6)$$

where, Vl_x is the liquid equivalent volume, Va_x is the volume adsorbed, and D is the density conversion factor, described above in this section. Using the Kelvin equation (Equation 2.8),

the core radii corresponding to the relative pressures are calculated:

$$R_{c_x} = \frac{-A}{\ln(p/p_{0_x})} \quad (3.7)$$

where R_{c_x} is the core radius, A is the adsorbate property factor, and p/p_{0_x} is the relative pressure value. A value of $A = 0.953$ is used in this work, with A coming from the Kelvin equation:

$$A = \frac{2\gamma V_m}{RT} = \frac{2\gamma\rho}{MRT} \quad (3.8)$$

where $\gamma = 8.94$ mN/m is the surface tension of liquid nitrogen at 77 K, V_m is the molar volume of liquid nitrogen, $M = 28.0134$ g/mol is molar mass of nitrogen gas, $\rho = 0.809$ g/cm³ is the density of liquid nitrogen, R is the universal gas constant, and T is the absolute temperature. The factor of 2 in equation 3.8 is a result of a Gaussian curvature of the meniscus surface in two dimensions in a cylindrical pore.

The statistical thickness of the remaining adsorbed layer on the walls of previously opened pores (T_{w_x}) is calculated using equation 3.4 at each value of measured p/p_0 . For the last p/p_0 (zero pressure), the value of T_{w_x} is assumed 0.

After all the necessary values have been determined, the calculation starts from the highest value of p/p_0 and proceeds through to lower values. Here, the index i will refer to a pressure interval, where $i = 1$ is the pressure interval between $\left(\frac{p}{p_0}\right)_1$ and $\left(\frac{p}{p_0}\right)_2$, while $\left(\frac{p}{p_0}\right)_1 > \left(\frac{p}{p_0}\right)_2$. The index j will refer to the previous intervals, where new pores were opened and the index k will refer to the total number of intervals j where new pores were found (ie. $j = 1$ to k).

There are three steps that are repeated for each pressure interval. First step involves evaluation of the difference in statistical thickness of adsorbed layer between the two pressure points of the selected interval:

$$\Delta T_{w_i} = T_{w_x} - T_{w_{x+1}} \quad (3.9)$$

The cross-sectional area (CSA_j) of the layer desorbed from the previously opened pores is calculated:

$$CSA_j = \pi \left[(R_{c_j} + \Delta T_{w_i})^2 - R_{c_j}^2 \right] \quad (3.10)$$

which is then used to determine the amount of gas desorbed from previously opened pores (Vd_j):

$$Vd_i = \sum (Lp_j) (CSA_j) \quad (3.11)$$

where Lp_j is the length of previously opened pores, calculated in the next step. For the first pressure interval ($i = 1$), there are no previously opened pores, so this step is skipped.

If the volume desorbed from the walls of previously opened pores for the given pressure interval is equal or greater than the current volume desorbed ($Vd_i \geq V_i - V_{i+1}$), then the desorbed gas comes only from the walls of previously opened pores and no new pores are found in this pressure interval. The total surface area of the exposed walls (SA_w) for all previously opened pores is calculated:

$$SA_{w_i} = \sum \pi (Lp_j) (D_{avg_j}) \quad (3.12)$$

where D_{avg_j} is the weighted average pore diameter, calculated later on. Again, for the first pressure interval there are no previously opened pores so the second part of this step is used, described in the next paragraph. The statistical thickness of the adsorbed layer is adjusted to account for the actual volume desorbed:

$$\Delta T_{w_i} = \frac{V_i - V_{i+1}}{SA_{w_i}} \quad (3.13)$$

If the volume desorbed from the walls of previously opened pores is less than the current volume desorbed ($Vd_i \leq V_i - V_{i+1}$), then the gas volume is a combination of desorption from walls of previously opened pores and core evaporation, leading to new pores being identified. The gas volume due to core evaporation is the difference mentioned below:

$$V_{c_i} = (V_i - V_{i+1}) - Vd_i \quad (3.14)$$

The core radius for the end of the pressure interval ($R_{c_{k+1}}$) is calculated from the equation 3.7 and a length-weighted average pore diameter, for the interval since the last time new pores were found, is calculated:

$$D_{avg_k} = \frac{2(R_{c_k} + R_{c_{k+1}})R_{c_k}R_{c_{k+1}}}{R_{c_k}^2 + R_{c_{k+1}}^2} \quad (3.15)$$

The value of p/p_0 corresponding to D_{avg_k} is obtained by rearranging equation 3.7:

$$P_{avg_k} = e^{\frac{-A}{D_{avg_k}}} \quad (3.16)$$

and the statistical thickness ($T_{w_{avg_k}}$) of adsorbed layer corresponding to P_{avg_k} is calculated using equation 3.4. The decrease in adsorbed layer thickness from beginning of the interval to P_{avg_k} is determined:

$$\Delta Td = T_{w_{avg_k}} - T_{w_{i+1}} \quad (3.17)$$

This allows for the core cross-sectional area (CSA_{c_k}) and length (LP_k) to be obtained:

$$CSA_{c_k} = \left[\frac{D_{avg_k}}{2} + \Delta Td \right]^2 \quad (3.18)$$

$$LP_k = \frac{V_{C_i}}{CSA_{C_k}} \quad (3.19)$$

The average pore diameter, calculated in equation 3.15, represents a cylindrical pore, with diameter $D_{avg k}$ and length LP_k , and its surface area is equal to the average surface area of pores found within this pressure interval.

The final step adjusts the current values of pore radii with the thickness of the desorbed layer. If there were new pores opened in the previous step, the average pore diameter for these pores is adjusted only by the desorption in the interval until $P_{avg k}$:

$$D_{avg k, new} = D_{avg k, old} + 2\Delta Td \quad (3.20)$$

The rest of the pore diameters (apart from the current $D_{avg k}$ and RC_{k+1}) and pore radii are adjusted by the change in statistical thickness of adsorbed layer:

$$D_{avg j, new} = D_{avg j, old} + 2\Delta Tw \quad (3.21)$$

$$RC_{j, new} = RC_{j, old} + \Delta Tw \quad (3.22)$$

These three steps, described above, are repeated for all the measured pressure intervals and all the pore radii (including RC_{k+1}) are converted to pore diameters as follows:

$$Dp_j = 2RC_j \quad (3.23)$$

Finally, the incremental pore volume (Vp_j) and the data for plotting the pore size distribution are calculated:

$$Vp_j = \pi LP_j \left(\frac{D_{avg j}}{2} \right)^2 \quad (3.24)$$

$$\left(\frac{dV}{d \log(D)} \right)_j = \frac{Vp_j}{\log(D_{avg j}/D_{avg j+1})} \quad (3.25)$$

3.2 Results and discussion - experimental study

A series of resorcinol-formaldehyde (RF) xerogels have been prepared and analysed for textural properties according to the procedures described above, in Section 3.1. Sodium carbonate was used in the original work by Pekala [47] and is still one of the most commonly used [55, 56, 76, 190, 191] substance that promotes the reaction between resorcinol and formaldehyde in an aqueous solution. Even though its role is not technically the one of a catalyst, being used up by the reaction, it is commonly referred to as a catalyst in the literature. Therefore, in this work the word catalyst is used to represent the metal salt added to the reaction mixture in order to promote the gelation of RF gels. Catalyst concentration will be expressed as the resorcinol/catalyst (R/C) molar ratio.

The contents of this section are organised as follows. First, the influence of catalyst concentration is studied in Section 3.2.1; followed by the effect of other processing parameters, namely the solvent exchange method (Section 3.2.2), processing temperature (Section 3.2.3), and drying method (Section 3.2.4). Finally, other sources of sodium ions as a catalyst for the reaction are explored in Section 3.2.5 with sodium carbonate replaced in varying ratios with sodium chloride and sodium sulphate. Data presented in sections 3.2.2, 3.2.3, and 3.2.4 have been published in the journal 'Gels' [192] and the manuscript is presented in Appendix D.1.1. Preliminary results obtained, but determined to be beyond the scope of this work, are presented and discussed in Appendix C.

3.2.1 Effect of sodium carbonate concentration

The concentration of the catalyst salt, which is linked to the initial solution pH, has a significant influence on the final properties of RF xerogels. In order to examine the influence of sodium carbonate concentration, referred to as R/C ratio here, a series of RF gel samples with R/C ratios 100, 200, 300, 400, 500, 600, and 800 were prepared. The solution compositions for these samples are presented in Table A.1 in appendices. All the samples studied in this section are prepared using the standard procedure described in Section 3.1 (85 °C, standard solvent exchange, and vacuum drying).

Nitrogen sorption isotherms for samples with varying R/C ratios are shown in Figure 3.10a with their corresponding pore size distributions in Figure 3.10b. As the R/C ratio increases, decreasing the catalyst concentration, the hysteresis loop observed for isotherms in Figure 3.10a systematically shifts towards higher relative pressures (p/p_0). This means that the pores present in these samples fill, and empty, at higher values of p/p_0 , suggesting larger pores are present, as per gas adsorption theory discussed in the background theory chapter. This yields the trends observed in the corresponding pore size distributions (Figure 3.10b), where the average pore size, as well as the width of the distribution, increase with increasing

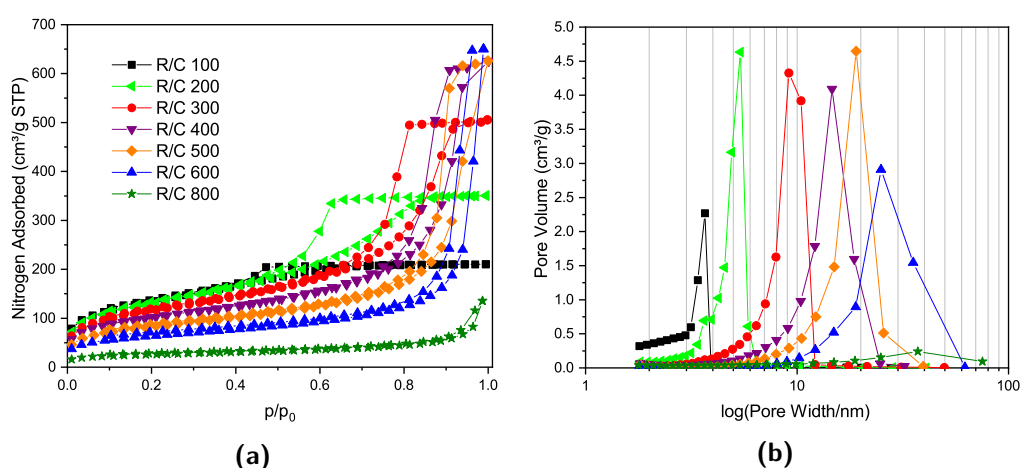


Figure 3.10 (a) Nitrogen sorption isotherms for gels prepared with varying R/C ratio and (b) corresponding pore size distributions

Table 3.2 Textural properties of gels prepared with varying catalyst concentration

R/C ratio	S_{BET} [m ² /g]	V_{T} [cm ³ /g]	V_{μ} [cm ³ /g]	$\bar{\phi}$ [nm]
100	480	0.32	0.05	3
200	470	0.54	0.04	5
300	420	0.78	0.04	8
400	360	0.97	0.04	12
500	300	0.97	0.04	16
600	230	1.00	0.04	24
800	90	0.21	0.02	15

S_{BET} - accessible surface area from BET analysis; V_{T} - total pore volume determined from adsorption at $p/p_0 \sim 1$; V_{μ} - micropore volume determined using t-plot method; $\bar{\phi}$ - average pore width from BJH analysis. Errors are omitted from the table as all values are reported to an accuracy less than the largest error for each variable.

R/C ratio. Figure 3.10a also shows an increase in the maximum nitrogen uptake at the highest value of p/p_0 with increasing R/C ratio, indicating increasing accessible pore volume. Data for the sample prepared with R/C 800 presented in Figure 3.10 does not follow these aforementioned trends and this will be discussed below.

Textural properties for the samples prepared in this section are presented in Table 3.2. A previous study in our group [79] has suggested that with increasing R/C ratio (decreasing catalyst concentration), there is a lower number of sites where clusters start to grow. This leads to larger particles, with the same amount of reagents in the solution, which will result in larger voids between these particles in the final gel. On the contrary, lower R/C ratio leads to a larger number of smaller particles with smaller spaces in between them, and some of these pore spaces are not accessible from the surface, leading to smaller values of total pore volume, as can be seen from the trends for both the total pore volume (V_{T}) and average pore width ($\bar{\phi}$) in Table 3.2. As expected, the surface area gradually decreases with decreasing catalyst concentration, while the average pore width increases. A large proportion of the pore voids present in the sample prepared with R/C 800 is likely to be in the macropore range, as classified by IUPAC [143], and is therefore out of the detectable range for nitrogen sorption measurements. Another reason for the seemingly outlying values for the R/C 800 gel, compared to the other ones in this set, could be due to a weak structure formed in this gel, which would lead to significant shrinkage during the drying step, and is reflected in reduced values of all the studied textural properties in Table 3.2.

In order to prove the necessity of the metal carbonate catalyst, a RF gel sample without any added sodium carbonate was prepared using the same procedure as for the other samples. After the gelation and curing steps, a powder precipitate was formed (Figure 3.11a), instead of a typical hydrogel material, and has deposited on the bottom of the jar. After decanting the liquid above the precipitate, the powder was processed using the same solvent exchange



Figure 3.11 Photographs of a RF gel prepared without catalyst (a) after gelation and curing steps; and (b) after drying (size of pieces $\sim 1-2$ cm)

and drying method as for the other samples and the dried material is shown in Figure 3.11b. Comparing the nitrogen sorption isotherm, shown in Figure 3.12, to a sample with low catalyst concentration (R/C 800) suggests that the negligible nitrogen adsorption within the studied pressure range is a result of a non-porous material, with no extractable textural properties from this analysis. Therefore, this confirms that the sodium carbonate plays a critical role in the process.

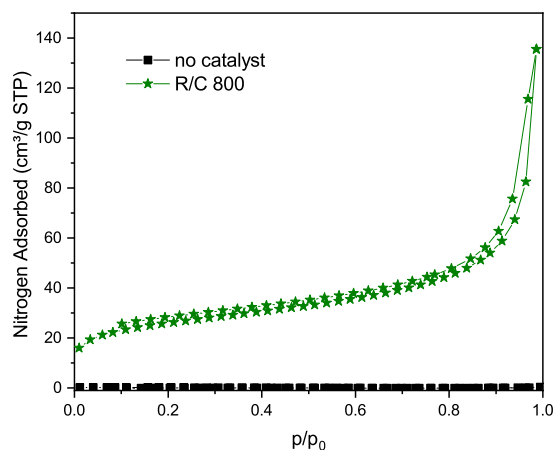


Figure 3.12 Nitrogen sorption isotherms for gels prepared without catalyst and with R/C 800

3.2.2 Improved solvent exchange

After the gelation step, the pore structure within the RF hydrogels contains water. Due to the high surface tension of water, over the temperature range used during RF gel manufacture, drying at this stage leads to significant shrinkage of the final material, as a consequence of the resulting high stresses that act on the pore walls. Therefore, it is desirable to replace the water with another solvent that exhibits a lower surface tension, and preferably a lower boiling point, than water, within the temperature range of interest. The surface tension of water is relatively high, even at elevated temperatures, e.g. 67.97 mN/m at 50 °C [193], and a number of alternative solvents, with reduced surface tensions, e.g. amyl acetate,

acetone, t-butanol, and isopropanol [55, 194], have been proposed for solvent exchange in previous studies. However, acetone offers an excellent combination of a reduction in surface tension (19.65 mN/m at 50 °C [112]) and relatively low cost compared to alternative solvents. Hence, acetone was used for solvent exchange within this study.

Generally, the hydrogels undergo solvent exchange for a period of 3 days with only an initial volume of acetone added to the drained, cured gel; however, this may not be the most appropriate method to retain the porous structure developed during synthesis. Replacement of the liquid within the pores is driven by diffusion, although agitation is often used to enhance contact of the material and fresh solvent; hence, sufficient time is required for full solvent exchange to occur. Another factor that is potentially important, in maximising the level of exchange, is the water concentration gradient between the pore liquid and the bulk solvent surrounding the sample. To investigate the effect of the solvent exchange method used, three batches of gels each with 60 ml total volume of liquids were synthesized (as described in Section 3.1), each of which, after curing, were washed with acetone, drained and, subsequently, agitated in acetone for 3 days. The key difference was that first two batches were used to investigate the effect of a different volume of acetone used in one application and were processed by adding the entire volume of acetone at the beginning of the 3 days, namely 180 or 240 ml, and the sample was left without further handling for the whole solvent exchange period; while the last batch was treated with a fresh volume of acetone each day for three successive days with the total volume of acetone used adding up to 240 ml, thus maintaining the same total volume of acetone as the second batch but splitting the total volume over multiple days.

Nitrogen sorption isotherms along with the corresponding pore size distributions (PSDs) for RF gels prepared with R/C ratios 100, 300, and 600 using standard and improved solvent exchange methods are presented in Figures 3.13a and 3.13b, respectively. Textural properties for RF gels with R/C ratios in the range 100 to 600 are shown in Table 3.3. It can be seen

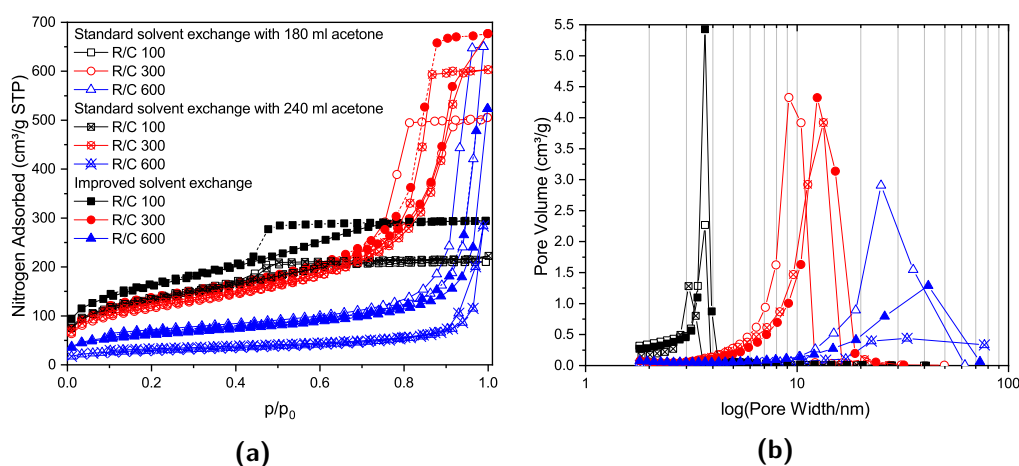


Figure 3.13 (a) Nitrogen sorption isotherms of gels prepared with standard and improved solvent exchange and (b) corresponding pore size distributions

Table 3.3 Textural properties of gels prepared with standard and improved solvent exchange

R/C	S_{BET} [m ² /g]			V_{T} [cm ³ /g]			V_{μ} [cm ³ /g]			$\bar{\phi}$ [nm]		
	Acetone exchange method			Acetone exchange method			Acetone exchange method			Acetone exchange method		
	Standard		Improved	Standard		Improved	Standard		Improved	Standard		Improved
	180 ml	240 ml		180 ml	240 ml		180 ml	240 ml		180 ml	240 ml	
100	480	470	580	0.32	0.33	0.46	0.05	0.05	0.06	3	3	3
200	470	520	500	0.54	0.70	0.73	0.04	0.06	0.05	5	5	6
300	420	430	470	0.78	0.93	1.05	0.04	0.05	0.06	8	10	10
400	360	300	220	0.97	0.95	0.98	0.04	0.04	0.03	12	14	24
500	300	220	230	0.97	0.96	1.17	0.04	0.03	0.03	16	24	28
600	230	110	220	1.00	0.44	0.81	0.04	0.02	0.04	24	27	21

S_{BET} - accessible surface area from BET analysis; V_{T} - total pore volume determined from adsorption at $p/p_0 \sim 1$; V_{μ} - micropore volume determined using t-plot method; $\bar{\phi}$ - average pore width from BJH analysis. Errors are omitted from the table as all values are reported to an accuracy less than the largest error for each variable.

that changing the acetone bath daily has a more pronounced positive effect on the total pore volume of the RF gel samples compared to just increasing the total acetone volume without changing the bath daily, especially for samples with lower R/C ratios. Improving the solvent exchange method, by increasing the concentration gradient daily, leads to pores with larger average diameter (Table 3.3). This, coupled with the increase in pore volume, is ascribed to a reduction in shrinkage during the drying stage. If the acetone bath is replaced daily, the water concentration gradient is renewed every day, thus there is an increased driving force, which removes more water from the pores. This leads to lower stresses being exerted on the pore walls during the drying stage, due to the lower surface tension of acetone compared to water. However, for samples with higher R/C ratios exhibiting a weaker gel structure, the improved method does not seem to have the same pronounced positive effect observed for the lower R/C gels with smaller average pore diameter. A possible explanation is that when the acetone bath is exchanged daily, the replenishment step slightly damages the softer structure, resulting in lower values of surface area and pore size.

The findings from this section of work suggest that there is significant advantage in using an improved solvent exchange method for most of the samples, hence, all samples in the following sections were prepared using daily replenishment of acetone within the solvent exchange stage, with the intention of maintaining the gel structure as close to the original hydrogel structure as possible, without the need to use cryogenic or supercritical processing steps. It is important to note that, in order to obtain improved gel characteristics, it is not necessary to increase the amount of acetone used during the solvent exchange, rather it is imperative to split this amount over the exchange period.

3.2.3 Effect of processing temperature

An important process parameter that needs to be considered is temperature, since it has an effect on factors such as solubility of species in the reaction mixture (e.g. growing RF clusters) and rate of reactions. The first stages of resorcinol-formaldehyde (RF) gel formation, immediately after mixing the components, are gelation and curing, which are usually carried out at elevated temperatures, and the final processing steps of gel production also include the use of a raised temperature during drying. Hence, this section focusses on a study of the temperature influence within the manufacturing process. In all previous experiments, 85 °C was selected as the gelation and curing temperature as gels previously obtained at this temperature have exhibited a viable structure, and it is also a commonly used value in the literature, allowing further comparisons to be made to previously reported results [55, 59, 93]. It has, however, been shown that RF cluster particles begin to grow once the solution reaches a temperature of at least 55 °C [79], which indicates a minimum threshold for investigation; since water is used as the solvent, in the synthesis outlined above, the upper temperature limitation is, therefore, set by the boiling point of water. Thus, the chosen temperature range studied was 45–95 °C, with 10 °C intervals and R/C ratios 100, 300, and 600 were selected to represent the studied range of catalyst concentration. This allowed the region both above and below the temperature necessary for cluster growth to be probed to determine whether a viable gel structure can be established and maintained at temperatures approaching both (i) the boiling point of water and (ii) lower, less energy demanding, temperatures. The R/C ratio was varied, as required, but all other synthesis parameters were kept constant as stated above; the only other change was that of oven temperature during the gelation and drying stages. Due to the enhanced performance observed above, improved solvent exchange was used exclusively, and the drying temperature, used in the vacuum stage, matched the gelation and curing temperatures, in order to restrict any post gelation changes in structure caused by exposure to a higher temperature during drying.

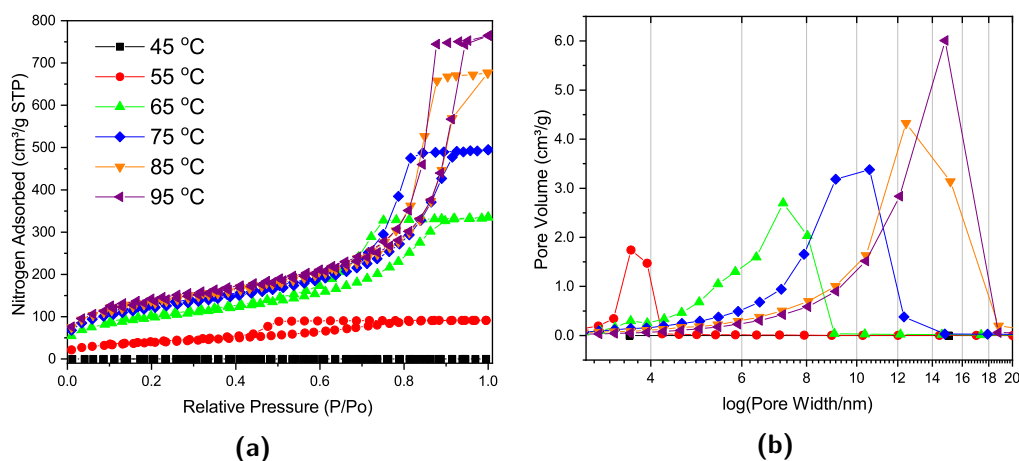


Figure 3.14 (a) Nitrogen sorption isotherms of gels prepared with R/C 300 and varying processing temperature and (b) corresponding pore size distributions

Table 3.4 Textural properties of gels prepared at different temperatures

T [°C]	S_{BET} [m ² /g]			V_{T} [cm ³ /g]			V_{μ} [cm ³ /g]			$\bar{\phi}$ [nm]		
	R/C ratio			R/C ratio			R/C ratio			R/C ratio		
	100	300	600	100	300	600	100	300	600	100	300	600
45	-	-	20	-	-	0.07	-	-	-	-	-	9
55	< 1	140	100	-	0.14	0.48	-	0.01	0.01	-	4	21
65	370	350	200	0.22	0.52	0.82	0.05	0.04	0.03	3	6	20
75	520	440	220	0.36	0.76	0.82	0.06	0.05	0.03	3	8	21
85	580	470	220	0.46	1.05	0.81	0.06	0.06	0.04	3	10	21
95	610	490	230	0.52	1.18	0.92	0.06	0.06	0.04	3	12	24

S_{BET} - accessible surface area from BET analysis; V_{T} - total pore volume determined from adsorption at $p/p_0 \sim 1$; V_{μ} - micropore volume determined using t-plot method; $\bar{\phi}$ - average pore width from BJH analysis. Errors are omitted from the table as all values are reported to an accuracy less than the largest error for each variable.

Figures 3.14a and 3.14b present nitrogen sorption isotherms and corresponding pores size distributions for RF gels prepared at different processing temperatures, respectively. The graphs in Figure 3.14 present only data for gels prepared with R/C 300 in order to show the obtained trends but keep clarity at the same time. Table 3.4 shows the textural properties for gels synthesized at different temperatures, obtained from nitrogen adsorption analysis. Gels prepared at lower temperatures either did not gel or exhibited a very weak structure that did not withstand the drying process; this led to materials with a low degree of porosity or even to non-porous materials. The effect of temperature can be seen more clearly in Figure 3.15, where the influence of gel preparation temperature, and R/C ratio, on the BET surface area is shown. It can be seen that, at low temperatures (45 and 55 °C), the surface areas obtained are very low, and are essentially independent of the R/C ratio used. At higher temperatures, the BET surface area seems to be only slightly dependent on temperature, and the effect of catalyst concentration dominates as the major factor in determining the final gel structure properties. These results are in disagreement with results from Tamon and Ishizaka [52] who reported that gelation temperature had no influence on the final gel structure. The difference is likely ascribed to the fact that their gelation step at either 25 or 50 °C was followed by a curing period of 5 days at 90 °C. Thus, the influence of the lower temperature gelation stage would have been masked by subsequent exposure to the same higher temperature during the curing stage.

Pore size distributions for the suites of samples prepared using different temperatures and R/C ratio 300 (Figure 3.14b) show that the pore size distribution shifts towards larger pore diameters with increasing gelation temperature. This implies that gels prepared at higher temperatures develop stronger crosslinkages, which leads to a lower degree of shrinkage during the drying stage. It can also be observed that the total pore volume, which is given by

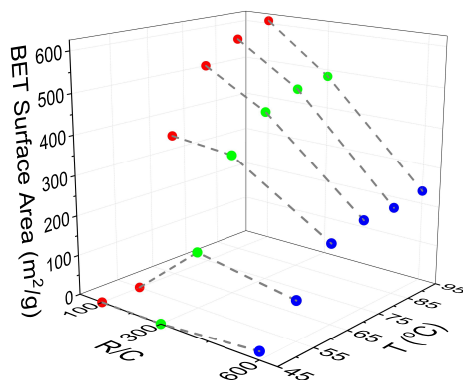


Figure 3.15 Dependence of BET surface area on gel preparation temperature and R/C ratio

the area under the pore size distribution curves (as well as presented in Table 3.4), increases with increasing temperature, further supporting the theory that shrinkage is reduced within the stronger structures created at higher temperatures. The gels prepared at 45 °C exhibited such low porosity that the values are not even discernible in Figure 3.14b, and are overlapped by other points; specific values are presented in Table 3.4. It is evident from these results that, in order to obtain a viable gel structure capable of enduring the drying process, the gelation temperature must be in excess of 55 °C, as suggested by Taylor et al. [79]; however, increasing the temperature further does not seem to have a significant impact on the surface area obtained. The other textural variables are affected slightly and it may be required to use elevated temperatures to optimize a particular variable or enhance the crosslinking within the final gel. This information could be used in process optimization of RF gel manufacture to reduce the heating costs associated with the gelation and drying processes for a specific set of required textural characteristics as defined by a selected application.

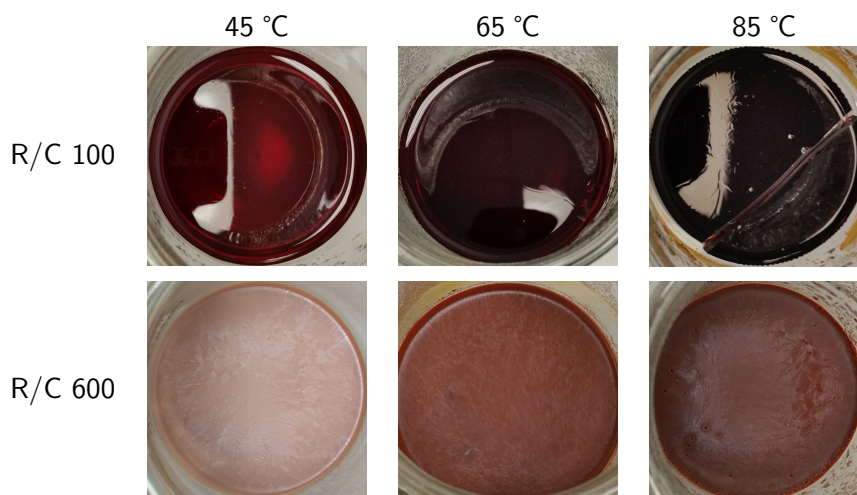


Figure 3.16 Photographs of RF hydrogels prepared at different temperatures (left to right) and R/C ratios (top to bottom).

Visual observation of RF hydrogels, right after gelation and curing and before solvent exchange, prepared at different temperatures, presented in Figure 3.16, shows a clear difference between these samples. RF hydrogels prepared with R/C 100 generally show a darker colour than their counterparts with a higher R/C ratio and are translucent rather than opaque. The clusters and voids present in the opaque gels are comparable to, or larger than, the wavelengths of visible light, therefore light gets diffracted and creates an opaque appearance. On the contrary, translucent gels contain smaller particles and voids, which agrees with the aforementioned theory by Taylor [79]. Increasing the gelation temperature leads to gels with darker colour, which could be a result of higher cross-linking density or higher degree of oxidation of these materials leading to darker discolouration.

3.2.4 Vacuum vs ambient pressure drying

The final stage of gel preparation is drying of solvent exchanged gels, which, in this case, involves subcritical drying of the gels to remove acetone. The gels prepared in this way exhibit a higher degree of shrinkage; however, it is much easier to implement, and more economical, when compared to supercritical drying with CO₂. Usually, in order to make the drying process faster, and to ensure that the final materials have been dried thoroughly, vacuum drying is utilized. Maintaining a vacuum during the drying is also not inexpensive, so it would be beneficial if RF gels could be dried under ambient pressure at elevated temperature, while retaining their final properties. Therefore, a series of gel samples were prepared, where the gel sample was divided in two halves post improved solvent exchange, using R/C ratios 100, 300, and 600. This ensured that any effects observed within the final structure only resulted from the selected drying procedure. One half of the sample was dried for 2 days under vacuum at 85 °C, while the other half was dried under ambient pressure at 85 °C for 1 day and subsequently moved to the vacuum oven with the other sample half for 1 day of further drying, this time sub-atmospherically. Most of the drying process occurs during the first day; while the second day is used to remove the final traces of acetone remaining in the pores.

Again, as in the previous sections, Figures 3.17a and 3.17b represent nitrogen sorption isotherms and corresponding pore size distributions for RF gels dried at ambient pressure and under vacuum, respectively. RF gels prepared using either of the drying methods exhibit a very similar shape of both the sorption isotherms and pore size distributions, suggesting only minor differences in structure. Table 3.5 shows the textural properties obtained for the gels prepared as outlined above. It can be observed that even though the gels dried under vacuum tend to have higher surface areas, pore volumes, micropore volumes, and larger average pore widths, the differences are insubstantial. This means that, if the requirements for the final material are not too strict, it should be possible to initially dry RF gels at ambient pressure, potentially even in the same oven as is used for gelation since the temperatures are equivalent. From an industrial perspective this could result in significant cost savings associated with the drying process of RF gels, and the handling of materials between unit

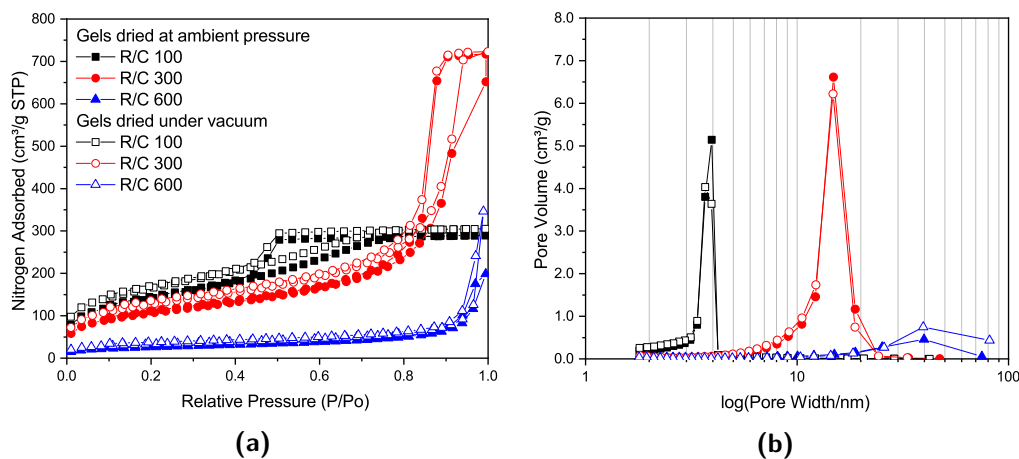


Figure 3.17 (a) Nitrogen sorption isotherms of gels dried at ambient pressure and under vacuum and (b) corresponding pore size distributions

operations, and could make such materials potentially cost-effective for new applications. For the purpose of this work, vacuum drying was used in all the other sections, since it seems to lead to a lower degree of shrinkage of the final RF xerogels.

Table 3.5 Textural properties of gels dried at ambient pressure and under vacuum

R/C	S_{BET} [m ² /g]		V_{T} [cm ³ /g]		V_{μ} [cm ³ /g]		$\bar{\phi}$ [nm]	
	Drying method		Drying method		Drying method		Drying method	
	A	V	A	V	A	V	A	V
100	510	590	0.45	0.47	0.04	0.06	3	3
300	380	460	1.11	1.12	0.04	0.06	13	12
600	90	120	0.31	0.54	0.01	0.02	18	30

S_{BET} - accessible surface area from BET analysis; V_{T} - total pore volume determined from adsorption at $p/p_0 \sim 1$; V_{μ} - micropore volume determined using t-plot method; $\bar{\phi}$ - average pore width from BJH analysis; A - ambient drying; V - vacuum drying. Errors are omitted from the table as all values are reported to an accuracy less than the largest error for each variable.

3.2.5 Different sources of sodium ions

It has been shown in Section 3.2.1 that the presence of a metal ion, when using carbonate as a catalyst, is crucial for a porous RF gel to form. Previous work in our group [195] has shown that if ammonium carbonate ((NH₄)₂CO₃) is used instead of sodium carbonate (Na₂CO₃), a non-porous material is formed, similar to when no catalyst is used. In the same work [195], when a given quantity of Na₂CO₃ was substituted by the same molar amount of (NH₄)₂CO₃ (ie. R/C unchanged), the final gel properties were similar to a gel with the corresponding amount of Na₂CO₃, not the combined carbonate amount. This suggests that the sodium, or more generally a metal, ion plays an important role in the process of RF gel formation; therefore, gelation is not exclusively driven by reaction solution

pH, as is often reported in the literature for base catalysed RF gels [59, 63, 121]. It has been suggested before that both cations and anions present in the solution have an impact on the material structure [92]. In order to shed more light on this, two other sodium salts, containing anions that do not hydrolyse, thus should not change the solution pH, were added to Na_2CO_3 to adjust the sodium ion concentration without changing the solution pH. Sodium chloride (NaCl) and sodium sulphate (Na_2SO_4) were chosen in this work and the combined amounts of both salts were based on molar ratio of sodium ions to resorcinol molecules in the solution, so that the total amount of sodium ions was kept constant and equal to the amount in solution for an RF gel prepared using only sodium carbonate and R/C 100 (as in the previous sections). For example, a sample of Na_2CO_3 200 NaCl 100 was made using the amount of Na_2CO_3 as for a standard gel with R/C 200 and amount of NaCl to adjust the sodium ion concentration in the reaction solution to match that of a standard gel solution for R/C 100, the numbers used in the sample name represent the individual R/C ratios for the salts used. When a gel was made without sodium carbonate, its R/C ratio was labelled as Na_2CO_3 INF. Reagent masses used to make these gels are presented in Tables A.2 and A.3 in appendices for NaCl and Na_2SO_4 , respectively.

Nitrogen sorption isotherms and with their corresponding pore size distributions for samples prepared in this section are presented in Figures 3.18, 3.19, 3.20, and 3.21 along with data for selected samples prepared with only sodium carbonate. It can be seen from Figure 3.18 that both nitrogen sorption isotherms and pore size distributions for gels made with Na_2CO_3 200 and added NaCl or Na_2SO_4 exhibit similar shapes to that of a standard gel with R/C 300, rather than R/C 100 or 200. The solutions for samples with modified catalyst composition had the same sodium ion concentration as a sample with R/C 100, so if sodium ion concentration was the main factor influencing the final structure, these should exhibit similar textural properties. However, the solution pH would differ from a standard R/C 100 solution, since both chloride and sulphate anions do not hydrolyse in an aqueous

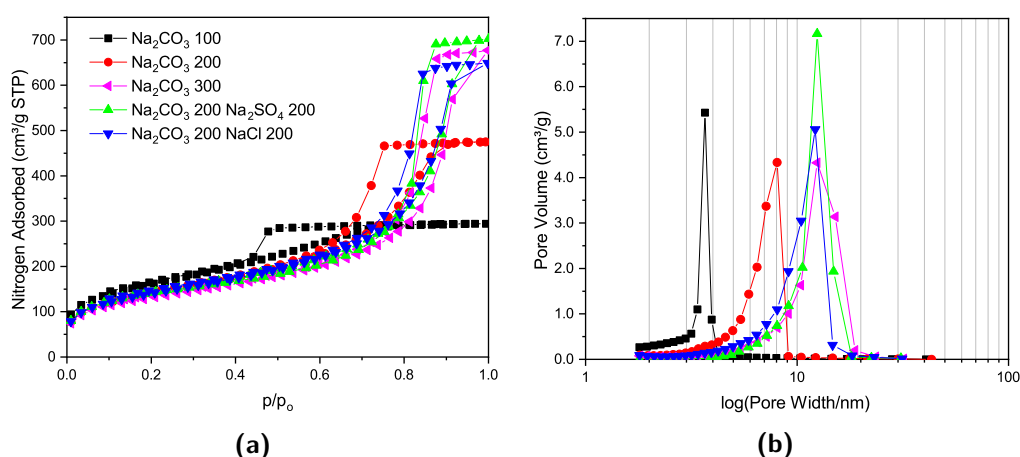


Figure 3.18 (a) Nitrogen sorption isotherms of gels with modified catalyst composition and (b) corresponding pore size distributions

Table 3.6 pH values of initial solutions and textural properties for gels with different R/C ratios of sodium carbonate (Na_2CO_3), sodium sulphate (Na_2SO_4), and sodium chloride (NaCl)

R/C			pH	S_{BET} [m^2/g]	V_{T} [cm^3/g]	V_{μ} [cm^3/g]	$\bar{\phi}$ [nm]
Na_2CO_3	Na_2SO_4	NaCl					
100	-	-	7.3	580	0.46	0.06	3
200	-	-	7.0	500	0.73	0.05	6
400	-	-	6.6	220	0.98	0.03	24
600	-	-	6.4	220	0.81	0.04	21
-	-	-	4.1	-	-	-	-
200	200	-	7.4	490	0.95	0.06	9
200	-	100	7.3	500	0.99	0.06	10
400	133	-	7.0	120	0.30	0.02	16
400	-	67	6.9	130	0.34	0.02	17
600	120	-	6.7	1	-	-	34
600	-	60	6.6	-	-	-	39
-	100	-	3.3	-	-	-	-
-	-	50	3.1	-	-	-	-

S_{BET} - accessible surface area from BET analysis; V_{T} - total pore volume determined from adsorption at $p/p_0 \sim 1$; V_{μ} - micropore volume determined using t-plot method; $\bar{\phi}$ - average pore width from BJH analysis. Errors are omitted from the table as all values are reported to an accuracy less than the largest error for each variable.

solution resulting in a similar pH to that of a R/C 200 solution. However, the pH values presented in Table 3.6 show a slight difference between the solutions with and without the additional salts present. It should be noted, that the pH probe used converts a voltage measurement into a pH value, which means the voltage reading could be influenced by the other ions present in the solution. Nevertheless, there is a general trend of decreasing pH with increasing R/C ratio, as a result of decreasing concentration of hydrolysing carbonate ions. Due to the strong electrolyte nature of Na_2CO_3 , its dissociation in an aqueous solution should not be affected by the addition of Na^+ ions.

Similar trends can be observed in Figures 3.19 and 3.20 where the nitrogen sorption data for samples with additional salts are closer to samples prepared with a higher R/C ratio than the ones with the same Na_2CO_3 amount or sodium ion concentration. Samples with Na_2CO_3 400 exhibit similar properties to a standard gel with R/C ratio 800. Interestingly, when either Na_2SO_4 or NaCl are added to a gel with Na_2CO_3 600, a non-porous material is obtained, similar to when no catalyst is used, even though RF gels prepared using only Na_2CO_3 at R/C ratio 600 are still porous materials.

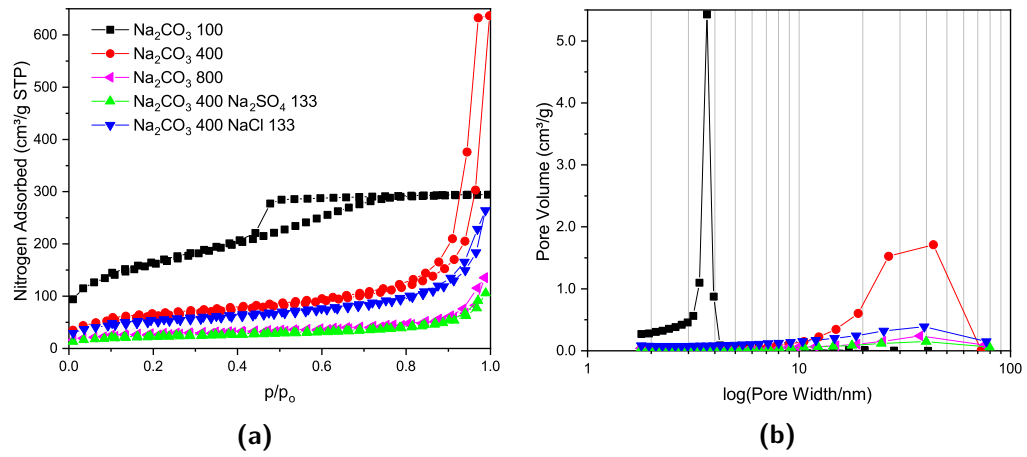


Figure 3.19 (a) Nitrogen sorption isotherms of gels with modified catalyst composition and (b) corresponding pore size distributions

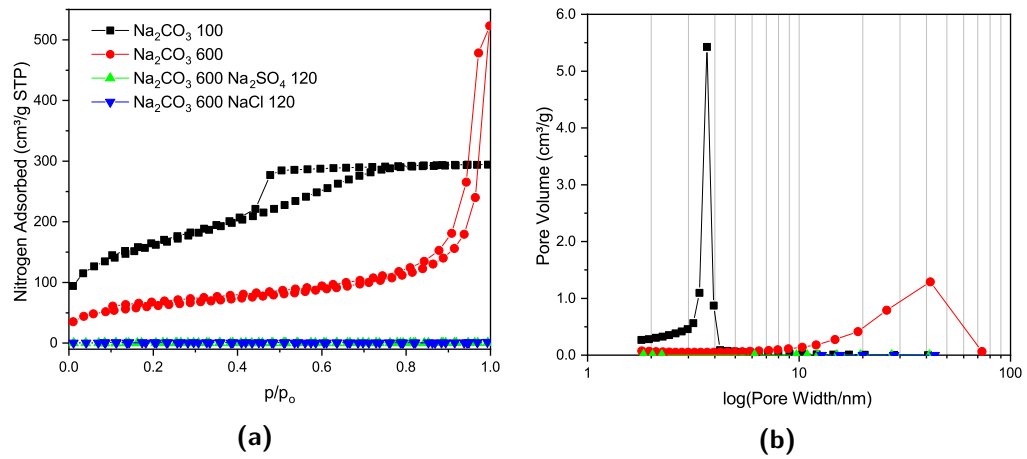


Figure 3.20 (a) Nitrogen sorption isotherms of gels with modified catalyst composition and (b) corresponding pore size distributions

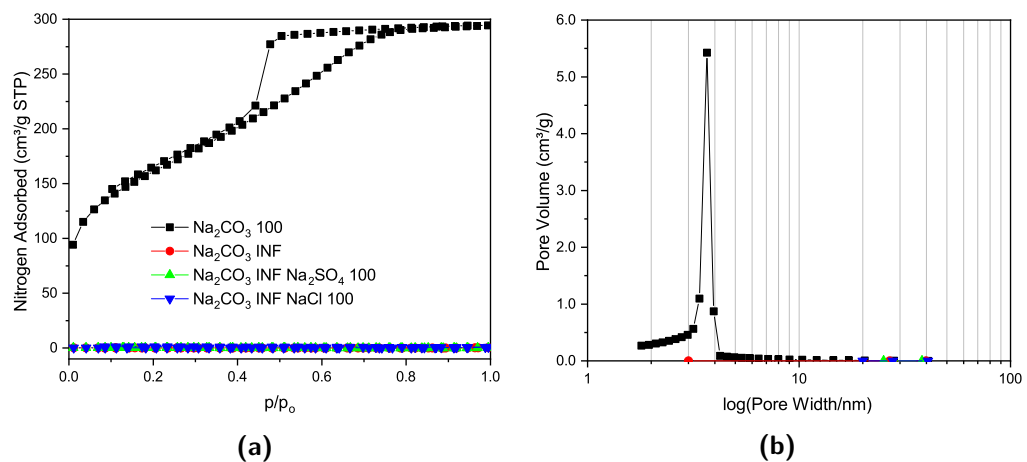


Figure 3.21 (a) Nitrogen sorption isotherms of gels with modified catalyst composition and (b) corresponding pore size distributions

As described in the introduction section, according to the work by Taylor *et al.* [79, 91], RF clusters that are formed in the reaction solution gradually grow and adhere to each other, resulting in the final structures observed in the dried materials. Textural properties of RF xerogels, therefore, depend on the final cluster size and their packing in three dimensions. The anions used in this part of the study are arranged in the reversed Hofmeister series [87], as presented in Section 1.2.3 for hydrophilic surfaces, in the following order of ability to salt-out macromolecules from solution: $\text{CO}_3^{2-} < \text{SO}_4^{2-} < \text{Cl}^-$. This suggests, that in the solution containing only the carbonate (CO_3^{2-}) ions, the growing clusters will precipitate from the solution at later stages compared with solutions, where a proportion of the carbonate ions are substituted by anions with higher salting-out ability, such as sulphate (SO_4^{2-}) and chloride (Cl^-) anions.

As clusters grow in the reaction solution, they can potentially grow at slightly different rates, based on the diffusion of reagents towards the reactive centres. When a cluster reaches critical size, leading to local phase separation, the newly created interface will lead to adsorption of species dissolved in the solution, reagents, on this interface. In a solution containing ions with a higher salting-out ability (SO_4^{2-} and Cl^-), clusters might precipitate at an earlier stage, leading to a faster subsequent growth of these clusters due to the reagent adsorption effects. This would lead to the clusters left in solution to grow at a slower pace, with the reactants being depleted by the faster growing precipitated clusters. This might result in an increased final size of clusters in from these solutions, compared to when only CO_3^{2-} is present. Without the SO_4^{2-} and Cl^- ions, larger amount of clusters grow at a similar rate for longer time, with larger clusters present when phase separations occurs, leading to more uniform, and on average smaller, particles present in the final material. The larger clusters, arising from an earlier phase separation, would have larger gaps in between them, observed as larger pore sizes from nitrogen sorption measurements. However, it is important to keep in mind that only pores up to the upper limit of mesopores, up to $\sim 50\text{-}100$ nm [142–144], are observable by this technique, with the macropores not filling, and thus, not contributing towards the average pore size.

Another factor that could have a potential influence on cluster growth in solution is the ionic strength of the reaction mixture. Ionic strength (I) of a solution is based on the concentration and charge of the ions present, and is calculated as follows:

$$I = \frac{1}{2} \sum_i c_i z_i^2 \quad (3.26)$$

where c_i is molar concentration of an ion, z_i is the ion charge, and i is index for each ion present in the solution. Calculated ionic strength of solutions with R/C 100 and 200 with sodium carbonate and added sodium chloride or sodium sulphate are presented in Table 3.7. It can be seen that due to the sulphate ion being divalent, the same as the carbonate ion, the ionic strength of solution Na_2CO_3 200 Na_2SO_4 200 is the same as for Na_2CO_3 100. However, the solution with sodium chloride (Na_2CO_3 200 NaCl 100), having the same

sodium ion concentration as the Na_2CO_3 100, has a higher value of ionic strength. Despite the significant difference in the value of I for solutions with sodium sulphate and sodium chloride, the textural properties of final RF gels prepared using these solutions are very similar. On the other hand, even though the solutions used for Na_2CO_3 100 and Na_2CO_3 200 Na_2SO_4 200 have identical values of I , the final gel properties vastly differ from each other. This suggests that the ionic strength of the initial solution is not a major factor influencing the final textural properties of a RF xerogel when different ions are present in the solution.

Table 3.7 Ionic strength of solutions with different R/C ratios of sodium carbonate (Na_2CO_3), sodium sulphate (Na_2SO_4), and sodium chloride (NaCl)

R/C			I [M]
Na_2CO_3	Na_2SO_4	NaCl	
100	-	-	0.0350
200	-	-	0.0175
200	200	-	0.0350
200	-	100	0.0584

A series of RF gels using only sodium chloride as a catalyst were prepared, in order to investigate if the presence of sodium ions is the major driving force for RF gel formation rather than solution pH. Samples with NaCl R/C 12.5, 200, and 400 (corresponding to sodium ion concentrations for Na_2CO_3 R/C ratios of 25, 400, and 800) were prepared; however, all of the final materials were found to be non-porous. The values of solution pH, after all the reagents have dissolved and a 30 minute stirring period, were measured as 3.4, 3.3, and 3.2 for NaCl R/C 12.5, 200, and 400, respectively. This suggests, that both the presence of sodium ions and appropriate solution pH value are necessary in order to obtain a viable porous gel structure.

An interesting observation can be made by visually comparing dried RF xerogels made with and without the additional salts, photographs of these xerogels are presented in Figure 3.22. Xerogels prepared with either sodium sulphate or sodium chloride added have a very similar appearance and differ significantly from the standard xerogels prepared with sodium carbonate only. It is also worth mentioning that samples with Na_2CO_3 R/C ratios 400 and 600 made with additional salts did not exhibit the usual level of shrinkage after subcritical drying, as all the other studied materials do, even though they were all cut into similar sized pieces (~ 1 cm), which can be used as a visual guide in comparing samples, prior to the solvent exchange step. This might be explained by the larger pore sizes present in these samples, eliminating capillary forces during drying while preserving the extent of cross-linking, leading to a lower degree of material shrinkage. If large macropores are present in these samples, as described above, the liquid-vapour interface would not cause a collapse of this large-scale porous structure, leading to only a small shrinkage of these materials even

under subcritical conditions. However, it is important to note that for many applications, such as gas storage, this macroporosity is not as useful as the presence of mesopores.



Figure 3.22 RF xerogels prepared with varying R/C ratios of Na_2CO_3 , Na_2SO_4 , and NaCl

3.3 Summary

The effects of various processing parameters on the final textural properties of RF gels were studied in this chapter, including the sodium carbonate catalyst concentration, solvent exchange method, processing temperature, drying method, and different sources of sodium ions. These were investigated by preparing RF gel samples and their subsequent analysis using nitrogen sorption measurements.

The main findings, based on the results of this chapter, are as follows:

1. Effect of sodium carbonate concentration:
 - (a) Increasing the sodium carbonate concentration (decreasing R/C ratio) leads to a decrease in observed pore size, caused by smaller particles present in the final material.
 - (b) Increasing R/C ratio is associated with decreasing accessible surface area and increasing total pore volume.
 - (c) High values of R/C ratio lead to a material with poor mechanical properties resulting in significant shrinkage during the drying process.
 - (d) If no catalyst is present, a non-porous material is obtained, showing the importance of the presence of catalyst in the process in order to obtain a viable porous structure.
2. Solvent exchange method:
 - (a) Increasing the amount of acetone used in one dose over 3 days from 180 ml to 240 ml leads to slight improvement of textural properties.
 - (b) Splitting the amount of acetone used over 3 days into 3 doses enhances the final textural properties (increased accessible surface area, total pore volume, and average pore size), suggesting a more thorough exchange of water within the pores with acetone.
 - (c) Samples with higher R/C ratios benefit less from the improved solvent exchange due to poor mechanical properties leading to potential structure damage during additional handling of the materials.
3. Processing temperature:
 - (a) Minimum gelation and curing temperature of 55 °C necessary to obtain a viable gel structure.
 - (b) Increase in processing temperature leads to better mechanical properties, due to enhanced cross-linking, and therefore, improved textural properties.
 - (c) Textural properties exhibit plateauing at higher temperatures.
4. Drying method:
 - (a) Vacuum drying preserves porous structure slightly better.
 - (b) Ambient pressure drying could be used if the requirements for the final material are not too strict.

5. Sodium ion sources:

- (a) Replacing proportion of the sodium carbonate with sodium chloride or sodium sulphate leads to materials with significantly different textural properties.
- (b) Introducing chloride or sulphate ions to the reaction solution leads to a similar effect as increasing R/C ratio of sodium carbonate, without significantly changing the reaction solution pH.
- (c) Ions present in the reaction solution have an effect on salting-out of growing clusters, affecting the final pore size presumably without changing the condensation and addition reactions.

The aforementioned findings show the importance of carefully controlling the manufacture process of RF gels in order to obtain a material with desired properties. It also shows the variety of materials that can be obtained by adjusting the RF gel synthesis, allowing tailoring of the structure for a particular application.

Chapter 4

Modelling porous xerogels

4.1 Cluster growth model

In order to enhance the understanding of structure formation within porous xerogel materials and help guide tailoring these materials to a particular application, a computational model, generating simulated structures, in two dimensions was developed. The model describing the formation, growth and aggregation of resorcinol-formaldehyde (RF) clusters was based on experimental data from the literature and this work (Chapter 3) in order to obtain structures similar to those observed experimentally.

A general understanding of the dependence of RF gel materials on some of the processing parameters was obtained by performing a related experimental study (Chapter 3) and reviewing previous experimental work within our group [79, 195, 196]. The catalyst salt present in the solution activates a proportion of the resorcinol molecules [59] to form anions, which are more reactive in the addition reaction with formaldehyde, compared to neutral resorcinol molecules, as described in more detail in Section 1.2. These activated species act as seeds for subsequent growth of the spherical particles observed by electron scanning microscopy of RF gels [54, 62, 102, 105].

Cluster formation and diffusion in the RF solution has been observed visually by Alshrah *et al.* [58] at ambient temperature. As the clusters grow within the reaction solution, they can adhere to other clusters, thus forming larger aggregates; these processes are more pronounced at elevated temperatures [79]. This aggregation has been noted in the work by Pol *et al.* [197], where RF resin synthesis has been assisted by ultrasound, forming individual spherical particles in solution within a short time frame. In a control experiment in the same work, performed as a stirred emulsion polymerization without sonication, small aggregates of RF particles were observed, again via scanning electron microscopy, after a longer gelation time, which is required for the reaction to complete without sonication. The particles prepared with ultrasound formed relatively quickly, leading to only a small

fraction of particles adhering to each other. However, the longer reaction times required during emulsion polymerization result in greater RF cluster adherence, leading to smaller aggregates. Larger agglomerates were not formed, due to the agitation from stirring, which prevents the particles from contacting for a sufficiently long time to form cross-links.

During the RF monolith manufacturing processes, used in the experimental part of this work, there is no agitation of the reacting solution, allowing the formation of three-dimensional particle networks, starting from individual clusters that create smaller aggregates, which generate the final structure spanning the reaction space [192]. The examples from the literature discussed here are not exhaustive but provide additional information about the generation of final structures in RF gels, and were used as a basis for the developed model. It should be noted that even though the model was based on experimental data for RF gels, due to the amount of data available in the literature and the experimental data from Chapter 3, it could be transferable to other materials, for which the structure is created via a similar route as the one described here for RF gels.

In order to capture the structure development process mentioned above, a model has been developed in this work that aims to mimic the growth processes deduced from experimental gel formation, and in particular moves away from a dependence on uniform sphere size as found in previous models [158–162], while adding cluster growth and concentration of activated species compared to previous work developed for similar systems [155, 156]. The model was developed in two dimensions, which allows visual understanding of the structure development, as well as evaluation of large system sizes, to explore the fractal properties of the structures created by the model. The generated structures are subsequently analysed for accessible pore space and accessible surface area, along with their fractal properties, using the correlation dimensions of the structures, and Hurst exponent of random walkers diffusing in the resulting accessible pore structures. These characteristics will provide insight into the interdependence of the structural properties of these materials and their synthesis conditions, such as concentrations of catalyst and solids, paving the way for the bespoke design of porous gels tailored to their applications.

For this purpose, in-house software was developed with GNU Fortran compiler and GNU parallel tool [198] using a lattice based kinetic Monte Carlo (kMC) method. A two-dimensional lattice, with periodic boundaries, was initially populated by monomers, in order to mimic total solids concentration (S_C), which in this case represents the fraction of occupied lattice sites. Values of S_C used in this work range from 10 to 50 %, moving in 10 % increments. Higher values of S_C , up to 90 %, were explored; however, most of the porosity developed for S_C above 50 % was observed as closed and not percolated in two dimensions, therefore, only structures up to 50 % S_C are analysed in the subsequent sections. A percentage of the monomers (C_C) were 'activated' to represent catalyst concentration and corresponding amount of activated monomers (resorcinol anions). These activated species

acted as seeds for cluster nucleation. In this work, $C_C = 1, 2,$ and 3% were used, based on the proportion of charged resorcinol molecules discussed in the work of Lin and Ritter [59].

In the following sections, the structure of the code used to generate simulated cluster structures is first presented, describing the code algorithm, along with the subroutines and the data structure used in the model, providing more detail about the variable type and the information flow with the subroutines. Initially, the model was developed using static clusters, followed by the implementation of cluster diffusion. Cluster structures, implementing diffusion, along with their analysis have been submitted to the journal 'RSC Advances' and the submitted manuscript is presented in Appendix D.2.

4.1.1 Code algorithm

The in-house software, mentioned above, was based on the previously discussed experimental evidence and the algorithm for modelling cluster growth and aggregation was developed using the following steps:

1. Populate lattice with cluster seeds and monomers.
2. Randomly select a species to diffuse based on the relative rate of species diffusion using the kinetic Monte Carlo algorithm; diffusion probability scales inversely with species size.
3. Attempt to diffuse the selected species in a random direction by one lattice site:
 - (a) If a cluster was selected in step 2, move all clusters within the same aggregate together and, if another cluster is adjacent at the new position, merge the two clusters/aggregates.
 - (b) If a monomer was selected in step 2, and if the new site is occupied by a cluster, attach the monomer to the cluster and increase the cluster size; do not accept the move if the new site is already occupied by another monomer.
4. Advance the simulation clock by a random value, the magnitude of which is based on the total kinetic Monte Carlo sum.
5. If a monomer was absorbed by a cluster or two clusters became linked, recalculate the kinetic Monte Carlo sum.
6. If there is more than one cluster aggregate and any monomers remaining in the simulation, go back to step 2 and repeat until there are no monomers and only one cluster aggregate remaining.
7. Write final cluster structure into a file.

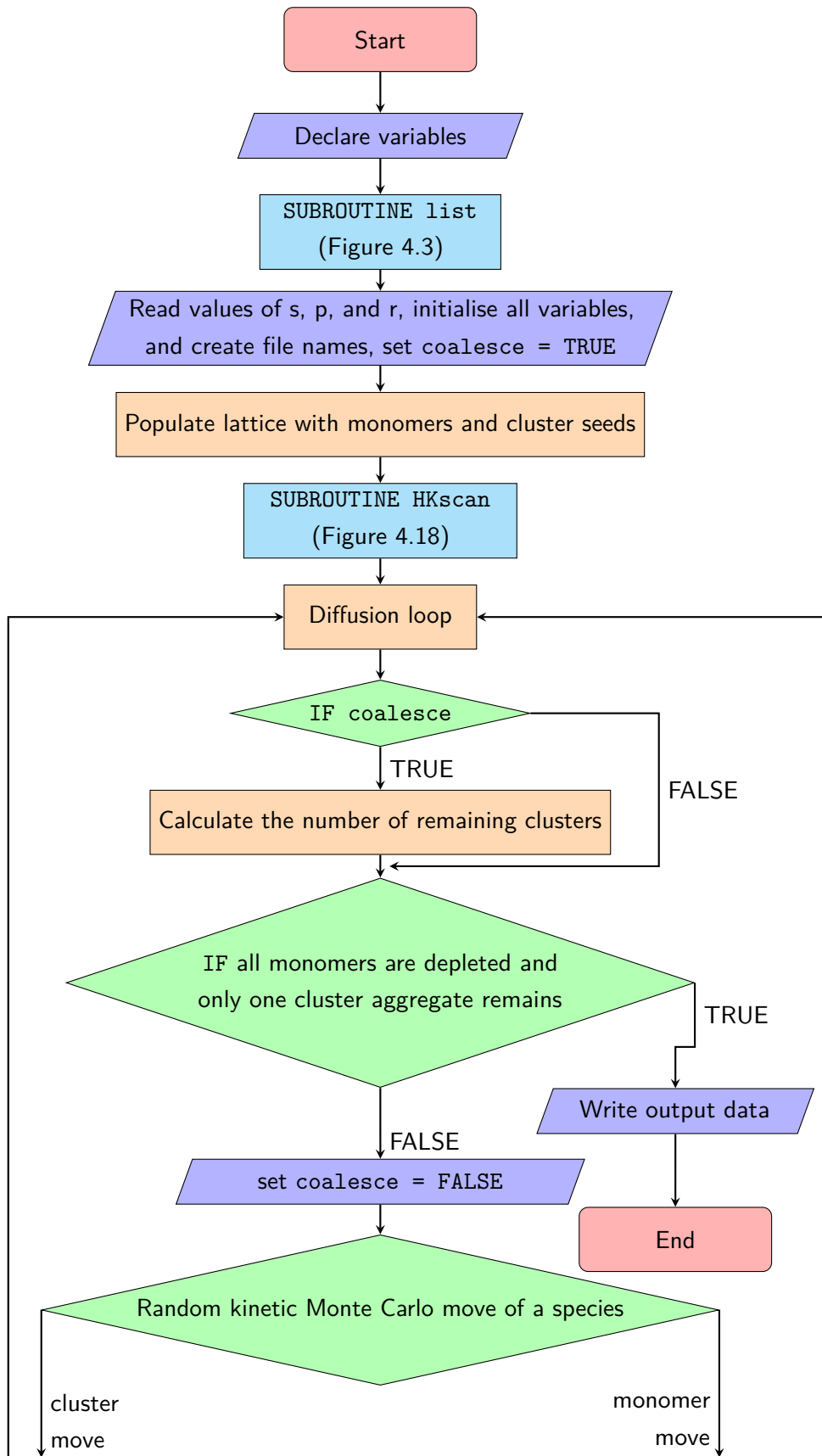
A flowchart of the main body of the code developed to generate simulated cluster structures is presented in Figure 4.1. Flowcharts of related subroutines are presented in Figures 4.3 to 4.5, 4.12, 4.14, and 4.16 to 4.19. Fortran code of the algorithm is presented in Appendix E.2.1.

First, all variables were declared, along with their types (integer, real number, character string, and logical) due to the option `IMPLICIT NONE` used in the beginning of the code, as a good coding practice.

After declaring all the used variables, a list of sites for cluster drawing is created using `list` and its related subroutines at the beginning of a simulation run. The simulation conditions in form of the values of solids content (S_C), percentage of activated monomers (C_C), and the run number are set, followed by initialising the values of used variables as required. File names for output files are created based on the simulation conditions. The lattices containing monomer and cluster distribution are populated at random based on the values of solids content and percentage of activated monomers. Separate lists for storing species coordinates and cluster sizes are created, and updated during the simulation run, in order to make selection of moves in the algorithm more efficient. Before the main diffusion loop is initiated, neighbouring sites of all clusters are checked, using `HK_scan` subroutine, and if two clusters are found next to each other, they are linked into a single aggregate. A conditional statement decides whether the number of remaining clusters needs to be recalculated and another one to decide if the simulation is deemed finished (if only a single cluster aggregate and no monomers remain).

A random species is selected to attempt a diffusion move, where the probability of a move is inversely proportional to the species size and is stored in the kinetic Monte Carlo sum. If a cluster is selected, the subroutine `diffuse_cluster` is used with all the clusters within the same aggregate moving by one lattice site in a random direction. This is followed by examining the perimeter of the cluster/aggregate to check if another cluster is not adjacent to it, using the `HK_scan` and its related subroutines. If a monomer is selected, the corresponding `diffuse_monomer` subroutine is called. If the newly selected site is occupied by another monomer, the move attempt is not accepted. If the monomer diffuses onto a site already occupied by a cluster, the `attach` subroutine removes it from the lattice and makes the appropriate cluster grow. Due to this cluster growth, the `HK_scan` subroutine is used again to check for new cluster links. The monomer is then removed from the monomer distribution lattice and the number of remaining monomers is adjusted accordingly.

The simulation clock is advanced after a diffusion move attempt by a randomly drawn value based on the total kinetic Monte Carlo sum. At the end of an iteration of the diffusion loop, the kinetic Monte Carlo sum is recalculated if a monomer was absorbed by a cluster or if two clusters/aggregates merged into one larger aggregate, resulting in reduction of the number of species in the simulation and change in species size. This is followed by selecting another species to diffuse at random until all monomers have been depleted and only a single cluster remains, after which the simulation is deemed finished.



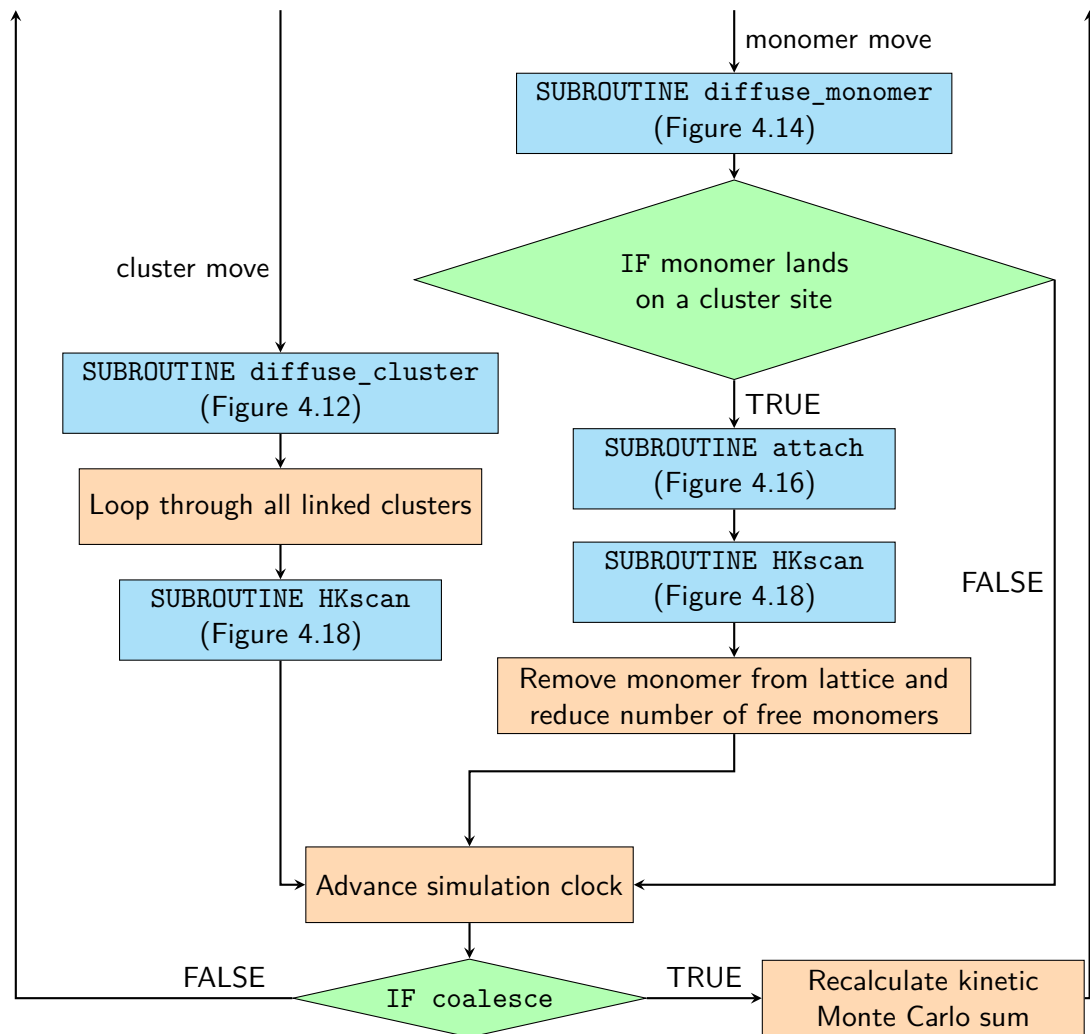


Figure 4.1 Schematic flowchart of code used for cluster growth and aggregation model

The data structure for the algorithm described in this section is presented here as well. The variables used in the algorithm are described along with their required dimensions (e.g. `Cluster(Nlat,Nlat)`) is a two-dimensional lattice with size `Nlat` in each dimension, leading to `Nlat × Nlat` array elements). The flow charts for data structures within this

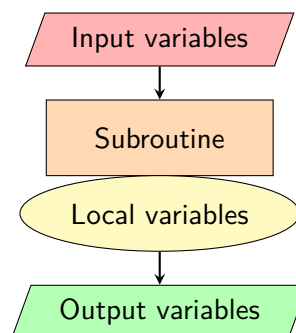


Figure 4.2 Example data structure

section use the following notation: orange rectangles for subroutines, red parallelograms for input, green parallelograms for output, and yellow ellipses for local variables, as presented in Figure 4.2. A summary table listing all the used variables, in alphabetical order, is presented, for reference, in Table 4.2 at the end of this section.

Run initialisation

At the beginning of a simulation run, values of the control variables are set. The run number (r) is an integer, with a value between 1 and 10, and is used to generate the seed for the random number generator. This ensures that when the run number is changed, the final structure will differ slightly from the previous ones, even with the same values of S_C and C_C , leading to multiple structure repeats, at the same conditions, for improved statistics. Both solids content and percentage of activated monomers are represented by an integer (s and p) and a real ($solid$ and $percentage$) variable each. The integer variables are used for creating file names and to calculate the real ones. $solid$ ($solid = s/10$) and $percentage$ ($percentage = p/100$) are used to calculate the total number of species in the simulation ($N_{max} = solid \times N_{lat}^2$), the number of activated monomers ($N_{act} = percentage \times N_{max}$), and the number of free monomers ($N_{mon} = N_{max} - N_{act}$).

Arrays with size based on the number of species in the simulation (N_{max} , N_{act} , and N_{mon}) are allocated using these variables at the beginning of a simulation run. The arrays $iCluster(N_{act}, N_{lat})$ and $jCluster(N_{act}, N_{lat})$ store coordinates of lattice sites occupied by clusters, with the first position indicating the cluster number and the second position being the cluster counter. $iMonomer(N_{mon})$ and $jMonomer(N_{mon})$ are the equivalent arrays for monomer positions, with only one position necessary for each monomer since all the monomers have size equal to 1. $Monomer(N_{lat}, N_{lat})$ and $Cluster(N_{lat}, N_{lat})$ matrices store the monomer and cluster distribution on the lattice, respectively, with the lattice sites occupied by monomers being equal to 1 on the $Monomer$ lattice. Sites occupied by clusters have the corresponding cluster number on the $Cluster$ lattice, allowing for easy identification of cluster sites on the lattice during the simulation run. Empty sites on both lattices are set to 0. $ClusterSize(N_{act})$ and $ClusterCounter(N_{act})$ are, as the names suggest, arrays storing the sizes and counters for all the clusters.

File names in the form of character variables are created using information about the file type, S_C , C_C , and run number. The corresponding $.dat$ files are opened either at the beginning, if data is written out during the simulation execution, or at the end, if the data output contains only final values. All the arrays used are initiated with either a value of 0 for all the elements or appropriate starting values. The random number generator is seeded with a value of $r*100$.

Activated monomers, that act as cluster seeds, are placed randomly on the lattice (`Cluster`), making sure that each site is occupied by only one cluster seed. Each cluster size is set to the value of 1 to begin with. This is followed by randomly distributing the monomers. Again, each site can contain only one species, so if a monomer is attempted to be placed on a site that is already occupied, another random site is selected until all the monomers are distributed. The position arrays (`iCluster`, `jCluster`, `iMonomer`, and `jMonomer`) are all populated with appropriate values as the species are being distributed on the lattice.

Before the main loop, performing the diffusion steps, begins, the `coalesce` logical variable is set to `TRUE` so that in the first run of the loop, the number of clusters is counted and the initial values are written into the output file. The logical variable `last` is set to `TRUE` before the loop as well, and is changed to `FALSE` once there are only 20 cluster aggregates remaining in the system, writing out data at every aggregate collision in the last stage of the simulation. Every time two clusters or aggregates merge into a larger aggregate, the `coalesce` variable is set to `TRUE`, so that the number of remaining aggregates and the kinetic Monte Carlo (kMC) sum are recalculated. The kMC time, number of remaining monomers and aggregates, output counter, and counter used for determining whether output will be created, are written into the output file every time the number of aggregates remaining is reduced by one hundredth of the total number of clusters. As mentioned above, when there are only 20 aggregates remaining, the output is written out every time the number of aggregates is reduced.

After the number of remaining cluster aggregates is recalculated, `coalesce` is set to `FALSE` again, so that the calculation is performed only when there is a reduction in the number of aggregates and does not unnecessarily slow down the simulation.

In order to account for cluster that are initially placed adjacent to another cluster, the `HK_scan` subroutine, and its related subroutines, is used for all the clusters to create links of such cluster pairs. The aforementioned subroutines are described in more detail below.

Drawing clusters

The `list` subroutine (Figure 4.3) is used to create an ordered list of sites for drawing clusters on the lattice. In order to do that, the `list` subroutine uses two related subroutines, namely `draw_list` (Figure 4.4) and `scan_list` (Figure 4.5). The `draw_list` subroutine draws an approximately circular cluster of increasing radius on a lattice by adding 1 to all the sites the cluster occupies. The method of cluster drawing is described in more detail in the following paragraph. This means that the outer-most layer of the newly added sites has the value of 1, while all the inside sites, that are not on the perimeter, contain higher values, as presented in Figure 4.7b. This structure is then analysed by the `scan_list` subroutine and all the newly added sites are recorded using relative coordinates of each of the sites with regards to the cluster centre. This process is repeated for increasing cluster radii until the radius reaches half of the lattice size ($N_{lat}/2$), where the lattice size was fixed in this

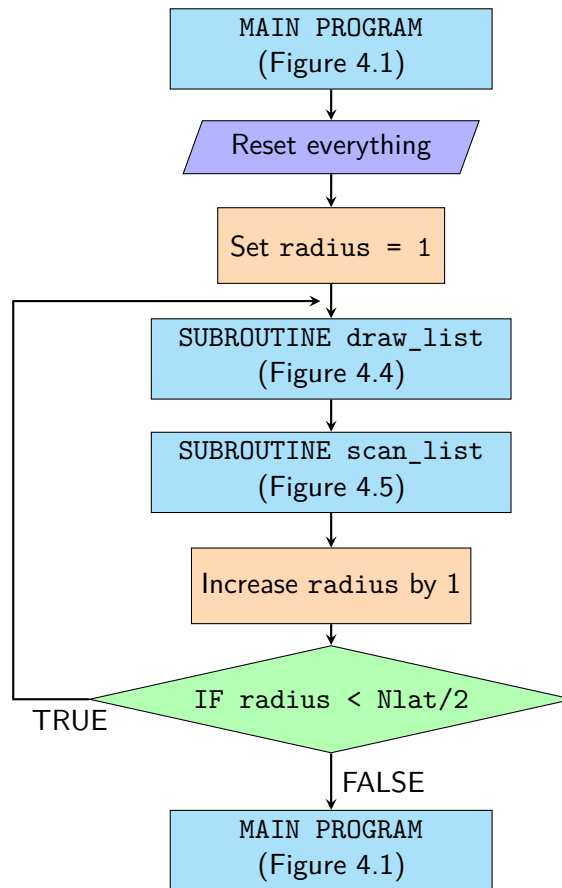


Figure 4.3 Schematic flowchart of `list` subroutine

work at size $N_{lat} = 1000$. This upper limit is well above cluster size expected in any simulation, with individual clusters each occupying only a small fraction of the lattice.

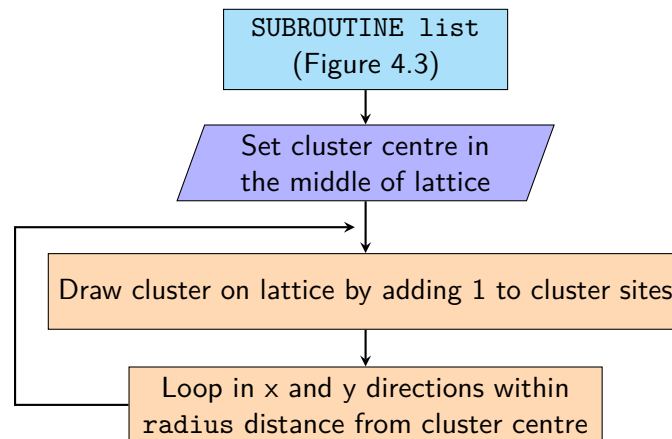


Figure 4.4 Schematic flowchart of `draw_list` subroutine

Figure 4.6 presents the data structure for `list` subroutine, and the related subroutines `draw_list` and `scan_list`. The `list` subroutine takes an input value of lattice size (N_{lat}) and creates local variables `radius` (radius of cluster being drawn),

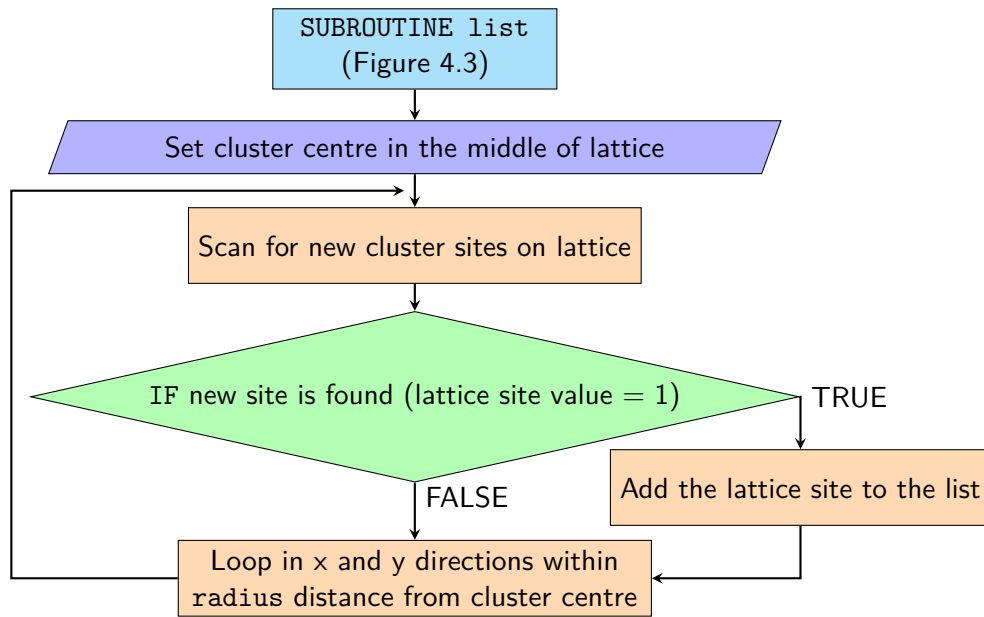


Figure 4.5 Schematic flowchart of `scan_list` subroutine

`Lattice(Nlat,Nlat)` (lattice onto which the cluster is drawn), and `No` (cluster site counter). As mentioned in the previous section (4.1.1), the cluster is first drawn by `draw_list` subroutine and subsequently analysed by `scan_list`. Input for `draw_list` subroutine includes `Nlat`, `radius`, and `Lattice`, thus passing on the information about lattice size, current cluster radius and cluster structure to the subroutine. Local variables for

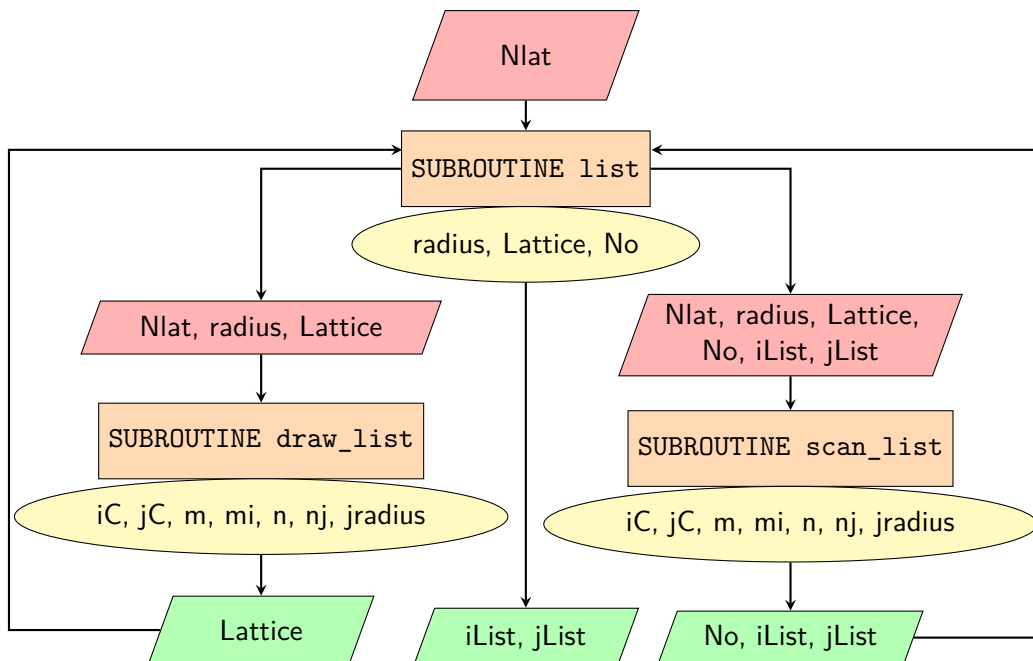


Figure 4.6 Data flow to and from `list` subroutine and its related subroutines `draw_list` and `scan_list`

both `draw_list` and `scan_list` are `iC` and `jC` (cluster centre coordinates), `m` and `n` (counters for looping in `i` and `j` directions), `mi` and `nj` (dummy variables derived from counters `m` and `n` with periodic boundaries taken into account), and `jradius` (radius in `j` direction during cluster drawing). The only output variable for `draw_list` is the updated `Lattice` with the cluster structure. For `scan_list` the input includes the same variables as for `draw_list` with additional input variables `No` (counter used for `iList` and `jList`), and `iList(Nlat × Nlat)` and `jList(Nlat × Nlat)` (arrays storing a list of positions for drawing clusters on lattice for `i` and `j` coordinates, respectively). The size of both `iList` and `jList` is sufficient for a cluster to occupy the whole lattice, however, this is never the case in this work. The output of `scan_list` includes `No` counter and updated `iList` and `jList` arrays. The overall outputs of the `list` subroutine are the completed `iList` and `jList` arrays with the list of positions.

Based on experimental evidence [54, 62, 102, 105], as discussed above, ‘circular’ islands were grown on the lattice. The mechanism of individual cluster growth is depicted in Figure 4.7, where the increasing numbers indicate lattice sites for cluster growth with each additional monomer attached to that cluster (Figure 4.7a). The colours used in Figure 4.7 represent layers of monomers being attached to a cluster; this way, the growing clusters retain a compact, approximately circular, shape rather than the branched shape that would result from a diffusion-limited aggregation mechanism, keeping the model structures closer to those observed experimentally. If a site was already occupied by another cluster, the next available site in the list was used.

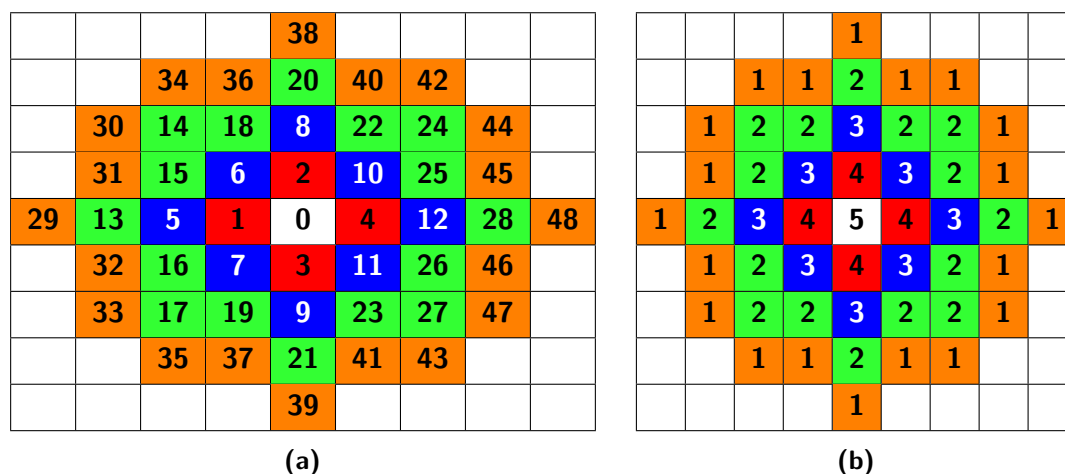


Figure 4.7 Schematic drawing of the cluster growth mechanism on a two-dimensional lattice with (a) numbers representing the position of each additional monomer added and (b) numbers used during cluster drawing in `draw_cluster` subroutine. The colours represent different layers of growth (1st layer ■, 2nd layer ■, 3rd layer ■, 4th layer ■).

When two clusters touched, they became linked into a larger cluster aggregate; the resulting cluster aggregates moved across the lattice together, but the individual clusters continued to grow independently. An example of individual cluster growth in an aggregate, formed

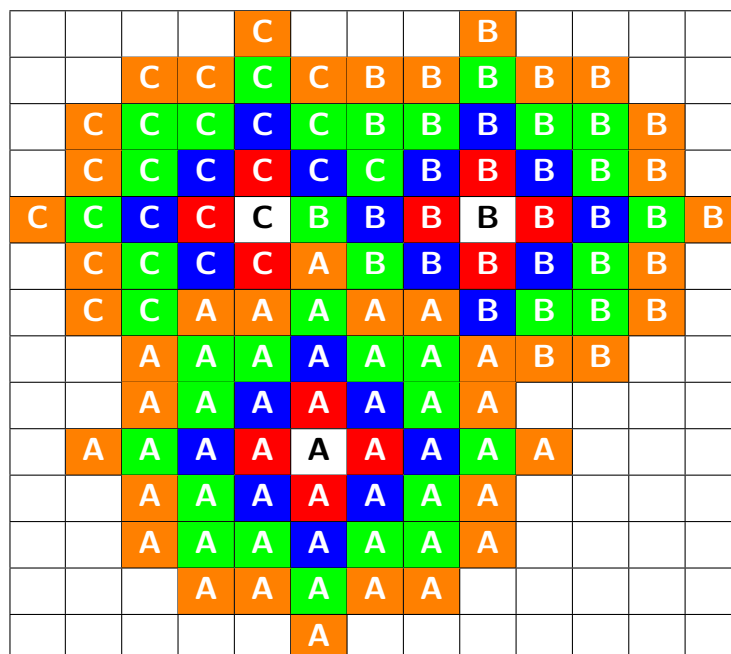


Figure 4.8 Schematic drawing of three clusters (labelled A, B, and C) growing adjacent to each other, indicating growth with cluster overlap. Colours represent different layers of growth (1st layer ■, 2nd layer ■, 3rd layer ■, 4th layer ■).

by three clusters, is shown in Figure 4.8. It can be seen that while cluster A (Figure 4.8) retains an approximately circular shape, cluster C grows around clusters A and B, keeping an outer circular arc shape where possible.

Cluster growth and aggregation is illustrated in Figure 4.9, where three clusters (black) gradually grow, on a lattice with periodic boundaries, consuming the monomers (red) around them. As can be seen from Figure 4.9, monomers and clusters diffuse freely on the lattice with monomers being gradually depleted by the growing clusters.

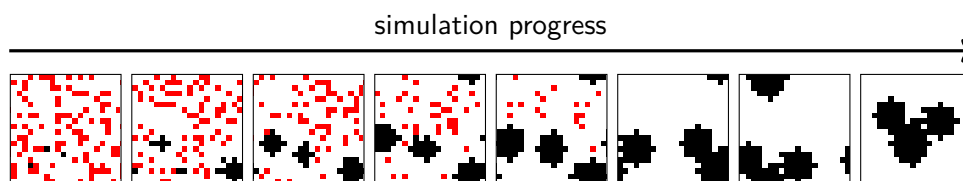


Figure 4.9 Cluster growth and diffusion mechanism example. Positions occupied by cluster points shown in black, and by monomers in red.

Diffusion

Diffusion of monomers, clusters, and cluster aggregates within the simulation is performed by two subroutines, `diffuse_cluster` and `diffuse_monomer`, based on the selected species. The selection of a species to diffuse is based on the kinetic Monte Carlo sum, as is explained below.

$\text{MCsum}(\text{Nmax})$ array stores the values of the kinetic Monte Carlo sum of all the species in the simulation (monomers, individual clusters, and cluster aggregates) and is used to determine which species will attempt a diffusion move in each time step. The first Nact positions contain the sums for clusters and the rest of the array is used for monomers. In the beginning of the simulation run, all clusters begin with a size of 1 lattice site, so the probability of a move for all the species present at that time is identical. Evolution of the kinetic Monte Carlo sum for an example system with 3 clusters and starting with 5 monomers is shown in Figure 4.10. The starting configuration (4.10a), includes all the species with equal probability of a move, due to their identical size. The total kMC sum for this example system starts at 8. In 4.10b, one of the monomers is consumed by the last cluster, increasing its size to 2, thus its probability of a move is half of all the others, since probability of a move scales inversely with size of a species. In 4.10c, a monomer is consumed by the second cluster, making its probability of an attempted move $\frac{1}{2}$, i.e. the same as the last cluster. In step d, the last cluster absorbs another monomer, making its size being equal to 3, and thus its kMC probability reduces to $\frac{1}{3}$, leading to the total kMC sum value $3\frac{5}{6}$.

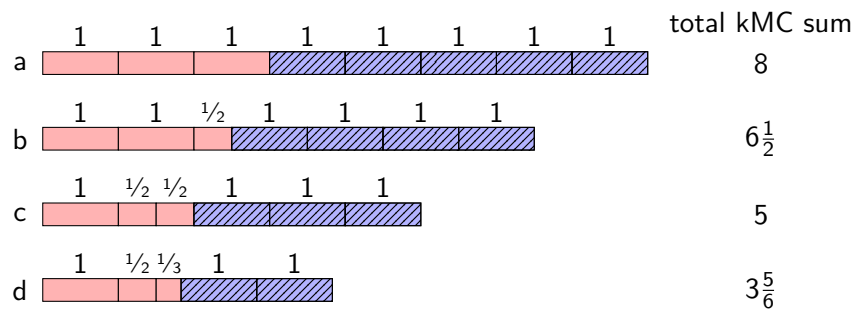


Figure 4.10 Schematic representation of kinetic Monte Carlo (kMC) sum for a system with 3 clusters (red) and monomers (blue with hatching) being consumed by the clusters, reducing their probability of a move attempt (shown above the cells)

A species is randomly selected to attempt a diffusion step using the kMC sum in the following fashion. A random number is selected between 0 and the maximum value of MCsum and this determines which species will attempt a diffusion step. An example for a system with 3 clusters (sizes 1, 2, and 3) and 2 monomers is shown in Figure 4.11. The random number for this attempt is chosen as 2.1 and the total kMC sum for the system is $3\frac{5}{6}$, leading to the first monomer being chosen in this step.

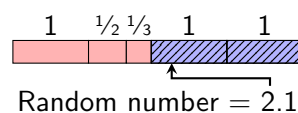


Figure 4.11 Schematic representation of determining the species to attempt a move using the kinetic Monte Carlo sum for a random number 2.1 for a system with 3 clusters (red) and 2 monomers (blue with hatching) clusters with their probability of a move attempt shown above the cells

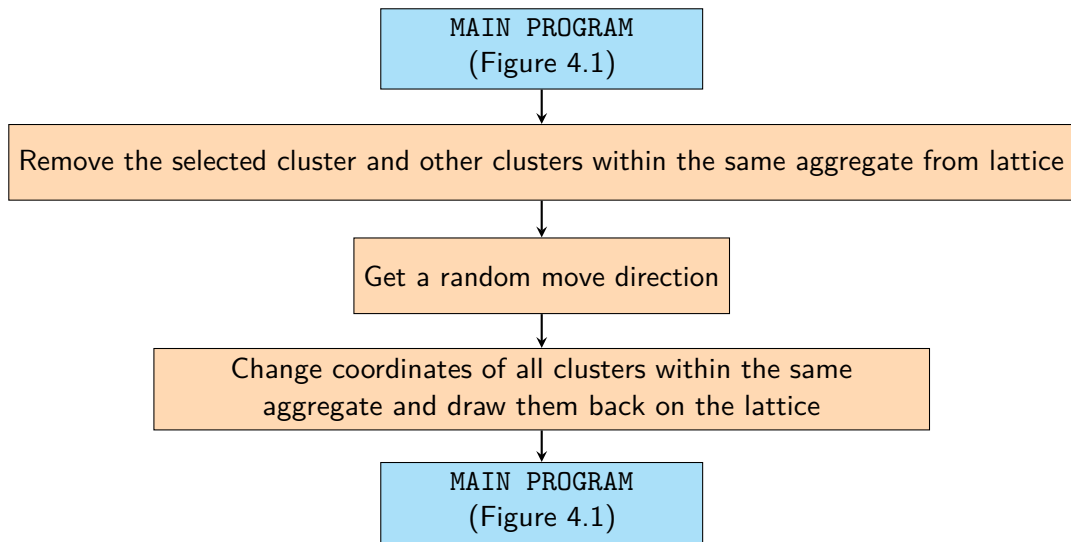


Figure 4.12 Schematic flowchart of `diffuse_cluster` subroutine

If a cluster is selected for the diffusion move, based on the random number and kMC sum (as presented in Figure 4.11), the `diffuse_cluster` subroutine is used, and its flowchart representation is shown in Figure 4.12. If a cluster is part of a larger aggregate, the whole aggregate moves as one. First, the selected cluster (with all the other clusters within the same aggregate) is removed from the lattice, using the cluster site coordinates stored in the `iCluster` and `jCluster` arrays. In order to find all the clusters linked to the one that has been selected, the `SuperCluster` array is scanned for all positions with a value of 1 in the row for the selected cluster, indicating which clusters are within the same aggregate.

Table 4.1 Example use of `SuperCluster` array

	1	2	3	4
1	1	0	1	1
2	0	1	0	0
3	1	0	1	1
4	1	0	1	1

`SuperCluster(Nact, Nact)` matrix is used to keep track of cluster links within the cluster aggregates. If two clusters are linked, and are, therefore, a part of the same aggregate, the positions on the `SuperCluster` matrix, with the coordinates of their respective numbers, are equal to 1 and all the other elements have the value of 0. An example data set for 4 clusters, with clusters 1, 3, and 4 linked into one aggregate and cluster 2 being separate, is shown in Table 4.1. The values on the matrix diagonal start with the value 1, since the clusters are always 'linked' to themselves. It can also be seen that the `SuperCluster` matrix is symmetrical along its diagonal. If two cluster aggregates are merged, all the links are copied over to all clusters of both aggregates.

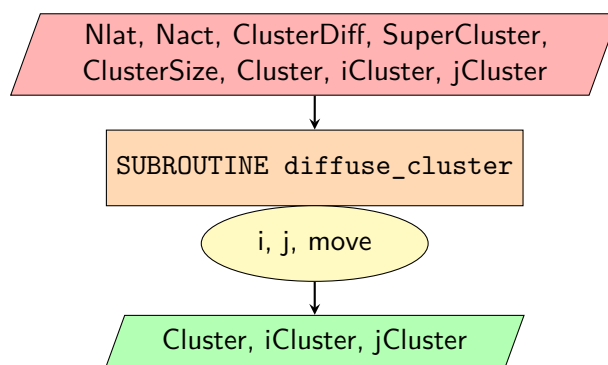


Figure 4.13 Data flow to and from `diffuse_cluster` subroutine

A move, based on a random number, is made in a random direction (up, down, left or right) and the coordinates (`iCluster` and `jCluster` arrays) are updated accordingly for all clusters within the aggregate. These new coordinates are then used to draw the clusters back onto the `Cluster` lattice, taking periodic boundary conditions into account. The subroutine for cluster diffusion, `diffuse_cluster` (Figure 4.13), uses input variables `Nlat`, `Nact` (number of cluster seeds at the beginning of the simulation, used for array size), `ClusterDiff` (number of a cluster selected for a diffusion step), `SuperCluster(Nact,Nact)` (array storing links within cluster aggregates, described in more detail below), `ClusterSize(Nact)` (sizes of all clusters), `Cluster(Nlat,Nlat)` (cluster distribution lattice), `iCluster(Nact,Nlat)` and `jCluster(Nact,Nlat)` (`i` and `j` coordinates of cluster sites). The local variables are `i`, `j` (counters), and `move` (variable used to determine move direction). The output are updated versions of arrays containing `i` and `j` coordinates of clusters (`iCluster` and `jCluster`) and the cluster distribution lattice (`Cluster`).

If a monomer was selected for the move, based on the random number and kMC sum (as presented in Figure 4.11), the `diffuse_monomer` subroutine is used (Figure 4.14). This subroutine works similar to the `diffuse_cluster` described above, moving one monomer at a time. However, unlike a cluster move, a monomer move can be rejected if another monomer occupies the site onto which the selected monomer would diffuse. It is important to note that even if the attempted move of a monomer is unsuccessful, the kMC clock is still advanced in this step. If a monomer move is successful, therefore the new position is not occupied by another monomer, the monomer is removed from the `Monomer` lattice. The coordinates in the `iMonomer` and `jMonomer` arrays are updated to the new position and the monomer is put back onto the `Monomer` lattice at the new coordinates.

Subroutine `diffuse_monomer` takes the input variables `Nlat`, `Nmon` (total number of monomers at the beginning of the simulation run, used for size of arrays), `MonDiff` (number of a monomer to attempt a diffusion step), `iMonomer(Nmon)` and `jMonomer(Nmon)` (`i` and `j` coordinates of monomers), and `Monomer(Nlat,Nlat)` (monomer distribution lattice), as presented in Figure 4.15. The local variables include `i`, `j` (coordinates), and `move`

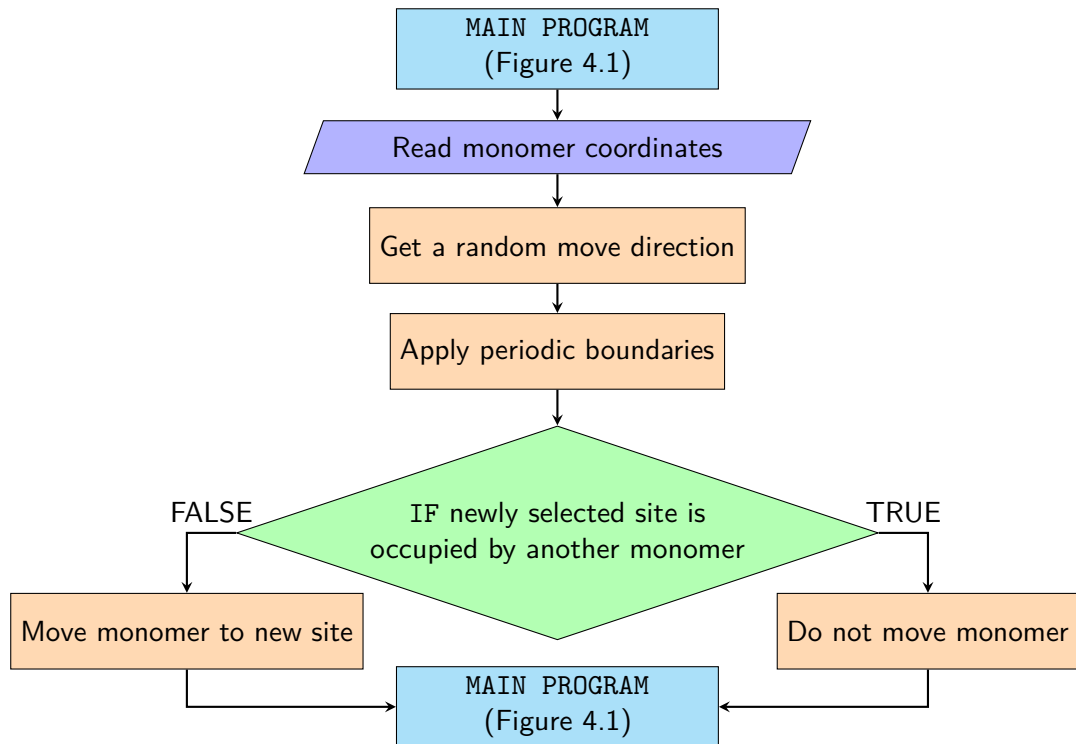


Figure 4.14 Schematic flowchart of `diffuse_monomer` subroutine

(variable used to determine move direction). The output are updated versions of arrays containing i and j coordinates for the monomers (`iMonomer` and `jMonomer`) and monomer distribution lattice (`Monomer`).

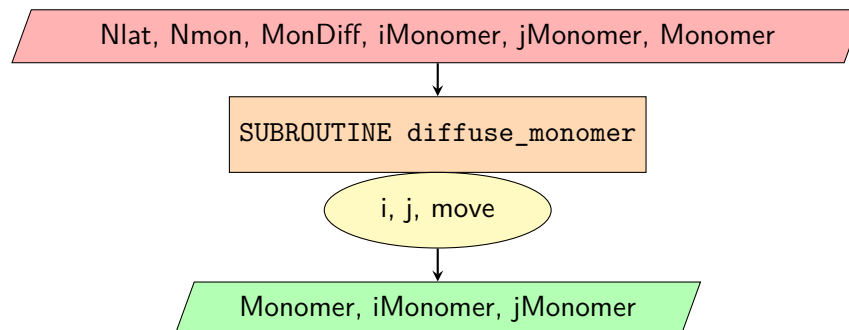


Figure 4.15 Data flow to and from `diffuse_monomer` subroutine

If the new monomer position is already occupied by a cluster, the monomer will be consumed by the cluster, resulting in cluster growth. In this case, `coalesce` is set to `TRUE` so that the kMC sum is recalculated after changing the number of species in the system and increasing the size of one of the clusters. The monomer coordinates in `iMonomer` and `jMonomer` are set to 0, to identify it as empty and the number of remaining monomers in the system is reduced by 1. The move probability for the absorbed monomer is set to 0, so that this monomer is not selected in the subsequent iterations of the main loop.

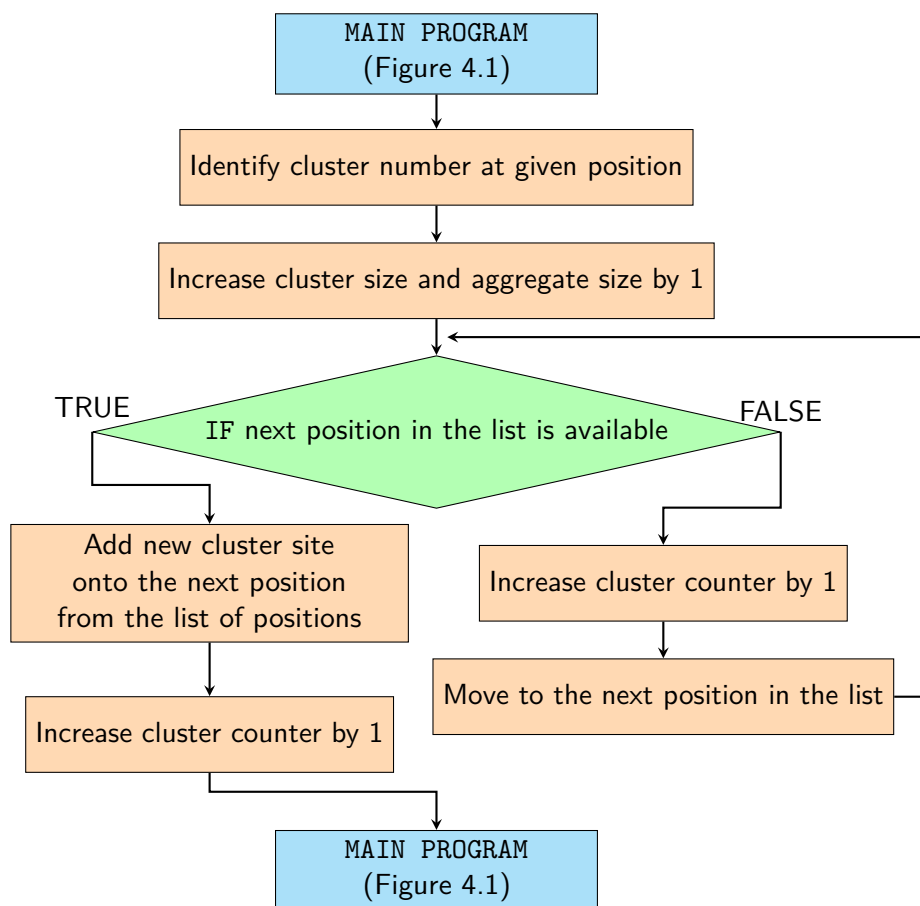


Figure 4.16 Schematic flowchart of `attach` subroutine

In order to add the absorbed monomer to a cluster, subroutine `attach` is called (Figure 4.16). First, the cluster number at the given position is identified, this is the cluster that is absorbing the monomer. The cluster size is increased by 1 to account for the cluster growth. This is followed by examining the next site in the list of positions for drawing the given cluster. If the next position is occupied by another cluster, the counter for the current cluster is increased and the next position is examined, until an available site is discovered. If the next

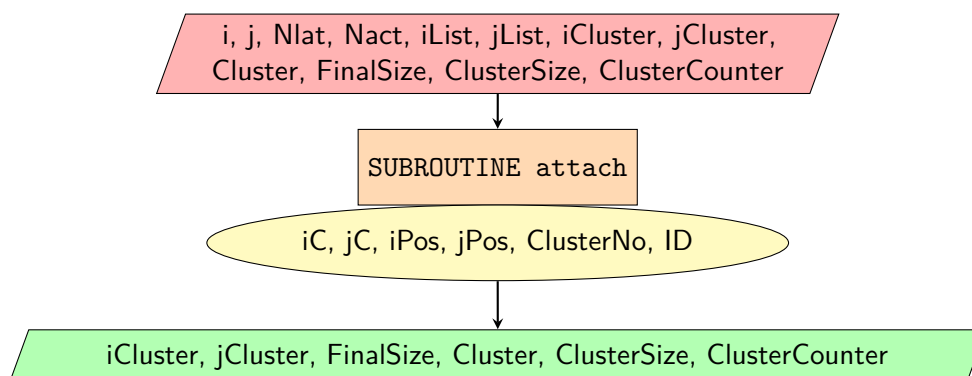


Figure 4.17 Data flow to and from `attach` subroutine

position analysed is available, the current cluster number is added on the cluster distribution lattice and the new position is recorded in the appropriate arrays. The position counter is advanced by one, to account for the newly added cluster site, and control is returned back to the main program.

As can be seen in Figure 4.17, the input for the `attach` subroutine consists of `i` and `j` (coordinates of the monomer being absorbed by a cluster), `Nlat`, `Nact`, `iList`, `jList`, `iCluster`, `jCluster`, `Cluster`, `FinalSize`, `ClusterSize`, and `ClusterCounter`. The local variables of `attach` are `iC` and `jC` (coordinates of centre of the cluster the monomer is being absorbed by), `iPos` and `jPos` (dummy variables for looping through cluster sites with periodic boundary conditions), `ClusterNo` (number of the cluster the monomer is being absorbed by), and `ID` (number of the cluster from `FinalSize` array). The output of the subroutine is made of updated arrays `iCluster`, `jCluster`, `Cluster`, `FinalSize`, `ClusterSize`, and `ClusterCounter`.

Cluster links

After either a cluster move or monomer absorption by a cluster, the perimeters of all the clusters within the aggregate are checked to determine that they are not touching a new cluster, using the `HK_scan` subroutine (Figure 4.18). This subroutine scans the perimeter of the selected cluster by looping backwards through the list of occupied positions for that cluster. For each position all four adjacent sites are checked to determine that they are not occupied by another cluster. If all of the four neighbouring sites are occupied by the selected cluster, the whole perimeter is scanned and control is returned to the main program.

If another cluster is found adjacent to the selected cluster, the `link_clusters` subroutine (Figure 4.19) is called. If the two clusters are already linked in the `SuperCluster` array, the rest of this subroutine is skipped and control is returned back to the `HK_scan` subroutine. If the two clusters are not yet linked, then the links of both clusters are copied over to each other, to ensure all clusters within the new aggregate are linked together, as described below. Sizes of the two aggregates are merged into one, and the former aggregate with a higher number is made to point to the one with a lower number.

If two clusters within the same aggregate are not linked when `link_clusters` is called, then the links of both clusters are copied over to `CopyRow(Nact)` array by adding the two corresponding rows in the `SuperCluster` array together. Identifiers (IDs) of both clusters/aggregates are determined using the `FinalSize` array. If there is a negative value for a cluster in the `FinalSize` array, it means that it is pointing to another cluster ID, as described above. The two aggregate IDs are compared and the lower value is used, changing the cluster with the higher ID, along with all the clusters originally pointing to this cluster, to point to the cluster with the lower ID. Finally, the values of combined links, stored in `CopyRow` array, are copied to all clusters in the newly formed aggregate.

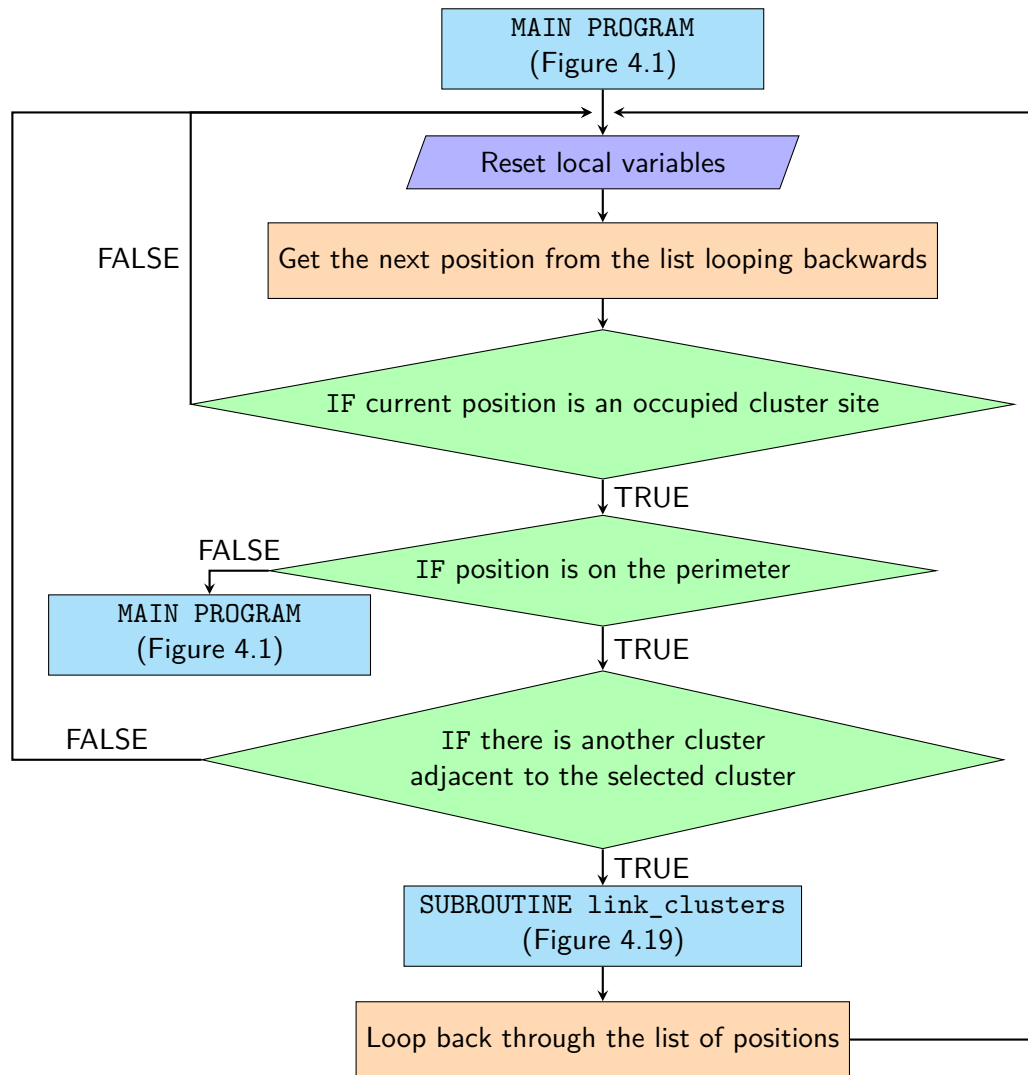


Figure 4.18 Schematic flowchart of `HKscan` subroutine

Figure 4.20 presents the data structure for subroutines `HK_scan` and `link_clusters`, which check for and create new links between clusters, respectively. The input for `HK_scan` includes `Nlat`, `Nact`, `Cluster`, `ClusterCounter(Nact)` (counter used for drawing clusters), `iCluster`, `jCluster`, `SuperCluster`, `iList`, `jList`, and `WorkCluster` (number of the cluster currently working with). Local variables for `HK_scan` are `i` (counter for looping through cluster positions), `iPos` and `jPos` (`i` and `j` coordinates of a selected cluster site), `neighbourUp`, `neighbourDown`, `neighbourLeft`, and `neighbourRight` (number of a cluster adjacent to the selected cluster), `up`, `down`, `left`, and `right` (adjacent sites to the currently selected site with periodic boundary conditions), `perimeter` (logical variable that is set to `FALSE` when a selected site is not on the cluster perimeter), and `touch` (logical variable that is set to `TRUE` if there is another cluster adjacent to a selected site). The output of `HK_scan` consists of updated `SuperCluster` array and logical variable `coalesce` (set to `TRUE` if a new cluster link has formed).

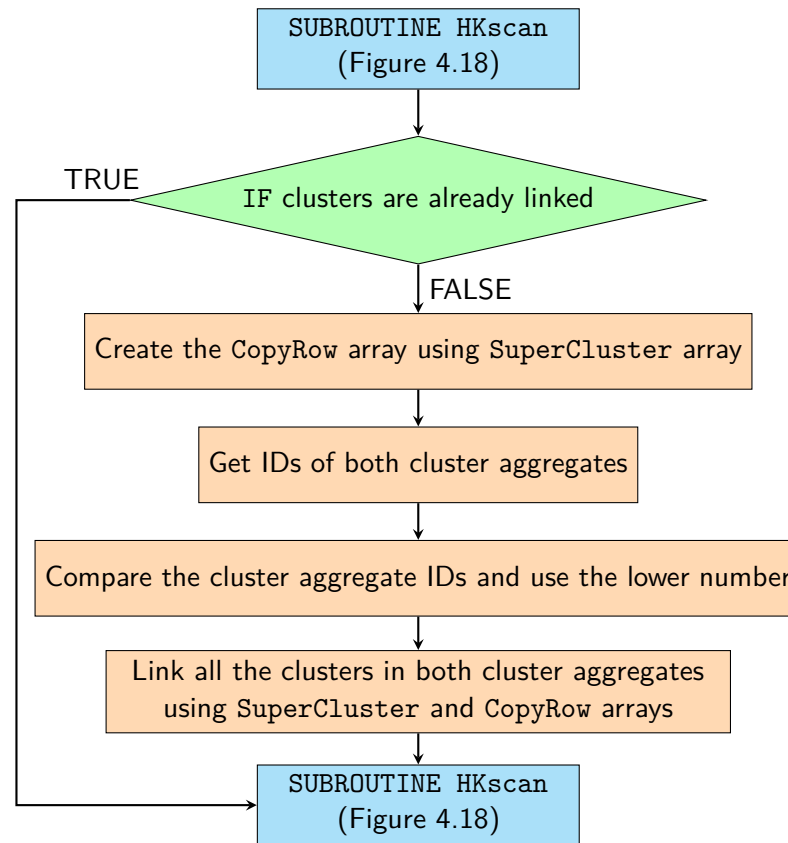


Figure 4.19 Schematic flowchart of `link_clusters` subroutine

`ClusterCounter` array stores, as the name suggests, counter for each cluster. The value for all clusters is set to 1 at the beginning of the simulation and is increased when the clusters are being drawn on the lattice, as they grow in size. However, if the next site in the list (`iList` and `jList`) is occupied by another cluster, the counter is increased until an available site is found. Therefore, the value of the counter might be higher than the actual cluster size. This also makes the process of drawing and diffusing clusters more efficient.

Subroutine `link_clusters` (Figure 4.20), called by `HK_scan`, takes the input values of `Nact`, `WorkCluster` (number of a selected cluster), `neighbour` (number of an adjacent cluster to create a link with), `SuperCluster`, and `FinalSize(Nact)` (array storing size of cluster aggregates, described in more detail below).

`FinalSize(Nact)` array is used to store sizes of cluster aggregates. When two clusters become linked into one aggregate, the total size of the aggregate is stored in the position of the cluster with a lower number, while the value for the cluster with a higher number will become the negative value of the number of the first cluster, effectively pointing to that cluster. For example, if two clusters, with numbers #1 and #2, and sizes 5 and 6, respectively, are being linked, then the values become `FinalSize(1) = 11` and `FinalSize(2) = -1` with cluster one storing the total size of the aggregate and cluster #2 pointing to cluster #1.

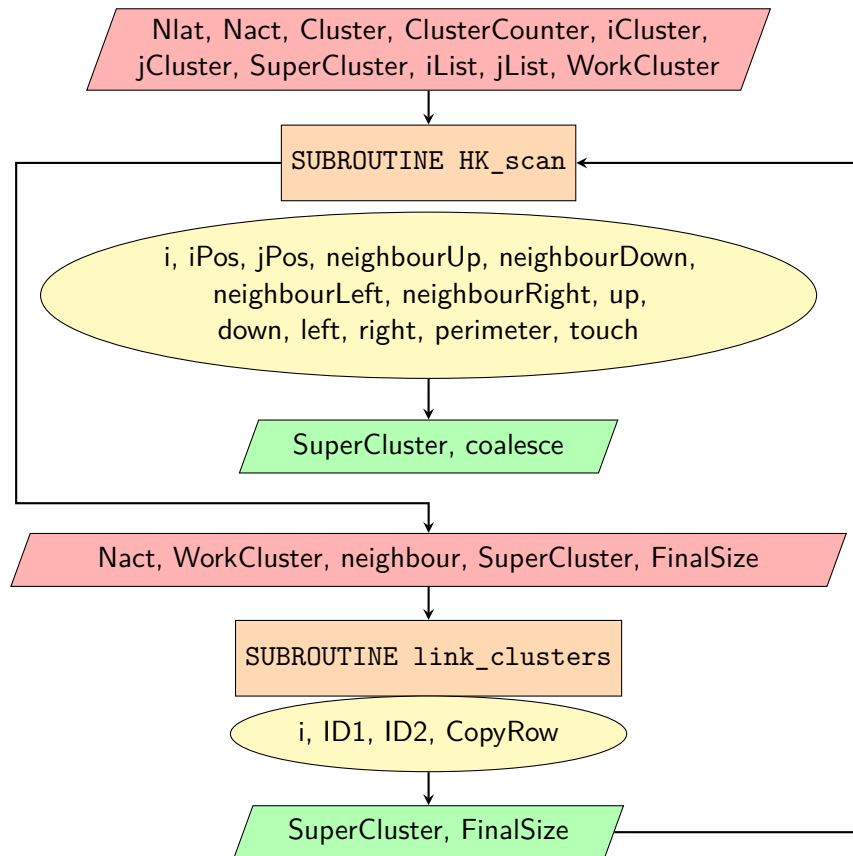


Figure 4.20 Data flow to and from `HK_scan` and `link_clusters` subroutines

Time increment

After an attempted species move, the kMC clock is advanced by a randomly drawn time increment (Δt) based on the kMC sum, according to equation 4.1, where R is a random number.

$$\Delta t = -\frac{\ln(R)}{kMC\ sum} \quad (4.1)$$

This means, that as the clusters grow in size, and the number of monomers is reduced, as the simulation proceeds, the time increments gradually increase. This represents a slower diffusion speed for larger species. When all the free monomers have been depleted, the counter `FreeMon` is set to -1.

If `coalesce` is `TRUE` at the end of an iteration of the main loop, the kMC sum is recalculated. The value for the first cluster is equal to its probability of a move (inverse of its size). If the cluster size in `FinalSize` is pointing to another cluster, then the kMC sum for this cluster is set to 0, so that each cluster aggregate is counted only once and the probability of its move is based on the total aggregate size. The kMC sum value for all the subsequent species is equal to its probability of a move added to the sum of all the previous probabilities.

Data output

Finally, `plotcluster` subroutine (Figure 4.21), used to write out cluster distribution into a file, takes the values of `Nlat` and `Cluster` as input and uses local variables `i` and `j` as loop counters for writing out data. There is no output for this subroutine, since it does not change any of the variables and only writes out data to a file.

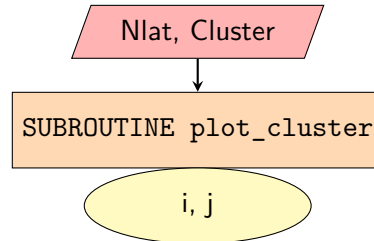


Figure 4.21 Data flow to and from `plot_cluster` subroutine

The main loop is exited after there are no more free monomers and only a single cluster aggregate remains in the system. The cluster distribution lattice (`Cluster`) is written out into a file with name `Cluster_0.s_0.0p_r.dat`, where `s` represents S_C , `p` represents C_C , and `r` the run number, as mentioned above. Final values of cluster sizes are written into a `Size_0.s_0.0p_r.dat` file, and cluster centre coordinates are written into a `Pos_0.s_0.0p_r.dat` file. Finally, all open files are closed and all allocatable arrays are deallocated.

In order to visualise the cluster distribution lattice, Matlab function `imwrite` was used with the colour map set to black and white, creating images of black cluster sites on a white background, as presented in the following sections.

Table 4.2 List of arrays along with their description and related subroutines

Variable name	Description	Related subroutines
<code>Cluster(Nlat,Nlat)</code>	cluster distribution lattice (i coordinate, j coordinate)	<code>diffuse_cluster</code> , <code>attach</code> , <code>HK_scan</code> , <code>plotcluster</code>
<code>ClusterCounter(Nact)</code>	counter for cluster drawing (position denotes cluster number)	<code>attach</code> , <code>HK_scan</code>
<code>ClusterDiff</code>	number of a cluster to diffuse	<code>diffuse_cluster</code>
<code>ClusterFile</code>	file name for storing cluster distribution lattice at the end of a simulation run	
<code>Clusters</code>	counter for number of remaining cluster aggregates in the simulation	
<code>ClusterSize(Nact)</code>	sizes of clusters (position denotes cluster number)	<code>diffuse_cluster</code> , <code>attach</code>

Table 4.2 List of arrays along with their description and related subroutines (continued)

Variable name	Description	Related subroutines
coalesce	logical variable that is set to TRUE when a monomer attaches to a cluster or two clusters become linked into an aggregate	HK_scan
current	counter for data output	
FinalFile	character variable for file name	
FinalSize(Nact)	size of cluster aggregates or points to another cluster within the aggregate (position denotes cluster number)	attach, link_clusters
FreeMon	number of monomers remaining in the simulation	
i	coordinate counter	attach
iCluster(Nact,Nlat)	i coordinates of the cluster sites (first position denotes cluster number, second position denotes cluster site number)	diffuse_cluster, attach, HK_scan
ID	cluster number used for pointing in FinalSize array	
iFile	file name for storing cluster centre coordinates	
iList(Nlat×Nlat)	i positions for drawing clusters on lattice (counter value)	attach, HK_scan, list, scan_list
iMonomer(Nmon)	i coordinates of the monomer sites (position denotes monomer number)	diffuse_monomer
ios	debugging variable used for file opening	
ireal	real dummy variable	
j	coordinate counter	attach
jCluster(Nact,Nlat)	j coordinates of the cluster sites (first position denotes cluster number, second position denotes cluster site number)	diffuse_cluster, attach, HK_scan

Table 4.2 List of arrays along with their description and related subroutines (continued)

Variable name	Description	Related subroutines
jFile	character variable for file name	
jList(Nlat×Nlat)	j positions for drawing clusters on lattice (counter value)	attach, HK_scan, list, scan_list
jMonomer(Nmon)	j coordinates of the monomer sites (position denotes monomer number)	diffuse_monomer
jreal	real dummy variable	
last	logical variable that is set to FALSE when 20 cluster aggregates remain in the simulation	
Lattice	dummy lattice for cluster drawing	draw_list, scan_list
MCmove	kinetic Monte Carlo sum of a species selected for a move attempt	
MCSum(Nmax)	array of kinetic Monte Carlo sums	
MonDiff	number of a monomer to diffuse	diffuse_monomer
Monomer(Nlat,Nlat)	monomer distribution on the lattice (i coordinate,j coordinate)	diffuse_monomer
move	variable for deciding direction of a diffusion move	
Nact	number of cluster seeds	attach, HK_scan, link_clusters
neighbour	cluster number of an adjacent cluster	link_clusters
Nlat	size of the lattice	diffuse_monomer, diffuse_cluster, attach, HK_scan, list, draw_list, scan_list, plotcluster
Nmax	total number of species in the simulation (cluster seeds and monomers)	diffuse_cluster
Nmon	number of monomers at the beginning of the simulation	diffuse_monomer
No	counter	scan_list

Table 4.2 List of arrays along with their description and related subroutines (continued)

Variable name	Description	Related subroutines
p	integer value of percentage of activated monomers	
percentage	real value of percentage of activated monomers	
r	run number	
radius	cluster radius during cluster drawing	draw_list, scan_list
s	integer value of solids content	
seed(12)	seed for the random number generator	
SizeFile	file name for storing cluster sizes at the end of a simulation run	
solid	real value of solids content	
SuperCluster(Nact,Nact)	links between clusters within aggregates (number of cluster 1, number of cluster 2)	diffuse_cluster, HK_scan, link_clusters
time	kinetic Monte Carlo time	
TimeFile	character variable for file name	
WorkCluster	cluster number currently working with	HK_scan, link_clusters
WorkMon	monomer number currently working with	

4.1.2 Static clusters

The first version of the code was based on a lattice-based model of cluster growth in two dimensions. The lattice was populated with cluster seeds and monomers, with monomers diffusing freely on the lattice, while the clusters remained static. When a monomer diffused onto a site occupied by a cluster, it attached to the cluster, resulting in growth.

In the static version of the code, the subroutines `list`, `diffuse_cluster`, `HKscan`, and their linked subroutines were not used yet. However, the cluster growth mechanism was similar to the one used in the `draw_list` subroutine, described above. Since the clusters were not moving, it was not necessary to know which clusters were linked together, so the `SuperCluster` and `FinalSize` arrays were not utilised yet.

Initially, the clusters were drawn on the lattice on the basis of their size but this led to some of the clusters occupying fewer lattice sites than their size, leading to material loss during the simulation run. This was due to cluster overlap, where clusters adjacent to each other would overwrite their positions. Therefore, another loop was added after the main drawing loop, where the cluster radius was artificially increased and more sites were assigned to a given cluster until the correct size was reached. These two loops were later merged into one, including a condition based on cluster size.

This still did not solve the mass loss problem fully, since if a cluster was not redrawn after another cluster has overwritten one (or more) of its sites, the final cluster size on the lattice would not match the correct value. Thus, before increasing the cluster size, the growing cluster was first removed from the lattice and then drawn back, using only empty unoccupied sites. This meant that the number of occupied sites matched the total solids content in the end of the simulation.

Every time a monomer was absorbed by a cluster, the positions in `iMonomer` and `jMonomer` arrays after the absorbed monomer were all shifted up one position, so that all empty positions are at the end of the arrays. This speeds up the code, since, as the number of remaining monomers decreases, computational time is not wasted on looping through empty positions. Later, this issue was solved by introducing the kMC sum along with cluster diffusion.

In order to run the simulation with different values of S_C and C_C , all of the above simulations were run using nested loops within the code. However, this means that the individual simulation runs were executed in series. The next step involved separating the runs into multiple executable files that could be run at the same time, in parallel.

Repeated erasing and redrawing of clusters is inefficient, especially for systems with higher solids contents, so the `list` subroutine was developed. This subroutine, as described above, creates a list of sites for cluster drawing with position relative to the cluster centre. This means that when an additional site needs to be added for a cluster during growth, the next available site is found in the list, making the process more efficient.

As only monomers were diffusing in this version of the model, all species had the same probability of a move, so the first version did not include the kinetic attributes of a Monte Carlo simulation. This also means, that time evolution was not introduced at this point. Even though these simulation runs were faster than the subsequent versions, they did not produce structures comparable to those observed experimentally. Example structures for varying values of S_C and C_C are shown in Figure 4.22.

It can be seen from Figure 4.22 that with increasing C_C , left to right in the figure, the cluster size decreases, as is expected and has been observed experimentally by dynamic light scattering [79]. Increasing the solids content does not seem to affect the final cluster size, only increasing the number of clusters present. However, even at higher values of S_C (bottom part of Figure 4.22), the cluster structures are not percolated and are made up of

small aggregates each with few clusters. This type of structure would not lead to a viable gel in the real system, since there is no spanning gel structure that would withstand the drying process, preserving the porous nature of the material.

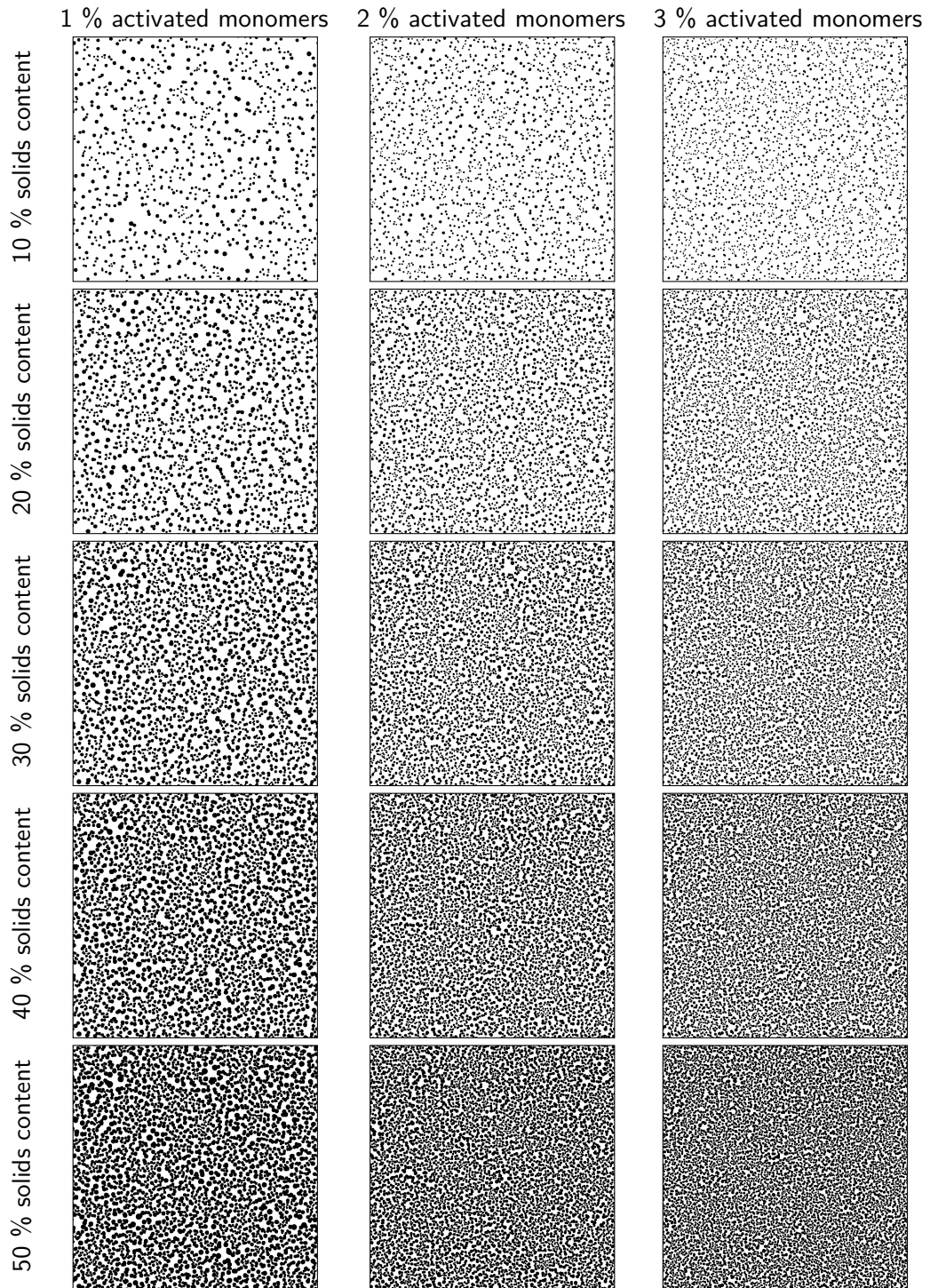


Figure 4.22 Model of static cluster growth, with increasing percentage of activated monomers (left to right) and increasing solids content (top to bottom). The lattice used is 1000×1000 .

The observations made here along with the fact that the growing clusters are not static in the real system, led to the introduction of cluster diffusion, as presented in the next section (4.1.3). It should be noted that the samples prepared in the experimental section of this work (Chapter 3) were consistently prepared with solids content 20 w/v%, a value that was within the range commonly used in the literature.

4.1.3 Diffusing clusters

Since the initial version of the model, involving static clusters and diffusing monomers, did not generate structures comparable to the ones reported from experiments, cluster diffusion was introduced. However, cluster diffusion is more complex than the simple diffusion of monomers.

First, cluster size and reduced probability of a move need to be taken into consideration when selecting a species to diffuse in each simulation step. This was achieved by introducing the kinetic Monte Carlo features, including the kMC sum. The `diffuse_cluster` subroutine was adapted from the `diffuse_monomer` subroutine to perform the cluster diffusion steps.

Another issue with cluster diffusion emerges once clusters start to form aggregates that diffuse as one species but the individual clusters keep growing on their own. Three arrays were introduced to store the relevant data. `ClusterSize` array stores the individual cluster size, used e.g. for drawing clusters on the lattice, `FinalSize` array stores the total size of each cluster aggregate, used for probability of a diffusion move, and `SuperCluster` stores the cluster links. All three of the aforementioned arrays are described in more detail in the beginning of this chapter.

As mentioned above, due to the stochastic nature of the process, multiple structures were generated with each set of conditions. This allows for better sampling and a more realistic representation of larger systems. A difference in the structures generated, using the same conditions but different seeds for the random number generator, can be observed in Figure 4.23. These three examples share similar structural features, however, even at first glance they differ from each other. These three snapshots can be considered as samples from three different places of the same material, or three sample repeats using the same conditions.

It should be noted that all the structure images presented here contain only one final cluster aggregate with periodic boundary conditions.

Selected final structures are presented in Figure 4.24, in order to show the effect of solids content and percentage of activated monomers on simulated structures, with inaccessible pore spaces highlighted in red. Increasing the percentage of activated monomers in the initial simulation results in the clusters within the final structure being smaller in size, thereby increasing their number. This results in a more branched structure, which leads to more

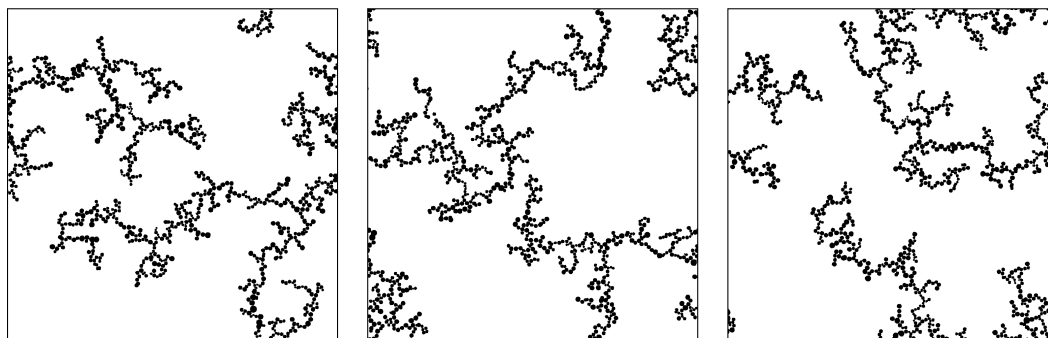


Figure 4.23 Model cluster structures with 10 % solids content and 1 % activated monomers using 3 different seeds for the random number generator

interconnected networks spanning the reaction space, making the whole structure more interdigitated.

By increasing the solids content, the grown structures are more densely packed, however, as previously discussed, they retain a percolated porous structure up to 50 % solids content. At higher solids contents (above 50 %), the structures end up being too dense and most of the pores are closed in two dimensions, and only the pores that might be on the structure surface would be externally accessible. It is worth noting that while these generated structures might be visualised as two-dimensional slices of a three-dimensional material, in reality some of the closed pores present in the two-dimensional structure might well be open pores in a three-dimensional structure. It can be seen, from Figure 4.24, that the structures created using lower solids contents, e.g. 10 and 20 %, contain pores that are quite open and generally exhibit wide necks, resulting in very few bottle-neck type pores. Conversely, structures with higher solids loading, e.g. 40 and 50 %, exhibit a complex series of interconnected pores with a higher fraction of constricted and closed pores.

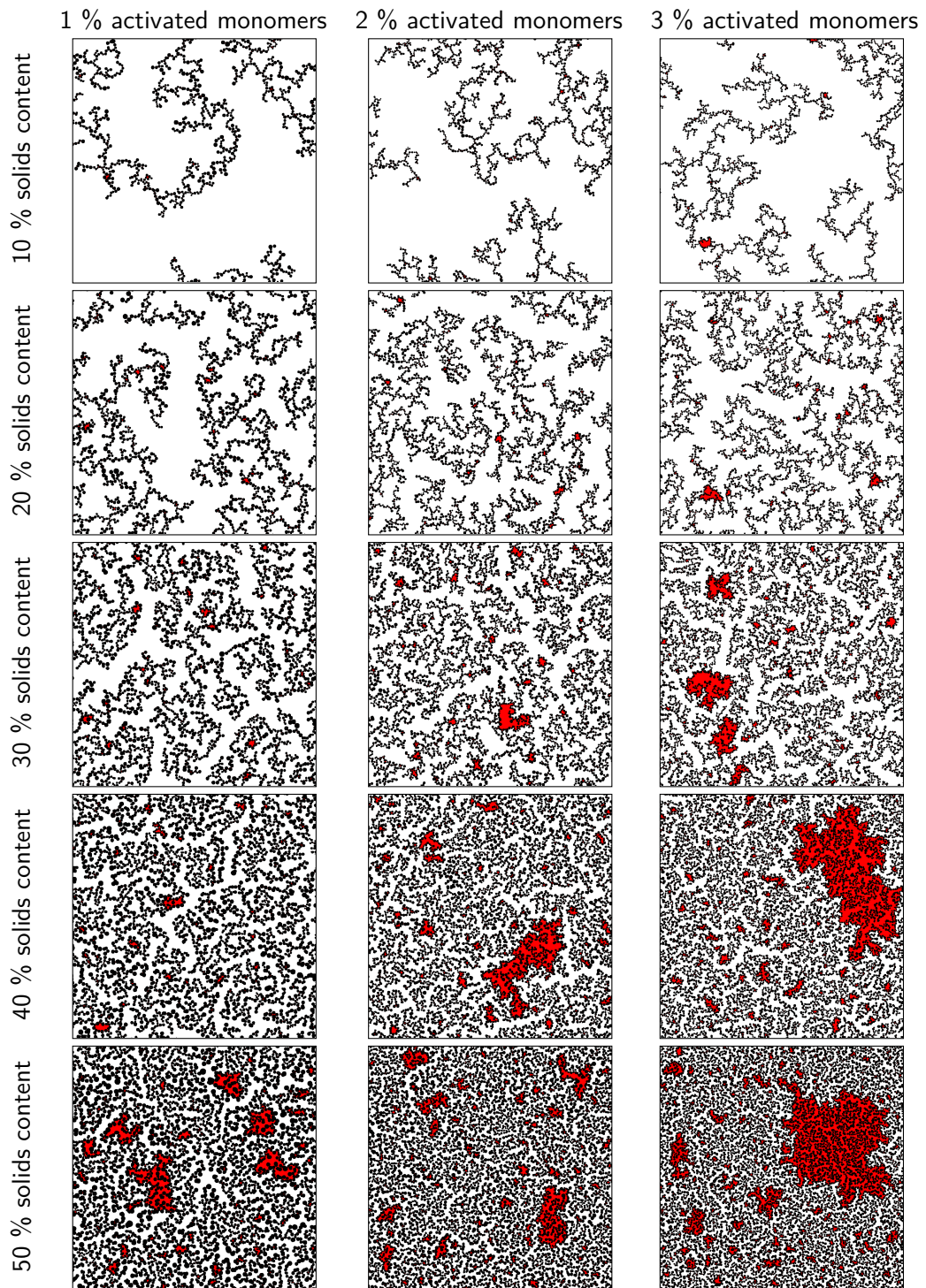


Figure 4.24 Model of cluster growth of RF gels, with increasing percentage of activated monomers (left to right) and increasing solids content (top to bottom). Areas of inaccessible pore spaces are highlighted in red. The lattice used is 1000×1000 .

4.2 Textural characterisation

Experimentally, porous materials are usually characterized by a range of techniques, including gas sorption, which gives information on their textural properties [47, 60, 92, 102, 105]. Accessible surface area and accessible pore volume are important characteristics of these materials and have a direct impact on their applications.

The generated structures, as presented in Figure 4.24, were analysed for accessible pore area and number of accessible surface sites. Firstly, the area of the percolating network of pores was identified for all the structures, represented in white in Figure 4.24, using algorithm presented in Appendix E.2.2. The number of accessible lattice sites was compared to the total number of unoccupied lattice sites for each generated structure and these ratios are shown in Figure 4.25a. Fortran code, used for calculations discussed here, is presented in Appendix E.2.3. Increasing both S_C and C_C results in a qualitatively observable decrease in the ratio of accessible sites (Figure 4.24), while quantitatively it is reflected in Figure 4.25a, and is a result of increased closed porosity within these structures.

The accessible surface areas of the pores, scaled to the gel mass, are shown in Figure 4.25b. It can be seen that the surface area decreases with increasing solids concentrations (S_C) and increases with increasing catalyst concentration (C_C). At higher values of S_C , the decrease is more pronounced, due to the increase in closed porosity, as discussed above. Higher values of C_C lead to higher numbers of accessible surface sites, with the difference more pronounced at lower values of S_C .

From previous experimental work within our group, the effect of solids content on the final RF xerogel structure was observed as insignificant [192]. However, it needs to be taken

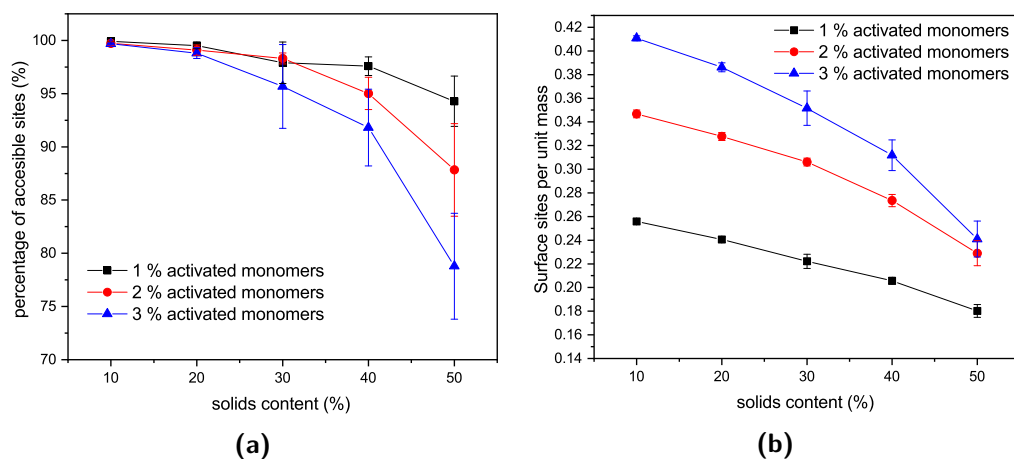


Figure 4.25 (a) Percentage of accessible sites (relative to all unoccupied sites on the lattice) vs solids content for three percentages of activated monomers and (b) accessible surface area (in number of lattice sites) vs solids content for three percentages of activated monomers. Error bars represent standard deviation of values for 10 independent runs for each set of conditions, and lines connecting the data points provide a visual guide only.

into account that the experimentally analysed samples are xerogels, which are affected by shrinkage during the drying process. Hydrogels with lower solids content will initially contain larger and more open pores; however, their solid network structure is relatively weak, resulting in significant shrinkage during drying. On the other hand, even though hydrogels with higher solids contents initially exhibit smaller pore voids, their gel structures are much stronger; thus, they are better able to withstand the forces exerted onto the pore walls during drying. Another factor to consider is that the range of solids content used in previous experiments was below 40 %, and the change in accessible surface sites is fairly small in this region, compared to higher values of S_C . The trends observed here, for the effect of amount of activated species (C_C) on both accessible pore volume and accessible surface sites, agree with experimental trends for catalyst concentration.

4.3 Fractal analysis

It has been reported previously that aerogel and xerogel materials tend to exhibit structures with fractal characteristics [51, 58, 96, 199]. These highly porous materials are generally characterized by their textural properties, such as accessible surface area, pore volume, and pore size distribution, some of which were explored in the previous section; however, fractal properties can add useful information about their structure.

In this section, the generated cluster structures were analysed for correlation dimension, to gain more information about the structure complexity (Section 4.3.1), followed by the Hurst exponent analysis of the accessible pore spaces using diffusion of a random Brownian particle (Section 4.3.2).

4.3.1 Correlation dimension

Correlation dimensions were calculated for the simulated structures, as outlined above, using the relationship proposed by Grassberger [200]. First, the correlation sum (C_r) was calculated using:

$$C_r = \frac{1}{N(N-1)} \sum_{i=1}^N \sum_{j=1; j \neq i}^N \theta(r - |X_i - X_j|) \quad (4.2)$$

where N is the total number of clusters in the structure, θ is the Heaviside function, r is the radius of a circle centred on each sampled cluster i , and X_i and X_j are the coordinates of the centres of clusters i and j . The correlation sum is calculated for increasing values of r around all clusters and the Heaviside function takes on a value of 1 when the value of $r - |X_i - X_j|$ is positive, meaning clusters i and j are within the selected r , and a value of 0 when the two clusters are further apart than the selected r , leading to a negative value of $r - |X_i - X_j|$. This effectively allows counting of the number of clusters found within different distances from selected clusters, taking periodic boundaries into account. An example schematic is presented in Figure 4.26, where the chosen cluster is shown in

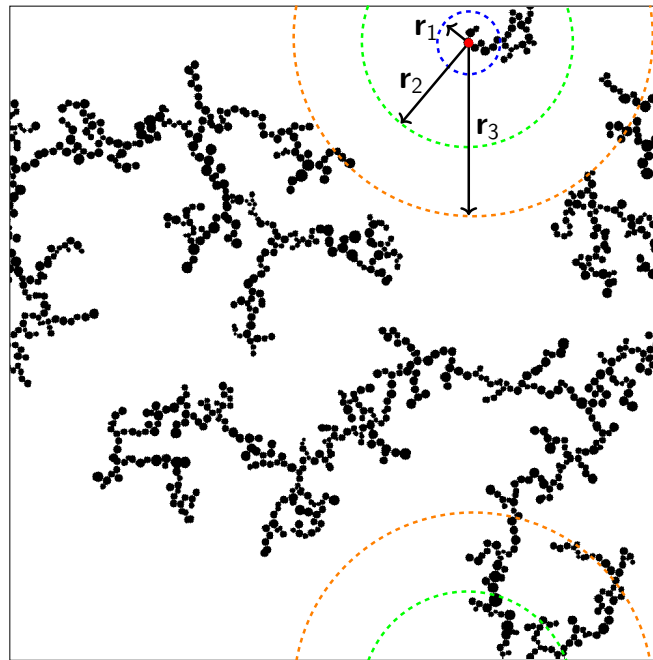


Figure 4.26 Schematic of increasing radii of separation for correlation sum calculation.

red, and circles with increasing radii centred around it are used to evaluate the Heaviside function, as shown in dashed lines ($r_1 < r_2 < r_3$). It can be seen that as the radius of the circle increases, so does the number of clusters included within the radius. Once the radius is large enough to cover all clusters present on the lattice, the correlation sum does not change its value when increasing the radius further. Fortran code, implemented here, is presented in Appendix E.2.4.

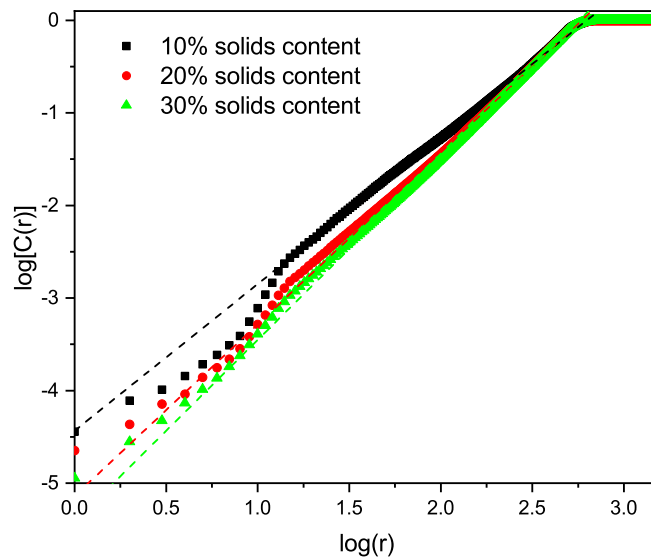


Figure 4.27 Example plots as used to calculate the correlation dimension for 1 % activated monomers and 10, 20, and 30 % solids content. The slope of the linear portion (indicated by the dashed lines) is equal to the correlation dimension.

The correlation dimension of the system is obtained using a log-log scale plot of correlation sum vs radius. For small values of r ($\log(r)$ below 1), there are effects due to the discrete nature of the lattice, while the plateau at large r ($\log(r)$ around 3 and above) is due to the large-scale effects of the periodic boundary conditions mentioned above (recall the lattice size is 1000×1000). Between these sections is the scaling region, the slope of which is equal to the correlation dimension. Example plots for structures with 1 % activated monomers and solids content 10, 20, and 30 %, are shown in Figure 4.27.

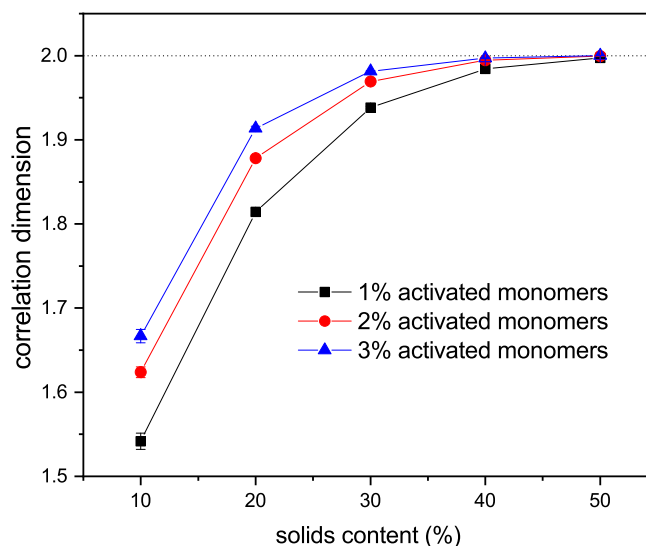


Figure 4.28 Correlation dimension vs solids content for three percentages of activated monomers, the dotted line indicates a correlation dimension value of 2.0. Error bars represent standard deviation of values for 10 independent runs for each set of conditions, and lines connecting the data points provide a visual guide only.

Values of correlation dimensions for the solids contents and percentages of activated monomers studied here are shown in Figure 4.28. The values obtained vary in the range ~ 1.5 to ~ 2.0 , increasing with increasing values of S_C and C_C . The lower limit is in line with expectations for cluster-cluster aggregation in dilute systems [201] while the upper limit is expected for dense media in two dimensions. This means that the aggregates fill space more completely as these parameters increase, as expected. At higher solids contents (50 % and above), the correlation dimension plateaus at a value of 2.0 for all percentages of activated monomers. The most substantial increase in correlation dimension can be observed between 10 and 20 % solids content, where, as can be seen in Figure 4.24, the structures differ most significantly, even visually. An experimental study by Huber *et al.* [202] used dynamic light scattering measurements to quantify the fractal dimensions of particles formed during RF gelation. They observed an increase in fractal dimension with catalyst concentration, which agrees with the trend observed here.

4.3.2 Hurst exponent

The Hurst exponent is related to fractal dimension [170] and can be used to describe the persistence of a time series [171]. If one considers a random walker on a two-dimensional lattice; a particle exhibiting Brownian motion on an empty lattice, with no obstacles, has a Hurst exponent value of $H = 1/2$. A random walker with a lower value $H < 1/2$ is described as antipersistent, which means that it is more likely to remain closer to the origin than the freely diffusing particle. A value of Hurst exponent $H > 1/2$ is attributed to persistent walkers, meaning they are more likely to leave the origin with a smoother, less rugged trace. If one now considers a random walker on a plane with obstacles, its trace will become more antipersistent, tending to confine it to a smaller area. As the obstacle structures become more complex and the voids more tortuous, thereby restricting the movement of the walker, the value of the Hurst exponent might be expected to get closer to $\sim 1/3$, the value found at the percolation threshold [172].

Hurst exponent values of accessible pores within the cluster structures, obtained using the model presented above, were calculated using a random walker with only percolated porous structures considered. Fortran code of the used algorithm is presented in Appendix E.2.5. The inaccessible pores excluded from analysis are coloured red in Figure 4.24. As mentioned above, and as seen from Figure 4.25a, increasing both values of S_C and C_C leads to more closed porosity in the system, which will have an effect on the values of the Hurst exponent as well.

For each simulation, the random walker was placed within the percolated pore structure and allowed to freely diffuse for 10 million steps (ten times the number of lattice sites). This was repeated for 1000 randomly distributed accessible positions on the lattice. Random walker traces in both x and y directions were then analysed for average displacement from the origin with varying time window size. This is shown in Figure 4.29, where traces of a random walker, in both x and y directions, are shown along with absolute displacements in both directions (ΔB_x and ΔB_y) for a selected time window (T_S). The time window slides along the time axis, and an average value of displacement in both directions is calculated for varying size of time windows. For a random walker, there is a relationship between the average displacement ($|\overline{\Delta B}|$) and time window size (T_S):

$$|\overline{\Delta B}| \propto T_S^H \quad (4.3)$$

Thus, calculating the slope of $\ln(|\overline{\Delta B}|)$ versus $\ln(T_S)$ provides the value of the Hurst exponent (H). In this work, 11 time window sizes were used, starting at 100 steps and increasing exponentially up to 102 400 steps. It is important that the highest time window size is significantly smaller than the total number of steps, to ensure sufficient points for the average displacement calculation, as the time window slides along the time axis.

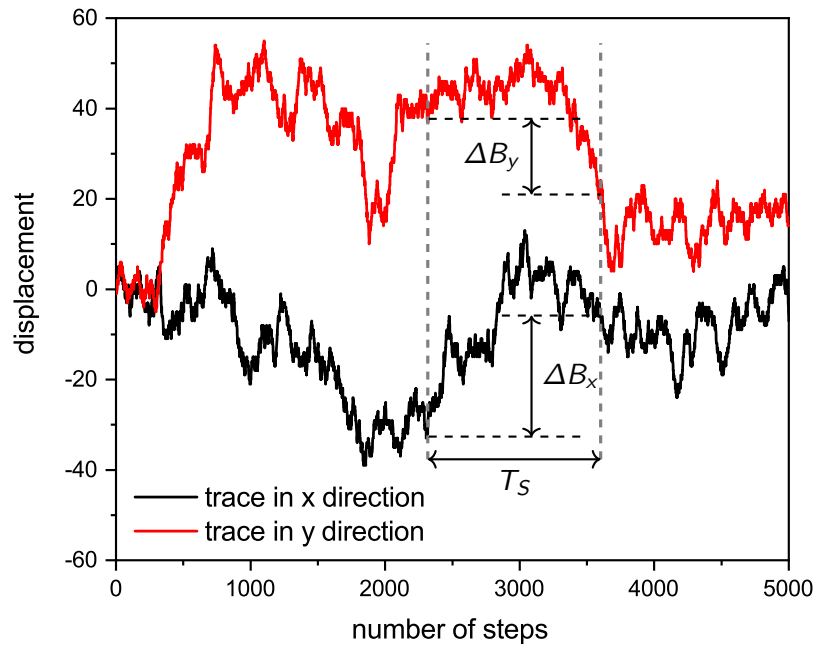


Figure 4.29 Example traces in x and y directions for a random walker.

The values of the Hurst exponent, for a random walker diffusing in the percolated pore structures described above, are shown in Figure 4.30. It can be seen that increasing values of both S_C and C_C cause a decrease in the Hurst exponent (H) values. As mentioned in Section 2.2.3, a random walker diffusing on an empty lattice has a value of $H = \frac{1}{2}$, exhibiting a random Brownian trace in both x and y dimensions. Deviation of the Hurst exponent from a value of $\frac{1}{2}$ towards $\frac{1}{3}$ suggests a more anti-persistent character of the walker trace. By increasing S_C , the obstacles encountered by the walker also increase and the pore structure becomes more tortuous with more constricted pores, this limits the free diffusion of the walker, leading to a decrease of its Hurst exponent value.

Increased tortuosity of accessible pore structures can be observed in Figures 4.31 and 4.32, where cluster structures with two different values of S_C are presented. The colours in Figure 4.31 represent the number of diffusion steps required to reach various points on the lattice starting from the indicated point. With increased S_C , the more constricted pores are increasingly difficult to access, as can be seen by the increased number of steps needed to reach these points. This is then reflected in the value of the Hurst exponent, as mentioned above.

Tortuosity ($t = \frac{n}{n_0}$), obtained by dividing the number of steps it takes to reach a point on the lattice containing a cluster structure (n) with a value for an empty lattice (n_0), is presented in Figure 4.32 for the same structures as used in Figure 4.31. A diffusion map for an empty lattice, using the same origin as in Figures 4.31 (containing values of n) and 4.32

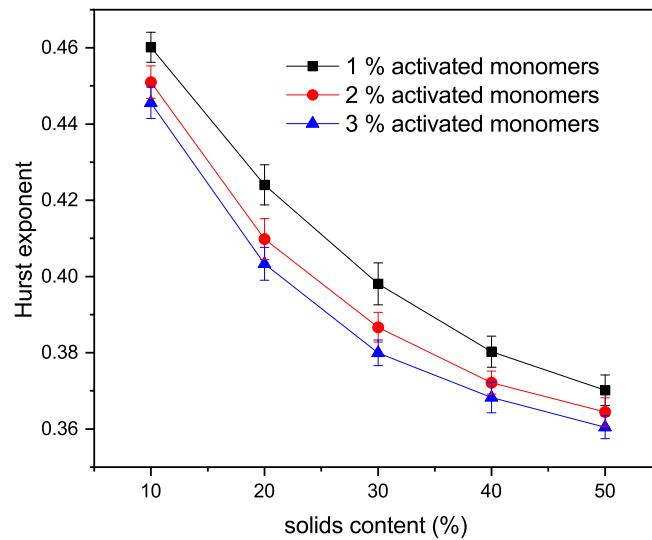


Figure 4.30 Hurst exponent vs solids content for three percentages of activated monomers. Error bars represent standard deviation of values for 10 independent runs for each set of conditions and lines connecting the data points provide a visual guide only.

(containing values of t), is presented in Figure 4.33 (containing values of n_0). For points where the obstacles do not impede particle diffusion, the value of tortuosity is equal to one, as observed around the origin point. When the number of steps to reach a selected point on the lattice is higher compared to an empty lattice, the value of tortuosity is higher than one and equal to the ratio of the two diffusion step numbers. It can be seen that for lower values of S_C (Figure 4.32a), most of the lattice is readily accessible for a diffusing particle with a tortuosity value of one for most of the pore structure. On the other hand, for higher

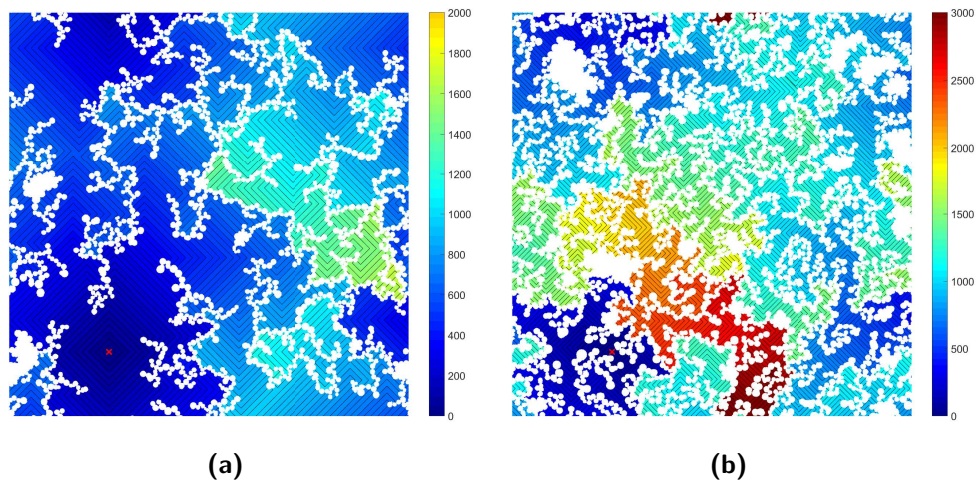


Figure 4.31 Diffusion maps of selected cluster structures with 1 % activated monomers and (a) 20 % solids content and (b) 40 % solids content. Colours represent number of diffusion steps needed to reach a point from a selected origin (marked with red cross) with lower step values shown in blue and higher step values shown in red. Cluster points and inaccessible pore areas are shown in white.

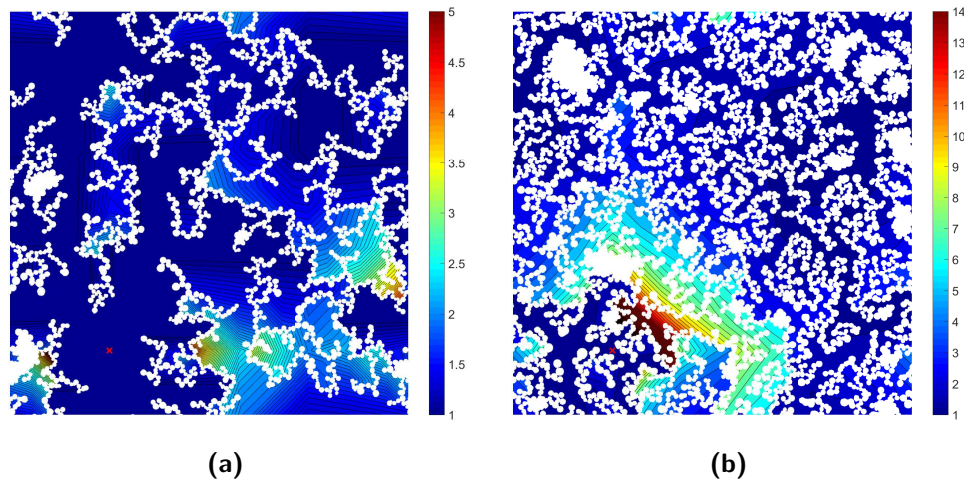


Figure 4.32 Tortuosity maps of selected cluster structures with 1 % activated monomers and (a) 20 % solids content and (b) 40 % solids content. Colours represent values of tortuosity from a selected origin (marked with red cross) with lower values shown in blue and higher values shown in red. Cluster points and inaccessible pore areas are shown in white.

values of S_C (Figure 4.32b), some parts of the pore structure are difficult to access, with tortuosity values up to 30.

These structural constrictions, reflected by the values of Hurst exponent, lead to pore voids that are more difficult to access externally, which affects the kinetics of diffusional processes in RF gels, such as solvent exchange or gas adsorption. Materials exhibiting lower values of Hurst exponent (more restricted pores), could find uses in applications such as drug delivery systems, where a gradual emptying of the pore voids is preferential to a rapid discharge of substances from a more open pore structure.

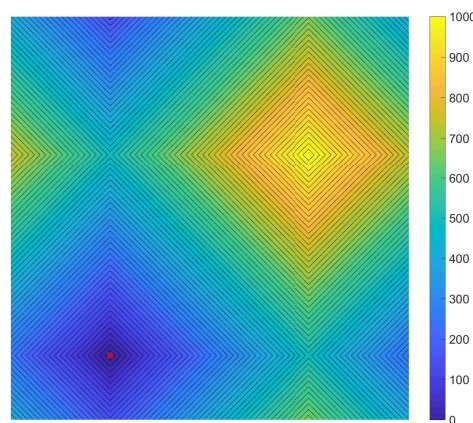


Figure 4.33 Diffusion map for an empty lattice. Colours represent number of diffusion steps needed to reach a point from a selected origin (marked with red cross) with lower step values shown in dark blue and higher step values shown in yellow.

An increase in number of activated sites increases the number of clusters in the structure, causing the structures to spread throughout the reaction space, again leading to a more complex pore structure and a higher ratio of closed porosity, in agreement with the trends observed for correlation dimension of the cluster structures, as discussed above.

4.4 Solvent exchange modelling

One of the manufacturing steps impacting the final textural properties of RF gel materials, is solvent exchange, as discussed in Section 1.2.4. Due to a lower value of surface tension of the selected solvent, compared to water, material shrinkage during subsequent drying is limited. However, in order to obtain satisfactory results, the exchange needs to be thorough so that any remaining water does not cause collapse of the porous gel structure.

Thus, solvent exchange, using the structures generated in Section 4.1.3, was modelled in this section, with the corresponding Fortran code presented in Appendix E.2.6. In order to simplify the problem, a two-dimensional slab of the material was considered, with the gel structure being periodic in the orthogonal dimension. This represents a hydrogel slice surrounded by solvent on both sides, leading to solvent diffusion into the porous structure from both sides, perpendicular to the material surface. The size of the external simulation box containing the solvent was set to match the number of accessible sites within each structure, resulting in equal concentrations in both regions once equilibrium is reached.

First, the accessible pore structure, used for the subsequent solvent exchange simulation, was identified. The accessible lattice sites were initially set to the value of 1 (resulting in an initial concentration inside the box $c_{in} = 1$), representing species 1 (water) entrained within the pore structure of a hydrogel material, while the sites outside the lattice contained species 0 (solvent). A lattice site was selected randomly during each simulation step. Simulation time was incremented by a value of $1/N_{lat}^2$, where $N_{lat} \times N_{lat}$ is the size of the lattice used in the simulation, with $N_{lat} = 1000$ in this work. This means that, on average, each lattice site was selected once during an increment of one time unit. If a selected site was either an inaccessible pore site or a cluster site, another site was randomly selected.

If a selected site was accessible, one of its four neighbours was randomly selected. There are four possible types of neighbour sites, as presented in Figure 4.34: a cluster site (black in Figure 4.34), a site containing a different or the same solvent as the selected site (red and blue in Figure 4.34, respectively), and a site outside the lattice (grey in Figure 4.34). If the selected neighbour site was occupied by a cluster or contained matching species (a and b in Figure 4.34, respectively), no exchange occurred and another site was selected. If the neighbour site contained a different species than the selected one (c in Figure 4.34), the species swapped places, effectively introducing diffusion. If the neighbour site was selected outside the lattice, the probability of swapping was based on a random number (R) and outside concentration (c_{out}). If the selected site contained a value of 1, it swapped with a

site outside the lattice if R , a randomly drawn number between 0 and 1, was higher than the outside concentration ($R > c_{out}$). Conversely, if the selected site contained a value of 0, a swap occurred if R was lower than the outside concentration. Ideal mixing was assumed for the sites outside the lattice and c_{out} was related to the average concentration on the lattice ($c_{in} + c_{out} = 1$). The simulation was halted when the average lattice concentration reached a selected value, in this work $c_{in} = 0.65$.

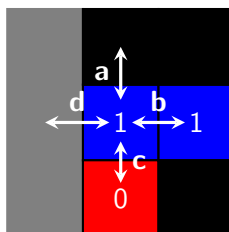


Figure 4.34 Schematic drawing of solvent exchange with lattice sites occupied by species 1 shown in blue, species 0 in red, cluster sites in black, and sites outside the lattice in grey

The aforementioned simulation was performed for all generated structures from Section 4.1.3, and 10 runs for an empty lattice, with varying seeds for the random number generator. Species distribution lattices for three values of c_{in} (taken at various time points of the simulations) and different structures are presented in Figure 4.35. It can be seen that, for an empty lattice (top row in Figure 4.35), the diffusion front of species 0 (red) gradually moves inwards with an even horizontal distribution of species. On the other hand, for the presented cluster structures (second to bottom row in Figure 4.35), the cluster structures act as barriers for diffusion, creating pockets of lower species 0 (red) concentration, compared to other sites at the same distance from the lattice edge.

Average concentration profiles for cluster structures, with varying S_C and C_C , and an empty lattice are presented in Figure 4.36 for $c_{in} = 0.65$. Here concentration calculated is as an average of values for the accessible sites at the same distance from the lattice edge plotted against this distance on the x axis, and averaged over 10 cluster structures at each set of conditions. There is good agreement for the average concentration profiles for all values of S_C and C_C with simulation for an empty lattice, as observed from Figure 4.36, suggesting that after reaching a certain average concentration value, the average distribution throughout the structure remains the same despite structural differences. However, different simulation times are required to reach the given concentration value, as presented in Figure 4.37.

The time required, to reach a given value of concentration, depends on the Hurst exponent, as discussed in more detail in the previous section. The distance a typical walker moves through the structure is given in Equation 4.4. The value of the Hurst exponent for an empty lattice is equal to $\frac{1}{2}$, as discussed above.

$$L = A \times t^H \quad (4.4)$$

In order to scale concentration curves for simulations performed with cluster structures and an empty lattice, corresponding values of A and H from Equation 4.4 were found. An

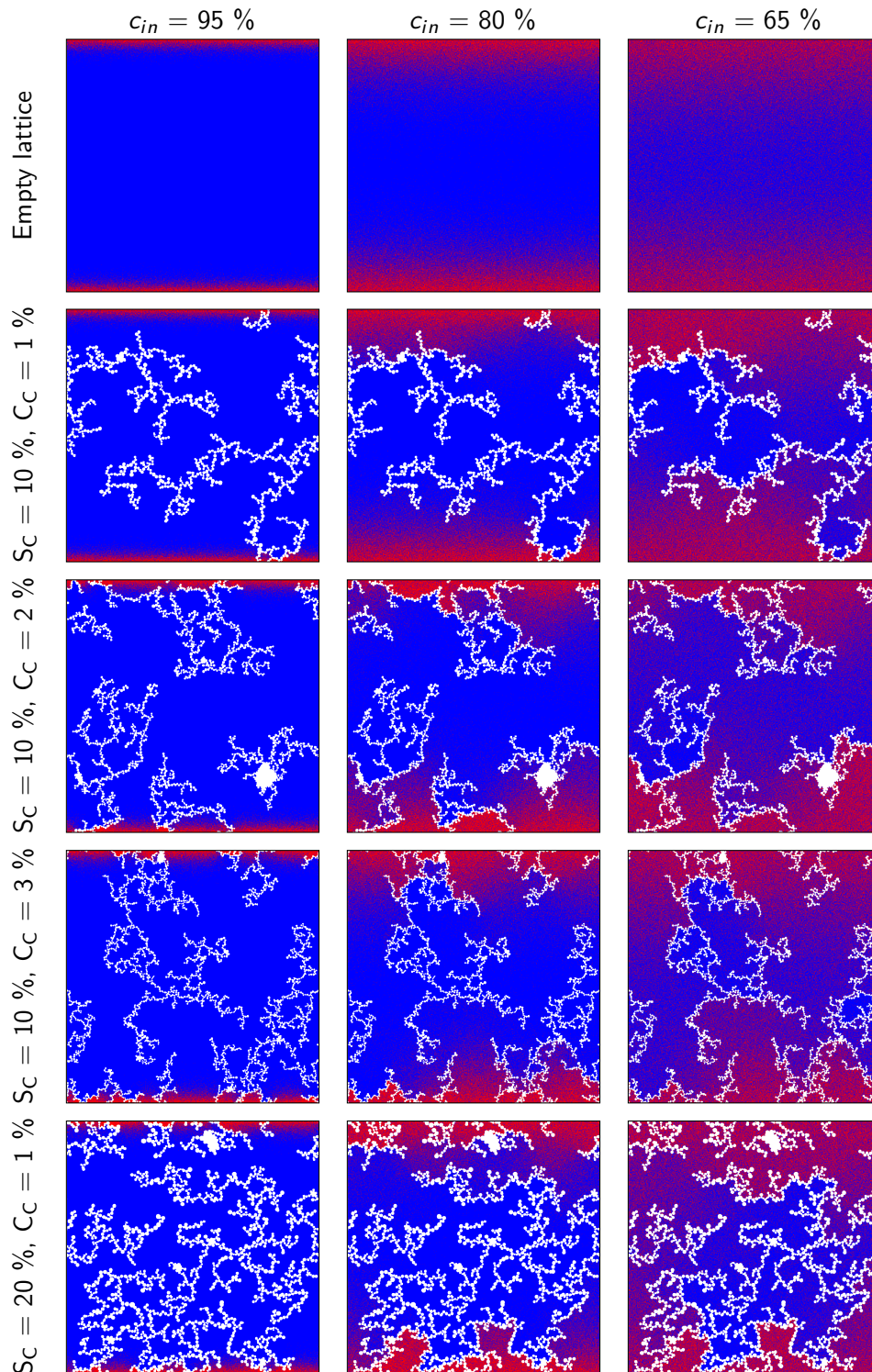


Figure 4.35 Solvent exchange modelling with structure parameters on the left and concentration of species 1 on the lattice on the top. Cluster sites and inaccessible pore sites are shown in white, species 1 in blue and species 2 in red. The lattice used is 1000×1000 .

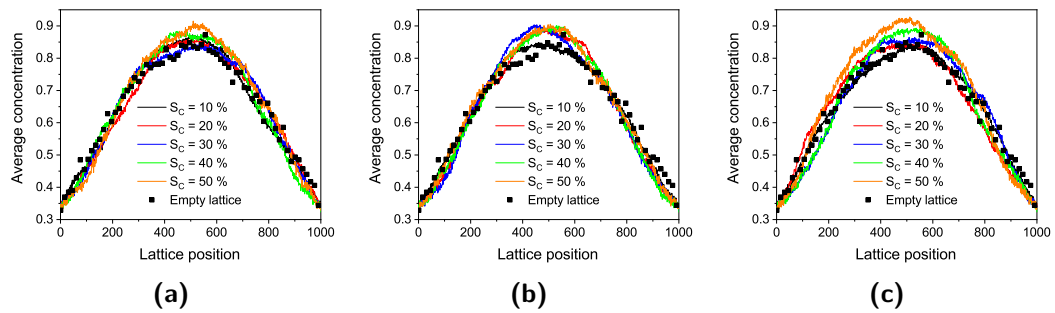


Figure 4.36 Comparison of average concentration profiles parallel to the lattice edge for an empty lattice at $c_{in} = 0.65$, varying S_C and (a) $C_C = 1\%$, (b) $C_C = 2\%$, and (c) $C_C = 3\%$

initial value of H was taken from the previous section, and overlap of the curves scaled with values in the range $H \pm 0.1$, with an increment of 0.01, was analysed. Firstly, the time values were scaled with the selected value of H , as $t_{scaled} = t^H$. In order to match the last concentration point ($c_{out} = 0.65$), a value of A was calculated as $A = \frac{t_{empty}(c_{out}=0.65)}{t_{scaled}(c_{out}=0.65)}$. The value of squared difference, between the scaled data and the data for an empty lattice, was evaluated for each set of H and A , and the set with the lowest difference value, and thus best overlap, was selected.

Comparison of concentration curves, before and after scaling, is presented in Figure 4.37. The curves for $S_C = 10\%$, $C_C = 1\%$ and an empty lattice are fairly similar even before scaling, due to the fact that the cluster structures at these conditions do not obstruct free diffusion significantly, leading to a value of H closest to $\frac{1}{2}$. On the contrary, for structures with higher values of S_C and C_C , the diffusion is notably hindered, leading to much longer times required to reach a given average concentration, observed particularly in Figure 4.37a. After scaling with the selected H and A , all curves collapse onto each other reasonably well, as presented in both Figures 4.37a and 4.37b.

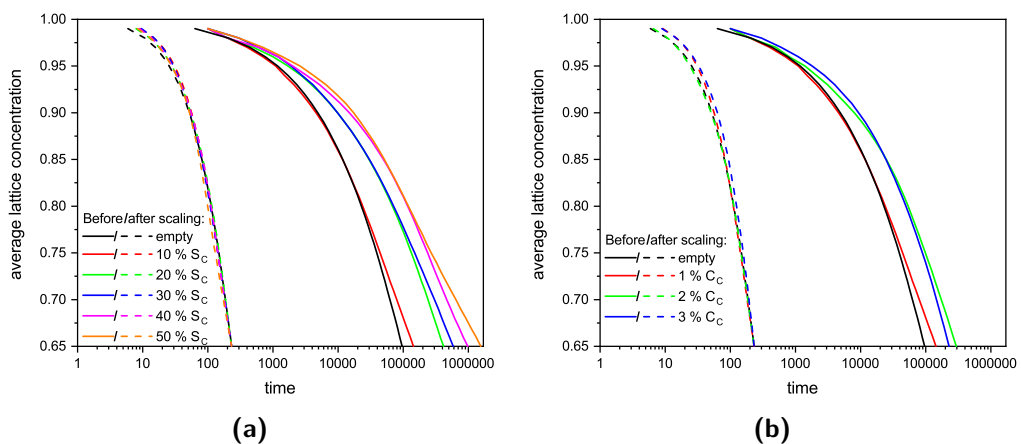


Figure 4.37 Comparison of concentration curves before (dashed lines) and after (dotted lines) scaling with data for an empty lattice for varying (a) S_C and (b) C_C . Time is measured in Monte Carlo steps per lattice site before scaling and scaled using the Hurst exponent, as described in the text.

The impact of varying S_C and C_C on the value of H can be seen in Figure 4.38a. Similar to the trend observed for random walkers (Figure 4.30), increasing both S_C and C_C results in a decrease in H . This decrease is caused by increased tortuosity of the porous structure, as observed above, which leads to slower exchange of solvent within these pores, which are difficult to access, due to hindered diffusion into these pores. The values of H calculated from solvent exchange simulation are lower than those obtained from random walkers, but the trends remain the same, as can be seen from correlation presented in Figure 4.38b. Although the values of the Hurst exponents do not match exactly, that they have the same trends is some endorsement of the scaling analysis performed for the solvent exchange simulation data. Furthermore, it indicates that some useful information on the fractal properties of real gels might be obtained from careful experiments that probe the kinetics of the process, and this is something that is recommended for future work.

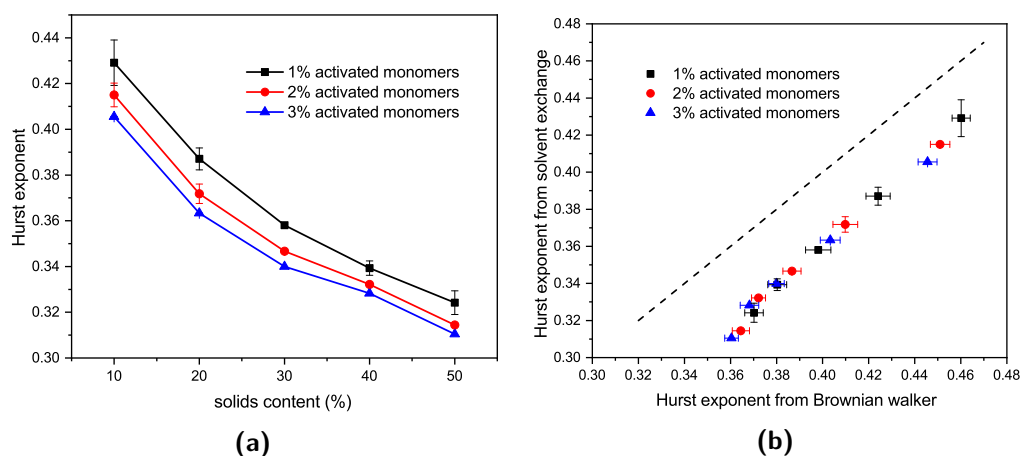


Figure 4.38 (a) Hurst exponent vs solids content for three percentages of activated monomers calculated from solvent exchange simulations. Error bars represent standard deviation of values for 10 independent runs for each set of conditions and lines connecting the data points provide a visual guide only. (b) Comparison of the Hurst exponent values calculated from Brownian walkers and solvent exchange simulations. Error bars represent standard deviation of values for 10 independent runs for each set of conditions and dashed line indicates the identity line.

4.5 Summary

In order to model aggregation and growth of cluster structures within RF gels, a two-dimensional lattice-based model using kinetic Monte Carlo was presented and analysed in this chapter for experimentally relevant characteristics, in particular textural and fractal properties.

The main outcomes of this chapter are as follows:

1. Code algorithm:
 - (a) A two-dimensional lattice-based model, using kinetic Monte Carlo, was developed on the basis of experimental evidence from literature.
 - (b) Diffusion probability of species was set inversely proportional to size.
 - (c) Compact, approximately circular, clusters were grown, in order to replicate clusters observed experimentally.
2. Static clusters:
 - (a) Increasing percentage of activated monomers leads to smaller clusters in the final structure.
 - (b) Final structures do not replicate experimentally observed ones due to the lack of cluster diffusion.
 - (c) High values of solids content required in order to obtain percolated cluster structures.
3. Diffusing clusters:
 - (a) Generated structures similar to the experimentally observed ones.
 - (b) Increasing percentage of activated monomers leads to smaller clusters and more spanning structures at the same solids content.
 - (c) Increasing solids content results in more dense structures, with percolated pore structures up to ~ 50 % solids content.
4. Textural characterisation:
 - (a) Increasing both solids content and percentage of activated monomers leads to a higher degree of closed porosity.
 - (b) Increasing solids content results in decrease in number of accessible surface sites per unit mass, due to the increased closed porosity.
 - (c) Increasing percentage of activated monomers leads to structures with higher surface area per unit mass, as a result of decreased cluster size.
5. Fractal analysis:
 - (a) The correlation dimension increases both with increasing solids content and percentage of activated monomers, suggesting increased structure complexity.

- (b) The correlation dimension asymptotes to 2.0 for higher solids contents, irrespective of percentage of activated monomers, with only small changes in structure complexity at high solids content.
 - (c) The Hurst exponent values were calculated from diffusion of a Brownian walker and the obtained values decrease with increasing both solids content and percentage of activated monomers.
6. Solvent exchange modelling:
- (a) Solvent diffusion into the cluster structure was hindered by the presence of cluster structures, creating pockets of higher and lower solvent concentration.
 - (b) Averaged concentration profiles for all simulations exhibited good overlap, suggesting an even distribution of solvent throughout the structures, after averaging over 10 structures, despite the observed solvent-rich and solvent-poor pockets.
 - (c) Scaling of concentration curves, using the Hurst exponent, provided good overlap with the data for an empty lattice, allowing evaluation of the Hurst exponent for the accessible porosity of cluster structures.
 - (d) The value of the Hurst exponent decreased with increasing both solids content and percentage of activated monomers, similar to the trends for random walkers.

Chapter 5

Gas sorption modelling

This chapter includes a discussion of gas sorption modelling, first in model pores and subsequently applied to the cluster structures from the previous chapter. First, this chapter examines the behaviour of a model gas and liquid, in order to develop a deeper understanding of the gas sorption model used in this work, followed by introduction of the calculation algorithm and the methodology for textural analysis of calculated gas sorption isotherms. The model used here implements two tunable variables: (i) temperature and (ii) parameter setting the ratio of interactions between the adsorbing fluid and solid adsorbate surface. The effect of these variables on the shape of a simulated gas sorption isotherm for a model slit pore, along with choice of the values for all subsequent calculations, is examined.

Gas sorption was analysed using model slit pores, with both ends open, in order to study the difference in the processes of pore filling and emptying, which leads to the phenomenon of hysteresis. This was followed by investigating the impact of varying pore length and width on the shape of the gas sorption isotherm. Subsequently, some other pore shapes were studied, namely pores with one end open and conical pores, which are likely to be found in the model cluster structures.

Since the cluster structures, presented in Chapter 4, contain pores of different sizes, a system with multiple pores of varying length or width was explored here. Finally, the cluster structures from the previous chapter were analysed using simulated gas sorption along with textural analysis for properties such as accessible surface area and pore size distributions, extracted from the isotherm data.

At the end of this chapter, a summary of the most significant findings of this chapter is presented.

5.1 Model gas and liquid

The adsorption model used in this study was based on the work of Monson [177], in which a grand canonical (μVT) ensemble system was considered with fixed chemical potential (μ), volume (V), and temperature (T). This represents a system in contact with a heat bath and a particle reservoir, and its grand potential (Ω) can be expressed as:

$$\Omega = \bar{E} - TS - \mu\bar{N} \quad (5.1)$$

where \bar{E} is the average energy per particle, T is absolute temperature, S is the entropy of the system, μ is chemical potential, and \bar{N} is the average occupancy of a site.

The Hamiltonian for a lattice gas system, with nearest neighbour interactions, is given by:

$$H = -\frac{\epsilon}{2} \sum_i \sum_a n_i n_{i+a} + \sum_i n_i \phi_i \quad (5.2)$$

where ϵ is the nearest neighbour interaction strength, n_i is the occupancy at site i , a is the series of nearest neighbour sites of site i , and ϕ_i is the external field at site i . The first set of summations gives the potential energy with the nearest neighbours, and the first term in Equation 5.2 corresponds to the latent heat of the system, while the second term is the energy contribution from an external field.

In a mean field theory approximation, the Helmholtz energy (F) can be expanded as follows:

$$F = TS + H = \bar{E} - TS$$

$$F = kT \sum_i [\rho_i \ln \rho_i + (1 - \rho_i) \ln(1 - \rho_i)] - \frac{\epsilon}{2} \sum_i \sum_a \rho_i \rho_{i+a} + \sum_i \rho_i \phi_i \quad (5.3)$$

where the term $kT \sum_i [\rho_i \ln \rho_i + (1 - \rho_i) \ln(1 - \rho_i)]$ corresponds to the entropy part of the Helmholtz energy. From Equations 5.1 and 5.3 an expression for grand potential with a mean field approximation can be derived from:

$$\Omega = -\frac{\epsilon}{2} \sum_i \sum_a \rho_i \rho_{i+a} + \sum_i \rho_i \phi_i + kT \sum_i [\rho_i \ln \rho_i + (1 - \rho_i) \ln(1 - \rho_i)] - \mu\bar{N} \quad (5.4)$$

Considering the case of a model bulk liquid with density $\rho = 1$, thus $\bar{N} = 1$, and no external field ($\phi = 0$), leads to the first term in Equation 5.4 being equal to -3 ($-\frac{\epsilon}{2} \sum_i \sum_a \rho_i \rho_{i+a} = -\frac{1}{2} \times 6$), due to the six nearest neighbours. The second and third terms are equal to 0 and the last term is simply μ . Thus, the grand potential for a model bulk liquid can be simplified to $\Omega = -3 - \mu$, which is an equation of a line intersecting both axes at a value of -3 .

Now, let us consider a model bulk gas, with a density of $\rho \ll 1$, but again without an external field in the bulk ($\phi = 0$). Due to the low density value, the first two sums in Equation 5.4 are approximately zero, and the entropy of the system in this case is a function

of density ($S = f(\rho)$). Using the ideal gas law we can obtain a relationship for the density, ρ :

$$\begin{aligned}\rho V &= N k_B T \\ \rho &= \frac{N}{V} = \frac{p}{k_B T} \\ T^* &= \frac{k_B T}{\epsilon_{\text{fluid-fluid}}} = 1 \implies \rho = p \\ \bar{N} &= \rho = e^{\frac{\mu}{k_B T}}\end{aligned}\quad (5.5)$$

where $\epsilon_{\text{fluid-fluid}}$ is the fluid-fluid interaction strength, k_B is the Boltzmann constant, and T^* is the temperature used in the simulation. The value of $T^* = 1$ was used and indicated by Monson [177], and corresponds to the critical temperature for condensation of a two-dimensional lattice gas with its nearest neighbours in mean field approximation. The effect of temperature is explored in more detail in Section 5.4.

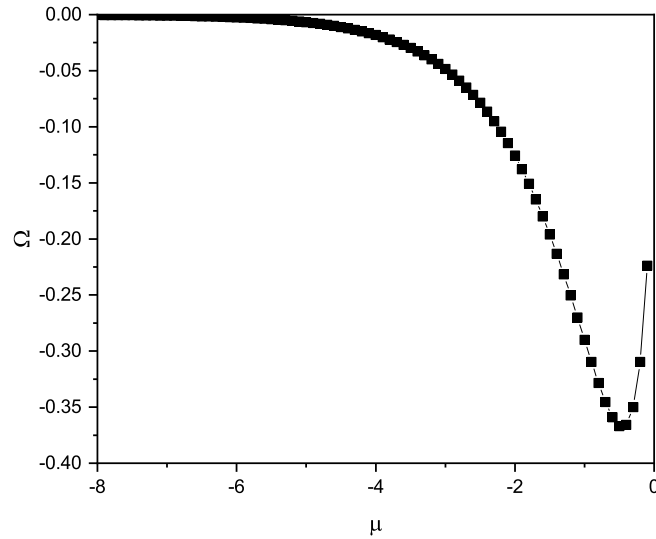


Figure 5.1 Dependence of grand potential of model bulk gas on chemical potential

Using the definition of density from Equation 5.5 in Equation 5.4, and omitting the first two terms of Equation 5.4, due to low values of ρ , gives:

$$\Omega = T^* \sum_i [e^\mu \ln e^\mu + (1 - e^\mu) \ln(1 - e^\mu)] - \mu \bar{N} \quad (5.6)$$

This leads to a minimum in grand potential at higher values of chemical potential, as can be seen in Figure 5.1.

In the case of a model gas adsorbing onto a flat surface; the sites adjacent to the surface differ from the bulk gas sites in that they have an external field contribution ($\phi \neq 0$), which comes from fluid-solid interactions. In this work, the external field was set using the ratio of fluid-solid to fluid-fluid interactions $\frac{\epsilon_{\text{fluid-solid}}}{\epsilon_{\text{fluid-fluid}}} = 3$, again based on the work of Monson [177]; the effect of this parameter is further examined in Section 5.4.

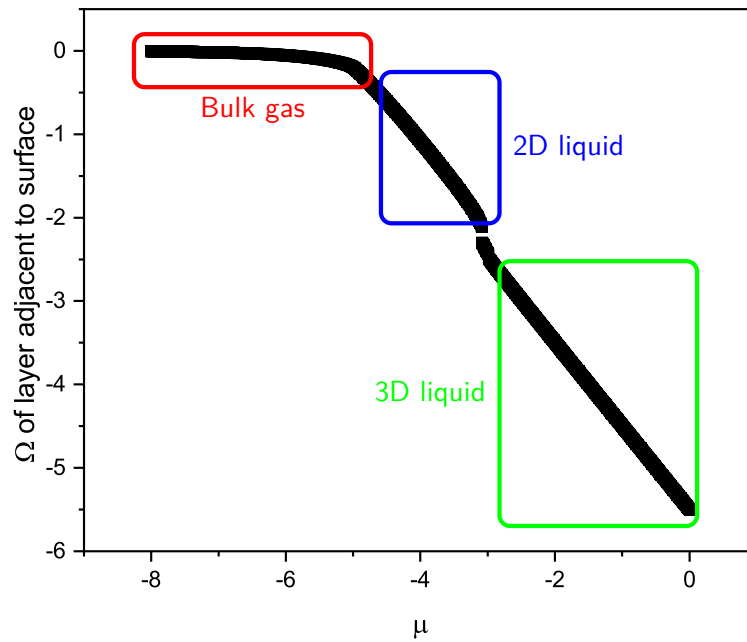


Figure 5.2 Dependence of grand potential of a fluid layer adjacent to a surface with increasing chemical potential

Figure 5.2 shows the dependence of grand potential of lattice sites adjacent to a surface on chemical potential of the system with three distinguishable regions. Firstly, at lower chemical potential (μ), all of the gas behaves like a bulk gas (red rectangle in Figure 5.2), similar to Figure 5.1. At medium values of μ , the gas physisorbs onto the surface, forming a two-dimensional liquid (blue rectangle in Figure 5.2). The intercept of this region is equal to -5 , which is a result of the four liquid neighbouring sites around each site in two dimensions (from Equation 5.4: $\Omega = -\frac{1}{2} * 4 - \frac{\epsilon_{\text{fluid-solid}}}{\epsilon_{\text{fluid-fluid}}} - \mu = -5 - \mu$). A schematic drawing is shown in Figure 5.3 with the selected site shown in black and the the aforementioned liquid neighbouring sites adjacent

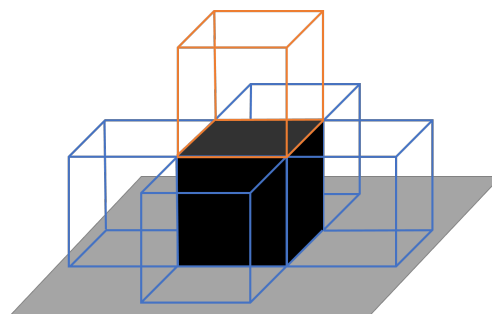


Figure 5.3 Schematic drawing of sites neighbouring a site adjacent to a surface

to the surface shown in blue. Eventually, when the chemical potential is increased to a high enough value, the bulk gas condenses, forming a three-dimensional bulk liquid (green rectangle in Figure 5.2). This results in adding one more liquid neighbouring site (shown in orange in Figure 5.3) and the intercept of this region is, therefore, equal to -5.5 . It should be noted that the chemical potential in this case is related to pressure in a real system.

5.2 Calculation algorithm

The gas sorption calculation algorithm, based on the work by Monson [177] as mentioned before, is presented in Figure 5.4. The original version of the code, received from Prof Monson, was set up to work with a three-dimensional slit pore that is periodic in one dimension. However, the used arrays, such as the density distribution lattice, were one-dimensional, storing the data in a raster scan method. In order to visualise the arrays more easily and build more complex structures than a single slit pore, the arrays were converted to two-dimensional versions. Fortran code, used in this work, is presented in Appendix E.2.7.

After declaring all the used variables, the pore dimensions, simulation temperature, number of adsorption and desorption steps, chemical potential increments, initial gas density, maximum number of iteration steps, density difference threshold for convergence, and a value to turn output for density distribution lattice on/off are read from an input file.

The required pore structure was generated using `ieta` lattice, where the wall sites were set to the value of 0 and accessible sites to the value of 1. In order to represent the pore structure being in contact with bulk gas, extra space of 10 lattice sites was added adjacent to the pore opening, or around the whole structure for cluster model. Using the `ieta` lattice, the values of the external field were calculated and stored in the `phi` lattice, as shown in Equation 5.7.

$$\phi_i = - \sum_a \left[(1 - \text{ieta}_{a_i}) \times \frac{\epsilon_{\text{fluid-solid}}}{\epsilon_{\text{fluid-fluid}}} \right] \quad (5.7)$$

where ϕ_i is the external field at site i , a are the nearest neighbours of site i , ieta_{a_i} is the value of `ieta` lattice for the nearest neighbour, and $\frac{\epsilon_{\text{fluid-solid}}}{\epsilon_{\text{fluid-fluid}}}$ is the interaction parameter. This leads to bulk gas sites having no external field contribution ($\phi_i = 0$), for sites with one wall site adjacent $\phi_i = -\frac{\epsilon_{\text{fluid-solid}}}{\epsilon_{\text{fluid-fluid}}}$, two adjacent wall sites $\phi_i = -2 \times \frac{\epsilon_{\text{fluid-solid}}}{\epsilon_{\text{fluid-fluid}}}$, and so on. Before the main sorption loop, the density of all the accessible gas sites (`rhoold`) was set to the initial value (`rhog`), previously read from the input file. There were two lattices storing density values, `rhoold` and `rhonew`. The former is used to store density values from before an iteration of the sorption loop, while the latter stores the values after an iteration.

An iteration of the sorption loop was initialised by incrementing the iteration counter `iter` and setting all the sums that are calculated at the end of an iteration to 0. This was

followed by calculating the new value of density for all accessible gas sites. First, the nearest neighbour sum (ρ_{nn}) was evaluated by adding up the density values of adjacent sites. Due

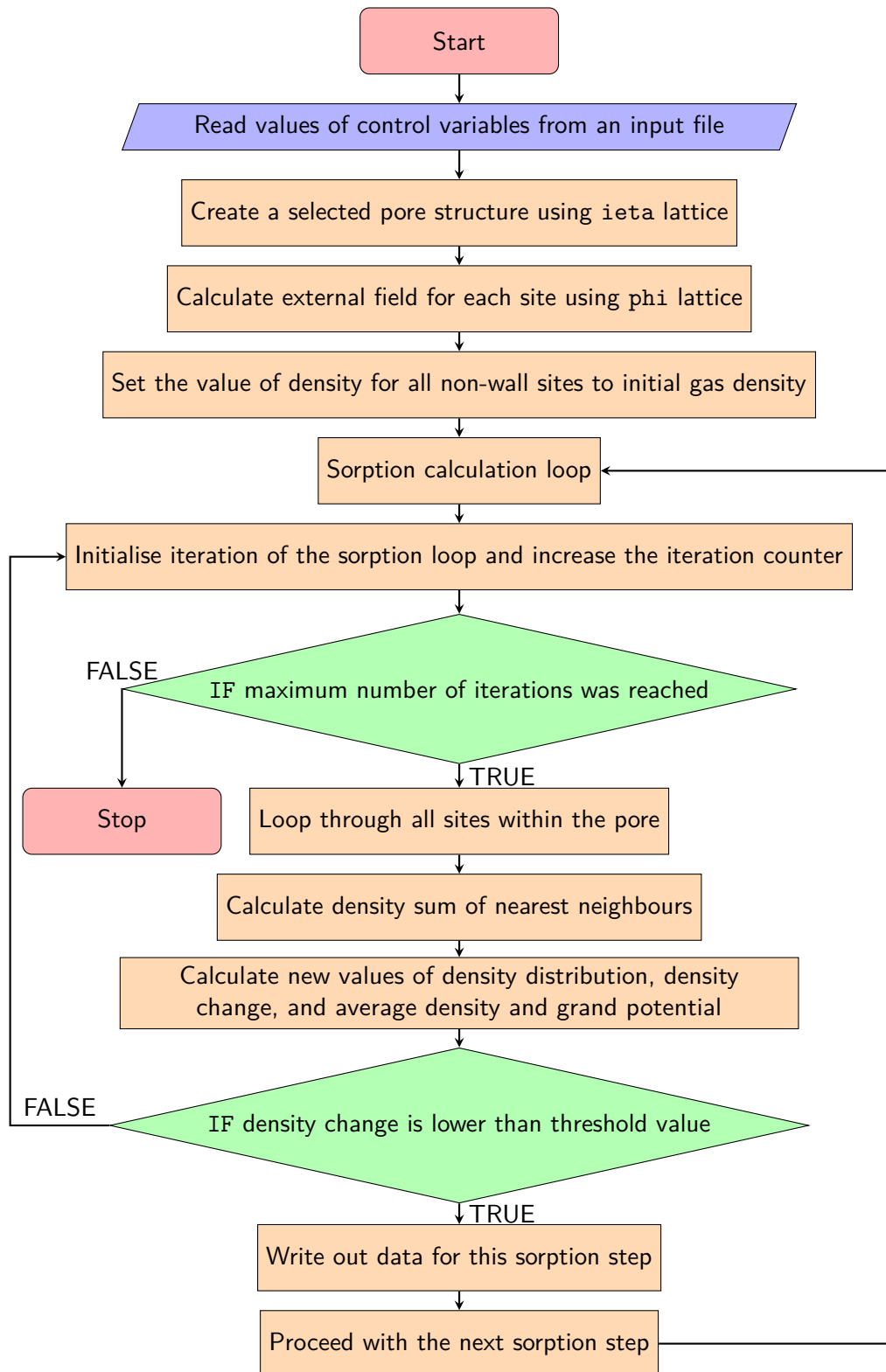


Figure 5.4 Schematic flowchart of gas sorption calculation algorithm

to the periodicity in the y direction, the density of the current site was added twice to the nearest neighbour sum since it is surrounded by two sites with matching density in the y direction, as presented in Equation 5.8.

$$\text{snn}_i = 2 \times \text{rhoold}_i + \sum_a \text{rhoold}_a \quad (5.8)$$

The new value of density for the selected site was then calculated, based on the nearest neighbour sum (snn_i), external field contribution (ϕ_i), chemical potential (μ), and temperature (T^*), as presented in Equations 5.9 and 5.10.

$$x_i = \frac{\text{snn}_i - \phi_i + \mu}{T^*} \quad (5.9)$$

$$\text{rhonew}_i = \frac{1}{1 + e^{-x_i}} \quad (5.10)$$

At the end of a sorption step, values of average density (rhoav) and grand potential (Equation 5.11) were calculated. The new values of density from rhonew were transferred to rhoold for the subsequent calculations.

$$\Omega = \frac{\frac{1}{2} \times \sum_{i=1}^N (\text{rhonew}_i \times \text{snn}_i) - \sum_{i=1}^N T^* \times \ln(1 + e^{x_i})}{N} \quad (5.11)$$

where Ω is the grand potential of the system, N is the number of accessible pore sites, and the other variables are as defined above.

In order to see if an iteration was converged, the difference between the old and the new density values was determined, to ensure a near-equilibrium state was achieved. For model pores, an average difference for the whole pore was used to determine whether the iteration was converged, whereas for cluster structures, a maximum value of the difference was used, to avoid changes in small pores being masked by their larger counterparts. If the value was lower than the selected threshold, the simulation proceeded to the next sorption step, otherwise another iteration at the current conditions was performed, unless the maximum number of iterations was reached. Because the maximum value of the density difference was used as the convergence factor for cluster structures, a higher value of the threshold was used (10^{-3}), compared to the value used for model pores (10^{-8}).

This procedure was repeated for a series of adsorption and desorption steps, with a linear increase either in chemical potential (μ) or relative activity (λ/λ_0), where the two variables are related as shown in Equation 5.12.

$$\mu = T^* \times \ln(\lambda/\lambda_0) - 3 \quad (5.12)$$

5.3 Textural analysis

Similar to the results obtained in the experimental part of this work, discussed in Chapter 3, the simulated gas adsorption isotherms were analysed here for textural properties, namely accessible surface area and pore size distribution, with their evaluation methodology described in Sections 5.3.1 and 5.3.2, respectively.

5.3.1 Accessible surface area

Analysis of the accessible surface area of structures examined in this chapter was performed in a similar manner as used in Chapter 3, using Brunauer-Emmett-Teller (BET) theory, which is described in more detail in Sections 2.1.2 and 3.1.5. The only difference, compared to experimental data analysis, is the nature of the input data used in this study. For a gas system containing only a single component, relative activity (λ/λ_0) can be related to the partial pressure of the gas and is, therefore, used here instead of p/p_0 . Similarly, the average density (ρ_{average}), calculated here, can be related to the volume of gas adsorbed on the sample surface, and is, thus, used here instead. This means, that the values of accessible surface area obtained from the BET calculations provide values in arbitrary units and are presented in that way.

5.3.2 Pore size distribution

In contrast to the BET calculation, discussed in the previous section, the algorithm for extracting pore size distribution (PSD) from simulated isotherms was adapted from the original method based on the Barrett-Joyner-Halenda (BJH) theory, discussed in Sections 2.1.3 and 3.1.5.

First, the Kelvin equation, discussed in Section 3.1.5, was adjusted, to account for the different shape of the condensed liquid meniscus at the pore opening. The simulations within this section were set up in two dimensions, with periodic boundary in the third dimension. Therefore, the meniscus shape for a slit pore, used here, differs from a cylindrical pore, which is the shape usually assumed for experimental samples. The adjusted Kelvin equation, to account for meniscus shape, is presented in Equation 5.13, where λ/λ_0 is relative gas activity, γ is the surface tension of the condensed gas, V_m is the gas molar volume, r is core liquid radius, R is the universal gas constant, and T is temperature. In order to allow comparison with experimental results, all the constant values were taken for nitrogen at 77 K, as in Section 3.1.5.

$$\ln\left(\frac{\lambda}{\lambda_0}\right) = \frac{\gamma V_m}{rRT} \quad (5.13)$$

The calculation algorithm from BJH theory accounts for the volume of gas desorbed from previously opened pores, in order to determine if new pores were emptied during a given pressure step. However, the λ/λ_0 interval, used in this work, is small enough that if a sufficient amount of gas desorbs in a calculation step, it can be assumed to be due to

pore emptying. Therefore, the algorithm is simplified here. The values of core radii (R_{C_i}) corresponding to the values of λ/λ_0 are calculated using Equation 5.14, where $(\lambda/\lambda_0)_i$ is the relative activity corresponding to R_{C_i} , and the constants (γ , V_m , R , and T) are grouped into value A , equal to half of the value for experimental calculations, due to the previously discussed difference in meniscus shape. It was indicated previously that the size of a lattice site in the model used here is ~ 1 nm [184]; therefore, a value of 1 nm is added to each radius, accounting for a monolayer remaining adsorbed on the pore walls after a pore empties.

$$R_{C_i} = \frac{-\gamma V_m}{RT \ln(\lambda/\lambda_0)_i} + 1 = \frac{-A}{\ln(\lambda/\lambda_0)_i} + 1 \quad (5.14)$$

Average pore size (D_{avg_i}) for each λ/λ_0 interval, used as the x axis for plotting the PSD, is obtained using Equation 5.15, as for the calculations in Chapter 3. Cumulative pore volume (PV_i), used as the y axis for plotting the PSD, is calculated using Equation 5.16, again related to the calculations in Chapter 3.

$$D_{avg_i} = \frac{2(R_{C_i} + R_{C_{i+1}}) \times R_{C_i} \times R_{C_{i+1}}}{R_{C_i}^2 + R_{C_{i+1}}^2} \quad (5.15)$$

$$PV_i = \frac{\rho_{average_i} - \rho_{average_{i+1}}}{\log(D_{avg_i}/D_{avg_{i+1}})} \quad (5.16)$$

5.4 Effect of temperature and interaction parameter

The values of temperature (T^*) and the ratio of solid-fluid to fluid-fluid interaction strength ($\frac{\epsilon_{fluid-solid}}{\epsilon_{fluid-fluid}}$), parameters used in this model, for gas sorption modelling were taken from the work by Monson [177], as mentioned above. However, in order to confirm that these values are appropriate for this work, gas sorption isotherms for a model slit pore of width 6 lattice sites and length 40 lattice sites with varying values of each of the two parameters were evaluated here.

Chemical potential (μ) can be related to relative activity (λ/λ_0) within the pore as $\lambda/\lambda_0 = e^{(\mu+3)/T^*}$, where T^* is a temperature term explained in more detail above. Hence, for a value of $T^* = 1.0$, relative activity reaches unity at $\mu = -3$.

Figure 5.5 shows the effect of changing the value of T^* on the calculated isotherm shape for a selected model slit pore. With a lower value of T^* , a narrow hysteresis loop can be observed for monolayer formation and no pore filling occurring within the range of relative activity (λ/λ_0). A higher value of temperature leads to a more gradual monolayer formation and a narrower hysteresis loop associated with pore filling/emptying. Due to the value of $T^* = 1$ being used in previous work [177], and the isotherm shape observed for this temperature value in Figure 5.5 being close to one expected from nitrogen sorption experiments for such a pore, this value was used in this work as well.

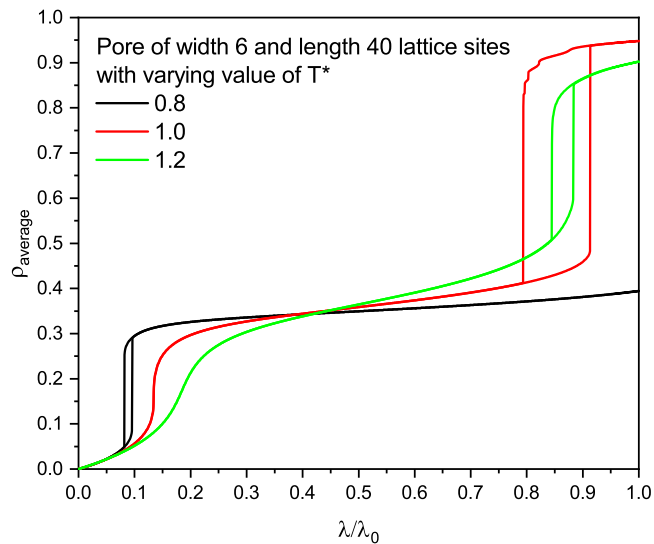


Figure 5.5 Sorption isotherms for a model slit pore of width 6 lattice sites and length 40 lattice sites with varying simulation temperature

The interaction parameter ($\frac{\epsilon_{\text{fluid-solid}}}{\epsilon_{\text{fluid-fluid}}}$) is related to the energy of adsorption in the first adsorbed layer, similar to the C constant from the BET equation (described in more detail in Sections 2.1.2 and 3.1.5). A low value of the parameter leads to very weak interactions between the adsorbing gas and pore walls, while a high value would result in a high energy of adsorption that is more similar to chemisorption rather than gas physisorption. In the work by Monson [177], the value of $\frac{\epsilon_{\text{fluid-solid}}}{\epsilon_{\text{fluid-fluid}}} = 3$ was used, thus values ranging from 1 to 5 with a step of 0.5 were explored here to explore the validity of the previously reported value. Figure 5.6 presents calculated gas sorption isotherms for a model slit pore, as for Figure 5.5, with varying values of the interaction parameter.

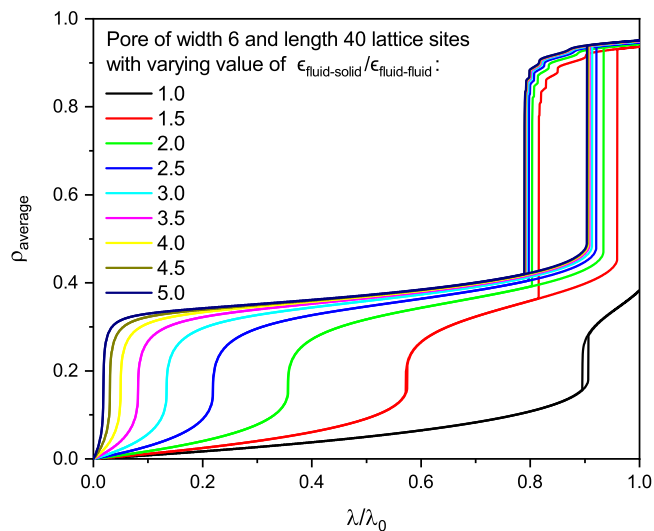


Figure 5.6 Sorption isotherms for a model slit pore of width 6 lattice sites and length 40 lattice sites with varying fluid-solid to fluid-fluid interaction strength

From Figure 5.6, it can be observed that isotherms calculated with values of $\frac{\epsilon_{\text{fluid-solid}}}{\epsilon_{\text{fluid-fluid}}}$ above 3 exhibit a very similar shape of the hysteresis loop as well as the general isotherm shape at higher values of λ/λ_0 . Higher values of the interaction parameter also lead to monolayer formation at lower λ/λ_0 values, with a steeper increase of average density over a narrower range of λ/λ_0 . This is caused by the first adsorbed layer being most influenced by the parameter value, as a result of the increased fluid-solid interactions. The effect is less pronounced for the subsequent layers since they interact with the previously adsorbed gas, leading to fluid-fluid interactions, instead of fluid-solid interactions that are influenced by the parameter value.

Decreasing the value of $\frac{\epsilon_{\text{fluid-solid}}}{\epsilon_{\text{fluid-fluid}}}$ shifts the monolayer formation to higher values of relative activity, as can be seen from Figure 5.6. The delayed monolayer formation, similar to a Type III isotherm based on the IUPAC classification [142], is still followed by a hysteresis loop shape similar to the ones observed for higher values of the interaction parameter due to the mitigated impact of the parameter on multilayer adsorption. However, for a $\frac{\epsilon_{\text{fluid-solid}}}{\epsilon_{\text{fluid-fluid}}} = 1$, the pore does not fill within the studied range of λ/λ_0 since a more pronounced adsorption occurs only above $\lambda/\lambda_0 \sim 0.9$. It can also be noted that the monolayer formation, for isotherm calculated with the lowest value of the interaction parameter, is accompanied by a hysteresis loop in this region, suggesting a presence of an energy barrier leading to a delayed adsorption of the monolayer. Since the value of the parameter, in this case, is equal to one, adsorption is no longer preferred, when compared to the fluid condensation, due to the sites adjacent to the walls having no external field contribution (as per Equation 5.7), the same as for bulk sites.

Hence, due to the trends observed in this section, the values of T^* and $\frac{\epsilon_{\text{fluid-solid}}}{\epsilon_{\text{fluid-fluid}}}$ were fixed for all subsequent calculations in this work, at 1 and 3, respectively.

5.5 Pores with both ends open

In order to investigate the phenomena happening during adsorption and desorption, a series of slit pores were examined in this section, with dimensions set by width and length, as well as analysing the influence of pore dimensions on the sorption isotherm shape. Here, both pore ends were open to the bulk gas, occupying 10 lattice sites to each side of the pore openings. Furthermore, the pores considered here are symmetrical in the y direction, so two-dimensional slices are presented here since they are representative of the whole pore. Periodic boundary conditions were applied in the y direction and in all directions within the bulk gas. Gas sorption was modelled by increasing (adsorption) and, subsequently, decreasing (desorption) the chemical potential (μ) of the system.

5.5.1 Filling and emptying of pores

In order to explore the processes of pore filling and emptying, a slit pore 10 lattice sites wide and 40 lattice sites long is used here. A schematic drawing of the pore is shown in Figure 5.7, with its simulated gas sorption isotherm shown in Figure 5.8.

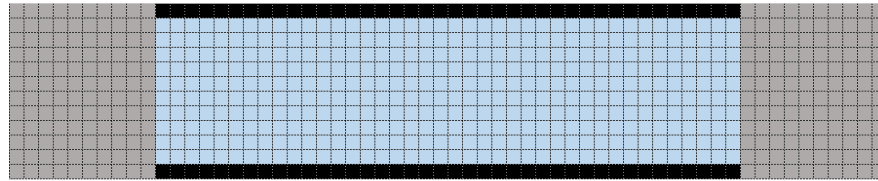


Figure 5.7 Model slit pore of width 10 lattice sites and length 40 lattice sites; pore walls are shown in black, bulk gas in grey, and sites within the pore in blue

Pore filling, via multilayers adsorbing onto the pore walls, as shown in Figure 5.9, agrees with the assumptions of the BET theory [146] used to analyse adsorption isotherms for accessible BET surface area. BET theory, as discussed in more detail in Section 2.1.2, assumes all surface sites are energetically equal and that the energy associated with the formation of the first layer is the heat of adsorption (ΔH_{ads}), while all subsequent layers are the result of liquid condensation, hence their energy of formation is equal to the heat of liquefaction (ΔH_{liq}). This agrees with the assumptions used here, where fluid-solid interactions (corresponding to ΔH_{ads}) are set to a higher value than fluid-fluid interactions (corresponding to ΔH_{liq}) and all wall sites are energetically homogeneous in the open slit pores used.

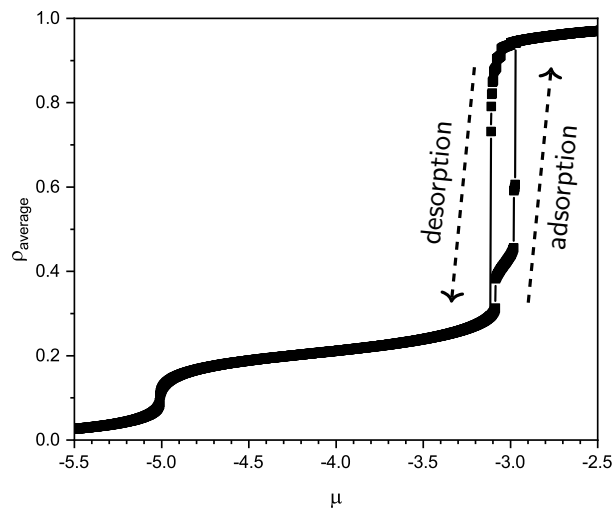


Figure 5.8 Sorption isotherm for a model slit pore of width 10 lattice sites and length 40 lattice sites

Considering the desorption curve of the hysteresis loop, shown in Figure 5.8, it is obvious that there is a difference between adsorption and desorption, within the region of μ approximately

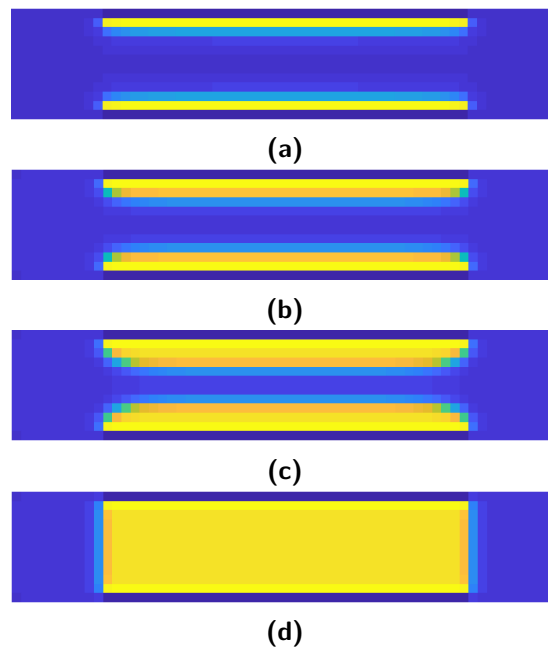


Figure 5.9 Filling of a model pore of width 10 lattice sites and length 40 lattice sites with formation of (a) a monolayer at $\mu = -3.087$, (b) the second layer at $\mu = -2.982$, (c) the third layer at $\mu = -2.973$, and (d) pore filling at $\mu = -2.97$

-2.9 to -3.1 ; the phenomenon of hysteresis is discussed further in Section 5.5.2. However, as can be seen from the density distributions within the pore shown in Figure 5.10, pore emptying happens by forming a liquid meniscus at the pore openings, and subsequent progress of the meniscus further into the pore. When the meniscus reaches a critical curvature, that is no longer stable according to the Kelvin equation, all remaining adsorbate within the pore is desorbed and a sharp decrease in the isotherm uptake is observed. The point at which a pore empties depends on its width and shape; in this work, only slit pores are considered, so the only parameter that influences pore emptying is pore width. This process of pore emptying, as observed in Figure 5.10, forms the basis of BJH theory [148], which is used to determine pore size distributions from gas sorption isotherms.

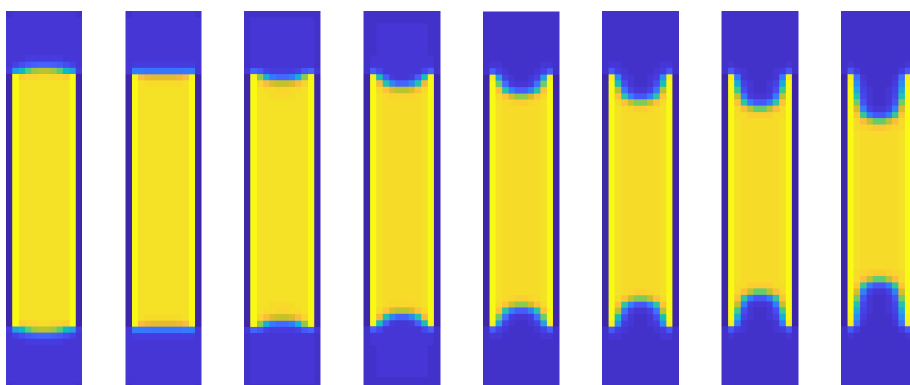


Figure 5.10 Emptying of a model pore of width 10 lattice sites and length 40 lattice sites shown for the region from $\mu = -3.0$ (left) to $\mu = -3.112$ (right)

From the adsorption branch of the isotherm curve (Figure 5.8), it can be seen that there are three regions where the average density (ρ_{average}) increases sharply in a narrow range of chemical potential (μ). The first sigmoidal increase, in the region around $\mu = -5.0$, corresponds to monolayer formation on the pore walls. This monolayer forms as a result of favourable interactions of the adsorbate with the wall sites. However, in a pore of finite length, there are always end sites, which lack one of the fluid-fluid interactions experienced with a neighbouring site, outside the pore, in the bulk gas. There is an energy penalty associated with these sites that is shared across all of the sites within the monolayer. When the system reaches a high enough value of μ to compensate for this energy penalty, a monolayer forms on the pore walls. The second layer forms at a higher value of μ due to the lack of fluid-solid interactions and only fluid-fluid interactions with sites of the previously formed monolayer. These interactions are less energetically favourable than the fluid-solid counterparts, and the penalty for the end sites still needs to be accounted for, so the system is required to reach a higher value of μ to compensate for these effects. In Figure 5.8, the formation of the second layer can be seen in the beginning of the hysteresis loop, around $\mu = -3.1$. The next layer forms in a similar manner to the second one; however, as the meniscus shape forms at the pore openings (Figure 5.9), the subsequent layers are shorter than those previously formed, thus the energy penalty for the end sites is shared amongst fewer sites. This leads to the formation of multilayers at increasingly higher values of μ .

5.5.2 Hysteresis

As mentioned above, if the mechanism for pore filling and emptying differs within a certain range of chemical potential μ , or partial pressure (p/p_0) in experiments, a hysteresis loop is observed for the gas sorption isotherm in this specific region of μ . The difference in the process between adsorption and desorption, for a selected slit pore, can be seen in Figures 5.9

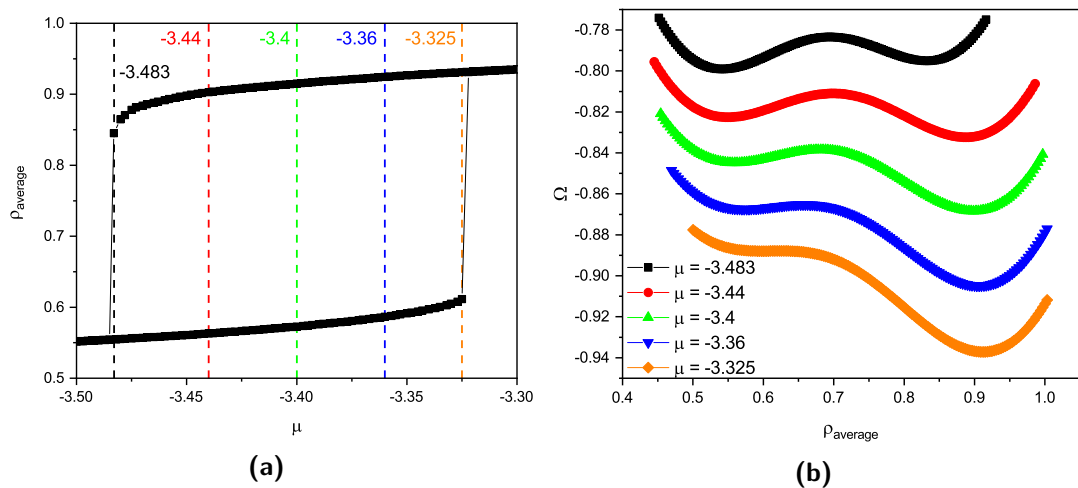


Figure 5.11 (a) Hysteresis loop within the gas sorption isotherm generated for a pore of width 4 lattice sites and length 40 lattice sites; dotted lines indicate values of chemical potential (μ) used for (b) free energy (Ω) curves with interpolated average density (ρ_{average})

and 5.10; where a hysteresis loop occurs as a result of the presence of an energy barrier between the gas and liquid phases in this region of μ . In this section, a pore of 4 lattice sites width and 40 lattice sites length is studied, and the related hysteresis loop is presented in Figure 5.11a using a selected μ range, providing a close-up view of the loop structure. Grand potentials (Ω) for the system were calculated at five values of chemical potential μ (Figure 5.11a), using interpolation of the density distribution between the adsorption and desorption branches of the isotherm, as shown in Figure 5.11b. At the lowest selected value of μ , the lower density (gas) phase presents a slightly lower energy state compared to the higher density (liquid) phase. A significant energy barrier can be observed between the two phases, which prevents the fluid within the pore from changing phase without a change in μ . Therefore, if a pore is filled with liquid, it will stay filled even if the gas phase presents a lower energy state. At higher values of μ , the liquid phase becomes the lower energy state and the energy barrier difference between the two states is reduced. At $\mu = -3.325$, the energy barrier is almost completely diminished, so above this value of μ , the barrier disappears completely and the system reaches an equilibrium at the lowest energy state, which is the liquid phase in this case.

5.5.3 Pore length

The influence of pore length on the gas sorption isotherm was examined in this section. For this purpose, gas sorption in pores, with a fixed width (6 lattice sites) and varying length, was calculated and the resulting isotherms can be seen in Figure 5.12. According to the IUPAC definition [144], a pore should have a depth greater than its width; therefore, slits with length below 6 lattice sites are technically not pores as such but are included here for comparison. It can be seen that for slits with lengths shorter than their width, there is no

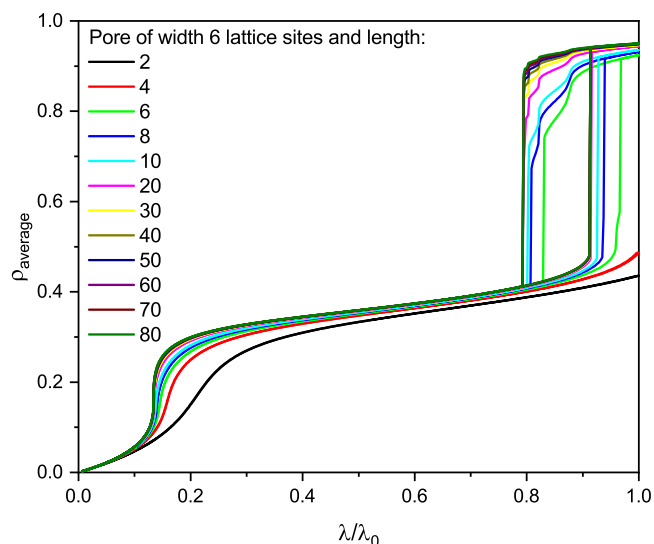


Figure 5.12 Sorption isotherms for model slit pores of width 6 lattice sites and varying pore length

hysteresis loop observed and the bulk of these slits do not fill at $\lambda/\lambda_0 = 1$, since there is no capillary condensation effect and only surface adsorption occurs. However, after reaching a critical pore length (at least 6 lattice sites in this case), only a small change in isotherm shape can be seen with further increase in length. There is a shift in monolayer coverage towards lower values of λ/λ_0 with increasing length, which is ascribed to the increasing number of sites that share the energy penalty from the pore end sites, as discussed in section 5.5.1.

5.5.4 Pore width

As observed previously, pore length has an insignificant effect on the final gas sorption isotherm shape. Simulated isotherms for pores with varying width and fixed length are presented in Figure 5.13. It can be seen that, as pore width increases, the hysteresis loop shifts towards higher values of λ/λ_0 .

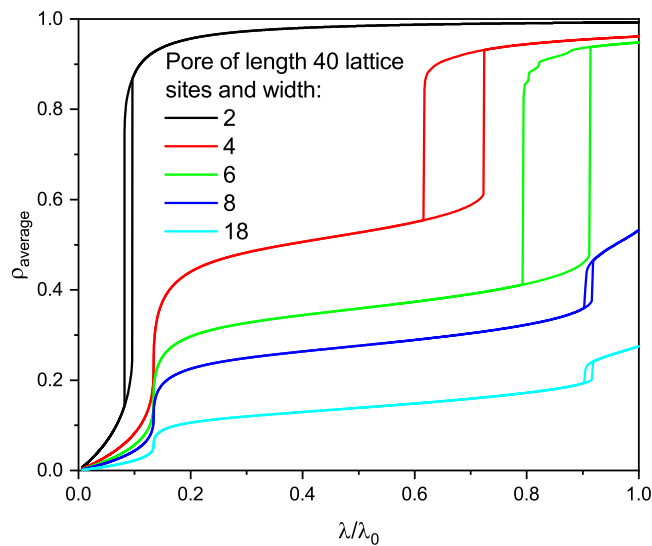


Figure 5.13 Sorption isotherms for model slit pores of length 40 lattice sites and varying pore width

The pore of width 2 lattice sites exhibits a narrow hysteresis loop at very low values of λ/λ_0 (~ 0.1), which is caused by the two walls forming monolayers adjacent to each other. This causes the monolayer to form at lower values of μ than for the other pores of the same length. The wider pores form a monolayer of adsorbed gas on the pore walls in the region $\lambda/\lambda_0 = 0.1$ to 0.2 , with the energy penalty resulting from the end sites being shared by the same amount of lattice sites. It can also be observed that pores with a width of at least 8 lattice sites do not fill at $\lambda/\lambda_0 = 1$ (corresponding to $\mu = -3$), as a result of the chemical potential not reaching a high enough value to fill these pores. This is one of the limits of gas sorption measurements, where only pores up to a certain size (usually considered up to ~ 100 nm for nitrogen sorption) are detectable by the techniques used for measurement.

However, for the model used in this work, the limit seems to be present at lower widths for pores open at both ends, as explored below.

As seen in Figure 5.13, wider pores open at both ends do not fill completely, hence, the limits present for these systems were explored in more detail. For this reason, behaviour of bulk fluid, introduced in Section 5.1, was compared to the presence of a single wall site. Figure 5.14a presents the dependence of fluid density on chemical potential for the two systems. It can be observed that there is a sharp increase in density at $\mu \sim -2.585$ for bulk fluid and this transition shifts towards $\mu \sim -2.88$ when a single wall site is present. This shift is caused by the external field contribution of the wall site, which acts as a seed for bulk fluid condensation. Without the external field contribution, the system has to reach a higher value of chemical potential in order to overcome the energy barrier for the phase transition.

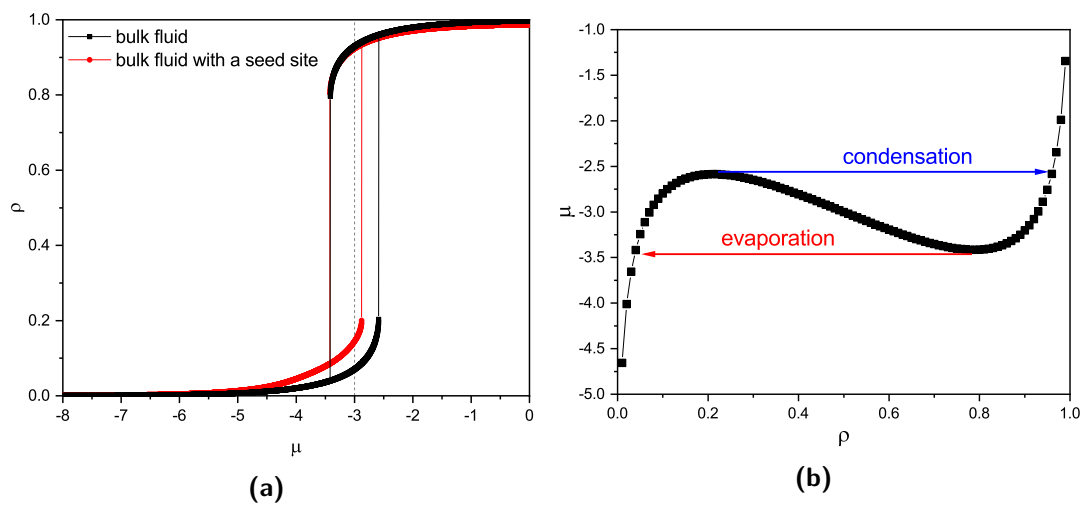


Figure 5.14 (a) Dependence of density (ρ) on chemical potential (μ) for condensation and evaporation of bulk fluid and fluid with a seed wall site, with the dashed line indicating $\mu = -3$ and (b) μ versus ρ calculated from Equation 5.18 with phase transitions shown

At equilibrium, the change in Helmholtz energy with density can be expressed using Equation 5.17. Using Equation 5.17 with Equation 5.3 gives Equation 5.18, which can be used to evaluate chemical potential corresponding to an average equilibrium bulk fluid density. Figure 5.14b presents the plot of Equation 5.18, for density values between 0 and 1. Comparing Figures 5.14a and 5.14b provides information about the μ values for bulk fluid condensation and evaporation by looking at the maximum, at lower density values, and the minimum, at higher values of ρ , in Figure 5.14b. It should be noted that in Figure 5.14b, the corresponding value of μ was calculated based on a changing value of ρ . However, for the simulations used in this work, the chemical potential of the system is set and the fluid density is calculated based on this value.

$$\frac{\partial F}{\partial \rho_i} = \mu \quad (5.17)$$

$$kT \ln \left(\frac{\rho_i}{1 - \rho_i} \right) - \epsilon \sum_a \rho_{i+a} + \phi_i = \mu \quad (5.18)$$

As the chemical potential increases, so does the fluid density. When $\mu = -2.585$ is reached, the bulk fluid system reaches the maximum seen in Figure 5.14b, at $\rho \sim 0.2$. Increase in μ above this value causes the fluid to condense, leading to a significant increase in the fluid density (from ~ 0.2 to ~ 0.9), as seen in Figure 5.14b. Further increase in μ above this value leads to the fluid density converging towards the value of 1. On the other hand, when the chemical potential is reduced, during desorption, the value of ρ decreases. In this case, when the value of $\mu = -3.5$ is reached, at $\rho \sim 0.2$, the bulk fluid undergoes a liquid-gas transition, leading to a marked decrease in system density, as observed in Figure 5.14a. The values of intermediate ρ values, in the region ~ 0.2 to ~ 0.8 , where the curve has a negative slope, are not stable, being between the values for gas and liquid phases.

Introducing a wall site, thus adding the external field contribution to the adjacent sites, leads to shifting of bulk filling to a lower value of μ . However, the presence of the external field does not impact the desorption behaviour. This behaviour is specific to pores open at both ends, where there is an energy barrier toward condensation of bulk fluid. As will be seen in the next sections, this is not the case for pores with only one end open, which are pores observed within the cluster structures presented in Chapter 4. It is also worth noting that in experimental gas sorption measurements, only relative pressure values below 1 are explored, in order to avoid bulk condensation of the used gas. Therefore, even though some of the pores with both ends open did not fill within the explored range of λ/λ_0 , values of μ until -3 are explored in this work, which are close to the condensation when a wall site is present, thus, mimicking experimental conditions.

5.6 Pores with one end open

In the previous section, only pores with both ends open to the bulk gas were considered. However, in real materials and cluster structures generated in Chapter 4, some pores have only one end open; therefore, these are compared here with pores with both ends open. A significant difference between these two types of pores is the presence of corner sites in the pores with one end open. These corner sites include interactions with two wall sites; thus, adsorbing gas onto these sites prior to monolayer formation in the whole pore [203].

Figure 5.15 presents a comparison of isotherms for pores, with one and both ends open for pore widths ranging from 2 to 8 lattice sites. It is evident that the hysteresis loops for pores with only one end open are much narrower than for the pores with both ends open. This is caused by the pore filling at lower values of λ/λ_0 due to the liquid meniscus already appearing at the bottom of the pore after monolayer formation. It is worth noting that pores with a width below 8 lattice sites empty at the same λ/λ_0 for both pore types, confirming that the desorption branch of the isotherm is more suitable for pore size analysis, since it

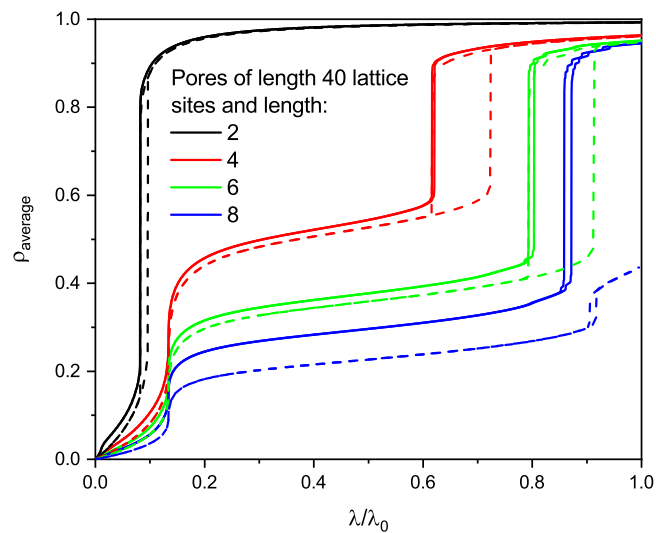


Figure 5.15 Sorption isotherms for model slit pores of length 40 lattice sites and varying pore width. Full lines are used for pores with one end open and dashed lines are used for pores with both ends open.

is more related to the size of a pore rather than its shape. The pores with width 8 lattice sites differ when one of the pore ends is closed, as the pore with both ends open does not fill at $\lambda/\lambda_0 = 1$, while its counterpart with only one end open has filled before reaching $\lambda/\lambda_0 = 1$. It should be noted that in real adsorbent materials, even the pore walls of open pores are not completely smooth, with certain level of roughness, with the surface defects acting as sites for preferential gas adsorption, similar to the corners in pores with one end open presented here [203–205].

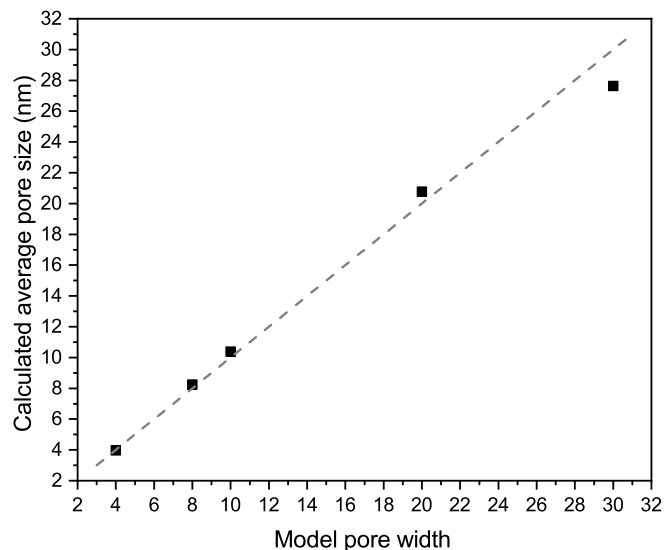


Figure 5.16 Correlation of calculated pore size and model pore width for pores with one end open and varying width

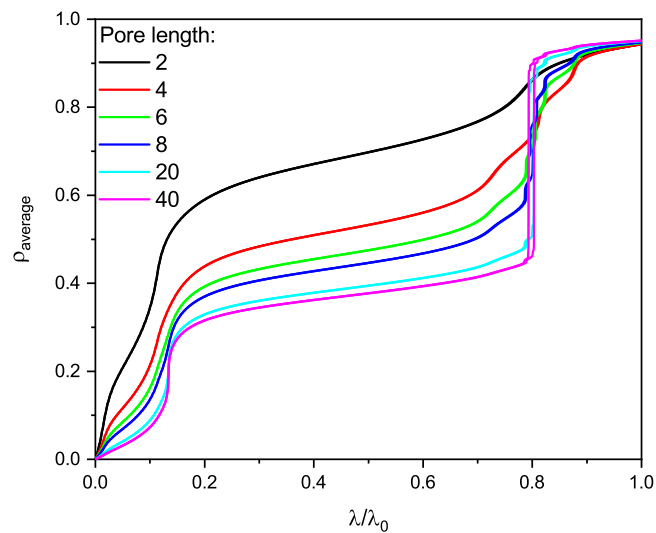


Figure 5.17 Sorption isotherms for model slit pores with one end open of width 6 lattice sites and varying pore length

Correlation of calculated pore sizes, using the peak position obtained by the method described in Section 5.3.2, and pore width in lattice sites for pores with one end open, due to these filling at $\lambda/\lambda_0 = 1$, are presented in Figure 5.16. It can be observed, that for pores up to width 20 lattice sites, the correlation between the two values is good. However, for a larger pore, 30 lattice sites wide, the calculated size deviates from the actual pore width. Therefore, there seems to be a limiting pore width for which the model can correctly predict the pore size. This may be due to the pores above 30 nm being at the upper end of the mesopore range, as per IUPAC classification [143].

The effect of length on the isotherm shape for pores with one end open, presented in Figure 5.17, is similar to the trend observed for pores with both ends open (Figure 5.12). Slits with length lower than 6 lattice sites are, again, not technically pores but are presented for comparison. It can be seen that for longer pores, pores with length 20 and 40 lattice sites in Figure 5.17, there is only a small influence of pore length on the isotherm shape, similar to pores with both ends open.

5.7 Pores with constant aspect ratio

Since some of the slits used in the previous sections, which did not fill after reaching $\lambda/\lambda_0 = 1$, hence did not fulfil the dimension requirements to be classified as pores, this section investigates pores with one end open and a fixed aspect ratio (width:length = 1:4). Keeping the ratio between the pore length and width fixed should ensure that even at higher values of pore width, the pore length is not a limiting factor. Calculated isotherms for pores with various width are presented in Figure 5.18. It can be observed, that for pore width 10 lattice sites, there is a single hysteresis loop at $\lambda/\lambda_0 \sim 0.9$, related to bulk of the pore filling and emptying. However, the larger pores (above width 10 lattice sites)

exhibit a smaller step at $\lambda/\lambda_0 \sim 0.9$, followed by a hysteresis loop associated with pore filling/emptying. This additional step is due to formation of additional adsorbed layer before the pore bulk fills.

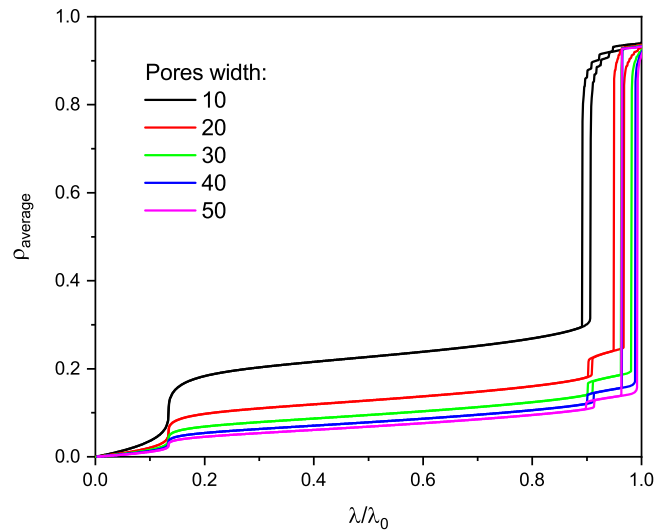


Figure 5.18 Sorption isotherms for pores with fixed aspect ratio (width:length = 1:4) and varying width

5.8 Multiple pores

In this section, model pores with one end open and varying widths, or lengths, were analysed in one simulation box as opposed to separately as before. These comparisons were performed in order to allow analysis of the shape of simulated gas sorption isotherms for a system with pores of different sizes present, as is the case for cluster structures, analysed in Section 5.10, as well as the majority of real samples of porous materials.

5.8.1 Varying pore width

Two combinatorial sets of model pores, with one end open and of different widths, were considered in this section. Their corresponding schematic representations are shown in Figure 5.19, with respective simulated gas sorption isotherms presented in Figure 5.20.

As can be seen from Figure 5.20, the simulated isotherms obtained for multiple pore systems, with pores of different widths, clearly show analogous hysteresis loops for component pores at the same values of relative activity λ/λ_0 , as for the individual respective pores. Due to the discrete pore sizes used in the lattice model, individual pore contributions to the overall sorption isotherm can be distinguished. In a real material, the pore sizes exhibit a polydispersity and differ in shape, leading to a distribution of pore sizes and a smoother sorption isotherm shape with less pronounced contributions from individual pores.

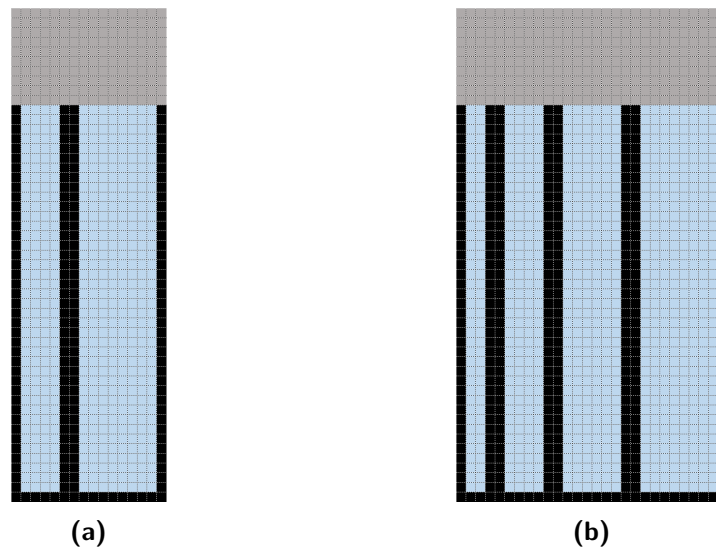


Figure 5.19 Multiple model pore systems with widths of (a) 4 and 8 lattice sites and (b) 2, 4, 6, and 8 lattice sites. Pore walls are represented in black, bulk gas in grey, and sites within the pore in blue.

5.8.2 Varying pore length

In Section 5.5.3, individual pores of different lengths were analysed. Here, two combined sets of pores of varying length were examined, with schematic representations presented in Figure 5.21, and the respective simulated gas sorption isotherms in Figure 5.22.

It can be seen, from Figure 5.22, that even though the isotherms differ slightly for individual pores, the combined isotherms do not explicitly show the contributions from individual pores. This, along with the findings presented above, suggests that the final isotherm shape is influenced much more by differing pore sizes rather than the length of these pores. This

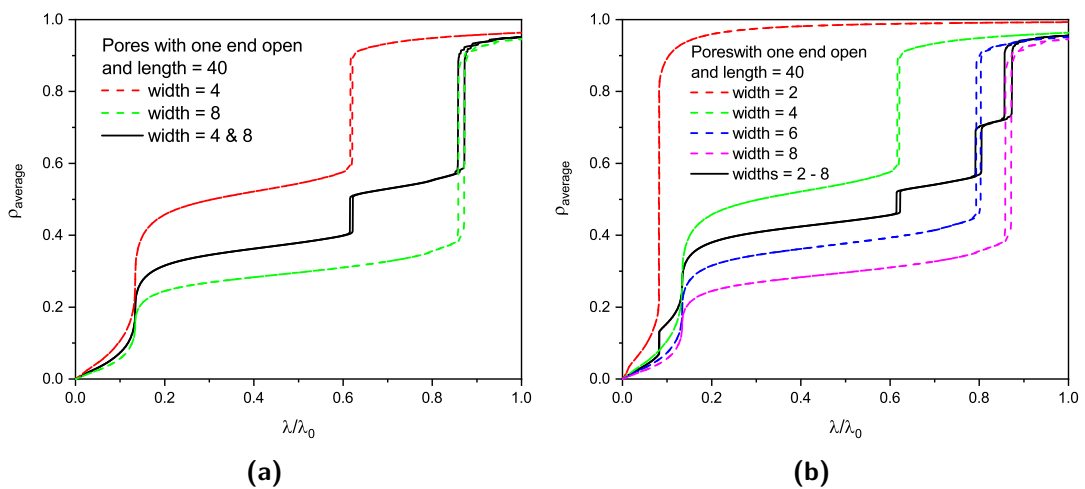


Figure 5.20 Sorption isotherms for individual and multiple model slit pores with widths of (a) 4 and 8 lattice sites and (b) 2, 4, 6, and 8 lattice sites. Dashed lines are used for individual pores and a solid line is used for combined multiple pore isotherms.

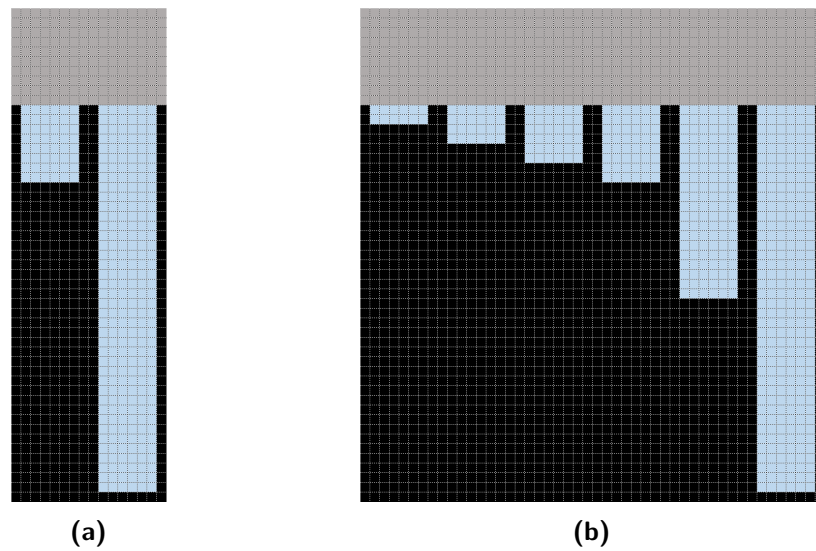


Figure 5.21 Multiple model pores with lengths of (a) 8 and 40 lattice sites and (b) 2, 4, 6, 8, 20 and 40 lattice sites. The pore walls are represented in black, bulk gas in grey, and the sites within the pore in blue.

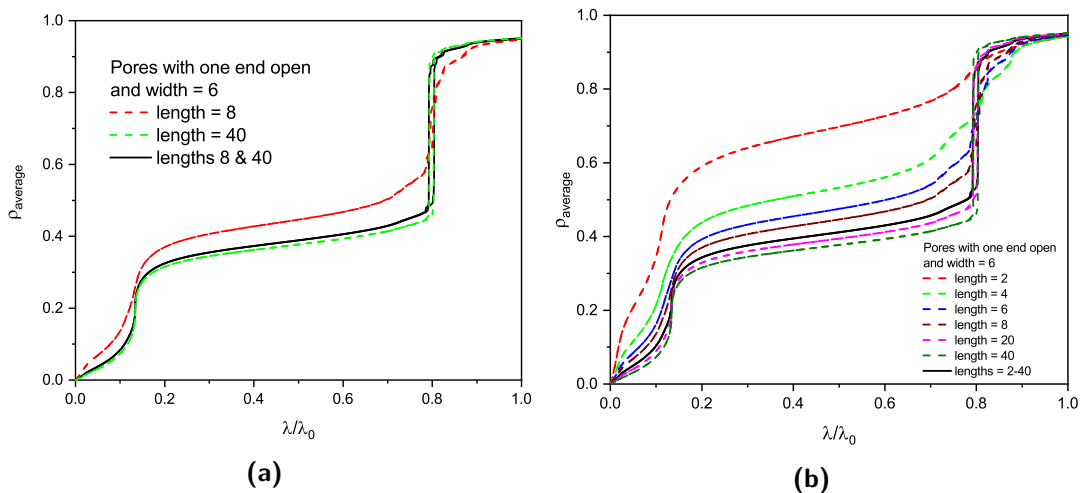


Figure 5.22 Sorption isotherms for individual and multiple combined model slit pores with lengths of (a) 8 and 40 lattice sites and (b) 2, 4, 6, 8, 20 and 40 lattice sites. Dashed lines are used for individual pores and a solid line is used for combined multiple pores.

agrees with the basis of BJH theory [148], where the surface area of pores being opened at a given pressure interval is calculated from an average pore width of these pores and the amount of gas desorbed, using an estimated average pore length.

5.9 Conical pores

When two circular clusters touch on a two-dimensional lattice, conical pores are formed at this point of contact. Therefore, gas sorption in conical pores, with different step sizes, was examined here, with their schematic representation in Figure 5.23.

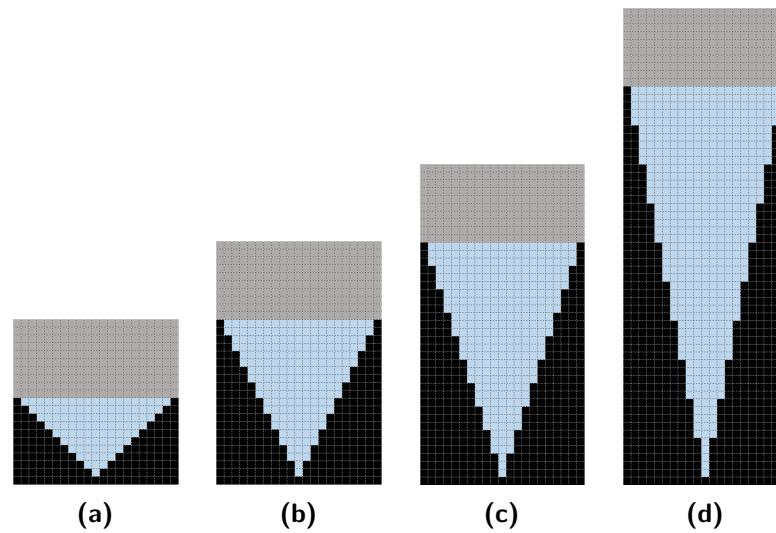


Figure 5.23 Model conical pores with width step sizes (a) 1, (b) 2, (c) 3, and (d) 5 lattice sites; pore walls are represented in black, bulk gas in grey, and sites within the pore in blue

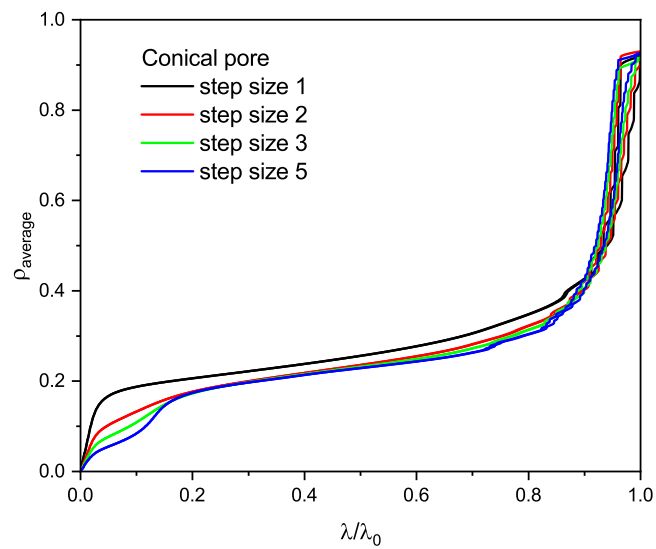


Figure 5.24 Sorption isotherms for conical pores with varying step size

From Figure 5.24, presenting the simulated sorption isotherms obtained for the aforementioned conical pores, it seems that the step size of a conical pore has an insignificant influence on the final shape of the gas sorption isotherm. This is most likely caused by the pores having the same widths at each step and only the length of each step differing. As was seen in Sections 5.5.3 and 5.8.2, the length of a pore does not have a major influence on the isotherm shape; thus, resulting in the isotherm not significantly affected by the step size of a conical pore. The hysteresis loop present at higher values of λ/λ_0 follows a step-wise filling and emptying of the conical pore sections with marked steps on both adsorption and desorption branches of the isotherms obtained via simulation.

5.10 Model cluster structures

Cluster structures, presented and discussed in Chapter 4, were analysed using the same calculations as for the model pores studied in previous sections. The average density was calculated based on the total lattice size (1000×1000 sites) in order to account for the lower degree of accessible porosity for structures generated with higher solids content. The threshold for density convergence was based, for calculations within this section, on local density changes rather than an average value for the whole lattice, in order to equilibrate filling or emptying of even small pores present in the structures and preventing their influence being masked by their larger counterparts.

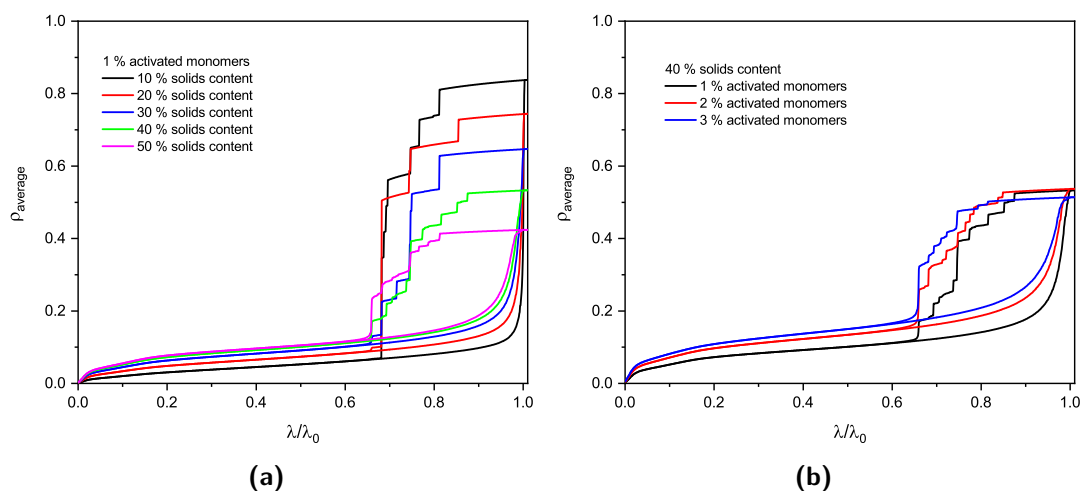


Figure 5.25 Simulated gas sorption isotherms for cluster structures with (a) 1 % activated monomers and varying solids content and (b) 40 % solids content and varying percentage of activated monomers

Example isotherms are presented in Figure 5.25, with the effect of varying S_C (solids content) observed in Figure 5.25a and the impact of changing C_C (percentage of activated monomers) in Figure 5.25b. Increasing the value of S_C results in lower adsorption capacity, derived from the highest point of adsorption isotherm, due to an increased amount of closed porosity, as well as a larger proportion of the lattice occupied by solid sites. Desorption branches of the isotherms for structures with higher values of S_C are also smoother, with less pronounced steps, suggesting a wider, more uniform, distribution of pore sizes compared to lower values of S_C , where significant drops can be observed, as a result of pores with distinguished sizes present. Figure 5.25b indicates that with increasing percentage of activated monomers, the pore structures empty at lower values of λ/λ_0 . This suggests a larger number of smaller pores are present in these structures, which was confirmed by calculating the pore size distribution for these materials, as shown in Section 5.10.1. Overall, all calculated isotherms exhibit a similar shape, and can be classified, according to the IUPAC specifications (discussed in Section 2.1.1), as Type IV isotherms with Type H2(b) hysteresis loops. This corresponds to mesoporous adsorbents with '*complex pore structures in which network effects are important*' [142].

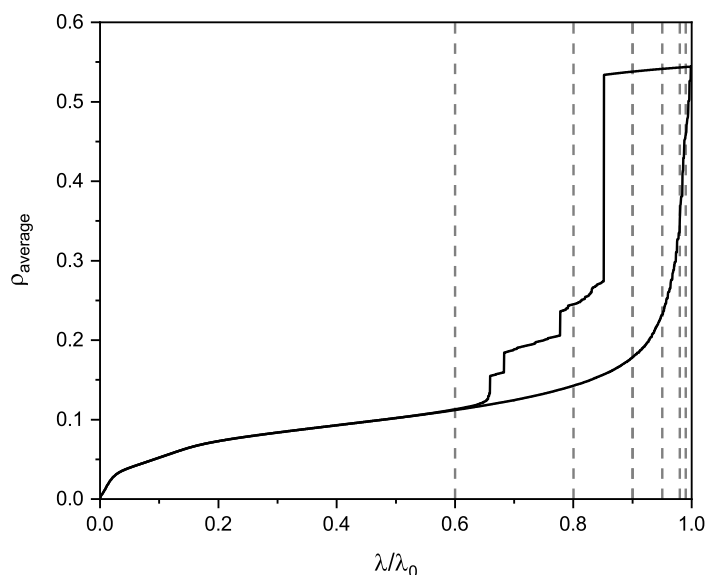


Figure 5.26 Calculated gas sorption isotherm for a cluster structure with $S_C = 40\%$ and $C_C = 1\%$ with grey dashed lines indicating values of λ/λ_0 0.6, 0.8, 0.9, 0.95, 0.98, and 0.99

In order to better understand the sorption processes in the complex cluster structures, pore filling and emptying for a structure with $S_C = 40\%$ and $C_C = 1\%$ was examined. The calculated isotherm, along with the values of λ/λ_0 at which the sorption was analysed, is presented in Figure 5.26 and the corresponding density distributions, for both adsorption and desorption, are shown in Figure 5.27. It can be observed from Figure 5.27 that as λ/λ_0 gradually increases, the pores are progressively filled during adsorption by condensed gas (red in Figure 5.27) via multilayer formation, similar to the model pores discussed above. Comparing this observation to the corresponding isotherm, presented in Figure 5.26, it can be observed that the average density, and thus adsorption, for adsorption branch successively increases, as a result of the aforementioned multilayer adsorption. Conversely, images for desorption branch above $\lambda/\lambda_0 = 0.8$ show the whole structure filled with condensed gas and only at $\lambda/\lambda_0 = 0.8$ large proportion of the accessible pores empties. This is due to the plateau present at λ/λ_0 above ~ 0.85 followed by a step decrease when large part of the pore structure empties in a narrow λ/λ_0 range.

5.10.1 Textural properties

Accessible surface area

Brunauer-Emmett-Teller (BET) theory [146] in conjunction with IUPAC recommendations [142], as discussed in Section 3.1.5, was applied to simulated gas sorption isotherms in order to obtain accessible surface areas of simulated cluster structures. Values for nitrogen gas adsorption were used; however, the resulting values of accessible surface area are reported in arbitrary units, as reported in Figure 5.28. It can be seen that the accessible surface area increases both with increasing solids content and percentage activated monomers within

the studied range of S_C . There was a sharp decrease in accessible surface area observed for cluster structures above S_C 50 % (not included here), caused by the presence of a large proportion of closed porosity. The observed decrease is more pronounced for structures with a higher percentage of activated monomers, as there is a larger number of smaller clusters present, which leads to a higher portion of closed pores in two dimensions.

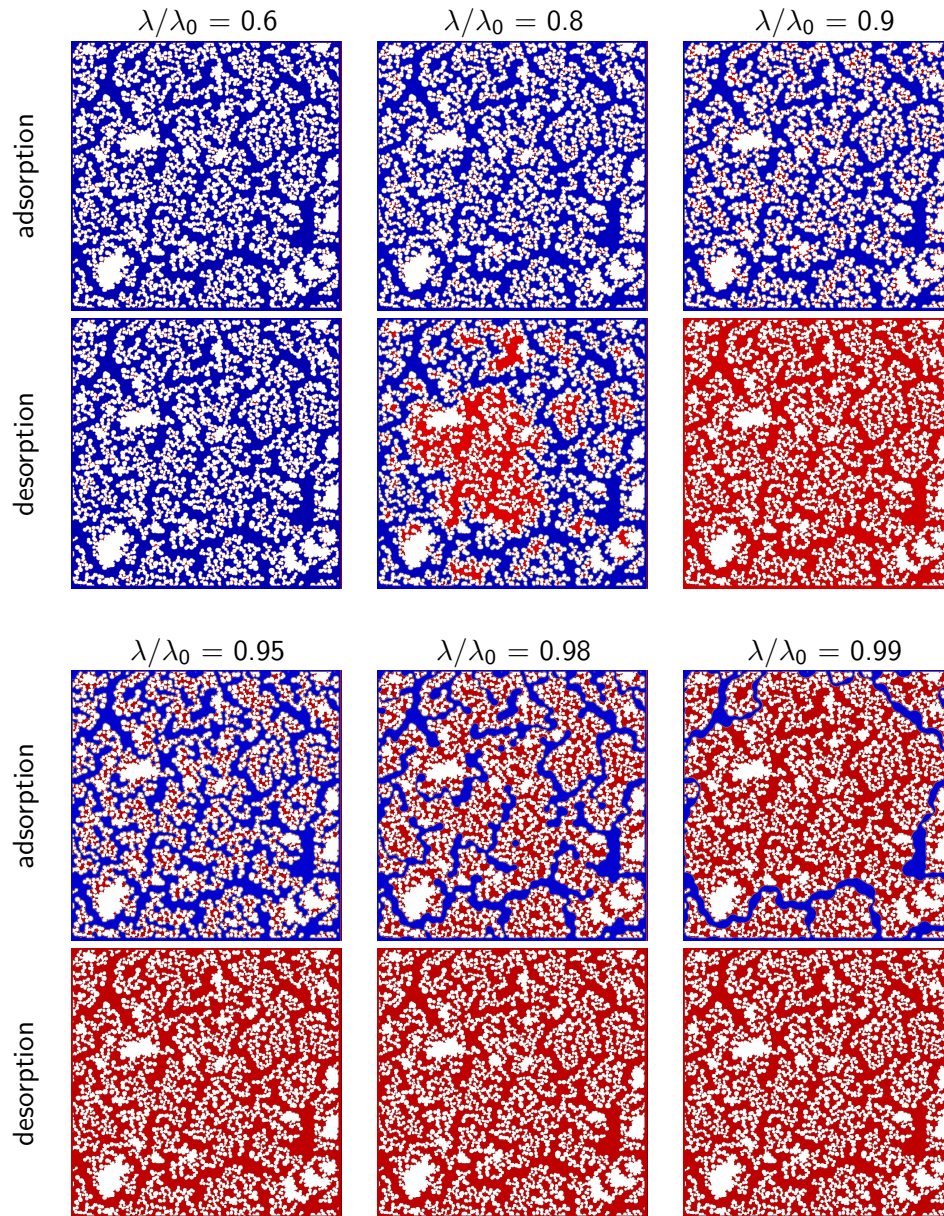


Figure 5.27 Density distribution for adsorption and desorption in a structure with $S_C = 40$ % and $C_C = 1$ % at varying values of λ/λ_0 . Cluster points and inaccessible pore areas are shown in white, gas sites in blue, and liquid sites in red.

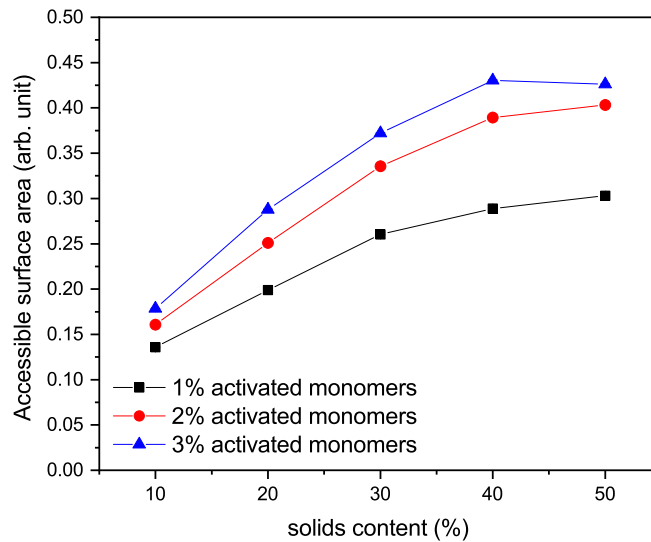


Figure 5.28 Accessible surface area versus solids content for simulated cluster structures with varying percentages of activated monomers

Pore size distribution

Simulated gas sorption isotherms, detailed in the previous section, were used to determine PSDs of the cluster structures. PSDs, extracted from desorption branches of isotherms presented in Figure 5.25, are shown in Figure 5.29 for structures with changing S_C (Figure 5.29a) and varying C_C (Figure 5.29b). Increasing the value of S_C , as presented in Figure 5.29a, results in only a small change in extracted PSD, with higher S_C structures containing a narrower distribution of smaller pores, due to more densely packed structures. Figure 5.29b shows that structures with a lower amount of activated monomers contain larger pores with a wider distribution of pore sizes compared to their counterparts with

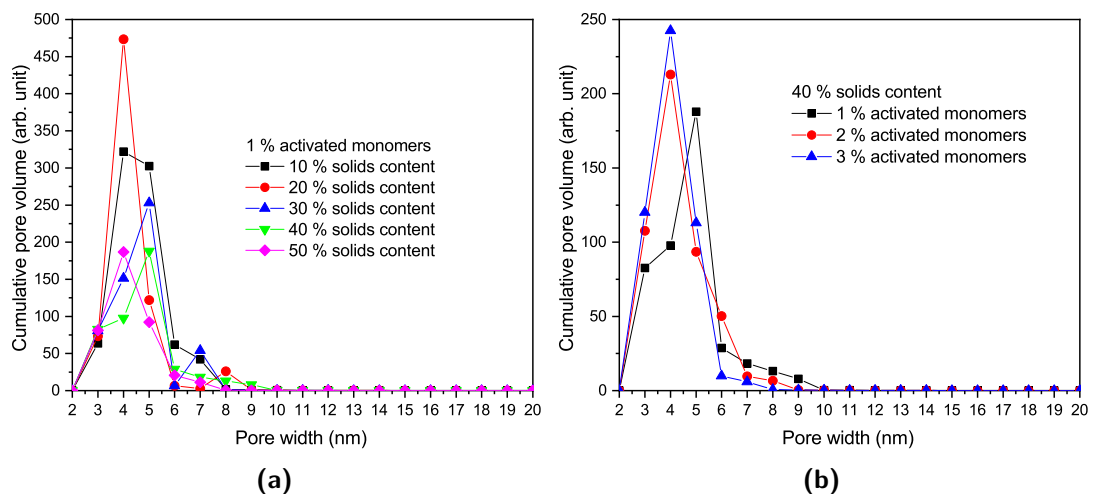


Figure 5.29 Calculated pore size distributions for cluster structures with (a) 1 % activated monomers and varying solids content and (b) 40 % solids content and varying percentages of activated monomers

higher levels of activated monomers. This observation is in agreement with experimental data obtained for xerogel structures, where materials with higher catalyst concentrations, therefore, higher percentages of activated monomers, exhibit smaller pores with narrower distributions of pore sizes.

5.11 Summary

Gas sorption modelling was explored in this chapter for model slit pores and cluster structures generated in the previous chapter, where model gas and liquid systems were studied for:

- (a) Dependence of grand potential of bulk model gas and liquid on chemical potential was explored and the corresponding dependencies were presented.
- (b) Gas adsorption onto a surface with monolayer coverage, followed by bulk condensation, was investigated with trends in grand potential of the layer adjacent to the surface discussed.

The main findings of this chapter are as follows:

1. Effect of temperature and interaction parameter:
 - (a) Deviating from the value of temperature $T^* = 1$, suggested in the work by Monson [177], caused undesirable change in isotherm shape, leading to unrealistic isotherm shapes. Increasing the value of T^* leads to a more gradual monolayer formation and a smaller hysteresis loop, while decreasing T^* results in occurrence of a hysteresis loop during monolayer formation and a lack of pore filling; thus, the value $T^* = 1$ was used for all subsequent calculations.
 - (b) Changing the ratio of fluid-solid to fluid-fluid interactions has a major impact on the monolayer formation and decreasing the parameter results in a shift of the monolayer formation towards higher values of λ/λ_0 , with the value of the parameter equal to 1 leading to an absence of pore filling at $\lambda/\lambda_0 = 1$. The value of the interaction parameter has a minor effect on the isotherm shape at higher λ/λ_0 values, except for $\frac{\epsilon_{\text{fluid-solid}}}{\epsilon_{\text{fluid-fluid}}} = 1$, as mentioned previously.
2. Pores with both ends open:
 - (a) Varying pore length has only a slight impact on the final isotherm shape, with longer pores giving almost identical isotherms. However, pore length has to be at least equal to the pore width in order for a pore filling to occur, in agreement with the IUPAC classification of a pore.
 - (b) Pore width has a significant influence on the isotherm shape, determining the position and presence of a hysteresis loop. However, the model is not capable of capturing adsorption in micropores due to the discrete nature of the lattice,

where a micropore width is formed only by two lattice sites, resulting in monolayer formation filling the pore. Increasing pore width leads to a hysteresis loop found at higher values of λ/λ_0 , although, increasing the width above a critical value leads to an absence of pore filling at $\lambda/\lambda_0 = 1$.

3. Pores with one end open:

- (a) Compared to their counterparts with both ends open, pores with only one end open, tend to fill at lower values of λ/λ_0 leading to narrower hysteresis loops. Still, the pore emptying occurs for both pore types at the same value of λ/λ_0 , if both pores were filled at $\lambda/\lambda_0 = 1$.
- (b) Due to the presence of the corner sites, acting as preferential adsorption sites, pore filling occurs at lower values of λ/λ_0 , resulting in pore filling for wider pores, compared to pores with both ends open.
- (c) Similar trends for pore length and width, as for pores with both ends open, were observed.
- (d) Good agreement is observed between the pore widths extracted from simulated isotherms and lattice width of the model slit pores, up to width 30 lattice sites, which is close to the upper size limit for mesopores.

4. Conical pores:

- (a) Conical pores, found at the contact of two circular clusters, give similar isotherms regardless of the step size. Due to the pore shape, the pore filling and emptying is observed in a step-wise manner.

5. Pores with constant aspect ratio:

- (a) Keeping the same ratio of width to length resulted in all the investigated pores to fill before $\lambda/\lambda_0 = 1$, removing the pore length as a limiting factor for wider pores.

6. Multiple pores:

- (a) System with multiple pores of different width gives isotherms with distinguished hysteresis loops, corresponding to each pore present, allowing determination of pore sizes from the calculated gas sorption isotherms.
- (b) In agreement with the observation for the influence of pore length on the isotherm shape for individual pores, a system with pores with varying length exhibits a very similar isotherm, regardless of the lengths of the pores present.

7. Cluster structures:

- (a) Gradual filling of porosity for the cluster structures generated in Chapter 4 and emptying related to the size of the pores present, along with a complex pore structure, leads to Type IV isotherms with Type H2(b) hysteresis loops, according to the IUPAC classification [142], corresponding to the presence of mesopores and a complex pore structure.
- (b) Increasing solids content leads to a higher degree of closed porosity, and thus, lower adsorption capacity. Furthermore, pore size distributions are more uniform for structures with higher S_C .
- (c) Pores within structures with higher C_C empty at lower values of λ/λ_0 , suggesting more smaller pores present, in agreement with the extracted pore size distributions.
- (d) Increasing both S_C and C_C leads to higher values of accessible surface area, with a plateau observed at higher S_C . Increase of accessible surface area with percentage of activated monomers, corresponding to catalyst concentration, agrees with the trends observed experimentally, in Chapter 3.

Chapter 6

Conclusions

RF gels seem to be promising candidates for applications as porous organic materials, finding use as replacements for materials currently used in these areas, or even in novel applications. However, an important factor determining the usefulness of RF gels for a particular application, as supported by review of relevant literature, is tailoring textural properties of the final materials by varying processing conditions. Therefore, this study focussed on an investigation of the impact of processing parameters on textural properties of RF gels, the development of a computational model mimicking the growth of structures similar to those observed experimentally, and their subsequent analysis. Since textural properties of experimental samples are usually assessed using gas sorption measurements, modelling of gas sorption within model pores, and generated cluster structures, was explored here as well.

As was observed in this study, processing parameters have a significant impact on the final textural properties of RF gel materials. The presence of sodium carbonate, the most commonly used catalyst salt, is one of the most influencing parameters, with low R/C ratios (higher catalyst concentration) resulting in small RF particles accompanied by smaller pores in the dried materials, whereas higher R/C ratios lead to increased pore volumes and average pore sizes, while decreasing accessible surface areas. The presence of sodium carbonate was found to be crucial in order to obtain a viable gel structure and materials prepared using low catalyst concentrations were found to have inferior mechanical properties associated with notable material shrinkage during drying.

A thorough exchange of water trapped within the RF hydrogel pores is important to minimise material shrinkage during subcritical drying, as used within this study. It was found within this work that increasing the amount of acetone used for solvent exchange in one dose leads to a slight enhancement of textural properties; however, splitting the same volume of acetone over the solvent exchange period improved the properties significantly, especially

for samples with lower R/C ratios, where additional sample manipulation likely reduced structural damage owing to their superior mechanical properties.

A reduction of processing temperature, used to obtain the final materials, would provide notable savings at industrial scale for RF gel manufacture. However, temperature has a significant influence on chemical and physical processes, with the formation of RF gels being no exception. Higher reaction temperatures lead to improved cross-linking between RF clusters and, thus, enhanced mechanical properties and reduced shrinkage, with at least 55 °C required in order to obtain a viable gel. However, plateauing of textural properties at higher temperatures was observed, suggesting the presence of an optimal temperature range offering desirable energy savings, while retaining sufficient performance of the final materials. Vacuum drying was found to preserve the porous structure of RF xerogels more efficiently, compared to drying at ambient pressure; however, if the material requirements are not too strict, ambient drying could be used at an industrial scale, as a cheaper alternative to vacuum drying.

Presence of sodium carbonate in the reaction solution was observed to be necessary in order to obtain a porous RF xerogel material. Previous study has confirmed that a metal ion is required in the solution, in addition to the hydrolysing anion from the catalyst salt that adjusts solution pH to an appropriate value. However, it was found, in this study, that the type of anion has an impact on gelation processes and, thus, the final material properties as well. Replacing a proportion of sodium carbonate with sodium sulphate or sodium chloride led to trends similar to those observed for increasing R/C ratio. This effect is most likely caused by different ions influencing salting-out of the growing RF clusters in the reaction solution, presumably without significantly altering the solution pH or RF gelation chemistry.

A computational model was developed in this work in order to model aggregation and growth of RF clusters. The lattice-based kinetic Monte Carlo model, set up in two dimensions with periodic boundary conditions, was developed on the basis of experimental evidence from literature. In order to mimic experimentally observed structures, compact, approximately circular, clusters were grown during simulations with the diffusion probability inversely proportional to species size. The first version of the model implemented static clusters; however, these did not fully represent experimental observations. Thus, cluster diffusion was included, resulting in more realistic cluster structures.

Increasing solids content (S_C) at the same percentage of activated monomers (C_C) resulted in a higher number of clusters, without significantly affecting their size, while increasing C_C at fixed S_C led to smaller particles and more spanning structures. This was reflected in observations for textural properties of the generated structures, where increasing both S_C and C_C caused a higher degree of closed porosity, yet, a percolated pore structure was retained up to $S_C \sim 50\%$. Due to the aforementioned effects, the number of accessible surface sites per unit mass increased with increased C_C but the opposite trend was observed for increased S_C .

The correlation dimension, reflecting structure complexity, was found to increase with increasing both S_C and C_C with a plateau observed at value 2.0 for higher S_C . The Hurst exponent, evaluated from both diffusion of Brownian walkers and simulated solvent exchange, exhibited opposite trends compared to correlation dimension, indicating a more tortuous pore structure at higher values of S_C and C_C .

In order to compare the generated cluster structures with trends observed in experimental RF gel samples, adsorption modelling was investigated in this work as well. Model liquid and gas, followed by model pores, were studied initially, in order to deepen the understanding of the applied model, and allow better interpretation of calculated gas sorption isotherms for cluster structures. Validity of the chosen values of model parameters (temperature, and ratio of fluid-solid to fluid-fluid interactions), suggested in a previous study, was confirmed and used for all subsequent calculations. The observations for varying model pore dimensions agree with the background theory, and the model could be used to distinguish multiple pores with varying width within the same simulation. Finally, an investigation of gas sorption using generated cluster structures supported trends observed for textural properties obtained above, for both cluster structures and experimental samples and isotherm shape, suggested the presence of complex mesopore structures.

Varying RF gel manufacturing conditions allows tuning of their final structure, giving the potential for tailoring of desired properties to a particular application. The diversity of materials, obtained by changing the processing conditions, makes RF gels a promising candidate for applications as porous materials in areas such as materials for catalyst support, gas separation and storage, insulation, porous electrodes, and water treatment. By understanding how different process variables influence the final materials, it should be possible to develop materials that are better suited for their current applications as well as potentially new applications.

Developing models that aid the exploration of formation and properties of porous materials is an important way to control high-performance materials. Different applications require varying textural properties. For example, adsorption materials benefit from high accessible surface areas with Brownian-like diffusion within the pore structure, found for structures generated with lower solids contents and higher catalyst concentration. On the other hand, drug release applications, require increased tortuosity of pore areas, observed for lower catalyst concentration and higher solids contents in this work, in order to reduce out-diffusion of the drug.

Chapter 7

Future work

Based on the observations made within this work, it would be beneficial to explore particular areas in further detail in future research. Such additional works could not be included in the current study due to the timeframe of the project, however, they are outlined below for consideration.

As observed in Section 3.2.5, the presence of other anions, in addition to carbonate (CO_3^{2-}), can have a major impact on final material properties. The effects of chloride (Cl^-) and sulphate (SO_4^{2-}) ions were partially explored in Section 3.2.5; however, it would be interesting to compare the results from this work with RF gels prepared using ions that are listed at the opposite end of the Hofmeister series, such as thiocyanate (SCN^-) and perchlorate (ClO_4^-) anions, or even different combinations of anions; thereby exploring the impact that anions have on the gelation processes of RF gels.

The solvent exchange simulations, presented in Section 4.4, allowed evaluation of the Hurst exponent of the porous structure for generated cluster structures. Performing corresponding experiments for RF gels could provide related information about the samples, allowing fractal analysis of the adsorbent pore structure. In order to retain solvent diffusion in one dimension, as for the simulations, a flat piece of an RF gel could be placed in a container, as presented in Figure 7.1. The gel sample could be either surrounded from both sides by a selected solvent (e.g. acetone in both parts A and B) or with the solvent on one side and water on the other side (e.g. water in part A and solvent in part B). The progress of solvent

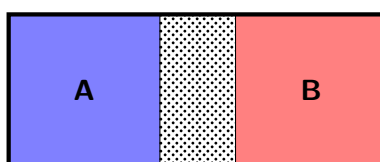


Figure 7.1 Schematic drawing of experimental setup for solvent exchange analysis with a gel sample (dotted) separating two parts of the vessel

exchange could be monitored by evaluating the concentration of one of the species in either compartment.

A set of further developments of the model proposed in this work could be also explored. The current version of the model used to generate cluster structures, presented in Section 4.1.1, uses a 100 % probability of clusters adhering to each other upon collision. However, in order to explore a wider range of structures, a probability term could be introduced into the algorithm. This term would be related to the inter-cluster cross-linking efficiency and could be related to temperature in a real system.

An obvious advancement of the model used to generate cluster structures, discussed in Chapter 4, is the introduction of a third dimension in order to make the structures more relevant to those observed experimentally. However, the additional dimension would lead to more extensive requirements for computational resources. This could be potentially mitigated by changing the model to an off-lattice version, where the empty lattice sites would not take up memory unnecessarily, and the requirements would be only a result of the number of species in the simulation, rather than lattice size. It is worth noting that all of the subroutines developed in this work would need to be adapted to account for this change. Another reason that the model described in this work was developed in two dimensions is the relative ease of graphical representation and analysis of the processes, which would be more challenging for a three-dimensional system.

Another addition to the model presented in this study could be the inclusion of cluster aggregate rotation into the model. Currently, only translational moves are allowed, without any structure rotation. However, adding rotational moves to the algorithm could allow exploration of a wider variety of final structures. It would also result in a model that is closer to the real system, where RF cluster aggregates rotate freely in the aqueous reaction solution, in addition to their translational movement.

A further potential extension to the model presented in this work, could be the implementation of ageing of necks formed between clusters in aggregates. This would mimic structure development at later stages of gelation, and could be undertaken, for example, by moving selected cluster sites, with the least amount of neighbouring cluster sites, to positions with a higher number of these neighbours.

Exploring the stability of the transition complex of a resorcinol anion, methanediol, and a metal cation in an aqueous solution, as proposed in Section 1.2.2 (Figure 1.11), using computational methods, could shed more light on the role of the metal cation, contributed by the catalyst salt, in the gelation processes of RF gels. It was shown in Chapter 3 that the presence of a metal ion was necessary in order to obtain a porous material but more research is required in order to understand its purpose. The understanding of the metal ion role in the RF gelation process could lead to improved tailorability of these materials.

References

- [1] A. G. Whitham and R. S. J. Sparks, "Pumice," *Bulletin of Volcanology*, vol. 48, pp. 209–223, aug 1986.
- [2] D. z. Çifçi and S. Meriç, "A review on pumice for water and wastewater treatment," *Desalination and Water Treatment*, vol. 57, pp. 18131–18143, aug 2016.
- [3] MPF, "File:Teidepumice.jpg - Wikimedia Commons," 2006.
- [4] D. Monniaux, "File:Cork p1160013.jpg - Wikimedia Commons," 2007.
- [5] S. Amorim, Corticeira and SGPS, "Annual Report and Accounts," tech. rep., Amorim Corticeira, 2012.
- [6] A. M. Pintor, C. I. Ferreira, J. C. Pereira, P. Correia, S. P. Silva, V. J. Vilar, C. M. Botelho, and R. A. Boaventura, "Use of cork powder and granules for the adsorption of pollutants: A review," *Water Research*, vol. 46, pp. 3152–3166, jun 2012.
- [7] H. Pereira, "The Rationale behind Cork Properties: A Review of Structure and Chemistry," *BioResources*, vol. 10, pp. 6207–6229, jul 2015.
- [8] S. Schiavoni, F. D'Alessandro, F. Bianchi, and F. Asdrubali, "Insulation materials for the building sector: A review and comparative analysis," *Renewable and Sustainable Energy Reviews*, vol. 62, pp. 988–1011, sep 2016.
- [9] M. O. Adebajo, R. L. Frost, J. T. Klopogge, O. Carmody, and S. Kokot, "Porous Materials for Oil Spill Cleanup: A Review of Synthesis and Absorbing Properties," tech. rep., 2003.
- [10] P. Liu, G. Chen, P. Liu, and G. Chen, "Application of Porous Metals," *Porous Materials*, pp. 113–188, jan 2014.
- [11] K. Nishiyabu, S. Matsuzaki, K. Okubo, M. Ishida, and S. Tanaka, "Porous Graded Materials by Stacked Metal Powder Hot-Press Moulding," *Materials Science Forum*, vol. 492-493, pp. 765–770, aug 2005.
- [12] A. Markaki, V. Gergely, A. Cockburn, and T. Clyne, "Production of a highly porous material by liquid phase sintering of short ferritic stainless steel fibres and a preliminary study of its mechanical behaviour," *Composites Science and Technology*, vol. 63, pp. 2345–2351, dec 2003.
- [13] J. Banhart, "Manufacture, characterisation and application of cellular metals and metal foams," *Progress in Materials Science*, vol. 46, pp. 559–632, jan 2001.
- [14] V. Shapovalov and L. Boyko, "Gasar—A new Class of Porous Materials," *Advanced Engineering Materials*, vol. 6, pp. 407–410, jun 2004.

- [15] H. Furukawa, K. E. Cordova, M. O’Keeffe, and O. M. Yaghi, “The chemistry and applications of metal-organic frameworks,” 2013.
- [16] H. B. Wu and X. W. D. Lou, “Metal-organic frameworks and their derived materials for electrochemical energy storage and conversion: Promises and challenges,” *Science Advances*, vol. 3, p. eaap9252, dec 2017.
- [17] O. K. Farha, I. Eryazici, N. C. Jeong, B. G. Hauser, C. E. Wilmer, A. A. Sarjeant, R. Q. Snurr, S. T. Nguyen, A. Ö. Yazaydin, and J. T. Hupp, “Metal–Organic Framework Materials with Ultrahigh Surface Areas: Is the Sky the Limit?,” *Journal of the American Chemical Society*, vol. 134, pp. 15016–15021, sep 2012.
- [18] H. Furukawa, Y. B. Go, N. Ko, Y. K. Park, F. J. Uribe-Romo, J. Kim, M. O’Keeffe, and O. M. Yaghi, “Isorecticular Expansion of Metal–Organic Frameworks with Triangular and Square Building Units and the Lowest Calculated Density for Porous Crystals,” *Inorganic Chemistry*, vol. 50, pp. 9147–9152, sep 2011.
- [19] K. Vikrant, V. Kumar, K.-H. Kim, and D. Kukkar, “Metal–organic frameworks (MOFs): potential and challenges for capture and abatement of ammonia,” *Journal of Materials Chemistry A*, vol. 5, pp. 22877–22896, nov 2017.
- [20] L. Huang, W. Guo, P. Deng, Z. Xue, and Q. Li, “Investigation of Synthesizing MCM-41/ZSM-5 Composites,” 2000.
- [21] N. Moreno, X. Querol, C. Ayora, C. F. Pereira, and M. Janssen-Jurkovicová, “Utilization of zeolites synthesized from coal fly ash for the purification of acid mine waters,” *Environmental Science and Technology*, vol. 35, no. 17, pp. 3526–3534, 2001.
- [22] E. Álvarez-Ayuso, A. García-Sánchez, and X. Querol, “Purification of metal electroplating waste waters using zeolites,” *Water Research*, vol. 37, pp. 4855–4862, dec 2003.
- [23] Z. Lai, G. Bonilla, I. Diaz, J. G. Nery, K. Sujaoti, M. A. Amat, E. Kokkoli, O. Terasaki, R. W. Thompson, M. Tsapatsis, and D. G. Vlachos, “Microstructural Optimization of a Zeolite Membrane for Organic Vapor Separation,” *SCIENCE*, vol. 300, no. 5618, pp. 456–460, 2003.
- [24] S. R. Venna and M. A. Carreon, “Highly permeable zeolite imidazolate framework-8 membranes for CO₂/CH₄ separation,” *Journal of the American Chemical Society*, vol. 132, pp. 76–78, jan 2010.
- [25] Z. Liang, M. Marshall, and A. L. Chaffee, “CO₂ adsorption-based separation by metal organic framework (Cu-BTC) versus zeolite (13X),” *Energy and Fuels*, vol. 23, pp. 2785–2789, may 2009.
- [26] I. Solmuş, C. Yamali, B. Kaftanoğlu, D. Baker, and A. Çağlar, “Adsorption properties of a natural zeolite-water pair for use in adsorption cooling cycles,” *Applied Energy*, vol. 87, pp. 2062–2067, jun 2010.
- [27] G. Gnana kumar, “Zeolites and Composites,” in *Nanomaterials and Nanocomposites*, pp. 187–222, Weinheim, Germany: Wiley-VCH Verlag GmbH & Co. KGaA, apr 2016.
- [28] P. Liu, G. Chen, P. Liu, and G. Chen, “Fabricating Porous Ceramics,” *Porous Materials*, pp. 221–302, jan 2014.
- [29] P. Liu, G. Chen, P. Liu, and G. Chen, “Applications of Porous Ceramics,” *Porous Materials*, pp. 303–344, jan 2014.
- [30] S. S. Kistler, “Coherent Expanded Aerogels,” *The Journal of Physical Chemistry*, vol. 36, no. 1, pp. 52–64, 1932.

- [31] A. Soleimani Dorcheh and M. H. Abbasi, "Silica aerogel; synthesis, properties and characterization," apr 2008.
- [32] H. Maleki, L. Durães, and A. Portugal, "An overview on silica aerogels synthesis and different mechanical reinforcing strategies," *Journal of Non-Crystalline Solids*, vol. 385, pp. 55–74, feb 2014.
- [33] A. Dąbrowski, P. Podkościelny, Z. Hubicki, and M. Barczak, "Adsorption of phenolic compounds by activated carbon—a critical review," *Chemosphere*, vol. 58, pp. 1049–1070, feb 2005.
- [34] O. Ioannidou and A. Zabaniotou, "Agricultural residues as precursors for activated carbon production—A review," *Renewable and Sustainable Energy Reviews*, vol. 11, pp. 1966–2005, dec 2007.
- [35] N. N. D. M.A. Tadda, A. Ahsan, A. Shitu, M. ElSergany, T. Arunkumar, Bipin Jose, M. Abdur Razzaque, "A review on activated carbon: process, application and prospects," *Journal of Advanced Civil Engineering Practice and Research*, vol. 2, no. 1, pp. 1–13, 2016.
- [36] A. M. Papadopoulos, "State of the art in thermal insulation materials and aims for future developments," *Energy and Buildings*, vol. 37, no. 1, pp. 77–86, 2005.
- [37] O. Kaynakli, "A review of the economical and optimum thermal insulation thickness for building applications," *Renewable and Sustainable Energy Reviews*, vol. 16, pp. 415–425, jan 2012.
- [38] H. Zhang, W. Z. Fang, Y. M. Li, and W. Q. Tao, "Experimental study of the thermal conductivity of polyurethane foams," *Applied Thermal Engineering*, vol. 115, pp. 528–538, mar 2017.
- [39] L. H. Baekeland, "The Synthesis, Constitution, and Uses of Bakelite.," *Industrial & Engineering Chemistry*, vol. 1, no. 3, pp. 149–161, 1909.
- [40] M. G. Looney and D. H. Solomon, "The chemistry of novolac resins. I. A review on the use of models," *Australian Journal of Chemistry*, vol. 48, no. 2, pp. 323–331, 1995.
- [41] A. M. Motawie and E. M. Sadek, "Adhesives and coatings from phenolformaldehyde/resorcinol-formaldehyde resins," *Polymers for Advanced Technologies*, vol. 9, pp. 837–843, dec 1998.
- [42] N. Li, Q. Zhang, J. Liu, J. Joo, A. Lee, Y. Gan, and Y. Yin, "Sol-gel coating of inorganic nanostructures with resorcinol-formaldehyde resin," *Chemical Communications*, vol. 49, pp. 5135–5137, may 2013.
- [43] A. C. Adiguzel Zengin, M. Crudu, S. S. Maier, V. Deselnicu, L. Albu, G. Gulumser, B. O. Bitlisli, B. Basaran, and M. M. Mutlu, "Eco-leather: Chromium-free Leather Production Using Titanium, Oligomeric Melamine-Formaldehyde Resin, and Resorcinol Tanning Agents and the Properties of the Resulting Leathers," *Ekoloji*, vol. 21, no. 82, pp. 17–25, 2012.
- [44] E. Scopelitis and A. Pizzi, "Urea-resorcinol-formaldehyde adhesives of low resorcinol content," *Journal of Applied Polymer Science*, vol. 48, pp. 2135–2146, jun 1993.
- [45] L. Muszyn, F. Wang, and S. M. Shalert, "Short-Term Creep Tests on Phenol-Resorcinol-Formaldehyde (Prf) Resin Undergoing Moisture Content Changes," *Wood and Fiber Science*, vol. 34, pp. 612–624, oct 2002.

- [46] S.-i. Tohmura, K. Miyamoto, and A. Inoue, "Acetaldehyde emission from glued-laminated timber using phenol-resorcinol-formaldehyde resin adhesives with addition of ethanol," *Journal of Wood Science*, vol. 51, pp. 421–423, aug 2005.
- [47] R. W. Pekala, "Organic Aerogels from the Polycondensation of Resorcinol with Formaldehyde," *Journal of Materials Science*, vol. 24, no. 9, pp. 3221–3227, 1989.
- [48] D. W. Schaefer, R. Pekala, and G. Beaucage, "Origin of Porosity in Resorcinol Formaldehyde Aerogels," *Journal of Non-Crystalline Solids*, vol. 186, pp. 159–167, 1995.
- [49] S. M. Lambert, G. E. Overturf, G. Wilemski, S. A. Letts, D. SchroenCarey, and R. C. Cook, "Fabrication of low-density foam shells from resorcinol-formaldehyde aerogel," *Journal of Applied Polymer Science*, vol. 65, no. 11, pp. 2111–2122, 1997.
- [50] H. Tamon, H. Ishizaka, M. Mikami, and M. Okazaki, "Porous structure of organic and carbon aerogels synthesized by sol-gel polycondensation of resorcinol with formaldehyde," *Carbon*, vol. 35, no. 6, pp. 791–796, 1997.
- [51] H. Tamon and H. Ishizaka, "SAXS Study on Gelation Process in Preparation of Resorcinol-Formaldehyde Aerogel," *Journal of Colloid and Interface Science*, vol. 206, no. 2, pp. 577–582, 1998.
- [52] H. Tamon and H. Ishizaka, "Influence of gelation temperature and catalysts on the mesoporous structure of resorcinol-formaldehyde aerogels," *Journal of Colloid and Interface Science*, vol. 223, no. 2, pp. 305–307, 2000.
- [53] F. Despetis, K. Barral, L. Kocon, and J. Phalippou, "Effect of aging on mechanical properties of resorcinol-formaldehyde gels," *Journal of Sol-Gel Science and Technology*, vol. 19, no. 1-3, pp. 829–831, 2000.
- [54] T. Yamamoto, T. Nishimura, T. Suzuki, and H. Tamon, "Effect of drying method on mesoporosity of resorcinol-formaldehyde drygel and carbon gel," *Drying Technology*, vol. 19, pp. 1319–1333, jul 2001.
- [55] S. A. Al-Muhtaseb and J. A. Ritter, "Preparation and properties of resorcinol-formaldehyde organic and carbon gels," *Advanced Materials*, vol. 15, no. 2, pp. 101–114, 2003.
- [56] N. Job, F. Panariello, J. Marien, M. Crine, J.-P. P. Pirard, and A. Léonard, "Synthesis optimization of organic xerogels produced from convective air-drying of resorcinol-formaldehyde gels," *Journal of Non-Crystalline Solids*, vol. 352, pp. 24–34, jan 2006.
- [57] A. M. ElKhatat and S. A. Al-Muhtaseb, "Advances in Tailoring Resorcinol-Formaldehyde Organic and Carbon Gels," *Advanced Materials*, vol. 23, no. 26, pp. 2887–2903, 2011.
- [58] M. Alshrah, L. H. Mark, C. Zhao, H. E. Naguib, and C. B. Park, "Nanostructure to thermal property relationship of resorcinol formaldehyde aerogels using the fractal technique," *Nanoscale*, vol. 10, no. 22, pp. 10564–10575, 2018.
- [59] C. Lin and J. A. Ritter, "Effect of synthesis pH on the structure of carbon xerogels," *Carbon*, vol. 35, no. 9, pp. 1271–1278, 1997.
- [60] V. Bock, A. Emmerling, and J. Fricke, "Influence of monomer and catalyst concentration on RF and carbon aerogel structure," *Journal of Non-Crystalline Solids*, vol. 225, no. 1-3, pp. 69–73, 1998.

- [61] R. Pekala, J. Farmer, C. Alviso, T. Tran, S. Mayer, J. Miller, and B. Dunn, "Carbon aerogels for electrochemical applications," *Journal of Non-Crystalline Solids*, vol. 225, pp. 74–80, apr 1998.
- [62] T. Yamamoto, T. Nishimura, T. Suzuki, and H. Tamon, "Control of mesoporosity of carbon gels prepared by sol-gel polycondensation and freeze drying," *Journal of Non-Crystalline Solids*, vol. 288, pp. 46–55, aug 2001.
- [63] N. Job, R. Pirard, J. Marien, and J. P. Pirard, "Porous carbon xerogels with texture tailored by pH control during sol-gel process," *Carbon*, vol. 42, no. 3, pp. 619–628, 2004.
- [64] N. Job, A. Théry, R. Pirard, J. Marien, L. Kocon, J. N. Rouzaud, F. Béguin, and J. P. Pirard, "Carbon aerogels, cryogels and xerogels: Influence of the drying method on the textural properties of porous carbon materials," *Carbon*, vol. 43, pp. 2481–2494, oct 2005.
- [65] N. Job, J. Marie, S. Lambert, S. Berthon-Fabry, and P. Achard, "Carbon xerogels as catalyst supports for PEM fuel cell cathode," *Energy Conversion and Management*, vol. 49, no. 9, pp. 2461–2470, 2008.
- [66] J. F. Vivo-Vilches, A. F. Pérez-Cadenas, F. J. Maldonado-Hódar, F. Carrasco-Marín, M. J. Regufe, A. M. Ribeiro, A. F. P. Ferreira, and A. E. Rodrigues, "Resorcinol–formaldehyde carbon xerogel as selective adsorbent of carbon dioxide present on biogas," *Adsorption*, vol. 24, pp. 169–177, feb 2018.
- [67] A. W. Franz, H. Kronemayer, D. Pfeiffer, R. D. Pilz, G. Reuss, W. Disteldorf, A. O. Gamer, and A. Hilt, "Formaldehyde," in *Ullmann's Encyclopedia of Industrial Chemistry*, pp. 1–34, Weinheim, Germany: Wiley-VCH Verlag GmbH & Co. KGaA, nov 2016.
- [68] V. J. Cogliano, Y. Grosse, R. A. Baan, K. Straif, M. B. Secretan, and F. E. Ghissassi, "Meeting Report: Summary of IARC Monographs on Formaldehyde, 2-Butoxyethanol, and 1-tert-Butoxy-2-Propanol," *IARC Monographs*, vol. 88, 2005.
- [69] B. Wheeler, "EU embalming fluid ban 'to change funerals'," nov 2018.
- [70] European Parliament and Council of the European Union, "Regulation (EU) No 649/2012 of the European Parliament and of the Council of 4 July 2012 concerning the export and import of hazardous chemicals," 2012.
- [71] K. Z. Gaca, J. A. Parkinson, and J. Sefcik, "Molecular Speciation and Mesoscale Clustering in Formaldehyde-Methanol-Water Solutions in the Presence of Sodium Carbonate," *Journal of Physical Chemistry B*, vol. 117, no. 36, pp. 10548–10555, 2013.
- [72] K. Z. Gaca, J. A. Parkinson, L. Lue, and J. Sefcik, "Equilibrium Speciation in Moderately Concentrated Formaldehyde-Methanol Water Solutions Investigated Using C-13 and H-1 Nuclear Magnetic Resonance Spectroscopy," *Industrial & Engineering Chemistry Research*, vol. 53, no. 22, pp. 9262–9271, 2014.
- [73] X.-x. Wang, H. Fu, D.-m. Du, Z.-y. Zhou, A.-g. Zhang, C.-f. Su, and K.-s. Ma, "The comparison of pKa determination between carbonic acid and formic acid and its application to prediction of the hydration numbers," *Chemical Physics Letters*, vol. 460, pp. 339–342, jul 2008.
- [74] R. N. Goldberg, N. Kishore, and R. M. Lennen, "Thermodynamic quantities for the ionization reactions of buffers," *Journal of physical and chemical reference data*, vol. 31, pp. 231–370, jun 2002.

- [75] C. E. Housecroft and A. G. Sharpe, *Inorganic Chemistry*. Pearson Education M.U.A., 2012.
- [76] K. Z. Gaca, J. A. Parkinson, and J. Sefcik, "Kinetics of early stages of resorcinol-formaldehyde polymerization investigated by solution-phase nuclear magnetic resonance spectroscopy," *Polymer*, vol. 110, pp. 62–73, 2017.
- [77] H. G. Peer, "The Reaction of Phenol with Formaldehyde .2. The Ratio of Ortho-Hydroxymethylphenol and Para-Hydroxymethylphenol in the Basecatalyzed Hydroxymethylation of Phenol," *Recueil Des Travaux Chimiques Des Pays-Bas-Journal of the Royal Netherlands Chemical Society*, vol. 78, no. 9-10, pp. 851–863, 1959.
- [78] S. Mulik and C. Sotiriou-Leventis, "Resorcinol-Formaldehyde Aerogels," in *Aerogels Handbook*, pp. 215–234, New York, NY: Springer New York, 2011.
- [79] S. J. Taylor, M. D. Haw, J. Sefcik, and A. J. Fletcher, "Gelation Mechanism of Resorcinol-Formaldehyde Gels Investigated by Dynamic Light Scattering," *Langmuir*, vol. 30, no. 34, pp. 10231–10240, 2014.
- [80] F. Hofmeister, "On the understanding of the effects of salts," *Arch. Exp. Pathol. Pharmacol.(Leipzig)*, vol. 24, pp. 247–260, 1888.
- [81] M. W. Washabaugh and K. D. Collins, "The Systematic Characterization by Aqueous Column Chromatography of Solutes Which Affect Protein Stability," *Journal of Biological Chemistry*, vol. 261, no. 27, pp. 12477–12485, 1986.
- [82] J. D. Batchelor, A. Olteanu, A. Tripathy, and G. J. Pielak, "Impact of Protein Denaturants and Stabilizers on Water Structure," *Journal of the American Chemical Society*, vol. 126, no. 7, pp. 1958–1961, 2004.
- [83] M. Boström, D. R. Williams, and B. W. Ninham, "Specific ion effects: Why DLVO theory fails for biology and colloid systems," *Physical Review Letters*, vol. 87, pp. 168103/1–168103/4, oct 2001.
- [84] M. C. Gurau, S.-M. Lim, E. T. Castellana, F. Albertorio, S. Kataoka, and P. S. Cremer, "On the Mechanism of the Hofmeister Effect," *Journal of the American Chemical Society*, vol. 126, no. 34, pp. 10522–10523, 2004.
- [85] Y. Zhang and P. S. Cremer, "Chemistry of Hofmeister Anions and Osmolytes," *Annual Review of Physical Chemistry*, vol. 61, pp. 63–83, mar 2010.
- [86] W. Kunz, "Specific ion effects in colloidal and biological systems," *Current Opinion in Colloid and Interface Science*, vol. 15, pp. 34–39, apr 2010.
- [87] N. Schwierz, D. Horinek, U. Sivan, and R. R. Netz, "Reversed Hofmeister series—The rule rather than the exception," *Current Opinion in Colloid & Interface Science*, vol. 23, pp. 10–18, jun 2016.
- [88] M. Alshrah, M.-P. Tran, P. Gong, H. E. Naguib, and C. B. Park, "Development of high-porosity resorcinol formaldehyde aerogels with enhanced mechanical properties through improved particle necking under CO₂ supercritical conditions," *Journal of Colloid and Interface Science*, vol. 485, pp. 65–74, jan 2017.
- [89] M. Yoshimune, T. Yamamoto, M. Nakaiwa, and K. Haraya, "Preparation of highly mesoporous carbon membranes via a sol-gel process using resorcinol and formaldehyde," *Carbon*, vol. 46, no. 7, pp. 1031–1036, 2008.
- [90] N. Rey-Raap, J. Angel Menéndez, and A. Arenillas, "RF xerogels with tailored porosity over the entire nanoscale," *Microporous and Mesoporous Materials*, 2014.

- [91] S. J. Taylor, M. D. Haw, J. Sefcik, and A. J. Fletcher, "Effects of Secondary Metal Carbonate Addition on the Porous Character of Resorcinol-Formaldehyde Xerogels," *Langmuir*, vol. 31, pp. 13571–13580, dec 2015.
- [92] N. Job, C. J. Gommès, R. Pirard, and J. P. Pirard, "Effect of the counter-ion of the basification agent on the pore texture of organic and carbon xerogels," *Journal of Non-Crystalline Solids*, vol. 354, no. 40–41, pp. 4698–4701, 2008.
- [93] E. G. Calvo, J. A. Menéndez, and A. Arenillas, "Influence of alkaline compounds on the porosity of resorcinol-formaldehyde xerogels," *Journal of Non-Crystalline Solids*, vol. 452, pp. 286–290, nov 2016.
- [94] M. Reuß and L. Ratke, "RF-aerogels catalysed by ammonium carbonate," *Journal of Sol-Gel Science and Technology*, vol. 53, pp. 85–92, jan 2010.
- [95] C. I. Merzbacher, S. R. Meier, J. R. Pierce, and M. L. Korwin, "Carbon aerogels as broadband non-reflective materials," *Journal of Non-Crystalline Solids*, vol. 285, pp. 210–215, jun 2001.
- [96] V. A. Emelichev and V. G. Ovchinnikov, "Optimization theory on antichains with the Steinitz exchange property," *Cybernetics*, vol. 21, no. 2, pp. 216–221, 1985.
- [97] O. Barbieri, F. Ehrburger-Dolle, T. P. Rieker, G. M. Pajonk, N. Pinto, and A. Venkateswara Rao, "Small-angle X-ray scattering of a new series of organic aerogels," *Journal of Non-Crystalline Solids*, vol. 285, pp. 109–115, jun 2001.
- [98] S. Mulik, C. Sotiriou-Leventis, N. Leventis, and L. N. Leventis, "Time-efficient acid-catalyzed synthesis of resorcinol-formaldehyde aerogels," *Chemistry of Materials*, vol. 19, pp. 6138–6144, dec 2007.
- [99] M. Reuß and L. Ratke, "Subcritically dried RF-aerogels catalysed by hydrochloric acid," *Journal of Sol-Gel Science and Technology*, vol. 47, pp. 74–80, jul 2008.
- [100] R. Brandt, R. Petricevic, H. Pröbstle, and J. Fricke, "Acetic Acid Catalyzed Carbon Aerogels," *Journal of Porous Materials*, vol. 10, no. 3, pp. 171–178, 2003.
- [101] J. F. Vivo-Vilches, A. F. Pérez-Cadenas, F. J. Maldonado-Hódar, F. Carrasco-Marín, C. Siquet, A. M. Ribeiro, A. F. Ferreira, and A. E. Rodrigues, "From Carbon Molecular Sieves to VOCs filters: Carbon gels with tailored porosity for hexane isomers adsorption and separation," *Microporous and Mesoporous Materials*, vol. 270, pp. 161–167, nov 2018.
- [102] D. Fairén-Jiménez, F. Carrasco-Marín, and C. Moreno-Castilla, "Porosity and surface area of monolithic carbon aerogels prepared using alkaline carbonates and organic acids as polymerization catalysts," *Carbon*, vol. 44, pp. 2301–2307, sep 2006.
- [103] J. Xu, A. Wang, and T. Zhang, "A two-step synthesis of ordered mesoporous resorcinol-formaldehyde polymer and carbon," *Carbon*, vol. 50, pp. 1807–1816, apr 2012.
- [104] J. Laskowski, B. Milow, and L. Ratke, "Subcritically dried resorcinol-formaldehyde aerogels from a base-acid catalyzed synthesis route," *Microporous and Mesoporous Materials*, vol. 197, pp. 308–315, 2014.
- [105] A. Awadallah-F, A. M. Elkhatat, and S. A. Al-Muhtaseb, "Impact of synthesis conditions on meso- and macropore structures of resorcinol-formaldehyde xerogels," *Journal of Materials Science*, vol. 46, pp. 7760–7769, dec 2011.
- [106] M. Wiener, G. Reichenauer, T. Scherb, and J. Fricke, "Accelerating the synthesis of carbon aerogel precursors," *Journal of Non-Crystalline Solids*, vol. 350, pp. 126–130, 2004.

- [107] B. Fang and L. Binder, "A modified activated carbon aerogel for high-energy storage in electric double layer capacitors," *Journal of Power Sources*, vol. 163, pp. 616–622, dec 2006.
- [108] A. Szczurek, G. Amaral-Labat, V. Fierro, A. Pizzi, E. Masson, and A. Celzard, "Porosity of resorcinol-formaldehyde organic and carbon aerogels exchanged and dried with supercritical organic solvents," *Materials Chemistry and Physics*, vol. 129, no. 3, pp. 1221–1232, 2011.
- [109] C. Ye, Z. An, and R. Zhang, "Super-elastic carbon-bonded carbon fibre composites impregnated with carbon aerogel for high-temperature thermal insulation," *Advances in Applied Ceramics*, pp. 1–8, jan 2019.
- [110] O. Czakkel, K. Marthi, E. Geissler, and K. László, "Influence of drying on the morphology of resorcinol-formaldehyde-based carbon gels," *Microporous and Mesoporous Materials*, vol. 86, pp. 124–133, nov 2005.
- [111] M. P. Chavhan and S. Ganguly, "Carbon cryogel from resorcinol formaldehyde: tuning of processing steps and activation for use in supercapacitor," *Materials Technology*, vol. 32, pp. 744–754, oct 2017.
- [112] J. J. Jasper, "The Surface Tension of Pure Liquid Compounds," *Journal of Physical and Chemical Reference Data*, vol. 1, no. 4, pp. 841–1010, 1972.
- [113] C. Carr and J. A. Riddick, "Physical Properties of Methanol-Water System," *Industrial and Engineering Chemistry*, vol. 43, no. 3, pp. 692–696, 1951.
- [114] R. R. Dreisbach and R. A. Martin, "Physical Data on Some Organic Compounds," *Am. Inst. Mining Met. Engrs., Tech. Pub. 2269, Petroleum Technol*, vol. 2875, no. 4, p. 1948, 1949.
- [115] E. Sada and T. Morisue, "Isothermal vapor-liquid equilibrium data of isopropanol-water system," *JOURNAL OF CHEMICAL ENGINEERING OF JAPAN*, vol. 8, pp. 191–195, jun 1975.
- [116] H. Kirss, E. Siimer, M. Kuus, and L. Kudryavtseva, "Isobaric vapor-liquid equilibria in the system o-xylene + amyl acetate + nonane," *Journal of Chemical and Engineering Data*, vol. 46, no. 1, pp. 147–150, 2001.
- [117] R. Span and W. Wagner, "A new equation of state for carbon dioxide covering the fluid region from the triple-point temperature to 1100 K at pressures up to 800 MPa," *Journal of Physical and Chemical Reference Data*, vol. 25, pp. 1509–1596, nov 1996.
- [118] N. Ni, M. Tesconi, S. E. Tabibi, S. Gupta, and S. H. Yalkowsky, "Use of pure t-butanol as a solvent for freeze-drying: A case study," *International Journal of Pharmaceutics*, vol. 226, pp. 39–46, sep 2001.
- [119] F. Schwertfeger, D. Frank, and M. Schmidt, "Hydrophobic waterglass based aerogels without solvent exchange or supercritical drying," *Journal of Non-Crystalline Solids*, vol. 225, pp. 24–29, apr 1998.
- [120] A. Moreno, A. Arenillas, E. Calvo, J. Bermúdez, and J. Menéndez, "Carbonisation of resorcinol-formaldehyde organic xerogels: Effect of temperature, particle size and heating rate on the porosity of carbon xerogels," *Journal of Analytical and Applied Pyrolysis*, vol. 100, pp. 111–116, mar 2013.
- [121] N. Rey-Raap, A. Arenillas, and J. A. Menéndez, "A visual validation of the combined effect of pH and dilution on the porosity of carbon xerogels," *Microporous and Mesoporous Materials*, 2016.

- [122] E. G. Rodrigues, M. F. Pereira, and J. J. Órfão, "Glycerol oxidation with gold supported on carbon xerogels: Tuning selectivities by varying mesopore sizes," *Applied Catalysis B: Environmental*, vol. 115-116, pp. 1–6, apr 2012.
- [123] J. Marie, S. Berthon-Fabry, M. Chatenet, E. Chaînet, R. Pirard, N. Cornet, and P. Achard, "Platinum supported on resorcinol–formaldehyde based carbon aerogels for PEMFC electrodes: Influence of the carbon support on electrocatalytic properties," *Journal of Applied Electrochemistry*, vol. 37, no. 1, pp. 147–153, 2007.
- [124] A. Smirnova, X. Dong, H. Hara, A. Vasiliev, and N. Sammes, "Novel carbon aerogel-supported catalysts for PEM fuel cell application," *International Journal of Hydrogen Energy*, vol. 30, no. 2, pp. 149–158, 2005.
- [125] H. Jin, H. Zhang, Y. Ma, T. Xu, H. Zhong, and M. Wang, "Stable support based on highly graphitic carbon xerogel for proton exchange membrane fuel cells," *Journal of Power Sources*, vol. 195, pp. 6323–6328, oct 2010.
- [126] C. Robertson and R. Mokaya, "Microporous activated carbon aerogels via a simple subcritical drying route for CO₂ capture and hydrogen storage," *Microporous and Mesoporous Materials*, vol. 179, pp. 151–156, 2013.
- [127] L. Zubizarreta, J. Menéndez, N. Job, J. Marco-Lozar, J. Pirard, J. Pis, A. Linares-Solano, D. Cazorla-Amorós, and A. Arenillas, "Ni-doped carbon xerogels for H₂ storage," *Carbon*, vol. 48, pp. 2722–2733, aug 2010.
- [128] M. Anas, S. Ünsal, and C. Erkey, "Investigation of various aerogels as adsorbents for methane storage," *The Journal of Supercritical Fluids*, vol. 141, pp. 166–172, nov 2018.
- [129] A. Awadallah-F, S. A. Al-Muhtaseb, and H.-K. Jeong, "Selective adsorption of carbon dioxide, methane and nitrogen using resorcinol-formaldehyde-xerogel activated carbon," *Adsorption*, vol. 23, pp. 933–944, nov 2017.
- [130] V. M. Magueijo, L. G. Anderson, A. J. Fletcher, and S. J. Shilton, "Polysulfone mixed matrix gas separation hollow fibre membranes filled with polymer and carbon xerogels," *Chemical Engineering Science*, vol. 92, pp. 13–20, apr 2013.
- [131] T. Yamamoto, A. Endo, T. Ohmori, and M. Nakaiwa, "Porous properties of carbon gel microspheres as adsorbents for gas separation," *Carbon*, vol. 42, no. 8-9, pp. 1671–1676, 2004.
- [132] Y.-R. Dong, M. Nakao, N. Nishiyama, Y. Egashira, and K. Ueyama, "Gas permeation and pervaporation of water/alcohols through the microporous carbon membranes prepared from resorcinol/formaldehyde/quaternary ammonium compounds," *Separation and Purification Technology*, vol. 73, no. 1, pp. 2–7, 2010.
- [133] X. Lu, M. C. Arduini-Schuster, J. Kuhn, O. Nilsson, J. Fricke, and R. W. Pekala, "Thermal conductivity of monolithic organic aerogels," *Science*, vol. 255, no. 5047, pp. 971–972, 1992.
- [134] N. Rey-Raap, E. Calvo, J. Menéndez, and A. Arenillas, "Exploring the potential of resorcinol-formaldehyde xerogels as thermal insulators," *Microporous and Mesoporous Materials*, vol. 244, pp. 50–54, may 2017.
- [135] J. Feng, C. Zhang, and J. Feng, "Carbon fiber reinforced carbon aerogel composites for thermal insulation prepared by soft reinforcement," *Materials letters*, vol. 67, no. 1, pp. 266–268, 2012.

- [136] M. Kakunuri, S. Vennamalla, and C. S. Sharma, "Synthesis of carbon xerogel nanoparticles by inverse emulsion polymerization of resorcinol–formaldehyde and their use as anode materials for lithium-ion battery," *RSC Advances*, vol. 5, pp. 4747–4753, dec 2015.
- [137] N. Rey-Raap, M.-L. C. Piedboeuf, A. Arenillas, J. A. Menéndez, A. F. Léonard, and N. Job, "Aqueous and organic inks of carbon xerogels as models for studying the role of porosity in lithium-ion battery electrodes," *Materials & Design*, vol. 109, pp. 282–288, nov 2016.
- [138] L. A. Rodrigues, T. M. B. Campos, M. O. Alvarez-Mendes, A. dos reis Coutinho, K. K. Sakane, and G. P. Thim, "Phenol removal from aqueous solution by carbon xerogel," *Journal of Sol-Gel Science and Technology*, vol. 63, pp. 202–210, aug 2012.
- [139] B. Yang, C. Yu, Q. Yu, X. Zhang, Z. Li, and L. Lei, "N-doped carbon xerogels as adsorbents for the removal of heavy metal ions from aqueous solution," *RSC Advances*, vol. 5, pp. 7182–7191, jan 2015.
- [140] P. Veselá and V. Slovák, "N-doped carbon xerogels prepared by ammonia assisted pyrolysis: Surface characterisation, thermal properties and adsorption ability for heavy metal ions," *Journal of Analytical and Applied Pyrolysis*, vol. 109, pp. 266–271, sep 2014.
- [141] N. A. Fathy, M. A. Shouman, and R. M. M. Aboelenin, "Nitrogen and phosphorous-doped porous carbon xerogels as metal-free catalysts for environmental catalytic peroxide oxidation of 4-nitrophenol," *Asia-Pacific Journal of Chemical Engineering*, vol. 11, pp. 836–845, nov 2016.
- [142] M. Thommes, K. Kaneko, A. V. Neimark, J. P. Olivier, F. Rodriguez-Reinoso, J. Rouquerol, and K. S. W. Sing, "Physisorption of gases, with special reference to the evaluation of surface area and pore size distribution (IUPAC Technical Report)," *Pure and Applied Chemistry*, vol. 87, no. 9-10, pp. 1051–1069, 2015.
- [143] K. S. W. Sing, D. H. Everett, R. A. W. Haul, L. Moscou, R. A. Pierotti, J. Rouquerol, and T. Siemieniowska, "Reporting Physisorption Data for Gas Solid Systems with Special Reference to the Determination of Surface-Area and Porosity (Recommendations 1984)," *Pure and Applied Chemistry*, vol. 57, no. 4, pp. 603–619, 1985.
- [144] J. Rouquerol, D. Avnir, C. W. Fairbridge, D. H. Everett, J. H. M. Haynes, N. Pernicone, J. D. F. Ramsay, K. S. W. Sing, and K. K. Unger, "Recommendations for the Characterization of Porous Solids," *Pure and Applied Chemistry*, vol. 66, no. 8, pp. 1739–1758, 1994.
- [145] I. Langmuir, "The adsorption of gases on plane surfaces of glass, mica and platinum.," *Journal of the American Chemical Society*, vol. 40, no. 9, pp. 1361–1403, 1918.
- [146] S. Brunauer, P. H. Emmett, and E. Teller, "Adsorption of Gases in Multimolecular Layers," *Journal of the American Chemical Society*, vol. 60, no. 2, pp. 309–319, 1938.
- [147] J. Rouquerol, P. Llewellyn, and F. Rouquerol, "Is the BET equation applicable to microporous adsorbents?," *Studies in Surface Science and Catalysis*, vol. 160, pp. 49–56, 2007.
- [148] E. P. Barrett, L. G. Joyner, and P. P. Halenda, "The Determination of Pore Volume and Area Distributions in Porous Substances. I. Computations from Nitrogen Isotherms," *Journal of the American Chemical Society*, vol. 73, no. 1, pp. 373–380, 1951.
- [149] ASTM D6556-17, "Standard Test Method for Carbon Black — Total and External Surface Area by Nitrogen Adsorption," *ASTM International*, 2017.

- [150] B. Lippens and J. de Boer, "Studies on pore systems in catalysts: V. The t method," *Journal of Catalysis*, vol. 4, pp. 319–323, jun 1965.
- [151] N. Job, R. Pirard, J.-P. Pirard, and C. Alié, "Non Intrusive Mercury Porosimetry: Pyrolysis of Resorcinol-Formaldehyde Xerogels," in *Particle & Particle Systems Characterization*, vol. 23, pp. 72–81, John Wiley & Sons, Ltd, jun 2006.
- [152] C. Gommès, N. Job, S. Blacher, and J.-P. Pirard, "Compressing some sol-gel materials reduces their stiffness: a textural analysis," *Studies in surface science and catalysis*, vol. 160, pp. 193–200, 2007.
- [153] A. F. Voter, "INTRODUCTION TO THE KINETIC MONTE CARLO METHOD," in *Radiation Effects in Solids*, pp. 1–23, Dordrecht: Springer Netherlands, 2007.
- [154] A. Chatterjee and D. G. Vlachos, "An overview of spatial microscopic and accelerated kinetic Monte Carlo methods," *Journal of Computer-Aided Materials Design*, vol. 14, no. 2, pp. 253–308, 2007.
- [155] P. Meakin, "Formation of fractal clusters and networks by irreversible diffusion-limited aggregation," *Physical Review Letters*, vol. 51, no. 13, pp. 1119–1122, 1983.
- [156] M. Kolb, R. Botet, and R. Jullien, "Scaling of Kinetically Growing Clusters," *Physical Review Letters*, vol. 51, no. 13, pp. 1123–1126, 1983.
- [157] P. Meakin and R. Jullien, "The effects of restructuring on the geometry of clusters formed by diffusion-limited, ballistic, and reaction-limited cluster–cluster aggregation," *The Journal of Chemical Physics*, vol. 89, pp. 246–250, jul 1988.
- [158] S. Gavalda, K. Kaneko, K. T. Thomson, and K. E. Gubbins, "Molecular modeling of carbon aerogels," *Colloids and Surfaces A: Physicochemical and Engineering Aspects*, vol. 187, pp. 531–538, 2001.
- [159] S. Gavalda, K. E. Gubbins, Y. Hanzawa, K. Kaneko, and K. T. Thomson, "Nitrogen adsorption in carbon aerogels: A molecular simulation study," *Langmuir*, vol. 18, no. 6, pp. 2141–2151, 2002.
- [160] V. Morales-Flórez, N. D. L. Rosa-Fox, M. Piñero, and L. Esquivias, "The cluster model: A simulation of the aerogel structure as a hierarchically-ordered arrangement of randomly packed spheres," *Journal of Sol-Gel Science and Technology*, vol. 35, no. 3, pp. 203–210, 2005.
- [161] V. Morales-Flórez, M. Piñero, N. de la Rosa-Fox, L. Esquivias, J. A. Anta, and J. Primera, "The cluster model: A hierarchically-ordered assemblage of random-packing spheres for modelling microstructure of porous materials," *Journal of Non-Crystalline Solids*, vol. 354, no. 2-9, pp. 193–198, 2008.
- [162] C. A. Ferreiro-Rangel and L. D. Gelb, "Investigation of the Bulk Modulus of Silica Aerogel Using Molecular Dynamics Simulations of a Coarse-Grained Model," *The Journal of Physical Chemistry B*, vol. 117, no. 23, pp. 7095–7105, 2013.
- [163] R. W. Pekala, C. T. Alviso, F. M. Kong, and S. S. Hulse, "Aerogels Derived from Multifunctional Organic Monomers," *Journal of Non-Crystalline Solids*, vol. 145, pp. 90–98, jan 1992.
- [164] H. S. Ma, J. H. Prévost, and G. W. Scherer, "Elasticity of DLCA model gels with loops," *International Journal of Solids and Structures*, vol. 39, no. 18, pp. 4605–4614, 2002.
- [165] B. Mandelbrot, "How long is the coast of Britain? Statistical self-similarity and fractional dimension," *Science*, vol. 156, pp. 636–638, may 1967.

- [166] P. S. Addison, *Fractals and chaos: an illustrated course*. CRC Press, 1997.
- [167] K. Vinoy, K. Jose, and V. Varadan, "Multi-band characteristics and fractal dimension of dipole antennas with Koch curve geometry," in *IEEE Antennas and Propagation Society International Symposium (IEEE Cat. No.02CH37313)*, vol. 4, pp. 106–109, IEEE, 2003.
- [168] P. Grassberger and I. Procaccia, "Measuring the strangeness of strange attractors," *Physica D: Nonlinear Phenomena*, vol. 9, pp. 189–208, oct 1983.
- [169] G. B. So, H. R. So, and G. G. Jin, "Enhancement of the Box-Counting Algorithm for fractal dimension estimation," *Pattern Recognition Letters*, vol. 98, pp. 53–58, oct 2017.
- [170] B. B. Mandelbrot, "Self-Affine Fractals and Fractal Dimension," *Physica Scripta*, vol. 32, pp. 257–260, oct 1985.
- [171] T. Gneiting and M. Schlather, "Stochastic models which separate fractal dimension and Hurst effect," *Society for Industrial and Applied Mathematics*, vol. 46, no. 2, pp. 269–282, 2001.
- [172] D. Stauffer and A. Aharony, *Introduction to percolation theory*. London: Taylor & Francis, 2nd ed., 1994.
- [173] K. Leung, A. Luzar, and D. Bratko, "Dynamics of Capillary Drying in Water," *Physical Review Letters*, vol. 90, p. 4, feb 2003.
- [174] S. Sharma and P. G. Debenedetti, "Evaporation rate of water in hydrophobic confinement," *Proceedings of the National Academy of Sciences*, vol. 109, pp. 4365–4370, mar 2012.
- [175] L. Sarkisov and P. A. Monson, "Modeling of adsorption and desorption in pores of simple geometry using molecular dynamics," *Langmuir*, vol. 17, no. 24, pp. 7600–7604, 2001.
- [176] K. S. Page and P. A. Monson, "Phase equilibrium in a molecular model of a fluid confined in a disordered porous material," jul 1996.
- [177] P. A. Monson, "Mean field kinetic theory for a lattice gas model of fluids confined in porous materials," *Journal of Chemical Physics*, vol. 128, no. 8, p. 84701, 2008.
- [178] J. R. Edison and P. A. Monson, "Dynamic mean field theory of condensation and evaporation in model pore networks with variations in pore size," *Microporous and Mesoporous Materials*, vol. 154, pp. 7–15, may 2012.
- [179] J. R. Edison and P. A. Monson, "Dynamic mean field theory for lattice gas models of fluid mixtures confined in mesoporous materials," *Langmuir*, vol. 29, no. 45, pp. 13808–13820, 2013.
- [180] J. R. Edison and P. A. Monson, "Dynamics of capillary condensation in lattice gas models of confined fluids: A comparison of dynamic mean field theory with dynamic Monte Carlo simulations," *Journal of Chemical Physics*, vol. 138, p. 234709, jun 2013.
- [181] D. Schneider, R. Valiullin, and P. A. Monson, "Modeling the influence of side stream and ink bottle structures on adsorption/desorption dynamics of fluids in long pores," *Langmuir*, vol. 31, no. 1, pp. 188–198, 2015.
- [182] J. A. Casselman, A. Desouza, and P. A. Monson, "Modelling the dynamics of condensation and evaporation of fluids in three-dimensional slit pores," *Molecular Physics*, vol. 113, pp. 1250–1260, may 2015.

- [183] A. Rathi, E. S. Kikkinides, D. M. Ford, and P. A. Monson, "A comparison of dynamic mean field theory and grand canonical molecular dynamics for the dynamics of pore filling and capillary condensation of fluids in mesopores," *Journal of Chemical Physics*, vol. 149, no. 1, p. 14703, 2018.
- [184] A. Svidrytski, A. Rathi, D. Hlushkou, D. M. Ford, P. A. Monson, and U. Tallarek, "Morphology of Fluids Confined in Physically Reconstructed Mesoporous Silica: Experiment and Mean Field Density Functional Theory," *Langmuir*, vol. 34, pp. 9936–9945, aug 2018.
- [185] I. Kim and D. Landau, "Monte Carlo simulation of a lattice gas model of multilayer adsorption," *Surface Science*, vol. 110, pp. 415–422, oct 1981.
- [186] L. Sarkisov and A. Harrison, "Computational structure characterisation tools in application to ordered and disordered porous materials," *Molecular Simulation*, vol. 37, no. 15, pp. 1248–1257, 2011.
- [187] P. A. Monson, "Understanding Adsorption/Desorption Hysteresis for Fluids in Mesoporous Materials Using Simple Molecular Models and Classical Density Functional Theory," *Microporous and Mesoporous Materials*, vol. 160, no. Supplement C, pp. 47–66, 2012.
- [188] L. D. Gelb, "Modeling amorphous porous materials and confined fluids," *MRS Bulletin*, vol. 34, pp. 592–601, aug 2009.
- [189] Micromeritics, "ASAP2420."
- [190] S. J. Kim, S. W. Hwang, and S. H. Hyun, "Preparation of carbon aerogel electrodes for supercapacitor and their electrochemical characteristics," *Journal of Materials Science*, vol. 40, no. 3, pp. 725–731, 2005.
- [191] K. Z. Gaca and J. Sefcik, "Mechanism and kinetics of nanostructure evolution during early stages of resorcinol-formaldehyde polymerisation," *Journal of Colloid and Interface Science*, vol. 406, pp. 51–59, 2013.
- [192] M. Prostředný, M. Abduljalil, P. Mulheran, and A. Fletcher, "Process Variable Optimization in the Manufacture of Resorcinol-Formaldehyde Gel Materials," *Gels*, vol. 4, no. 2, p. 36, 2018.
- [193] N. B. Vargaftik, B. N. Volkov, and L. D. Voljak, "International Tables of the Surface Tension of Water," *Journal of Physical and Chemical Reference Data*, vol. 12, no. 3, pp. 817–820, 1983.
- [194] S. R. Mukai, C. Tamitsuji, H. Nishihara, and H. Tamon, "Preparation of mesoporous carbon gels from an inexpensive combination of phenol and formaldehyde," *Carbon*, vol. 43, no. 12, pp. 2628–2630, 2005.
- [195] S. J. Taylor, *Monitoring the gelation mechanism of resorcinol-formaldehyde xerogels*. PhD thesis, University of Strathclyde, 2014.
- [196] L. Anderson, *The effect of the catalyst on the formation of RF xerogels*. PhD thesis, University of Strathclyde, 2013.
- [197] V. G. Pol, L. K. Shrestha, and K. Ariga, "Tunable, functional carbon spheres derived from rapid synthesis of resorcinol-formaldehyde resins," *ACS Applied Materials and Interfaces*, vol. 6, no. 13, pp. 10649–10655, 2014.
- [198] O. Tange, "Gnu parallel—the command-line power tool," *The USENIX Magazine*, vol. 36, no. 1, pp. 42–47, 2011.

- [199] C. S. Sharma, M. M. Kulkarni, A. Sharma, and M. Madou, "Synthesis of carbon xerogel particles and fractal-like structures," *Chemical Engineering Science*, vol. 64, no. 7, pp. 1536–1543, 2009.
- [200] P. Grassberger and I. Procaccia, "Characterization of strange attractors," *Physical review letters*, vol. 50, no. 5, p. 346, 1983.
- [201] T. Vicsek, *Fractal growth phenomena*. World Scientific, 1st ed., 1989.
- [202] M. M. Huber, H. Klein, and L. Ratke, "DLS-Based Fractal Analysis in Early Stage Gelation," *Particle & Particle Systems Characterization: Measurement and Description of Particle Properties and Behavior in Powders and Other Disperse Systems*, vol. 20, pp. 379–381, dec 2003.
- [203] B. Coasne and R. J.-M. Pellenq, "Grand canonical Monte Carlo simulation of argon adsorption at the surface of silica nanopores: Effect of pore size, pore morphology, and surface roughness," *Journal of Chemical Physics*, vol. 120, no. 6, pp. 2913–2922, 2004.
- [204] S. Naumov, A. Khokhlov, R. Valiullin, J. Kärger, and P. A. Monson, "Understanding capillary condensation and hysteresis in porous silicon: Network effects within independent pores," *Physical Review E - Statistical, Nonlinear, and Soft Matter Physics*, vol. 78, no. 6, 2008.
- [205] S. Naumov, R. Valiullin, J. Kärger, and P. A. Monson, "Understanding adsorption and desorption processes in mesoporous materials with independent disordered channels," *Physical Review E - Statistical, Nonlinear, and Soft Matter Physics*, vol. 80, no. 3, 2009.
- [206] P. J. Flory, "Molecular Size Distribution in Three Dimensional Polymers. I. Gelation," *Journal of the American Chemical Society*, vol. 63, no. 11, pp. 3083–3090, 1941.

Appendix A

Reaction solution compositions

Table A.1 RF gel solution compositions for study of R/C ratio effect

R/C ratio	m(R) [g]	m(F) [g]	m(Na ₂ CO ₃) [g]
100	7.7170	4.2087	0.07428
200	7.7409	4.2218	0.03726
300	7.7490	4.2262	0.02486
400	7.7530	4.2284	0.01866
500	7.7554	4.2297	0.01493
600	7.7570	4.2306	0.01244
800	7.7590	4.2317	0.00934

R corresponds to resorcinol and F to formaldehyde

Table A.2 RF gel solution compositions for study of sodium chloride as additional source of sodium ions

Sample name	m(R) [g]	m(F) [g]	m(Na ₂ CO ₃) [g]	m(NaCl) [g]
Na ₂ CO ₃ 200 NaCl 200	7.7409	4.2218	0.03726	0.04083
Na ₂ CO ₃ 400 NaCl 133	7.7530	4.2284	0.01866	0.06134
Na ₂ CO ₃ 600 NaCl 120	7.7570	4.2306	0.01244	0.06819
Na ₂ CO ₃ INF NaCl 100	7.7651	4.2349	0.00000	0.08191

R corresponds to resorcinol and F to formaldehyde, numbers in sample name correspond to R/C ratios of catalyst salts, INF represents infinite R/C ratio (zero concentration)

Table A.3 RF gel solution compositions for study of sodium sulphate as additional source of sodium ions

R/C ratio	m(R) [g]	m(F) [g]	m(Na ₂ CO ₃) [g]	m(Na ₂ SO ₄) [g]
Na ₂ CO ₃ 200 Na ₂ SO ₄ 200	7.7089	4.2043	0.03710	0.04972
Na ₂ CO ₃ 400 Na ₂ SO ₄ 133	7.7048	4.2021	0.01854	0.07454
Na ₂ CO ₃ 600 Na ₂ SO ₄ 120	7.7035	4.2014	0.01236	0.08281
Na ₂ CO ₃ INF Na ₂ SO ₄ 100	7.7008	4.1999	0.00000	0.09934

R corresponds to resorcinol and F to formaldehyde, numbers in sample name correspond to R/C ratios of catalyst salts, INF represents infinite R/C ratio (zero concentration)

Appendix B

Nitrogen sorption measurement validation

As all experimentally obtained RF gel samples were analysed, for their textural properties, using nitrogen sorption measurements, two tests were performed in order to validate the reliability and repeatability of the data determined by this method. Firstly, a blank tube measurement with free space correction was undertaken, in order to ensure that the baseline error of the measurement was within an acceptable limit, as presented in section B.1. Subsequently, six samples of silica alumina standard, supplied by the equipment manufacturer, were analysed to confirm repeatability of measurements, as described in section B.2.

B.1 Free space correction

As mentioned above, in order to ensure the baseline error of the gas uptake for nitrogen sorption measurements was within reasonable limits, a blank tube test, along with a free space correction, was performed. First, an empty sample tube was degassed for one hour at 250 °C under vacuum to ensure that any species adsorbed on the glass surface were removed, so that analysis was not affected. A subsequent adsorption run was undertaken, with the adsorption branch of the isotherm shown in Figure B.1.

To correct for the error related to cold free space measurement prior to analysis, the volume of nitrogen gas adsorbed at $p/p_0 \sim 0.95$ was added to the original value of cold free space. In this case 0.11 cm³ was added to the initial value of 84.2795 cm³, leading to a corrected cold free space value of 84.3895 cm³. After replotting the adsorption data (Figure B.1), the baseline error was reduced to ± 0.02 cm³/g.

This result shows that the errors in the volumes of adsorbed nitrogen gas are within a very small range, providing reliable data that can be used for analysis of textural properties of the prepared samples with sufficient precision.

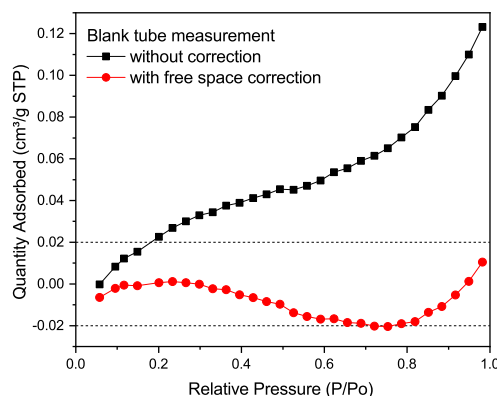


Figure B.1 Isotherms, with and without free space correction, for a blank tube test, dashed lines show the maximum deviation of $\pm 0.02 \text{ cm}^3/\text{g}$ for corrected baseline values

B.2 Silica alumina standard measurement

Due to extended time periods needed to perform nitrogen sorption analysis and the number of samples analysed, it was impractical to run multiple repeats of the measurement for a given RF gel sample, unless there was a perceived discrepancy in the results obtained. However, in order to make sure that the measurements provided reproducible results, a set of 6 samples of silica alumina standards, supplied by the equipment manufacturer (Micromeritics), was used to obtain a suite of repeat runs. Silica alumina is the standard material recommended for sorption analysis (by Micromeritics) for amorphous porous samples with surface areas in the range 10 to greater than $300 \text{ m}^2/\text{g}$, and average pore sizes in the range 0.4 to 300 nm.

The six batches were taken from the same bottle of standard, and 6 different sample tubes were used with a different analysis port for each measurement. All the samples were degassed according to Micromeritics' recommendations, i.e. heating the samples under vacuum to $90 \text{ }^\circ\text{C}$ for one hour, followed by heating them to $350 \text{ }^\circ\text{C}$ while maintaining vacuum, for 4 hours. Nitrogen sorption isotherms for the six samples, along with their corresponding pore size distributions, are presented in Figure B.2.

As can be seen from Figure B.2, both the nitrogen sorption isotherms and the extracted pore size distributions overlap well for all six samples analysed. The textural properties of the silica alumina samples are shown in Table B.1. Average values, and the standard error for each textural property, are listed in the lower part of the table, and variables are rounded to the same order of magnitude as their respective error value. Within the main body of this work, all the variables are rounded to a precision less than the largest error for each variable (i.e. S_{BET} to $10 \text{ m}^2/\text{g}$, V_{T} and V_{μ} to $0.01 \text{ cm}^3/\text{g}$, and $\bar{\phi}$ to 1 nm).

It can be seen from Table B.1 that the values of accessible surface area and total pore volume obtained for all six samples compare well to the values reported by the manufacturer. No information is provided for the micropore volume, most likely because the value is relatively low for this material. It is interesting that the average pore diameter reported by

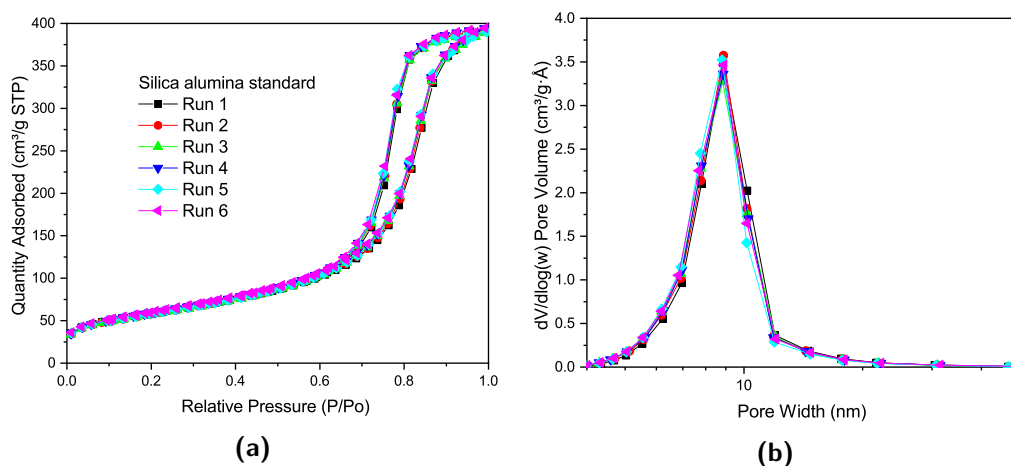


Figure B.2 (a) Nitrogen sorption isotherms obtained for six samples of silica alumina standard at $-196\text{ }^{\circ}\text{C}$ and (b) corresponding pore size distributions determined using the BJH theory

the manufacturer is higher than the value obtained in this work, however, this could be a result of sample ageing, where slight structural changes may have occurred during storage.

The error associated with the average pore size is actually larger than the standard error of the mean presented in Table B.1. The diameter of the nitrogen probe molecule is $\sim 0.4\text{ nm}$, hence, the values of average pore sizes within the main body of this work are reported as whole numbers. It should be noted that the trends observed within the sample sets studied in this work are still statistically significant, even when reporting all the aforementioned values as described above.

Table B.1 Textural properties of six silica alumina standard samples, with standard errors calculated for each property

	S_{BET} [m^2/g]	V_{T} [cm^3/g]	V_{μ} [cm^3/g]	$\bar{\phi}$ [nm]
Run 1	209	0.606	0.007	8.7
Run 2	210	0.607	0.004	8.6
Run 3	206	0.601	0.004	8.5
Run 4	211	0.610	0.004	8.6
Run 5	210	0.603	0.006	8.4
Run 6	215	0.610	0.005	8.5
Average	210 ± 3	0.606 ± 0.004	0.005 ± 0.002	8.6 ± 0.1
Manufacturer values	214 ± 6	0.62 ± 0.08	-	11.5 ± 1.5

S_{BET} - accessible surface area from BET analysis; V_{T} - total pore volume determined from adsorption at $p/p_0 \sim 1$; V_{μ} - micropore volume determined using t-plot method; $\bar{\phi}$ - average pore width from BJH analysis.

Appendix C

Preliminary results

C.1 Titration study

The gelation of RF gels is a pH dependent process, as discussed in Section 1.2.2. Therefore, titrations of RF reaction solutions, with different R/C ratios, were performed in order to investigate the evolution of solution pH during addition of formaldehyde. Firstly, resorcinol and sodium carbonate were dissolved in deionised water. Titration of this solution was performed using 0.2 M aqueous formaldehyde solution, administered using a syringe, allowing controlled addition. The experimental setup used for titrations, discussed in this section, is presented in Figure C.1. The end of the tube attached to the syringe was fitted with a plastic pipette tip, to allow drop-wise addition of the formaldehyde solution. Solution pH was monitored using a pH probe, connected to a computer for data logging, and all measurements were performed under stirring, using a magnetic stirrer bar, to ensure efficient mixing.

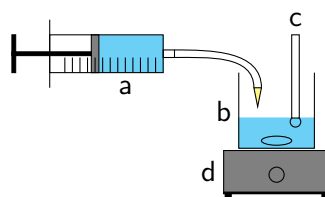


Figure C.1 Schematic drawing of setup for titration measurements, with (a) syringe containing formaldehyde solution, (b) beaker containing aqueous solution of resorcinol and sodium carbonate with a magnetic stirrer bar, (c) pH probe, and (d) magnetic stirrer

Solution compositions were calculated so that upon addition of the whole required volume of the formaldehyde solution, the mixture was equivalent to the solution used for production of an analogous RF gel, as described in Section 3.2.1, and $R/F = 0.5$ was reached. Figure C.2a shows solution pH for different sodium carbonate amount and changing R/F ratio. It should be noted that, in Figure C.2a, addition of formaldehyde solution reduces the calculated R/F ratio; thus, the data is collected from right to left, in this case. The difference in pH values,

between the solutions, results from the varying amount of sodium carbonate present, where a higher carbonate amount results in a higher solution pH, due to its hydrolysis, as discussed in more detail in Section 1.2.1. Dividing the R/F values by their corresponding R/C ratios, as presented in Figure C.2b, shifts the depression observed in all the curves to a $(R/F)/(R/C)$ value ~ 0.01 . This suggests that there is a common phenomenon occurring in all four analysed RF solutions causing a decrease, and subsequent increase, in solution pH. The data for R/C 600 exhibits a more pronounced shape at lower $(R/F)/(R/C)$ ratios, most likely due to a lower carbonate concentration masking the processes occurring within the solution to a lesser extent. Due to a potential change in the amount and type of monomeric species, present in the RF reaction solution, after gradual addition of formaldehyde, compared to instant addition, textural properties of RF gels, prepared using both methods, were examined in Section C.2.

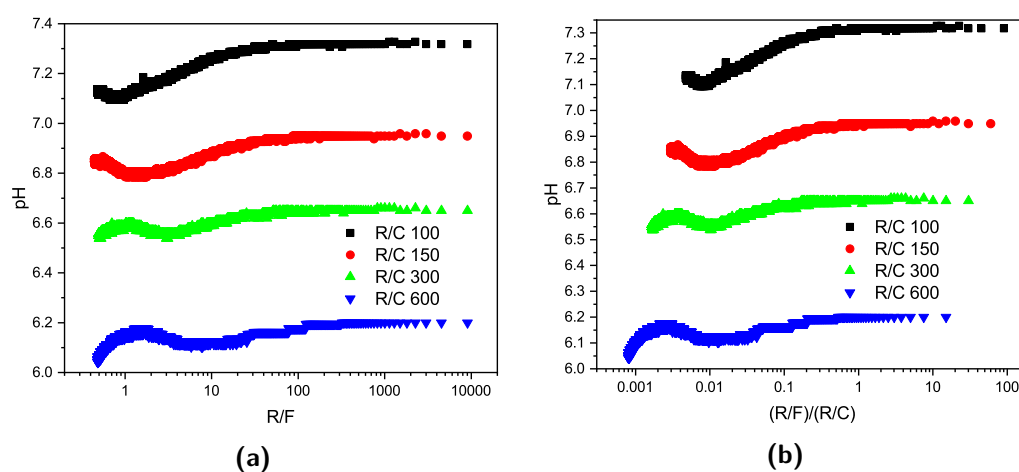


Figure C.2 Solution pH data during titration of resorcinol/sodium carbonate solution with formaldehyde solution

C.2 Gradual addition of formaldehyde

As observed in the previous section, a change in solution pH is observed during titration of resorcinol/sodium carbonate solutions with formaldehyde solution at a particular $(R/F)/(R/C)$ ratio, suggesting a reaction causing this pH change. However, this gradual addition of formaldehyde to the reaction solution might have an effect on the amount and type of derivatives generated in the RF reaction solution, as well. Thus, RF gels were prepared, using the methodology presented in Section 3.1, while adding the formaldehyde solution instantly at the beginning (standard method) or gradually over a 30 minute stirring period at ambient temperature, in order to investigate the effect of gradual addition of formaldehyde on the final textural properties, with varying R/C ratios. Nitrogen sorption isotherms, along with their corresponding pore size distributions (PSDs), obtained as discussed in Section 3.1, for samples prepared in this section are presented in Figure C.3, with a summary of their textural properties presented in Table C.1.

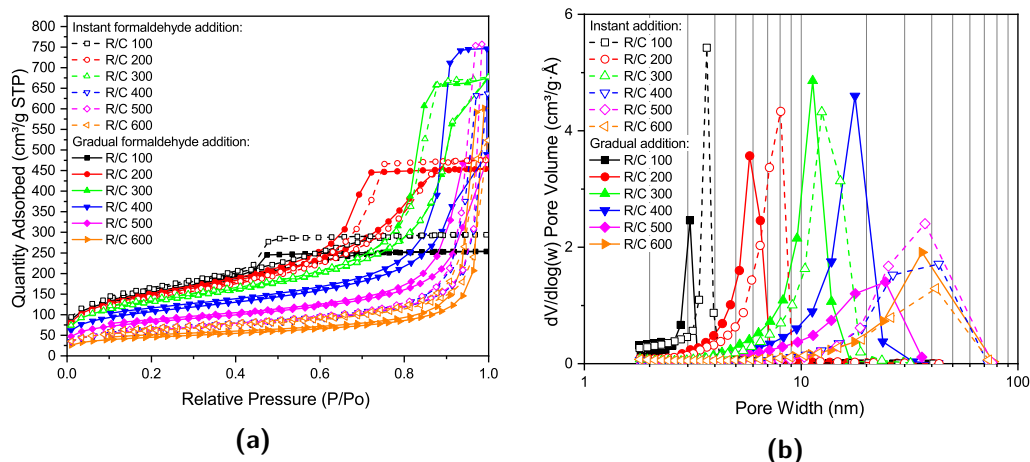


Figure C.3 (a) Nitrogen sorption isotherms for gels prepared with instant and gradual addition of formaldehyde and (b) corresponding pore size distributions

Comparing pore sizes found within the F gels obtained with instant and gradual addition of formaldehyde, presented in Figure C.3b, a relative shift of the distribution curves can be observed. For samples with lower R/C ratios (i.e. higher catalyst concentration), gradual addition of formaldehyde results in a shift of the observed PSD towards smaller pore sizes, with the effect less pronounced for RF gels prepared with higher R/C ratios. By starving the reaction system of formaldehyde in the initial stages, RF particles might grow more slowly and, potentially, to smaller sizes. This size difference would have a more pronounced effect on the overall smaller particles, present at lower R/C ratios, compared to their larger counterparts, found at higher R/C ratios.

Table C.1 Textural properties of gels prepared with instant and gradual formaldehyde addition

R/C	S_{BET} [m ² /g]		V_{T} [cm ³ /g]		V_{μ} [cm ³ /g]		$\bar{\phi}$ [nm]	
	Instant	Gradual	Instant	Gradual	Instant	Gradual	Instant	Gradual
100	580	540	0.46	0.39	0.06	0.06	3	3
200	500	530	0.73	0.70	0.05	0.05	6	5
300	470	470	1.05	1.04	0.06	0.06	10	10
400	220	390	0.98	0.76	0.03	0.06	24	14
500	230	300	1.17	0.74	0.03	0.04	28	14
600	220	160	0.81	0.93	0.04	0.02	21	28

S_{BET} - accessible surface area from BET analysis; V_{T} - total pore volume determined from adsorption at $p/p_0 \sim 1$; V_{μ} - micropore volume determined using t-plot method; $\bar{\phi}$ - average pore width from BJH analysis. Errors are omitted from the table as all values are reported to an accuracy less than the largest error for each variable.

Gradual addition of formaldehyde to RF reaction solution under stirring might also lead to a more even distribution of formaldehyde amongst the clusters growing within the solution, without pockets of higher local concentration, which could lead to more pronounced growth of certain clusters. In the case of formaldehyde added over a longer period, mixing would ensure that all the clusters are, on average, exposed to the same amount of formaldehyde, without the formaldehyde being depleted at a faster rate by some of the clusters. Dynamic equilibrium of RF cluster growth might also be altered, due to a lower concentration of free formaldehyde present during gradual addition, as it is consumed by the reaction, compared to a high formaldehyde concentration present in the solution after instant addition of the whole amount. The change in solution pH is also more gradual, compared to instant formaldehyde addition, due to the slightly acidic nature of formaldehyde and methanol, which are being added over a longer time period, leading to the reactions occurring at the initial stages at higher pH, and only at later stages would the solution pH decrease more significantly. Due to RF addition reactions favoured at more basic pH, this could lead to a higher extent of the addition reactions occurring during the initial stages with gradual formaldehyde addition. Due to the formalin solution containing ~ 63 wt% of water and methanol, the solids content of the solution remains higher for a longer time, again, resulting in the initial reactions occurring under different conditions, compared to the later stages. All of these effects might have an impact on RF cluster growth within the reaction solution, and thus, influencing the final structure of the RF gel prepared with a gradual addition of formaldehyde. However, a more thorough investigation of the aforementioned effects would be required in order to draw definite conclusions, which is beyond the scope of this work.

C.3 Gelation time

Within a gelling system, such as RF reaction solutions, when a three-dimensional structure spans throughout the reaction space, gelation is observed. This is attributed to the extent of chemical cross-links leading to an infinitely large molecule present within the system [206] and is usually associated with a significant increase in solution viscosity. There are different methods used for evaluation of the gelation point but, experimentally, the most simple method is a tilt test, as discussed below.

Experimentally, gelation time was assessed, in this work, by periodically tilting the reaction jars to an angle of 45° , as they were heated in an oven at 85°C . Sample gelation was assumed to have occurred when no flow was observed upon tilting the jar. Increasing R/C ratio (i.e. decreasing catalyst concentration) leads to longer gelation times, due to fewer larger RF particles growing to fill the reaction space, as discussed in Section 1.2.4. Increasing solids content decreases the gelation time, as a result of more material being present, leading to faster filling of the reaction space. The sample with 10 % solids content and R/C ratio 600 did not gel within the observed time frame and is, therefore, not included here.

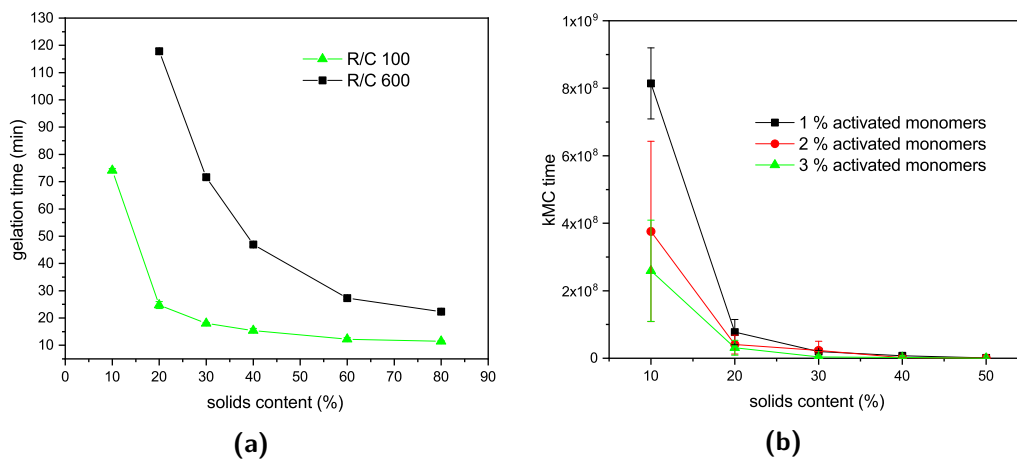


Figure C.4 Comparison of gelation time from (a) experiments and (b) simulation

In simulations, described in more detail in Section 4.1, gelation was assumed when only a single cluster aggregate remained. Due to the nature of kinetic Monte Carlo (kMC) simulation used in this work, each time increment corresponds to, on average, each species having one diffusive hopping attempt. The time evolution, used in this work, is described in more detail in Section 4.1.1. A trend similar to the experimental data obtained, as described above and presented in Figure C.4a, can be observed in Figure C.4b. Even though similar trends are observed for experimental and simulation results in this section, a more in-depth study would be required to compare these data directly. In experiments, gelation time observed most likely occurs before there is only a single cluster aggregate remaining in the solution, with some of the material still dissolved in the form of smaller aggregates.

Appendix D

Publications

D.1 Published

D.1.1



Article

Process Variable Optimization in the Manufacture of Resorcinol–Formaldehyde Gel Materials

Martin Prostedný, Mohammed G. M. Abduljalil, Paul A. Mulheran and Ashleigh J. Fletcher * 

Department of Chemical and Process Engineering, University of Strathclyde, Glasgow G1 1XJ, UK; martin.prostedny@strath.ac.uk (M.P.); mohammed.abduljalil@strath.ac.uk (M.G.M.A.); paul.mulheran@strath.ac.uk (P.A.M.)

* Correspondence: ashleigh.fletcher@strath.ac.uk; Tel.: +44-(0)-141-548-2431

Received: 15 December 2017; Accepted: 12 April 2018; Published: 17 April 2018



Abstract: Influence of process parameters of resorcinol–formaldehyde xerogel manufacture on final gel structure was studied, including solids content, preparation/drying temperature, solvent exchange, and drying method. Xerogels produced using a range of solids content between 10 and 40 *w/v*% show improved textural character up to 30 *w/v*% with a subsequent decrease thereafter. Preparation/drying temperature shows a minimal threshold temperature of 55 °C is required to obtain a viable gel structure, with minimal impact on gel properties for further thermal increase. Improving the solvent exchange method by splitting the same amount of acetone used in this phase over the period of solvent exchange, rather than in a single application, shows an increase in total pore volume and average pore diameter, suggesting less shrinkage occurs during drying when using the improved method. Finally, comparing samples dried under vacuum and at ambient pressure, there seems to be less shrinkage when using vacuum drying compared to ambient drying, but these changes are insubstantial. Therefore, of the process parameters investigated, improved solvent exchange seems the most significant, and it is recommended that, economically, gels are produced using a solids content of 20 *w/v*% at a minimum temperature of 55 °C, with regular solvent replenishment in the exchange step, followed by ambient drying.

Keywords: xerogel; Brunauer-Emmett-Teller theory; Barrett-Joyner-Halenda analysis; temperature; solids content; drying; solvent exchange

1. Introduction

Resorcinol–formaldehyde (RF) aerogels are a family of porous materials, first discovered in 1989 [1] by Pekala, and which have seen extensive application, due to their tailorable textural properties, in a range of applications, including as catalyst supports [2–4], in gas storage systems [5,6] and gas separation devices [7,8], in the fabrication of fuel cells [9,10], and as a core component in insulation [11,12]. The control of the porous character of these materials underpins their vast applicability, allowing tailored synthesis in terms of surface area, pore volume and pore size; however, the mechanism by which these gel materials form is not completely understood and there is significant scope for materials and process optimization.

It is generally accepted that the sol-gel polycondensation reaction of resorcinol (R) and formaldehyde (F) proceeds as shown in Figure 1; the reaction is also usually performed at above ambient temperatures. The reaction can be seen to proceed via an initial addition reaction between R and F, forming a hydroxymethyl derivative species, which undergoes self-condensation to create oligomeric chains that form clusters, and finally, a cross-linked 3D gel network. Our previous work, utilizing light scattering techniques, has provided insight into the mechanism of cluster growth, whereby, in a system with fixed reaction parameters, thermodynamics controls the size of growing

clusters, while there is kinetic control of cluster population [13]. The reaction is promoted by the presence of a metal salt, known within the field as a catalyst. The most commonly used catalyst is sodium carbonate (Na_2CO_3), as originally used by Pekala, and the role of the metal carbonate is thought to be two-fold. While the carbonate is known to act as a base, promoting the initial reaction between resorcinol and formaldehyde through proton abstraction, the metal ion is thought to stabilise the colloidal suspension involved in development of clusters dispersed within the solvent matrix [14]. Hence, many studies have previously focused on the use of different catalytic species to control the final gel material [13–19]. However, it should be noted that the polycondensation reaction can also be influenced by a variety of other synthesis parameters, resulting in a modification of the porous character of the final aerogel product [20,21]. This includes synthesis parameters such as resorcinol to carbonate molar ratio (R/C) and the mass of solids dissolved within a fixed volume of solvent (deionised water) [22], as well as process variables, which can also affect the end material. Recent research has shown that both the time allowed for the reaction mixture to be stirred before heating [23], and the shape of the mould used to form the RF aerogel [24], can also have a significant effect on the internal structure of the gel product. The post-synthetic processing of RF gels is also subject to significant variation, in terms of solvent exchange and drying methods used, the former is usually selected to enhance the latter. Drying methods include supercritical drying, freeze drying or ambient temperature drying, with or without vacuum.

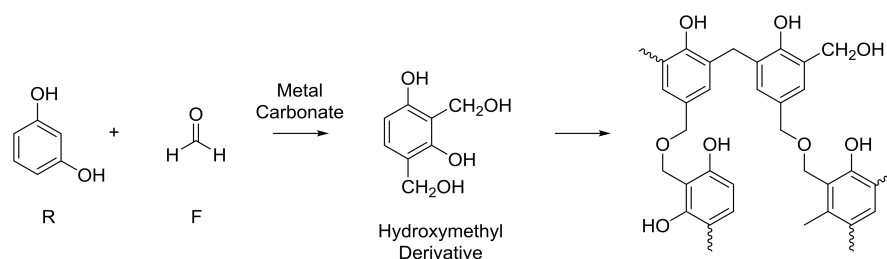


Figure 1. General reaction mechanism proposed in the reaction of resorcinol and formaldehyde. R: resorcinol; F: formaldehyde.

Kistler was instrumental in developing the first aerogels from silica based materials, and in his work, he had observed that evaporative drying results in destructive forces acting on the pore walls as a consequence of surface tension, and subsequent collapse of the gel [25]; he also established that, due to the high critical temperature and pressure of H_2O [26], and its poor solubility in supercritical solvents [27], the water entrained within the gel first had to be exchanged with a solvent that was completely miscible with the supercritical solvent. Following this work, the Lawrence Berkeley Laboratory [28] discovered that supercritical CO_2 could be used as a direct solvent replacement in the drying of silica aerogels [28], presenting a safer route to gel production. Pekala subsequently used this discovery, in conjunction with previous knowledge on RF resins to prepare organic aerogels [1,29]. Further studies, since then, discovered that other drying methods can be used, e.g., conventional evaporative drying to form xerogels [30] and freeze drying to form cryogels [31–34]. Czakkel et al. [32] compared the effects of evaporative drying in an inert atmosphere, freeze drying and supercritical drying, on the textural properties of RF gels, and found that the cryogels exhibited the highest pore volumes and surface areas due to the improved solvent quality of *t*-butanol; the evaporative samples showed less developed structures due to increased shrinkage arising from the formation of a liquid–vapour interface and resultant surface tension [20]. This indicates that the final drying step is critical to retention of porous character; however, Jabeen also demonstrated that exchanging entrained water with a solvent of lower surface tension reduced gel shrinkage and, as a result, increased pore volume [35]. The results indicate that, even in the event of a prolonged solvent exchange, residual water is retained within the pores of the gel, resulting in increased surface tension during drying,

and impacting on the porous structure obtained. Another way to avoid liquid–vapour interfaces is to use freeze-drying [12–15]. It has been noted, in previous studies, that supercritical drying and freeze-drying are expensive to perform, and require specialist knowledge [34,36]; hence, a route to gel production that avoids such methods would be economically beneficial.

These previous works have established a base from which most researchers work to produce RF gels but, to date, there has been no overarching study that has investigated process optimization holistically, which is essential for the scaled production of these materials. Hence, the aim of this current work is to optimise synthesis parameters and process variables to provide tailored production of selected textural characteristics in the final material. This involves determination of the impact of the solvent exchange method, total solids content, and drying method used, with respect to with varying R/C ratio. This optimal system was then studied further by altering the temperature at which the steps of synthesis, curing and drying were all set, to determine the validity of the widely accepted temperature of 85 °C in the synthetic procedure, as this has potential impact on the basis of both economics and safety. Low temperature nitrogen sorption measurements were used to characterise the textural properties of the synthesised aerogels, allowing changes in the internal structure of the xerogel to be monitored and quantified.

2. Results and Discussion

2.1. Effect of Solvent Exchange Method

Gels, produced as outlined above, generally undergo solvent exchange for a period of three days with only an initial volume of acetone added to the drained, cured gel; however, this may not be the most appropriate method to retain the porous structure developed during synthesis. Due to the high surface tension value for water, over the synthetic temperature range used to produce RF gels, the process of drying hydrogels leads to significant shrinkage of the material, as a consequence of the resulting high stresses that act on the pore walls. Therefore, it is desirable to replace the water, entrained within the pores, with a liquid that exhibits a lower surface tension, and preferably a lower boiling point, than water, within the temperature range of interest. The surface tension of water is high, even at elevated temperatures, e.g., 67.94 N/m at 50 °C [37], and a number of alternative solvents, with reduced surface tensions e.g., amyl acetate, acetone, t-butanol and isopropanol [20,38], have been proposed for solvent exchange in previous studies; however, acetone offers an excellent combination of a reduction in surface tension (19.65 N/m at 50 °C [39]) and relatively low cost compared to alternative solvents. Hence, acetone was used for solvent exchange within this study.

Replacement of the liquid within the pores is driven by diffusion, although agitation is often used to enhance contact of the material and fresh solvent; hence, sufficient time is required for full exchange to occur. Another factor that is potentially important, in maximizing the level of exchange, is the water concentration gradient between the pore liquid and the bulk solvent surrounding the sample. To investigate the effect of the solvent exchange method used, three batches of gels, individually of 60 mL total liquid volume, were synthesised, each of which, after curing, were washed with acetone, drained and, subsequently, agitated in acetone for three days. The key difference was that the first two batches were used to investigate the effect of a different volume of acetone used in one application and were processed by adding the entire volume of acetone at the beginning of the three days, namely 180 or 240 mL, and the sample was left without further handling for the whole solvent exchange period, while the third batch was treated with a fresh volume of acetone each day for three successive days with the total volume of acetone used adding up to 240 mL, thus maintaining the same total volume of acetone as the second batch but splitting the total volume over multiple days.

The data obtained for the pore size distributions of the three batches of gels are shown in Figure 2, and it can be seen that changing the acetone bath daily has a more pronounced positive effect on the total pore volume of the RF gel samples compared to just increasing the total acetone volume without changing the bath daily, especially for samples with lower R/C ratios. Improving the solvent exchange

method, by increasing the concentration gradient daily, leads to pores with larger average diameter (Table 1). This, coupled with the increase in pore volume, is ascribed to a reduction in shrinkage during the drying stage. If the acetone bath is replaced daily, the water concentration gradient is renewed every day, thus there is an increased driving force, which removes more water from the pores. This leads to lower stresses being exerted on the pore walls during the drying stage, due to the lower surface tension of acetone compared to water. However, for samples with higher R/C ratios exhibiting a weaker gel structure, the improved method does not seem to have the same pronounced positive effect observed for the lower R/C gels with smaller average pore diameter. A possible explanation is that when the acetone bath is exchanged daily, the replenishment step slightly damages the softer structure, resulting in lower values of surface area and pore size. The findings from this section of work suggest that there is significant advantage in using an improved solvent exchange method for most of the samples, hence, all samples in the following sections were prepared using daily replenishment of acetone within the solvent exchange stage, with the intention of maintaining the gel structure as close to the original hydrogel structure as possible, without the need to use cryogenic or supercritical processing steps. It is important to note that, in order to obtain improved gel characteristics, it is not necessary to increase the amount of acetone used during the solvent exchange, rather it is imperative to split this amount over the exchange period.

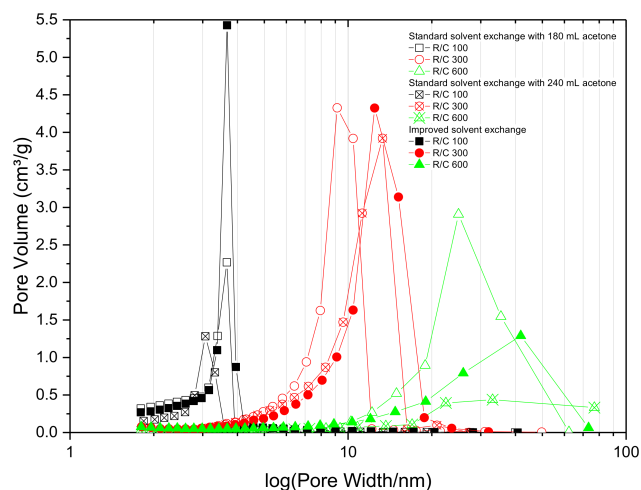


Figure 2. Effect of solvent exchange method on pore size distribution for resorcinol–formaldehyde xerogels with varied resorcinol:carbonate (R/C) molar ratio.

Table 1. Textural properties of resorcinol–formaldehyde xerogels prepared with standard and improved solvent exchange.

R/C	S_{BET} (m^2/g)			V_{T} (cm^3/g)			V_{μ} (cm^3/g)			$\bar{\varphi}$ (nm)		
	Acetone Exchange Method			Acetone Exchange Method			Acetone Exchange Method			Acetone Exchange Method		
	Standard	240 mL	Improved	Standard	240 mL	Improved	Standard	240 mL	Improved	Standard	240 mL	Improved
100	480	470	580	0.33	0.33	0.46	0.052	0.046	0.059	3	3	3
200	470	530	500	0.54	0.71	0.73	0.040	0.056	0.052	5	5	6
300	420	430	470	0.78	0.93	1.05	0.043	0.052	0.060	8	10	11
400	370	300	220	0.97	0.95	0.99	0.046	0.035	0.033	12	14	24
500	300	220	230	0.97	0.96	1.17	0.039	0.033	0.034	16	24	29
600	230	110	220	1.01	0.44	0.81	0.036	0.019	0.036	24	27	22

S_{BET} —surface area from Brunauer-Emmett-Teller (BET) analysis; V_{T} —total pore volume determined from adsorption at $p/p^{\circ} \sim 1$; V_{μ} —micropore volume determined using t-plot method; $\bar{\varphi}$ —average pore width from Barrett-Joyner-Halenda (BJH) analysis. Errors are omitted from the table as all values are reported to an accuracy less than the largest error for each variable.

2.2. Effect of Changing Solids Content

There is a tendency within the literature to use solids contents of ~ 20 w/v% in the production of RF gels [13,14,40,41]; however, the amount of solid material within the reaction volume would be expected to affect the solid:liquid ratio, hence, the final gel characteristics. Here, RF gels were synthesised over the range of solids content between 10 and 40 w/v%, using R/C ratios of 100, 300 and 600. Note that these samples were prepared at 85 °C, using improved solvent exchange (see Section 2.1) and vacuum drying (see Section 2.3). For the samples synthesised using a solids content of 10 w/v%, gelation was unsuccessful for R/C ratios greater than 600, hence, the range used in this study, but it should be noted that R/C ratio can be increased as the solids content increases but would not allow a direct comparison within this work, thus R/C 600 was the highest value studied here. For solids contents ≥ 20 w/v%, some of the samples exhibited cracking during the drying stage, which affected their final characteristics.

From Table 2, it can be observed that, at constant R/C molar ratio, there is no significant change in specific surface area as mass content changes; however, the total pore volume is seen to increase with solids content, up to ≤ 30 w/v%, after which point, the pore volume is slightly reduced at low R/C but still increases at higher R/C values. This can be ascribed to interplay between R/C ratio, i.e., particle nucleation number, and solids content, i.e., available material for particle growth; this means that the higher R/C ratios are more greatly affected by the additional mass available, due to the lower number of particles formed. The decrease at low R/C may be attributable to inhomogeneity during the gelation process, when no active agitation is applied, or possibly due to the increased mass per unit volume, which increases the relative density and reduces the void space available. Similarly, at constant R/C molar ratio, the average pore size increases with increasing solids content, again to 30 w/v%, whereupon it decreases steadily with increasing reactant concentration. Increasing the mass of reactants at a fixed R/C ratio, increases both the monomer concentration and that of sodium carbonate, as the catalyst, which leads to an increase in the number of particles formed during gelation; this could result in the observed decrease in average pore size. It should be noted that the pore diameters determined for R/C 100 are constant at three nanometers; however, differentiation at this level is hindered by the size of the probe molecule, which only allows integer values to be reported.

Table 2. Textural properties of resorcinol–formaldehyde xerogels prepared using different percentage solids contents.

w/v% Solids	S_{BET} (m ² /g)			V_{T} (cm ³ /g)			V_{μ} (cm ³ /g)			$\bar{\varphi}$ (nm)		
	R/C Ratio			R/C Ratio			R/C Ratio			R/C Ratio		
	100	300	600	100	300	600	100	300	600	100	300	600
10	500	370	-	0.36	0.85	-	0.057	0.037	-	3	9	-
20	500	490	280	0.32	0.91	1.00	0.065	0.064	0.046	3	8	18
25	550	410	190	0.42	1.00	1.07	0.054	0.042	0.030	3	10	32
30	570	490	260	0.46	1.08	1.17	0.055	0.064	0.045	3	9	28
35	570	450	260	0.45	0.98	1.23	0.051	0.050	0.038	3	9	27
40	540	550	330	0.44	1.07	1.53	0.048	0.077	0.056	3	9	29

S_{BET} —surface area from BET analysis; V_{T} —total pore volume determined from adsorption at $p/p^{\circ} \sim 1$; V_{μ} —micropore volume determined using t-plot method; $\bar{\varphi}$ —average pore width from BJH analysis. Errors are omitted from the table as all values are reported to an accuracy less than the largest error for each variable.

Figure 3 shows the pore size distribution of RF gel samples prepared at a constant R/C molar ratio of 300, and using different percentage solids contents. It can be seen that there is no significant change in the pore size distribution as the reactant concentration changes; however, it can be observed that RF gels with solids contents of 25 and 30 w/v% exhibit the narrowest distribution, with a sharp peak at ~ 15 nm. From Figure 4, meanwhile, it is obvious that altering the solids content has no major effect on overall shape of the adsorption–desorption isotherm of N₂, with all samples exhibiting Type IV isotherms [42]. The quantity of N₂ adsorbed increases with increasing relative pressure and a solids

content of 30 $w/v\%$ shows the highest adsorption capacity of all levels tested. The combination of a discrete pore size distribution and high pore volume (Table 2) indicates that the selection of 20 $w/v\%$ in the synthetic matrix is in line with process optimization.

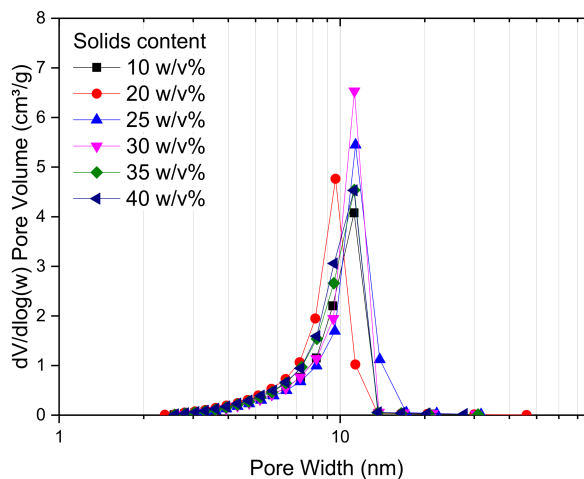


Figure 3. Pore size distribution obtained for resorcinol–formaldehyde xerogels synthesised using a resorcinol:cataylst molar ratio of 300 and varied percentage solids contents.

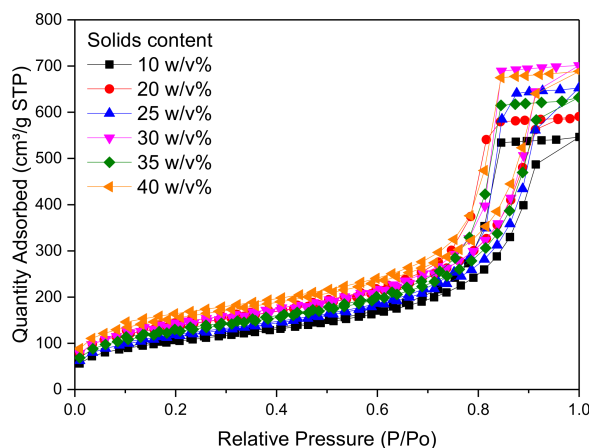


Figure 4. Nitrogen adsorption-desorption isotherms obtained for resorcinol–formaldehyde xerogels using a resorcinol:cataylst molar ratio of 300 and varied percentage solids content.

2.3. Ambient Pressure vs. Vacuum Drying

The final stage of gel preparation is drying of solvent exchanged gels, which, in this case, involves subcritical drying of the gels to remove acetone. The gels prepared in this way exhibit a higher degree of shrinkage; however, it is much easier to implement, and more economical, when compared to supercritical drying with CO_2 . Usually, in order to make the drying process faster, and to ensure that the final materials have been dried thoroughly, vacuum drying is utilised. Maintaining a vacuum during drying is also not inexpensive, so it would be beneficial if RF gels could be dried under ambient pressure at elevated temperature, while retaining their final properties. Therefore, a series of gel samples were prepared, where the gel sample was divided in two halves post improved solvent exchange. This ensured that any effects observed within the final structure only resulted from the

selected drying procedure. One half of the sample was dried for two days under vacuum at 85 °C, while the other half was dried under ambient pressure at 85 °C for one day and subsequently moved to the vacuum oven with the other sample half for one day of further drying, this time sub-atmospherically. Most of the drying process occurs during the first day; while the second day is used to remove the final traces of acetone remaining in the pores.

Table 3 shows the textural properties obtained for the gels prepared as outlined above. It can be observed that even though the gels dried under vacuum tend to have higher surface areas, pore volumes, micropore volumes, and larger average pore widths, the differences are insubstantial. This means that, if the requirements for the final material are not too strict, it should be possible to initially dry RF gels at ambient pressure, potentially even in the same oven as is used for gelation, since the temperatures are equivalent. From an industrial perspective, this could result in significant cost savings associated with the drying process of RF gels, and the handling of materials between unit operations, and could make such materials potentially cost-effective for new applications.

Table 3. Textural properties of resorcinol–formaldehyde gels dried at ambient pressure and under vacuum.

R/C	S_{BET} (m ² /g)		V_{T} (cm ³ /g)		V_{μ} (cm ³ /g)		$\bar{\varphi}$ (nm)	
	Drying Method		Drying Method		Drying Method		Drying Method	
	Ambient	Vacuum	Ambient	Vacuum	Ambient	Vacuum	Ambient	Vacuum
100	510	600	0.45	0.47	0.037	0.064	4	3
300	380	460	1.11	1.12	0.044	0.064	13	12
600	90	120	0.31	0.54	0.014	0.023	19	30

S_{BET} —surface area from BET analysis; V_{T} —total pore volume determined from adsorption at $p/p^{\circ} \sim 1$; V_{μ} —micropore volume determined using t-plot method; $\bar{\varphi}$ —average pore width from BJH analysis. Errors are omitted from the table as all values are reported to an accuracy less than the largest error for each variable.

2.4. Influence of Synthetic and Processing Temperature

In light of the three previous steps, it seems reasonable that the preparation of gels using 20 w/v% solids content, with an improved solvent exchange step and either ambient or vacuum drying should yield reasonably optimal materials. The constraint of several process variables also indicates that it should be possible to obtain materials with a high degree of reproducibility; however, this is dependent on control of one significant parameter, which can have significant impact on the overall process costs, i.e., temperature. The first stages of resorcinol–formaldehyde (RF) gel formation, immediately after mixing the components, are gelation and curing, which are usually carried out at elevated temperatures, and the final processing steps of gel production also include the use of a raised temperature during drying. Hence, the final parameter studied here was the influence of temperature within the manufacturing process. In all previous experiments, 85 °C was selected as the gelation and curing temperature as gels previously obtained at this temperature have exhibited a viable structure, and it is also a commonly used value in the literature, allowing further comparisons to be made to previously reported results [20,43,44]. It has, however, been shown that RF cluster particles begin to grow once the solution reaches a temperature of at least 55 °C [13], which indicates a minimum threshold for investigation; since water is used as the solvent, in the synthesis outlined above, the upper temperature limit is, therefore, set by the boiling point of water. Thus, the chosen temperature range studied was 45–95 °C, with 10 °C intervals. This allowed the region both above and below the temperature necessary for cluster growth to be probed to determine whether a viable gel structure can be established and maintained at temperatures approaching both (i) the boiling point of water and (ii) lower, less energy demanding, temperatures. R/C ratio was varied, as required, but all other synthesis parameters were kept constant as stated above; the only other change was that of oven temperature during the gelation and drying stages. Due to the enhanced performance observed above, improved solvent exchange was used exclusively, and the drying temperature, used in the vacuum

stage, matched the gelation and curing temperatures, in order to restrict any post gelation changes in structure caused by exposure to a higher temperature during drying.

Table 4 shows the textural properties for gels synthesised at different temperatures, obtained from nitrogen adsorption analysis. Gels prepared at lower temperatures either did not gel or exhibited a very weak structure that did not withstand the drying process; this led to materials with a low degree of porosity or even to non-porous materials. The effect of temperature can be seen more clearly in Figure 5, where the influence of gel preparation temperature, and R/C ratio, on Brunauer-Emmett-Teller (BET) surface area is shown. It can be seen that, at low temperatures (45 and 55 °C), the surface areas obtained are very low, and are essentially independent of the R/C ratio used. At higher temperatures, the BET surface area seems to be only slightly dependent on temperature, and the effect of catalyst concentration dominates as the major factor in determining the final gel structure properties. These results are in disagreement with results from Tamon and Ishizaka [45] who reported that gelation temperature had no influence on the final gel structure. The difference is likely ascribed to the fact that their gelation step at either 25 or 50 °C was followed by a curing period of five days at 90 °C. Thus, the influence of the lower temperature gelation stage would have been masked by subsequent exposure to the same higher temperature during the curing stage.

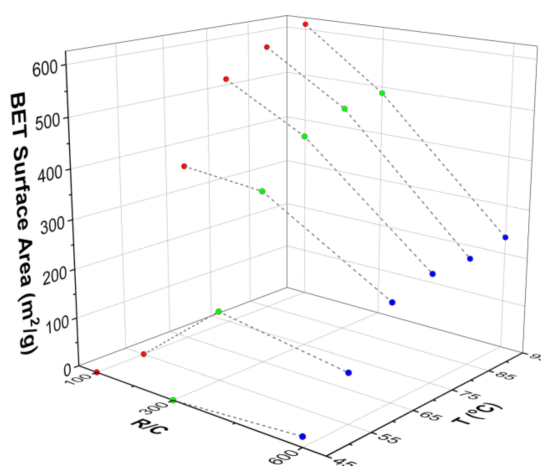


Figure 5. Dependence of BET surface area on resorcinol–formaldehyde xerogel preparation temperature and resorcinol:catalyst (R/C) molar ratio.

Table 4. Textural properties of resorcinol–formaldehyde xerogels prepared at different temperatures.

T (°C)	S_{BET} (m ² /g)			V_{T} (cm ³ /g)			V_{μ} (cm ³ /g)			$\bar{\varphi}$ (nm)		
	R/C Ratio			R/C Ratio			R/C Ratio			R/C Ratio		
	100	300	600	100	300	600	100	300	600	100	300	600
45	-	<1	20	-	-	0.07	-	-	0.002	-	-	9
55	<1	140	100	-	0.14	0.48	-	0.010	0.011	-	4	22
65	370	350	200	0.22	0.52	0.82	0.054	0.036	0.027	3	6	20
75	530	440	220	0.37	0.77	0.82	0.064	0.052	0.030	3	8	21
85	580	470	220	0.46	1.05	0.81	0.059	0.060	0.036	3	11	22
95	610	490	230	0.52	1.18	0.92	0.057	0.064	0.038	4	12	24

S_{BET} —surface area from BET analysis; V_{T} —total pore volume determined from adsorption at $p/p^{\circ} \sim 1$; V_{μ} —micropore volume determined using t-plot method; $\bar{\varphi}$ —average pore width from BJH analysis. Errors are omitted from the table as all values are reported to an accuracy less than the largest error for each variable.

Pore size distributions for the suites of samples prepared using different temperatures, and R/C ratio 300, are presented in Figure 6, and the results show that the pore size distribution shifts towards

larger pore diameters with increasing gelation temperature. This implies that gels prepared at higher temperatures develop stronger crosslinkages, which leads to a lower degree of shrinkage during the drying stage. It can also be observed that the total pore volume, which is given by the area under the pore size distribution curves, increases with increasing temperature, further supporting the theory that shrinkage is reduced within the stronger structures created at higher temperatures. The gels prepared at 45 °C exhibited such low porosity that the values are not even discernible in Figure 6, and are overlapped by other points; specific values are presented in Table 4.

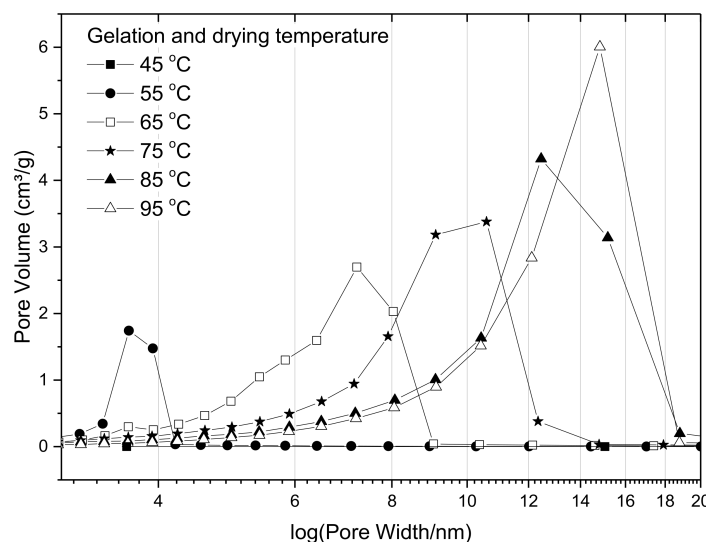


Figure 6. Effect of gelation temperature on pore size distributions for resorcinol–formaldehyde xerogels prepared using resorcinol:catalyst molar ratio of 300 and 20 *w/v*% solids content.

Morphological images of xerogel samples synthesised at 45 and 85 °C, with R/C ratios 100 and 600, are shown in Figure 7. It can be observed that the samples prepared with R/C ratio 100 do not show any significant textural features at this macroscopic level, which is expected considering the results from nitrogen sorption measurements. The pore size for these samples is below the limit at this magnification and due to the porous nature of the samples, it was not possible to achieve higher magnifications without using a higher thickness of gold coating, which would obscure any fine textural features. By contrast, there is a clear difference in morphology between the samples prepared with R/C 600 at different temperatures. The xerogel prepared at 85 °C (Figure 7d) exhibits a typical porous structure, composed of RF clusters crosslinked into a 3D network with some of the macropores clearly visible. While there are visible differences between samples prepared at 85 °C (Figure 7b,d), the xerogels prepared at 45 °C (Figure 7a,c) exhibit a very similar structure independent of catalyst amount. This agrees with the textural data obtained from nitrogen sorption measurements.

It is evident from these results that, in order to obtain a viable gel structure capable of enduring the drying process, the gelation temperature must be in excess of 55 °C, as suggested by Taylor et al. [13]; however, increasing the temperature further does not seem to have a significant impact on the surface area obtained. The other textural variables are affected slightly and it may be required to use elevated temperatures to optimise a particular variable or enhance the crosslinking within the final gel. This information could be used in process optimization of RF gel manufacture to reduce the heating costs associated with the gelation and drying processes for a specific set of required textural characteristics, as defined by a selected application.

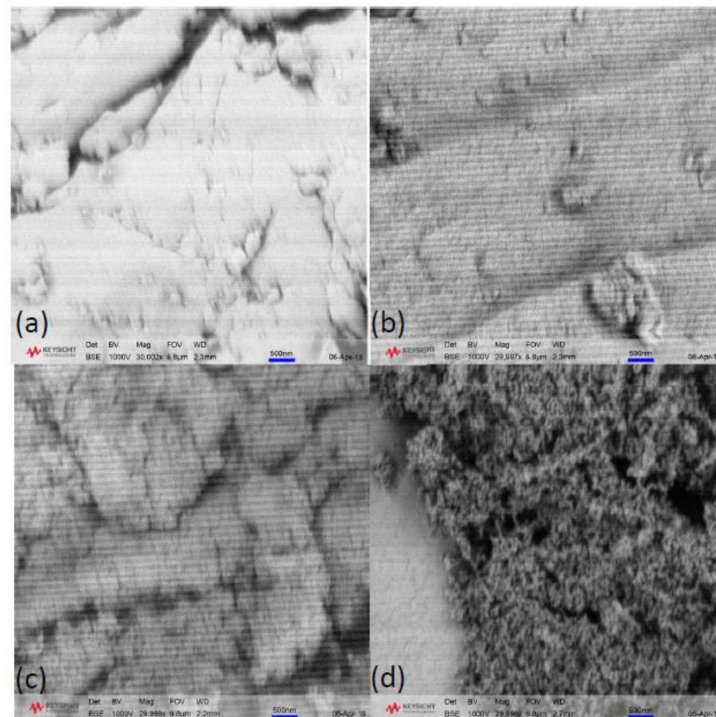


Figure 7. SEM micrographs of resorcinol–formaldehyde xerogels prepared at (a) 45 °C with resorcinol:catalyst molar ratio of 100, (b) 85 °C with resorcinol:catalyst molar ratio of 100, (c) 45 °C with resorcinol:catalyst molar ratio of 600, and (d) 85 °C with resorcinol:catalyst molar ratio of 600 at 30,000 \times magnification.

3. Conclusions

The work presented here demonstrates the need to carefully control the synthesis and process parameters used in RF gel production, in order to obtain the optimal material for a given application. Solids content is integral to gel viability, with low solids contents resulting in weaker structures that fail to gel at higher R/C ratios, and very high solids contents resulting in increased densification of the material and a reduction in porosity. It was observed that 30 $w/v\%$ represents an upper bound for solids content in the systems studied here, and such materials exhibited the highest accessible pore volume; however, surface area was unaffected by increased mass, at constant R/C. It is suggested that the increased mass of reactants (both monomer and catalyst) increased particle number and decreased average pore size. Within the systems studied, those gels created using solids contents of 20–30 $w/v\%$ exhibited the narrowest distribution; thus, the combination of discrete pore size distribution and high pore volume, with lower reactant costs, indicates 20 $w/v\%$ is optimal for gel production. In line with previous studies, a minimum temperature of 55 °C was shown to be critical in viable gel formation; gels prepared at lower temperatures either did not gel or exhibited a very weak structure with low or negligible porosity, independent of R/C. Gels prepared at higher temperatures showed insignificant changes in surface area with temperature, with the effect of catalyst concentration dominating gel formation; while pore diameter increases with increasing gelation temperature, due to stronger crosslinkages, hence, a lower degree of shrinkage during processing. This indicates that, while the gelation temperature must be in excess of 55 °C, increasing the temperature further has little impact on the final surface area, allowing a lower temperature to be used for gel synthesis if this is a key measure of gel performance. Post-synthesis, the regular replacement of the solvent exchange fluid has

a marked positive effect on total pore volume, leading to pores with larger average diameters, which is ascribed to a reduction in shrinkage during the drying stage, due to the increased driving force for water removal, hence, lower stresses being exerted on the pore walls during processing. It is, therefore, not necessary to increase the amount of solvent used within the exchange but it is imperative to increase the number of solvent changes over the exchange period. Finally, the differences between gels dried at atmospheric and sub-atmospheric pressure show little difference in their textural character, hence, it may be possible to dry RF gels at ambient pressure, potentially even in the same oven as gelation, to reduce both heating and pump costs. Combined, these results provide guidance to reduce the costs of RF gel manufacture, without impinging on the desired qualities of the materials produced.

4. Materials and Methods

4.1. Sample Preparation

Unless otherwise stated, all resorcinol–formaldehyde (RF) gel samples were prepared using an analogous procedure, excepting for the specific parameter investigated in each section of the study. All chemicals were used as received from the supplying company, and deionised water was produced in-house (Millipore Elix[®] 5 with Progard[®] 2 (Merck, Watford, UK)). Firstly, the appropriate amount of resorcinol (Sigma Aldrich, Gillingham, UK, ReagentPlus, 99%) was added to a premeasured volume of deionized water in a jar containing a magnetic stirrer bar. Upon dissolution of all of the added resorcinol, a corresponding amount of sodium carbonate (Sigma Aldrich, anhydrous, $\geq 99.5\%$), on a molar basis, was weighed out and added to the solution. As outlined above, sodium carbonate acts as a catalyst, by a combination of increasing the solution pH in the basic region via hydrolysis of the carbonate ion, and by the introduction of sodium ions, which, it has been suggested, assist in the addition of formaldehyde to resorcinol [46]. Catalyst concentration is expressed as resorcinol/catalyst molar ratio (R/C) and the range studied here is R/C 100–600. After all solids were dissolved, the required amount of formaldehyde, in the form of formalin solution (Sigma Aldrich, 37 wt % formaldehyde in water, containing 10–15 wt % methanol as a polymerization inhibitor), was added, and the solution was stirred in a closed jar for 30 min. All samples were prepared with 20 *w/v*% solids content, unless otherwise stated, and the total volume used was 60 mL, made up of water and methanol, contributed by the formalin solution used. At the end of the period of agitation, stirrer bars were removed from the solution, and the jar lid was hand-tightened, before moving the jar to an oven (Memmert UFE400, Schwabach, Germany) preheated to 85 °C, unless otherwise stated. Samples formed during this study gelled within 1–2 h [13]; however, samples were left to cure for three days in order to ensure sufficient time for crosslinking to occur. After three days, the jars containing the gels were removed from the oven and left to cool to room temperature. The formed gels were cut into smaller pieces before washing and solvent exchange with acetone (Sigma Aldrich, $\geq 99.5\%$). Standard solvent exchange involved addition of ~180 or ~240 mL of acetone to the drained gel, before resealing the lid and, in order to minimise acetone losses, wrapping with paraffin film. Sealed jars were put on a shaker unit (VWR 3500 Analog Orbital Shaker, Lutterworth, UK) and agitated for three days. In the improved solvent exchange method, the exchanged acetone was drained and replaced with 80 mL of fresh solvent on each successive day for three days. After three days of either solvent exchange method, the gel was drained and placed in a vacuum oven (Townson and Mercer 1425 Digital Vacuum Oven, Stretford, UK), preheated to 85 °C (or, in the case of the temperature study samples, the drying temperature was set to match the curing temperature), to dry for two days. Finally, the sample was transferred to a labelled sample tube for storage.

4.2. Sample Characterisation

Nitrogen adsorption-desorption measurements were used to obtain textural properties for the RF gel samples prepared in this study. Nitrogen sorption was performed at -196 °C using a Micromeritics ASAP 2420 (Hexon, UK) surface area and porosity analyser. Prior to analysis, samples were outgassed

under vacuum below 10 μmHg at 50 $^{\circ}\text{C}$ for 30 min and then at 110 $^{\circ}\text{C}$ for 2 h; except for samples where the influence of temperature was investigated, for these samples, outgassing temperatures matched the gelation and drying temperatures used, and the time for outgassing was adjusted accordingly to ensure removal of all volatile contaminant species. Samples were analysed using a 40 pressure point adsorption and 30 pressure point desorption cycle. All samples were characterised for surface area (m^2/g), using Brunauer-Emmett-Teller (BET) theory [47], and the Rouquerol correction for microporous samples [42]; total pore volume (cm^3/g); micropore volume (cm^3/g) from the t-plot method [48]; and average pore size (nm) from the Barrett-Joyner-Halenda method [49].

Scanning electron microscopy (SEM) micrographs were recorded in backscattered mode at 1000 V using a Field Emission Scanning Electron Microscope (Keysight, U9320B, Wokingham, UK) at magnification 30,000 \times . Prior to analysis, samples were ground into a fine powder, coated with a 10 nm gold layer using an EM ACE 200 sputter-coater (Leica Inc., Milton Keynes, UK), and attached to aluminium stubs with carbon tape.

Acknowledgments: Martin Prostedný thanks the University of Strathclyde and the Department of Chemical and Process Engineering for financial support. Mohammed G. M. Abduljalil thanks the Libyan Government for financial support. The authors would also like to acknowledge that the SEM analysis was carried out in the CMAC (Continuous Manufacturing and Crystallisation) National Facility, housed within the University of Strathclyde's Technology and Innovation Centre, and funded with a UKRPIF (UK Research Partnership Institute Fund) capital award, SFC (Scottish Funding Council) ref. H13054, from the Higher Education Funding Council for England (HEFCE).

Author Contributions: Martin Prostedný, Mohammed G. M. Abduljalil, Paul A. Mulheran and Ashleigh J. Fletcher contributed equally to conceiving and designing the experiments, analysing the data and writing and revising the manuscript. Martin Prostedný and Mohammed G. M. Abduljalil performed the experiments.

Conflicts of Interest: The authors declare no conflict of interest.

References

1. Pekala, R.W. Organic aerogels from the polycondensation of resorcinol with formaldehyde. *J. Mater. Sci.* **1989**, *24*, 3221–3227. [[CrossRef](#)]
2. Marie, J.; Berthon-Fabry, S.; Chatenet, M.; Chaînet, E.; Pirard, R.; Cornet, N.; Achard, P. Platinum supported on resorcinol–formaldehyde based carbon aerogels for PEMFC electrodes: Influence of the carbon support on electrocatalytic properties. *J. Appl. Electrochem.* **2007**, *37*, 147–153. [[CrossRef](#)]
3. Job, N.; Marie, J.; Lambert, S.; Berthon-Fabry, S.; Achard, P. Carbon xerogels as catalyst supports for PEM fuel cell cathode. *Energy Convers. Manag.* **2008**, *49*, 2461–2470. [[CrossRef](#)]
4. Smirnova, A.; Dong, X.; Hara, H.; Vasiliev, A.; Sammes, N. Novel carbon aerogel-supported catalysts for PEM fuel cell application. *Int. J. Hydrogen Energy* **2005**, *30*, 149–158. [[CrossRef](#)]
5. Robertson, C.; Mokaya, R. Microporous activated carbon aerogels via a simple subcritical drying route for CO_2 capture and hydrogen storage. *Microporous Mesoporous Mater.* **2013**, *179*, 151–156. [[CrossRef](#)]
6. Gross, A.F.; Vajo, J.J.; Van Atta, S.L.; Olson, G.L. Enhanced hydrogen storage kinetics of LiBH_4 in nanoporous carbon scaffolds. *J. Phys. Chem. C* **2008**, *112*, 5651–5657. [[CrossRef](#)]
7. Yamamoto, T.; Endo, A.; Ohmori, T.; Nakaiwa, M. Porous properties of carbon gel microspheres as adsorbents for gas separation. *Carbon* **2004**, *42*, 1671–1676. [[CrossRef](#)]
8. Dong, Y.-R.; Nakao, M.; Nishiyama, N.; Egashira, Y.; Ueyama, K. Gas permeation and pervaporation of water/alcohols through the microporous carbon membranes prepared from resorcinol/formaldehyde/quaternary ammonium compounds. *Sep. Purif. Technol.* **2010**, *73*, 2–7. [[CrossRef](#)]
9. Alcántara, R.; Lavela, P.; Ortiz, G.F.; Tirado, J.L. Carbon microspheres obtained from resorcinol-formaldehyde as high-capacity electrodes for sodium-ion batteries. *Electrochem. Solid-State Lett.* **2005**, *8*, A222–A225. [[CrossRef](#)]
10. Glora, M.; Wiener, M.; Petricevic, R.; Probstle, H.; Fricke, J. Integration of carbon aerogels in PEM fuel cells. *J. Non-Cryst. Solids* **2001**, *285*, 283–287. [[CrossRef](#)]
11. Lu, X.; Arduini-Schuster, M.; Kuhn, J.; Nilsson, O.; Fricke, J.; Pekala, R. Thermal conductivity of monolithic organic aerogels. *Science* **1992**, *255*, 971–972. [[CrossRef](#)] [[PubMed](#)]

12. Feng, J.; Zhang, C.; Feng, J. Carbon fiber reinforced carbon aerogel composites for thermal insulation prepared by soft reinforcement. *Mater. Lett.* **2012**, *67*, 266–268. [[CrossRef](#)]
13. Taylor, S.J.; Haw, M.D.; Sefcik, J.; Fletcher, A.J. Gelation mechanism of resorcinol-formaldehyde gels investigated by dynamic light scattering. *Langmuir* **2014**, *30*, 10231–10240. [[CrossRef](#)] [[PubMed](#)]
14. Taylor, S.J.; Haw, M.D.; Sefcik, J.; Fletcher, A.J. Effects of secondary metal carbonate addition on the porous character of resorcinol-formaldehyde xerogels. *Langmuir* **2015**, *31*, 13571–13580. [[CrossRef](#)] [[PubMed](#)]
15. Rey-Raap, N.; Angel Menéndez, J.; Arenillas, A. Simultaneous adjustment of the main chemical variables to fine-tune the porosity of carbon xerogels. *Carbon* **2014**, *78*, 490–499. [[CrossRef](#)]
16. Rey-Raap, N.; Angel Menéndez, J.; Arenillas, A. RF xerogels with tailored porosity over the entire nanoscale. *Microporous Mesoporous Mater.* **2014**, *195*, 266–275. [[CrossRef](#)]
17. Job, N.; Gommès, C.J.; Pirard, R.; Pirard, J.-P. Effect of the counter-ion of the basification agent on the pore texture of organic and carbon xerogels. *J. Non-Cryst. Solids* **2008**, *354*, 4698–4701. [[CrossRef](#)]
18. Fairen-Jimenez, D.; Carrasco-Marin, F.; Moreno-Castilla, C. Porosity and surface area of monolithic carbon aerogels prepared using alkaline carbonates and organic acids as polymerization catalysts. *Carbon* **2006**, *44*, 2301–2307. [[CrossRef](#)]
19. Laskowski, J.; Milow, B.; Ratke, L. Subcritically dried resorcinol-formaldehyde aerogels from a base-acid catalyzed synthesis route. *Microporous Mesoporous Mater.* **2014**, *197*, 308–315. [[CrossRef](#)]
20. Al-Muhtaseb, S.A.; Ritter, J.A. Preparation and properties of resorcinol-formaldehyde organic and carbon gels. *J. Adv. Mater.* **2003**, *15*, 101–114. [[CrossRef](#)]
21. El Khatat, A.M.; Al-Muhtaseb, S.A. Advances in tailoring resorcinol-formaldehyde organic and carbon gels. *Adv. Mater.* **2011**, *23*, 2887–2903. [[CrossRef](#)] [[PubMed](#)]
22. Tamon, H.; Ishizaka, H.; Mikami, M.; Okazaki, M. Porous structure of organic and carbon aerogels synthesized by sol-gel polycondensation of resorcinol with formaldehyde. *Carbon* **1997**, *35*, 791–796. [[CrossRef](#)]
23. Gaca, K.Z.; Parkinson, J.A.; Sefcik, J. Kinetics of early stages of resorcinol-formaldehyde polymerization investigated by solution-phase nuclear magnetic resonance spectroscopy. *Polymer* **2017**, *110*, 62–73. [[CrossRef](#)]
24. Rojas-Herrera, J.; Lozano, P.C. Mitigation of anomalous expansion of carbon xerogels and controllability of mean-pore-size by changes in mold geometry. *J. Non-Cryst. Solids* **2017**, *458*, 22–27. [[CrossRef](#)]
25. Pierre, A.C.; Pajonk, G.M. Chemistry of aerogels and their application. *Chem. Rev.* **2002**, *102*, 4243–4265. [[CrossRef](#)] [[PubMed](#)]
26. Lide, D.R. *CRC Handbook of Chemistry and Physics, Internet Version 2006*; Taylor and Francis: Boca Raton, FL, USA, 2006.
27. Barbieri, O.; Ehrburger-Dolle, F.; Rieker, T.P.; Pajonk, G.M.; Pinto, N.; Rao, A.V. Small-angle X-ray scattering of a new series of organic aerogels. In Proceedings of the 6th International Symposium on Aerogels (ISA-6), Albuquerque, NM, USA, 8–11 October 2000; pp. 109–115.
28. Fricke, J.; Tillotson, T. Aerogels: Production, characterization, and applications. *Thin Solid Films* **1997**, *297*, 212–223. [[CrossRef](#)]
29. Pekala, R.W.; Kong, F.M. A synthetic route to organic aerogels-mechanism, structure, and properties. *J. Phys. Colloq.* **1989**, *50*, 33–40. [[CrossRef](#)]
30. Job, N.; Pirard, R.; Marien, J.; Pirard, J.P. Porous carbon xerogels with texture tailored by pH control during sol-gel process. *Carbon* **2004**, *42*, 619–628. [[CrossRef](#)]
31. Tamon, H.; Ishizaka, H.; Yamamoto, T.; Suzuki, T. Preparation of mesoporous carbon by freeze drying. *Carbon* **1999**, *37*, 2049–2055. [[CrossRef](#)]
32. Czakkel, O.; Marthi, K.; Geissler, E.; Laszlo, K. Influence of drying on the morphology of resorcinol-formaldehyde-based carbon gels. *Microporous Mesoporous Mater.* **2005**, *86*, 124–133. [[CrossRef](#)]
33. Yamamoto, T.; Nishimura, T.; Suzuki, T.; Tamon, H. Control of mesoporosity of carbon gels prepared by sol-gel polycondensation and freeze drying. *J. Non-Cryst. Solids* **2001**, *288*, 46–55. [[CrossRef](#)]
34. Job, N.; They, A.; Pirard, R.; Marien, J.; Kocon, L.; Rouzaud, J.N.; Beguin, F.; Pirard, J.P. Carbon aerogels, cryogels and xerogels: Influence of the drying method on the textural properties of porous carbon materials. *Carbon* **2005**, *43*, 2481–2494. [[CrossRef](#)]
35. Jabeen, N.; Mardan, A. Effect of water removal on the textural properties of resorcinol/formaldehyde gels by azeotropic distillation. *J. Mater. Sci.* **1998**, *33*, 5451–5453. [[CrossRef](#)]

36. Schwertfeger, F.; Frank, D.; Schmidt, M. Hydrophobic waterglass based aerogels without solvent exchange or supercritical drying. *J. Non-Cryst. Solids* **1998**, *225*, 24–29. [[CrossRef](#)]
37. Vargaftik, N.; Volkov, B.; Voljak, L. International tables of the surface tension of water. *J. Phys. Chem. Ref. Data* **1983**, *12*, 817–820. [[CrossRef](#)]
38. Mukai, S.R.; Tamitsuji, C.; Nishihara, H.; Tamon, H. Preparation of mesoporous carbon gels from an inexpensive combination of phenol and formaldehyde. *Carbon* **2005**, *43*, 2628–2630. [[CrossRef](#)]
39. Jasper, J.J. The surface tension of pure liquid compounds. *J. Phys. Chem. Ref. Data* **1972**, *1*, 841–1010. [[CrossRef](#)]
40. Zanto, E.J.; Al-Muhtaseb, S.A.; Ritter, J.A. Sol-gel-derived carbon aerogels and xerogels: Design of experiments approach to materials synthesis. *Ind. Eng. Chem. Res.* **2002**, *41*, 3151–3162. [[CrossRef](#)]
41. Berthon, S.; Barbieri, O.; Ehrburger-Dolle, F.; Geissler, E.; Achard, P.; Bley, F.; Hecht, A.-M.; Livet, F.; Pajonk, G.M.; Pinto, N. DLS and SAXS investigations of organic gels and aerogels. *J. Non-Cryst. Solids* **2001**, *285*, 154–161. [[CrossRef](#)]
42. Thommes, M.; Kaneko, K.; Neimark, A.V.; Olivier, J.P.; Rodriguez-Reinoso, F.; Rouquerol, J.; Sing, K.S.W. Physisorption of gases, with special reference to the evaluation of surface area and pore size distribution (iupac technical report). *Pure Appl. Chem.* **2015**, *87*, 1051–1069. [[CrossRef](#)]
43. Calvo, E.; Menéndez, J.; Arenillas, A. Influence of alkaline compounds on the porosity of resorcinol-formaldehyde xerogels. *J. Non-Cryst. Solids* **2016**, *452*, 286–290. [[CrossRef](#)]
44. Lin, C.; Ritter, J.A. Effect of synthesis pH on the structure of carbon xerogels. *Carbon* **1997**, *35*, 1271–1278. [[CrossRef](#)]
45. Tamon, H.; Ishizaka, H. Influence of gelation temperature and catalysts on the mesoporous structure of resorcinol-formaldehyde aerogels. *J. Colloid Interface Sci.* **2000**, *223*, 305–307. [[CrossRef](#)] [[PubMed](#)]
46. GrenierLoustalot, M.F.; Larroque, S.; Grande, D.; Grenier, P.; Bedel, D. Phenolic resins: 2. Influence of catalyst type on reaction mechanisms and kinetics. *Polymer* **1996**, *37*, 1363–1369. [[CrossRef](#)]
47. Brunauer, S.; Emmett, P.H.; Teller, E. Adsorption of gases in multimolecular layers. *J. Am. Chem. Soc.* **1938**, *60*, 309–319. [[CrossRef](#)]
48. Lowell, S.; Shields, J.E.; Thomas, M.A.; Thommes, M. Micropore analysis. In *Characterization of Porous Solids and Powders: Surface Area, Pore Size and Density*; Springer: Berlin, Germany, 2004; pp. 129–156.
49. Barrett, E.P.; Joyner, L.G.; Halenda, P.P. The determination of pore volume and area distributions in porous substances. I. Computations from nitrogen isotherms. *J. Am. Chem. Soc.* **1951**, *73*, 373–380. [[CrossRef](#)]



D.1.2

Journal of Sol-Gel Science and Technology (2019) 89:21–28
<https://doi.org/10.1007/s10971-018-4595-0>

BRIEF COMMUNICATION: CHARACTERIZATION METHODS OF SOL-GEL AND HYBRID MATERIALS



The impact of deuterium oxide on the properties of resorcinol-formaldehyde gels

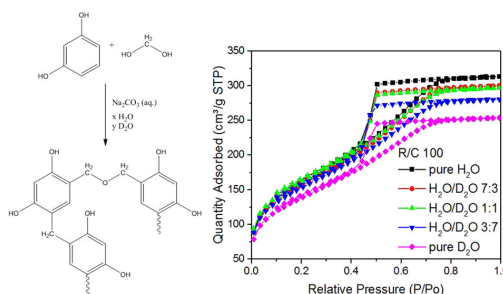
Martin Prostedny¹ · Jack Ballantine¹ · Jan Sefcik¹ · Ashleigh J. Fletcher¹

Received: 30 November 2017 / Accepted: 19 January 2018 / Published online: 12 February 2018
 © The Author(s) 2018. This article is an open access publication

Abstract

Resorcinol-formaldehyde gels offer a range of properties that can be exploited in a variety of applications, but better understanding of gel formation mechanisms is needed to enable rational control and optimisation of the physico-chemical characteristics of these materials. Our previous studies have focussed on investigating the formation pathways of these gels, using nuclear magnetic resonance and dynamic light-scattering techniques, as well as evaluating their final physical and chemical properties, via sorption and spectroscopic methods. Nuclear magnetic resonance has been used over the years to probe the chemical species formed during resorcinol-formaldehyde gel polymerisation, but the technique typically involves the prior addition of deuterium oxide to provide a deuterium lock for NMR measurements. However, the effect of deuterium oxide to resorcinol-formaldehyde systems is currently unknown, although the substitution of water by deuterium oxide has been previously reported to alter the chemical and physical properties of reacting systems. In this work we examine the effect of adding deuterium oxide to resorcinol-formaldehyde sol-gel synthesis at different dilution levels and the impact that this addition has on the final characteristics of the synthesised gels, in order to assess the validity of using NMR with a deuterium lock for the investigation of polymerisation mechanism in resorcinol-formaldehyde sol-gel processes.

Graphical Abstract



Keywords Isotope effect · Nuclear magnetic resonance · Xerogel · BET · Adsorption isotherm · Pore size

Highlights

- Successful synthesis of resorcinol-formaldehyde gels using D₂O as synthetic solvent
- D₂O shown to have insignificant effect on resorcinol-formaldehyde gel properties

✉ Ashleigh J. Fletcher
 ashleigh.fletcher@strath.ac.uk

¹ Department of Chemical and Process Engineering, University of Strathclyde, 75 Montrose Street, Glasgow G1 1XJ, UK

- High catalyst concentration systems less affected due to shorter gelation times
- Low catalyst concentration systems more greatly affected due to weaker structure
- Established use of D₂O in NMR studies of resorcinol-formaldehyde gels has minimal impact

1 Introduction

Resorcinol-formaldehyde (RF) gels were originally discovered a few decades ago [1]; however, despite numerous previous studies into the preparation and use of these materials, the mechanism of RF gel formation is still not fully understood. The original base-mediated procedure, using sodium carbonate, proposed by Pekala [1], is still one of the most commonly used [2–6]. It should be noted that the description of sodium carbonate, other metal carbonates or other bases used in the synthesis of RF gels as catalysts is not accurate, as these species are not recoverable after gel formation. However, following the convention of nomenclature within this field, the term catalyst will be used in this paper to refer to the base, here sodium carbonate, added to the synthetic matrix. In the synthesis of RF gels, the first step is an addition of formaldehyde to resorcinol. In a basic solution, resorcinol forms an anion with the negative charge concentrated at the ortho and para positions of the benzene ring. Consequently, positions next to these sites become chemically activated and subsequently react with formaldehyde. However, formaldehyde is present in a hydrated form as methylene glycol and its oligomers in aqueous solutions used in RF gel synthesis [7] and thus a range of hydroxymethyl derivatives are formed in the initial reaction step [8], as shown in Fig. 1.

This step is conventionally thought to be followed by a polycondensation reaction between hydroxymethyl derivatives [4]. However, we have recently established that the gel formation process involves a more subtle interplay of chemical and physical processes, where nanoscale clusters assemble early on in the at temperatures in excess of 55 °C [2], whereas no condensation products can be seen using liquid phase nuclear magnetic resonance (NMR) [8]. These clusters appear at elevated temperatures due to microphase separation or formation of mesostructured liquid phases containing initial hydroxymethyl resorcinol derivatives. Subsequent polycondensation is most likely to proceed within these clusters, which grow over time, as observed by dynamic light scattering until they fill the available space in the solution and/or there is complete consumption of at least one reactant. Depending on the amount of catalyst used, these clusters grow to different sizes. At higher R/C ratios (less catalyst), RF clusters grow into larger sizes, thereby leading to larger voids between the clusters as compared to lower R/C ratios (more catalyst) [2]. However, regardless of the catalyst concentration used, the reactions resulting in the formation and growth of the RF clusters remain the same, where the initial stages are chemically controlled processes,

followed by the physical formation and aggregation of clusters, thereby highlighting the interplay between chemistry and physics in development of the microstructure of RF gels.

As mentioned above, speciation at various stages of RF polymerisation has been previously probed, in order to better understand the processes involved in formation of RF gels, and reactions between formaldehyde and resorcinol have been studied using NMR. The species present in RF mixtures have been previously investigated by several researchers, including Werstler [9] who used ¹³C NMR (diluting samples by 20%, assumed here by volume, with D₂O), Christiansen [10] again using ¹³C NMR (with ~20% of solvent weight comprised of D₂O), and more recently by Lewicki et al. [11] using ¹H NMR (with samples quenched in deuterated DMSO-d₆) and by Gaca et al. [8] using a combination of ¹H, ¹³C and 2D [1H, 13C] heteronuclear single quantum coherence (HSQC) NMR (with samples prepared using water/D₂O (7:3 v/v) mixtures). We also investigated speciation in aqueous methanolic formaldehyde solutions using ¹H, ¹³C and 2D [1H, 13C] HSQC NMR (with samples prepared using water/D₂O (7:3 v/v) mixtures) under conditions used for RF polymerization, allowing the development of a detailed thermodynamic model accounting for oligomerization of methylene glycol species in such solutions [7]. Rivlin et al. [12] also recently investigated kinetics and equilibria in D₂O solutions of formaldehyde using ¹H and ¹³C NMR, providing equilibrium and rate constants of formaldehyde-based species.

As can be seen from previous literature, up to 20–30% of solvent by volume has been used to obtain a deuterium lock for NMR measurements, even in nominally aqueous solutions. However, it is well known that substitution of D₂O for H₂O may affect chemical and/or physical processes due to its different molecular weight, interactions (e.g., hydrogen bonding), density, viscosity, etc. This is generally ascribed to the differences in the hydrogen-bonded structures of D₂O and H₂O, as reflected in many thermodynamic properties [13], and results from differences in the zero-point energy of the two species as a consequence of the dissimilarity in mass [14, 15]. Diffusional rate differences have long been related to mass differences [16], where the heavier species exhibits reduced mobility. However, there are many instances where substitution with a heavier isotope results in an increase in the rate of a process, known as an inverse isotope effect, as observed in a variety of systems [17–21]. It has also been reported that hydrophobic effects are more pronounced in D₂O compared with H₂O [22, 23] and the presence of D₂O can have an effect on phase separation temperature of

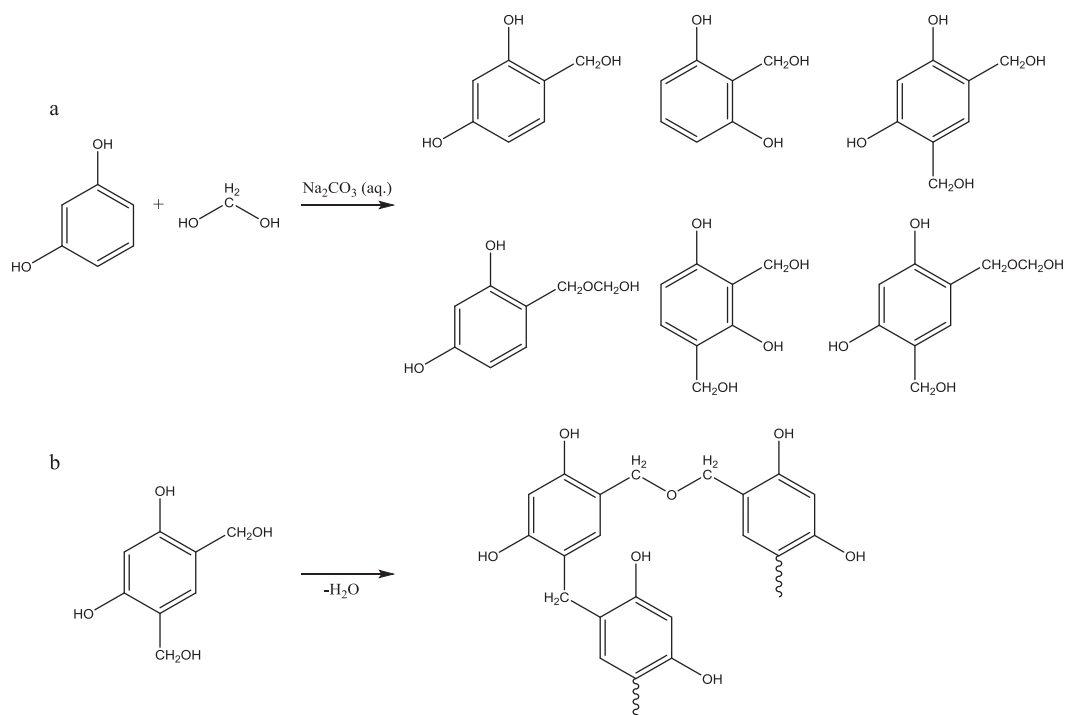


Fig. 1 a Reaction of resorcinol with formaldehyde in a basic aqueous solution showing number of different derivatives present in solution followed by **b** an example condensation reaction between hydroxymethyl derivatives

microemulsions [24], both of which would have an effect on the microphase separation of clusters during formation of RF gels. Hence, microstructure formation processes present in sol-gel systems, resulting from the interplay of chemical and physical processes, may be influenced by the mere presence of D₂O, as well as the quantitative amount of D₂O added to reaction mixtures, with the directionality of the effect also unknown; this may, therefore, limit the validity of insights about polymerisation and structure formation mechanisms obtained from previous NMR studies. It is imperative that these systems are studied in the gel form to eliminate any additional effects incurred by post-gel treatment, e.g., carbonisation. In this work we aim to assess the effects of added D₂O in RF sol-gel reaction mixtures on properties of resulting xerogels with a view to validating the use of NMR as a probe technique for the study of RF gels specifically, as well as a model for other polymeric materials.

2 Sample preparation

All RF gel samples were prepared using a procedure developed previously [2]. In order to investigate the

influence of deuterium oxide (D₂O) on the final properties of RF gels, samples with different H₂O/D₂O volumetric ratios were synthesized. Only water added to the system was taken into account for the ratio, omitting any water contributed by the formaldehyde stock solution. Samples with following H₂O/D₂O v/v ratios were prepared: 1 : 0 (pure water), 7 : 3, 1 : 1, and 0 : 1 (pure D₂O). These values were chosen in order to bracket values used in previous studies [8–10], where 30% D₂O was the highest dilution used by Gaca et al. [8]. All chemicals were used as received and deionised water was produced in-house (Millipore Elix 5 with Progard 2).

First, the appropriate amount of resorcinol (SigmaAldrich, ReagentPlus, 99%) was added to a premeasured volume of deionised water and/or D₂O (SigmaAldrich, 99.9 atom % D) in a jar containing a magnetic stirrer bar. Upon dissolution of all of the added resorcinol, a corresponding amount of sodium carbonate (SigmaAldrich, anhydrous, ≥ 99.5%), on a molar basis, was weighed out and added to the solution. Sodium carbonate drives the reaction by a combination of increasing the solution pH in the basic region, via hydrolysis of the carbonate ion, and by the introduction of sodium ions, which it has been suggested

assist the addition of formaldehyde to resorcinol [25]. As previously mentioned, sodium carbonate is termed a catalyst and its concentration is expressed as resorcinol/catalyst molar ratio (R/C) and R/C values of 100, 300 and 600 were studied here. After all the solids were dissolved, the required amount of stock formaldehyde solution (SigmaAldrich, 37 wt% formaldehyde in water, containing 10–15 wt% methanol as a formaldehyde polymerisation inhibitor) was added and the solution stirred in a closed jar for 30 min. All samples were prepared with 20 w/v% solids content and the total volume used was 30 ml, composed of water, deuterium oxide and methanol, contributed by the formalin solution used. At the end of the period of agitation, the stirrer bar was removed from the solution and the jar lid was hand tightened, before moving the jar to an oven (Memmert UFE400) preheated to 85 °C. Samples formed during this study gelled within 1–2 h [2], established by the lack of flow within the mixture when the jar was tilted at a 45° angle; however, samples were left to cure for 3 days in order to ensure sufficient time for crosslinking to occur. After 3 days, the jars containing the gels were removed from the oven and left to cool to room temperature. The formed gels were cut into smaller pieces before washing and solvent exchange with acetone (SigmaAldrich, ≥ 99.5%). Standard solvent exchange involved addition of ~40 ml of acetone to the gel, before resealing the lid and, in order to minimise acetone losses, wrapping the jar/lid junction with paraffin film. Sealed jars were put on a shaker unit (VWR 3500 Analog Orbital Shaker) and agitated for 3 days. Each successive day, the exchanged acetone was drained and replaced with 40 ml of fresh solvent. After 3 days of solvent exchanging, the gel was drained and placed in a vacuum oven (Towson and Mercer 1425 Digital Vacuum Oven), preheated to 85 °C, to dry for 2 days. Finally, the sample was transferred to a labelled sample tube for storage.

3 Sample characterisation

Nitrogen adsorption/desorption measurements were used to obtain textural properties for the RF gel samples prepared in this study. Nitrogen adsorption was performed at –196 °C using a Micromeritics ASAP 2420 surface area and porosity analyser. Before analysis, samples were outgassed under vacuum below 10 μm Hg at 50 °C for 30 min and then at 110 °C for 2 h. Samples were characterised using a 40-point adsorption and 30-point desorption cycle for surface area (m²/g), using Brunauer–Emmett–Teller (BET) theory [26] and the Rouquerol correction for microporous samples [27]; total pore volume (cm³/g) was calculated from the equilibrium measurement of nitrogen adsorbed at ~0.98 bar (i.e., the saturation vapour pressure of N₂ at 77 K), micropore volume (cm³/g) from the t-plot method [28] and average pore size (nm) from the Barrett–Joyner–Halenda method [29].

4 Results and discussion

Nitrogen adsorption/desorption data presented in Figs. 2 and 3 show a difference between the textural properties of gels prepared with different ratios of H₂O:D₂O in the reaction solution. The R/C 100 series exhibits a clear trend of decreasing accessible pore volume (Fig. 2a), determined from the highest point of the nitrogen adsorption isotherm, with increasing D₂O concentration, while maintaining a similar pore size distribution (Fig. 2b). The isotherms obtained are classified as Type IV(a) [27] for all R/C 100 samples and the hysteresis loop (Type H2(a)) is indicative of a collection of narrow-necked pores [27]. Despite the invariance in pore diameter that is observed for the R/C 100 samples, the marked reduction in pore volume with increasing dilution by D₂O is also evident in the pore size

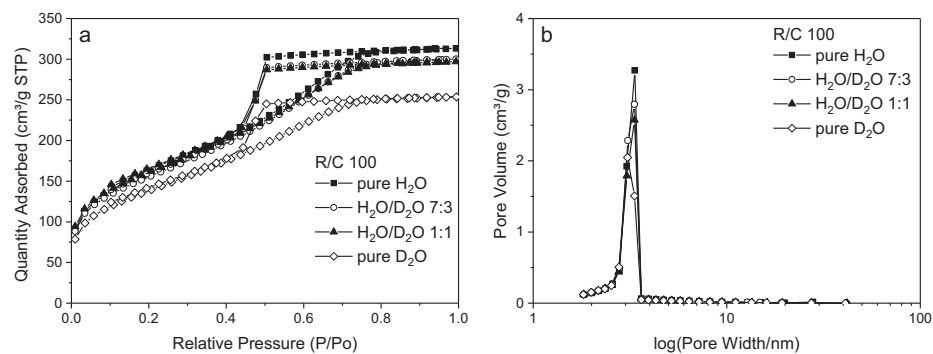


Fig. 2 **a** Nitrogen adsorption/desorption isotherms and **b** pore-size distributions gels prepared at R/C100

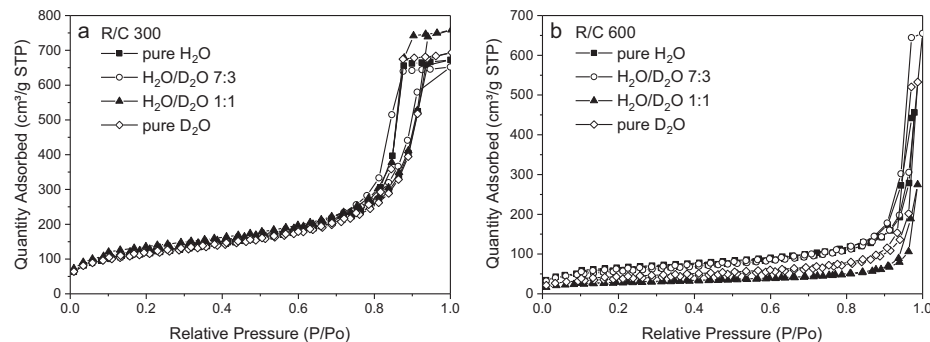


Fig. 3 Nitrogen adsorption/desorption isotherms for gels prepared at R/C ratios of **a** 300 and **b** 600

distribution series (Fig. 2b). By contrast, the samples with higher R/C ratios do not seem to follow an evident trend. Again, there is obvious alteration of the magnitude of adsorption; however, for both R/C 300 and R/C 600, the absolute isotherm shape is unaltered by the presence of D₂O (Fig. 3) and is also classified as Type IV(a) [27] in both cases. It is notable that the family of isotherms obtained for undeuterated RF gels are in agreement with those previously reported in the literature [2, 30]. Pore-size distributions are not shown for R/C ratios 300 and 600 due to the lack of a distinct plateau at the higher pressures in the isotherm data. The points very close to partial pressure $P/P_0 = 1$ are subject to variation, due to experimental errors at these conditions, including absolute temperature within the system and pressure differences; therefore, the estimated pore size distribution could be significantly affected and is not shown here. Correspondingly, we report the pore widths as the estimated average pore diameter. It is possible, however, to classify the hysteresis loops observed; in both cases these are Type H1 [27], which suggests a narrow range of pores, the limiting diameter of which may be an ink bottle type neck to the cavities, which is less pronounced for the higher R/C ratio. This, in tandem with the results for R/C 100, suggests a move from well-defined narrow-necked pores to a network that has cavity filling issues, due to constrictions in the porous network.

Previous works have indicated the absorption of gases/vapours into RF gel materials during adsorption measurements [31, 32], which is now believed to also extend to nitrogen adsorption at its condensation temperature. In addition, other authors have suggested that previous observations of microporous character in such gel materials indicate the occurrence of absorption in addition to adsorption in the system [33–35]; however, for most gas-polymer systems ‘sorbed volumes are vanishingly small’ and issues have been experienced previously for low-pressure experimental arrangements due to the ‘low

solubility of permanent gases in polymers’, which includes nitrogen gas [31]. The RF gels studied here exhibit a high degree of crosslinking within their structures, which has been shown to reduce the degree of diffusion in polyethylene materials [36]; hence, similar behaviour would be expected here and compounds the expected low diffusivity for a polar organic material and a non-polar gas, such as nitrogen. The use of alternative techniques to estimate surface area have shown widely different correlations when compared with BET surface area [33, 35, 37, 38], suggesting that there are limitations in any selected technique, whereas other authors have also highlighted the potential of microporous materials including carbonaceous samples, to undergo deformation during the adsorption of probe gases including nitrogen [39]. It may therefore be argued that as the adsorption methods adopted here use a final pressure close to the saturated vapour pressure of nitrogen at 77 K, all porous voids are filled within the process, and that the absorption character of the materials studied here can be quantified by the microporous character observed within the material. By assuming that this portion of the uptake is due to absorption, the remaining nitrogen uptake can be ascribed to adsorption only processes. Comparison of the data obtained on this basis also indicates that there is little difference observed for these materials.

In order to understand the differences exhibited by the gels prepared at different concentrations of D₂O, it is important to consider which factors are changing within the reaction system, i.e., the substitution of H₂O by D₂O, and the potential influence that this may have on materials development. The impact of the introduction of D₂O can be twofold within the reaction system; first, it can act as a solvent for the reaction matrix. An additional issue with this factor is that the condensation reaction between the hydroxymethyl derivatives, formed by reaction of resorcinol and formaldehyde, forms water as a byproduct, which, in turn, would dilute the D₂O concentration as the reaction proceeds.

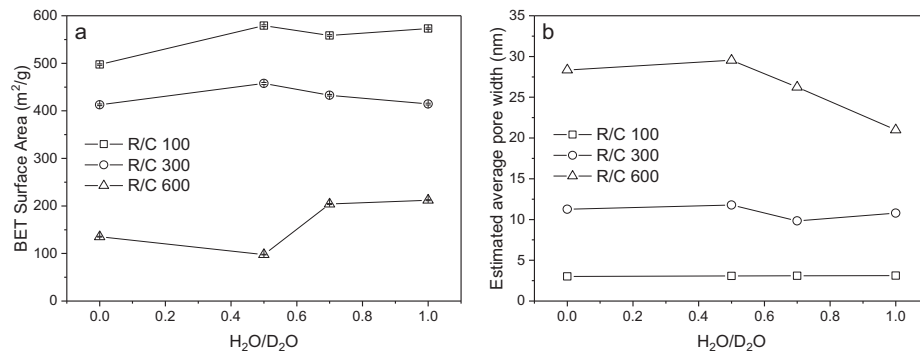


Fig. 4 **a** BET surface area and **b** estimated average pore width from Barrett–Joyner–Halenda method vs H₂O/D₂O v/v ratio

Hence, the presence of D₂O would have a more pronounced effect on the early stages of the synthesis, rather than the latter steps. The RF gels prepared with higher R/C ratios, especially R/C 600, result in a very weak structure, which is more prone to shrinkage during the drying process. This can lead to higher variation of sample structure and character, and a reduction in the noticeable effect of D₂O presence. The second impact of D₂O is in its role in isotopic exchange. The -OH groups of methylene glycol (hydrated formaldehyde) and hydroxymethyl derivatives of resorcinol contain acidic hydrogen atoms that can be exchanged with deuterium atoms from D₂O. Using mass spectroscopy, Efimova et al. [40] have shown that majority of the hydrogen–deuterium (H–D) exchange for proteins takes place within a minute. The O–D bond is slightly shorter and is known to be stronger than the corresponding O–H bond [13], which would have an effect on the polycondensation reactions within the RF gel systems. A larger quantity of deuterium atoms exchanged into positions in the hydroxymethyl groups can therefore lead to a decrease in polycondensation reaction kinetics. At lower R/C ratios, the RF sample gels much faster than its higher R/C analogues [2]. This means that the H–D exchange at the hydroxyl groups will have less time to occur at lower R/C ratios; thus, isotopic exchange will have a less pronounced effect on the final gel structure. In this work, the R/C 100 samples show a difference in magnitude of adsorption but no differences in isotherm type, hysteresis loop shape or average pore diameter; hence, it can be reasoned that the changes described above have little effect in terms of exchange, whereas the difference may be related to the role of D₂O as a solvent. In the previous work of Gaca et al. [8], R/C ratios even lower than 100 were used, which suggests there would be an even less pronounced effect with regards to H–D exchange. They have also observed a relatively quick drop in reagent concentration [8], indicating that the initial speciation takes place early on and would not be significantly influenced by the presence of D₂O in the system.

In accordance with the results discussed above, it can be seen (Fig. 4) that samples prepared with R/C 100 show little variation in both BET surface area and estimated average pore diameter with decreasing D₂O content compared with higher R/C ratios. There is marked variation for samples prepared using R/C 600 and it is likely to be that ratios above this value would result in greater variance in the resulting gels. It may also be the case that the large changes in character for the higher R/C ratios, most heavily influenced by D₂O concentration, exacerbate the differences observed in the final volume of nitrogen adsorbed as the materials become weak and prone to manufacturing effects; this could also explain the disparity noted in the estimated average pore diameter, which show a marked increase in variance as R/C is increased. A summary of textural properties obtained from nitrogen adsorption is also presented in Table 1 and the whole suite of results suggest that the use of D₂O within an RF gel matrix has a minor effect on textural characteristics at low concentration, especially when coupled with low R/C ratio.

5 Conclusions

By studying the effect of a gradual replacement of H₂O by D₂O in the synthetic matrix of RF gel synthesis on final material textural characteristics, it has been shown that the presence of D₂O has only a minor influence on the end gel structure obtained, which becomes less pronounced as R/C ratio decreases. This effect is most likely caused by the two concurrent roles that D₂O has in the synthetic mixture. First, isotopic exchange will occur between hydrogen atoms of the hydroxyl groups present in the intermediate species and the deuterium atoms of D₂O; this interchange will alter the kinetics of the condensation stage of the reaction due to the difference in bond strength. Second, D₂O will also act as a solvent, an effect that will be altered by dilution effects as

Table 1 Textural properties of gels prepared with R/C ratios of 100, 300 and 600 and different H₂O/D₂O v/v ratios

R/C	H ₂ O/ D ₂ O	BET Surface area (m ² / g)	Total pore volume (cm ³ /g)	Micropore volume (cm ³ / g)	Estimated average pore width (nm)
100	1:0	573 (2)	0.48	0.0494 (4)	3
	7:3	558 (2)	0.46	0.0477 (5)	3
	1:1	579 (2)	0.46	0.0613 (6)	3
	0:1	497 (1)	0.39	0.0425 (5)	3
300	1:0	414 (2)	1.04	0.0480 (5)	11
	7:3	433 (2)	1.01	0.0495 (4)	10
	1:1	458 (2)	1.17	0.0646 (5)	12
	0:1	431 (2)	1.07	0.0517 (3)	11
600	1:0	212 (1)	0.71	0.0352 (2)	21
	7:3	204 (1)	1.01	0.0300 (3)	26
	1:1	98 (1)	0.42	0.0179 (2)	30
	0:1	135 (1)	0.82	0.0200 (2)	28

H₂O is generated by condensation reactions, nevertheless changing the environment in which the formation and growth of gel clusters takes place. Higher R/C ratio systems will be more affected by isotopic substitution due to a combination of long gelation times and the weaker structures generally formed as catalyst quantity is decreased. By contrast, low R/C systems would be less influenced by the inclusion of D₂O into the synthetic matrix, retaining most of the core characteristics irrespective of additive concentration, as shown above. Herein, we have shown that the use of D₂O in NMR studies of RF gels is viable, with only a minor impact on final gel textural character, and is particularly suitable at the concentrations and lower R/C ratios used in previous studies.

Compliance with ethical standards

Conflict of interest The authors declare that they have no conflict of interest.

Open Access This article is distributed under the terms of the Creative Commons Attribution 4.0 International License (<http://creativecommons.org/licenses/by/4.0/>), which permits unrestricted use, distribution, and reproduction in any medium, provided you give appropriate credit to the original author(s) and the source, provide a link to the Creative Commons license, and indicate if changes were made.

References

- Pekala RW (1989) Organic aerogels from the polycondensation of resorcinol with formaldehyde. *J Mater Sci* 24(9):3221–3227
- Taylor SJ, Haw MD, Sefcik J, Fletcher AJ (2014) Gelation mechanism of resorcinol-formaldehyde gels investigated by dynamic light scattering. *Langmuir* 30(34):10231–10240
- Gaca KZ, Sefcik J (2013) Mechanism and kinetics of nanostructure evolution during early stages of resorcinol-formaldehyde polymerisation. *J Colloid Interf Sci* 406:51–59
- Al-Muhtaseb SA, Ritter JA (2003) Preparation and properties of resorcinol-formaldehyde organic and carbon gels. *Adv Mater* 15(2):101
- Morales-Torres S, Maldonado-Hódar FJ, Pérez-Cadenas AF, Carrasco-Marín F (2010) Textural and mechanical characteristics of carbon aerogels synthesized by polymerization of resorcinol and formaldehyde using alkali carbonates as basification agents. *Phys Chem Chem Phys* 12(35):10365–10372
- Taylor SJ, Haw MD, Sefcik J, Fletcher AJ (2015) Effects of secondary metal carbonate addition on the porous character of resorcinol-formaldehyde xerogels. *Langmuir* 31(50):13571–13580
- Gaca KZ, Parkinson JA, Lue L, Sefcik J (2014) Equilibrium speciation in moderately concentrated formaldehyde-methanol water solutions investigated using C-13 and H-1 nuclear magnetic resonance spectroscopy. *Ind Eng Chem Res* 53(22):9262–9271. <https://doi.org/10.1021/ie403252x>
- Gaca KZ, Parkinson JA, Sefcik J (2017) Kinetics of early stages of resorcinol-formaldehyde polymerization investigated by solution-phase nuclear magnetic resonance spectroscopy. *Polymer* 110:62–73
- Werstler DD (1986) Quantitative C-13 NMR characterization of aqueous formaldehyde resins. 2. Resorcinol-formaldehyde resins. *Polymer* 27(5):757–764
- Christiansen AW (2000) Resorcinol-formaldehyde reactions in dilute solution observed by carbon-13 NMR spectroscopy. *J Appl Polym Sci* 75(14):1760–1768
- Lewicki JP, Fox CA, Worsley MA (2015) On the synthesis and structure of resorcinol-formaldehyde polymeric networks - precursors to 3D-carbon macroassemblies. *Polymer* 69:45–51
- Rivlin M, Eliav U, Navon G (2015) NMR studies of the equilibria and reaction rates in aqueous solutions of formaldehyde. *J Phys Chem B* 119(12):4479–4487
- Nemethy G, Scheraga HA (1964) Structure of water and hydrophobic bonding in proteins. IV. The thermodynamic properties of liquid deuterium oxide. *J Chem Phys* 41(3):680–689
- Franks F (1972) *Water: A Comprehensive Treatise*, vol. 1. Plenum Press, New York and London, (1972)
- Shirota H, Pal H, Tominaga K, Yoshihara K (1996) Deuterium isotope effect on the solvation dynamics of methanol: CH₃OH, CH₃OD, CD₃OH, and CD₃OD. *J Phys Chem* 100(35):14575–14577
- Mills R, Harris K (1976) The effect of isotopic substitution on diffusion in liquids. *Chem Soc Rev* 5:215–231
- Forsythe KM, Makri N (1998) Path integral study of hydrogen and deuterium diffusion in crystalline silicon. *J Chem Phys* 108(16):6819–6828
- Szabo Z, Grenthe I (1998) Mechanisms of ligand substitution reactions in ternary dioxouranium (VI) complexes. *Inorg Chem* 37(24):6214–6221
- Stutz J, Ezell M, Finlayson-Pitts B (1997) Inverse kinetic isotope effect in the reaction of atomic chlorine with C₂H₄ and C₂D₄. *J Phys Chem A* 101(49):9187–9190
- Pyun S-I, Lim C, Kim K-B (1994) An investigation of the electrochemical kinetics of deuterium insertion into a Pd membrane electrode in 0.1 M LiOD solution by the ac impedance technique. *J Alloy Compd* 203:149–156
- Fletcher AJ, Thomas KM (2007) Kinetic isotope quantum effects in the adsorption of H₂O and D₂O on porous carbons. *J Phys Chem C* 111(5):2107–2115
- Efimova Y, Haemers S, Wierczynski B, Norde W, Van Well A (2007) Stability of globular proteins in H₂O and D₂O. *Biopolymers* 85(3):264–273

23. Dougan L, Koti ASR, Genchev G, Lu H, Fernandez JM (2008) A single-molecule perspective on the role of solvent hydrogen bonds in protein folding and chemical reactions. *ChemPhysChem* 9 (18):2836–2847
24. Huang J, Sung J, Wu X-L (1989) The effect of H₂O and D₂O on a water-in-oil microemulsion. *J Colloid Interf Sci* 132(1):34–42
25. GrenierLoustalot MF, Larroque S, Grande D, Grenier P, Bedel D (1996) Phenolic resins .2. Influence of catalyst type on reaction mechanisms and kinetics. *Polymer* 37(8):1363–1369
26. Brunauer S, Emmett PH, Teller E (1938) Adsorption of gases in multimolecular layers. *J Am Chem Soc* 60:309–319
27. Thommes M, Kaneko K, Neimark AV, Olivier JP, Rodriguez-Reinoso F, Rouquerol J, Sing KSW (2015) Physisorption of gases, with special reference to the evaluation of surface area and pore size distribution (IUPAC Technical Report). *Pure Appl Chem* 87 (9-10):1051–1069
28. Lowell S, Shields JE, Thomas MA, Thommes M (2004) Micro-pore Analysis. In: *Characterization of Porous Solids and Powders: Surface Area, Pore Size and Density*. The Netherlands, Springer, pp 129–156
29. Barrett EP, Joyner LG, Halenda PP (1951) The determination of pore volume and area distributions in porous substances. I. Computations from nitrogen isotherms. *J Am Chem Soc* 73 (1):373–380. <https://doi.org/10.1021/ja01145a126>
30. Mirzaeian M, Hall PJ (2009) The control of porosity at nano scale in resorcinol formaldehyde carbon aerogels. *J Mater Sci* 44 (10):2705–2713
31. Vieth WR (1991) *Diffusion in and through Polymers: Principles and Applications*. Hanser, Munich, Vienna, New York, Barcelona
32. Strobl G (2007) *The semicrystalline state. The Physics of Polymers: Concepts for Understanding Their Structures and Behavior*. Berlin, Springer, pp 165–222
33. Berthon S, Barbieri O, Ehrburger-Dolle F, Geissler E, Achard P, Bley F, Hecht A-M, Livet F, Pajonk GM, Pinto N (2001) DLS and SAXS investigations of organic gels and aerogels. *J Non-Cryst Solids* 285(1):154–161
34. Saliger R, Bock V, Petricevic R, Tillotson T, Geis S, Fricke J (1997) Carbon aerogels from dilute catalysis of resorcinol with formaldehyde. *J Non-Cryst Solids* 221(2):144–150
35. Czakkel O, Marthi K, Geissler E, László K (2005) Influence of drying on the morphology of resorcinol–formaldehyde-based carbon gels. *Microporous Mesoporous Mater* 86(1):124–133
36. Michaels AS, Bixler HJ (1961) Solubility of gases in polyethylene. *J Polym Sci Part A Polym Chem* 50(154):393–412
37. Schaefer DW, Pekala R, Beaucage G (1995) Origin of porosity in resorcinol-formaldehyde aerogels. *J Non-Cryst Solids* 186:159–167
38. Brandt R, Fricke J (2004) Acetic-acid-catalyzed and subcritically dried carbon aerogels with a nanometer-sized structure and a wide density range. *J Non-Cryst Solids* 350:131–135
39. Balzer C, Braxmeier S, Neimark AV, Reichenauer G (2015) Deformation of microporous carbon during adsorption of nitrogen, argon, carbon dioxide, and water studied by in situ dilatometry. *Langmuir* 31(45):12512–12519
40. Efimova Y, van Well A, Hanefeld U, Wierczinski B, Bouwman W (2005) On the scattering length density of proteins in H₂O/D₂O: Determination of H-D exchange using ES⁺I-MS. *J Radioanal Nucl Chem* 264(2):271–275

D.2 Submitted

Journal Name

ARTICLE TYPE

Cite this: DOI: 00.0000/xxxxxxxxxx

Modelling the formation of porous organic gels - how structural properties depend on growth conditionsMartin Prostredny,^a Ashleigh Fletcher,^a and Paul Mulheran^{*a}

Received Date

Accepted Date

DOI: 00.0000/xxxxxxxxxx

There has been significant research interest invested into the study of the formation and properties of porous organic materials, due to their widespread applications. However, present models in the literature do not fully explain the observations made for these systems, therefore, this work presents a model developed to fully capture growth from the monomeric species present in the initial stages of the gelation composition. In this work, we employ a two-dimensional lattice-based kinetic Monte Carlo model to investigate how growth processes impact the structural properties of model gels. Experimentally, gel growth is primarily controlled through catalyst concentration, which determines the density of species that are activated for rapid growth, and solids concentration; our model captures both of these dependencies. Increasing both solids content and percentage of activated monomers leads to a higher ratio of closed porosity, and higher values of accessible surface area with increasing level of activation. The generated structures are analysed for their fractal properties using a correlation dimension. Increasing both solids content and percentage of activated species leads to an increase in correlation dimension, which plateaus at a value of 2, independent of catalyst concentration, suggesting little structural change at high solid loadings, over 50 %. The Hurst exponent of a random walker diffusing in the accessible pores shows the opposite trend, varying from $\frac{1}{2}$ for unconstrained diffusion and reducing to $\frac{1}{3}$ for diffusion through the pore network at the threshold of percolation. These characteristics support visual observations of increasing complexity and tortuosity of pore structures in the model cluster structures. The implications of these results, for the design of porous structures tailored to particular applications, are discussed.

1 Introduction

Porous organic materials have been studied extensively, particularly due to their applications in many fields such as thermal insulation^{1,2}, porous electrode materials^{3,4} and adsorbents^{5,6}. Resorcinol-formaldehyde (RF) gels are one type of these materials, providing the option, for these materials, to use them either in their organic dried^{7,8} or electrically conductive carbonized forms^{3,4,6}. We have previously studied the RF gel manufacturing procedure⁹ in order to better understand the underlying processes that occur during the gelation of these materials, investigating the materials in their dried organic form to preserve the structure created during the gelation process.

The initial stages of RF gelation consist of monomer and cluster formation and their subsequent growth into larger, more complex structures¹⁰. The process is pH sensitive with basic synthesis routes being more commonly used in the literature^{11,12}. The catalyst is usually a weak base in the form of an inorganic hy-

drolysing salt, which allows adjustment of the solution pH with the most common example being sodium carbonate (Na_2CO_3). Under basic conditions, resorcinol forms anions in solution that react with formaldehyde, creating monomers that undergo successive condensation reactions resulting in cluster growth and aggregation¹⁰. The process of hydrogen abstraction from neutral resorcinol molecules is notably faster than the formation and growth of clusters, as previously observed by NMR¹³, which was taken into account when developing the cluster growth and aggregation model presented here.

Two potential formation pathways for RF gels have been proposed in the literature: microphase separation¹⁴ and colloidal aggregation¹⁵. However, it seems that both options represent two extreme views of the same complex process, involving the growth and aggregation of primary spherical particles, leading to analogous final gel structures¹⁶. In this work, a model pathway resembling colloidal aggregation is developed, due to its prevalence in the literature¹⁷⁻²².

Studies have previously focused on the generation of porous model gel structures that could be compared to those obtained

^a Department of Chemical and Process Engineering, University of Strathclyde, Glasgow G1 1XJ, UK. Tel: +44 (0) 141 548 2385; E-mail: paul.mulheran@strath.ac.uk

experimentally. Early works by Meakin²³ and Kolb *et al.*²⁴ introduced a two-dimensional lattice model of diffusion-limited cluster-cluster aggregation. These models were developed with colloidal particle aggregation in mind, without the primary particles changing size, such as for agglomeration of metal or polymeric particle sols. Some other works included reordering of the initially formed structures to represent some of the patterns observed in silica gel materials²⁵. However, the bonds in silica gels are more likely to undergo hydrolysis, especially under acidic conditions, than their organic counterparts. Here, the mechanism for base-catalysed RF gels is considered, where hydrolysis of the formed ether bonds is not favoured, therefore not leading to structural reorganisation at the later stages of gelation.

Gavalda *et al.*^{26,27} modelled carbon aerogel structures using random close-packed, slightly overlapping, spheres with mesopores between the particles, and micropores incorporated within the particles. However, all particles were assumed to be equal in size, which is not always the case in a real system, where particles can vary over a range of sizes. Work by Morales-Flórez *et al.*^{28,29} used an algorithm with randomly-packed spheres in several hierarchically-ordered levels in order to simulate silica (SiO₂) and titania (TiO₂) porous materials. Even though the final structures obtained vary in shape, the primary spherical particles used to form the final clusters are all identical in size. A molecular dynamics study by Ferreiro-Rangel and Gelb³⁰ used a coarse-grained model for silica aerogel simulation; although again, using a uniform size of primary particles, which were allowed to diffuse and bond together to form the final structure. These examples from the literature show a trend of using monodisperse particles in order to model structures for porous xerogel and aerogel materials, which might not reflect all of the characteristics of these materials, since the experimentally obtained aero- and xerogels are not formed by particles of identical size³¹. As far as we are aware, no study prior to this has tried to replicate the formation of gel structures starting from monomeric species, through nucleation and growth of primary particles, to the final aggregated state.

Both experimentally and via simulation, porous materials are usually analysed for their textural properties, such as accessible surface area, pore volume, and pore size distribution. However, it has been reported previously that aerogel and xerogel materials tend to exhibit structures with fractal characteristics^{32–35}, even though some early studies suggested a lack of fractal properties of RF gels¹⁴. Fractal properties can add useful information about their structure and therefore, fractal analysis of porous materials has been performed, in the past, using both simulations^{30,36} and experiments, through techniques including dynamic light scattering³³ and small angle X-ray scattering^{32,33,35}, adding more information about the structure of these materials.

A number of methods can be used to characterize a structure in terms of a fractal dimension, including correlation dimension (D_C), box-counting dimension (D_B), and information dimension (D_I). this work uses the correlation dimension, which is related to the other dimensions through $D_C \leq D_I \leq D_B$ ³⁷.

The Hurst exponent is related to fractal dimension³⁸ and can be used to describe the persistence of a time series³⁹. If one con-

siders a random walker on a two-dimensional lattice; a particle exhibiting Brownian motion on an empty lattice, with no obstacles, has a Hurst exponent value of $H = 1/2$. A random walker with a lower value $H < 1/2$ is described as antipersistent, which means that it is more likely to remain closer to the origin than the freely diffusing particle. A value of $H > 1/2$ is attributed to persistent walkers, meaning they are more likely to leave the origin with a smoother, less rugged trace. If one now considers a random walker on a plane with obstacles, its trace will become more antipersistent, tending to confine it to a smaller area. As the obstacle structures become more complex and the voids more tortuous, thereby restricting the movement of the walker, the value of H might be expected to approach $\sim 1/3$, the value found at the percolation threshold⁴⁰.

In this work, a cluster growth and aggregation model, using kinetic Monte Carlo simulations, is presented. The model aims to mimic the growth processes deduced from experimental gel formation, and in particular moves away from the dependence on uniform sphere size found in previous models^{26–30}, while adding cluster growth and concentration of activated species compared to previous work developed for similar systems^{23,24}. We develop a two-dimensional model, which allows visual understanding of the structure development, as well as evaluation of large system sizes, to explore the fractal properties. The generated structures are subsequently analysed for accessible pore space and accessible surface area, along with their fractal properties, using the correlation dimensions of the structures, and Hurst exponent of random walkers diffusing in the resulting accessible pore structures. These characteristics will provide insight into the interdependence of the structural properties of these materials and their synthesis conditions, such as concentrations of catalyst and solids, paving the way for the bespoke design of porous gels tailored to their applications.

2 Cluster growth and aggregation model

Our model, describing the formation, growth and aggregation of resorcinol-formaldehyde (RF) clusters, is developed on the basis of experimental evidence found in the literature. A general understanding of the dependence of RF gel materials on some of the processing parameters was obtained by performing a related experimental study⁹ and reviewing our previous experimental work^{10,41,42}. The catalyst salt present in the solution activates a proportion of the resorcinol molecules⁴³ to form anions, which are more reactive in the addition reaction with formaldehyde. These activated species act as seeds for subsequent growth of the spherical particles that are observed by electron microscopy of RF gels^{15,44–46}.

Cluster formation and diffusion in the RF solution has been observed visually by Alshrah *et al.*³⁵. As the clusters grow within the reaction solution, they can adhere to other clusters, thus forming larger aggregates, with these processes more pronounced at elevated temperatures¹⁰. This aggregation has been noted in the work by Pol *et al.*⁴⁷, where RF resin synthesis has been assisted by ultrasound, forming individual spherical particles in solution within a short time frame. In a control experiment in the same work, performed as a stirred emulsion polymerization without

sonication, small aggregates of RF particles were observed, again via scanning electron microscopy, after a longer gelation time, which is required for the reaction to complete without sonication. The particles prepared with ultrasound formed relatively quickly, leading to a small fraction of particles adhering to each other. However, the longer reaction times required during emulsion polymerization result in greater RF cluster adherence, leading to small aggregates. Larger agglomerates were not formed due to the agitation from stirring, which prevents the particles from contacting for a sufficiently long enough time to form cross-links.

During the RF monolith manufacturing processes, there is no agitation of the reacting solution allowing the formation of three-dimensional particle networks, starting from individual clusters that create smaller aggregates, which generate the final structure spanning the reaction space⁹. The examples from the literature discussed here are not exhaustive but provide additional information about the generation of final structures in RF gels, and were used as a basis for the developed model. It should be noted that even though the model was based on experimental data for RF gels, due to the amount of data available in the literature and our previous experimental experience, it could be transferable to other materials, for which the structure is created via a similar route as the one described here for RF gels.

For this purpose, in-house software was developed with GNU Fortran compiler and GNU parallel tool⁴⁸ using a lattice based kinetic Monte Carlo method. A two-dimensional lattice, with periodic boundaries, was initially populated by monomers, in order to mimic total solids concentration (S_C), which in this case represents the fraction of occupied lattice sites. Values of S_C used in this work range from 10 to 50 %, moving in 10 % increments. Higher values of S_C , up to 90 %, were explored; however, most of the porosity above 50 % was observed as closed and not percolated in two dimensions, therefore, only structures up to 50 % S_C are considered here. A percentage of the monomers (C_C) were 'activated' to represent catalyst concentration and corresponding amount of activated monomers (resorcinol anions). These activated species acted as seeds for cluster nucleation. In this work, $C_C = 1, 2, \text{ and } 3\%$ were used, based on the proportion of charged resorcinol molecules discussed in the work of Lin and Ritter⁴³.

The monomers, and growing clusters, were allowed to diffuse on the lattice, where the probability of a cluster moving was inversely proportional to its size. When a monomer diffused onto a site occupied by a cluster, it attached to the cluster, resulting in growth. Based on experimental evidence^{15,44–46}, as discussed above, 'circular' islands grew on the lattice, as illustrated in Figure 1.

The mechanism of individual cluster growth is depicted in Figure 1, where the increasing numbers indicate lattice sites for cluster growth with each additional monomer attached to that cluster. The colours used in Figure 1 represent layers of monomers being attached to a cluster; this way, the growing clusters retain a compact, approximately circular, shape rather than the branched shape that would result from a diffusion-limited aggregation mechanism, keeping the model structures closer to those observed experimentally. If a site was already occupied by an-

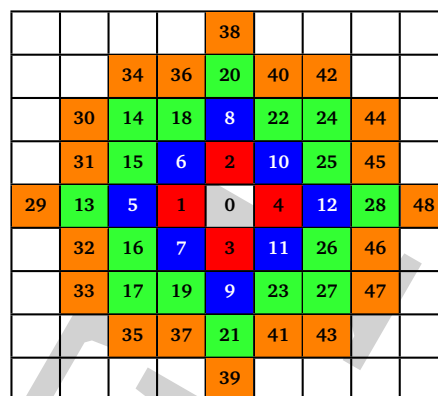


Fig. 1 Schematic drawing of the cluster growth mechanism on a two-dimensional lattice with numbers representing the position of each additional monomer added; the colours represent different layers of growth (1st layer ■, 2nd layer ■, 3rd layer ■, 4th layer ■).

other cluster, the next available site in the list was used.

When two clusters touched, they became linked into a larger cluster aggregate; the resulting cluster aggregates moved across the lattice together, but the individual clusters continued to grow independently. An example of individual cluster growth in an aggregate, formed by three clusters, is shown in Figure 2. It can be seen that while cluster A (Figure 2) retains an approximately circular shape, cluster C grows around clusters A and B, keeping an outer circular arc shape where possible. Cluster growth and aggregation is illustrated in Figure 3, where three clusters (black) gradually grow, on a lattice with periodic boundaries, consuming the monomers (red) around them. As can be seen from Figure 3, monomers and clusters diffuse freely on the lattice with monomers being gradually depleted by the growing clusters.

The simulation was deemed to be finished when there was only one spanning cluster aggregate remaining in the system. Selected final structures are shown in Figure 4 in order to show the effect of solids content and percentage of activated monomers on simulated structures. Increasing the percentage of activated monomers in the initial simulation results in the clusters in the final structure being smaller in size, thereby increasing their number. This results in a more branched structure, which leads to more interconnected networks spanning the reaction space, making the whole structure more interdigitated. By increasing the solids content, the grown structures are more densely packed, however, as previously discussed, they retain a percolated porous structure up to 50 % solids content. At higher solids contents (above 50 %), the structures end up being too dense and most of the pores are closed in two dimensions, and only the pores that might be on the structure surface would be externally accessible. It is worth noting that while these generated structures might be visualised as two-dimensional slices of a three-dimensional material, in reality some of the closed pores present in the two-dimensional structure might well be open pores in a three-dimensional structure.

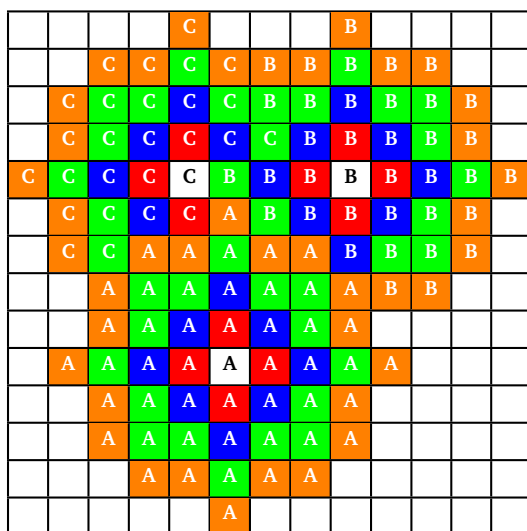


Fig. 2 Schematic drawing of three clusters (labelled A, B, and C) growing adjacent to each other, indicating growth with cluster overlap. Colours represent different layers of growth (1st layer ■, 2nd layer ■, 3rd layer ■, 4th layer ■).

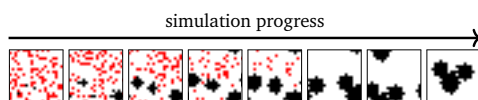


Fig. 3 Cluster growth and diffusion mechanism example. Positions occupied by cluster points shown in black, and by monomers in red.

It can be seen, from Figure 4, that the structures created using lower solids contents, e.g. 10 and 20 %, contain pores that are quite open and generally exhibit wide necks, resulting in very few bottle-neck type pores. Conversely, structures with higher solids loading, e.g. 40 and 50 %, exhibit a complex series of interconnected pores with a higher fraction of constricted and closed pores.

Due to the random nature of kinetic Monte Carlo simulations, a series of 10 runs was performed for each set of conditions (solids content and percentage of activated monomers) by using a different seed for the Fortran built-in random number generator at the beginning of the simulation. Figure 4 shows only the first run for each set of the presented model parameters, these being wholly representative of the trends for each set of parameters, with inaccessible pore spaces highlighted in red.

3 Textural characterization

Experimentally, porous materials are usually characterized by various techniques, such as gas sorption, for their textural properties^{11,44,46,49,50}. Accessible surface area and accessible pore volume are important characteristics of these materials and have a direct impact on their applications.

The generated structures, as presented in Figure 4, were analysed for accessible pore area and number of accessible surface sites. Firstly, the area of the percolating network of pores was identified for all the structures, represented in white in Figure 4. The number of accessible lattice sites was compared to the total number of unoccupied lattice sites for each generated structure and these ratios are shown in Figure 5a. Increasing both S_C and C_C results in a qualitatively observable decrease in the ratio of accessible sites (Figure 4), while quantitatively it is reflected in Figure 5a and is a result of increased closed porosity within these structures.

The accessible surface areas of the pores, scaled to the gel mass, are shown in Figure 5b. It can be seen that the surface area decreases with increasing solids concentrations (S_C) and increases with increasing catalyst concentration (C_C). At higher values of S_C , the decrease is more pronounced due to the increase in closed porosity, as discussed above. Higher values of C_C lead to higher numbers of accessible surface sites, with the difference more pronounced at lower values of S_C .

From previous experimental work within our group, the effect of solids content on the final RF xerogel structure was observed as insignificant⁹. However, it needs to be taken into account that the experimentally analysed samples are xerogels, which are affected by shrinkage during the drying process. Hydrogels with lower solids content will initially contain larger and more open pores; however, their solid network structure is relatively weak, resulting in significant shrinkage during drying. On the other hand, even though hydrogels with higher solids contents initially exhibit smaller pore voids, their gel structures are much stronger; thus, they are better able to withstand the forces exerted onto the pore walls during drying. Another factor to consider is that the range of solids content used in previous experiments was below 40 %, and the change in accessible surface sites is fairly small in this region, compared to higher values of S_C . We note that the trends observed here for the effect of amount of activated species (C_C) on both accessible pore volume and accessible surface sites agree with experimental trends for catalyst concentration.

4 Fractal analysis

As mentioned in the introduction, fractal properties of aerogel and xerogel materials have been studied both experimentally³²⁻³⁵ and using simulations^{30,36}, providing additional information about the nature of porous materials. Therefore, the generated cluster structures were analysed for correlation dimension (section 4.1) to gain more information about the structure complexity. The Hurst exponent values were calculated for the accessible pore spaces using diffusion of a random Brownian walker (section 4.2).

4.1 Correlation dimension

Correlation dimensions were calculated for the simulated structures, as outlined above, using the relationship proposed by Grassberger⁵¹. First, the correlation sum (C_r) was calculated us-

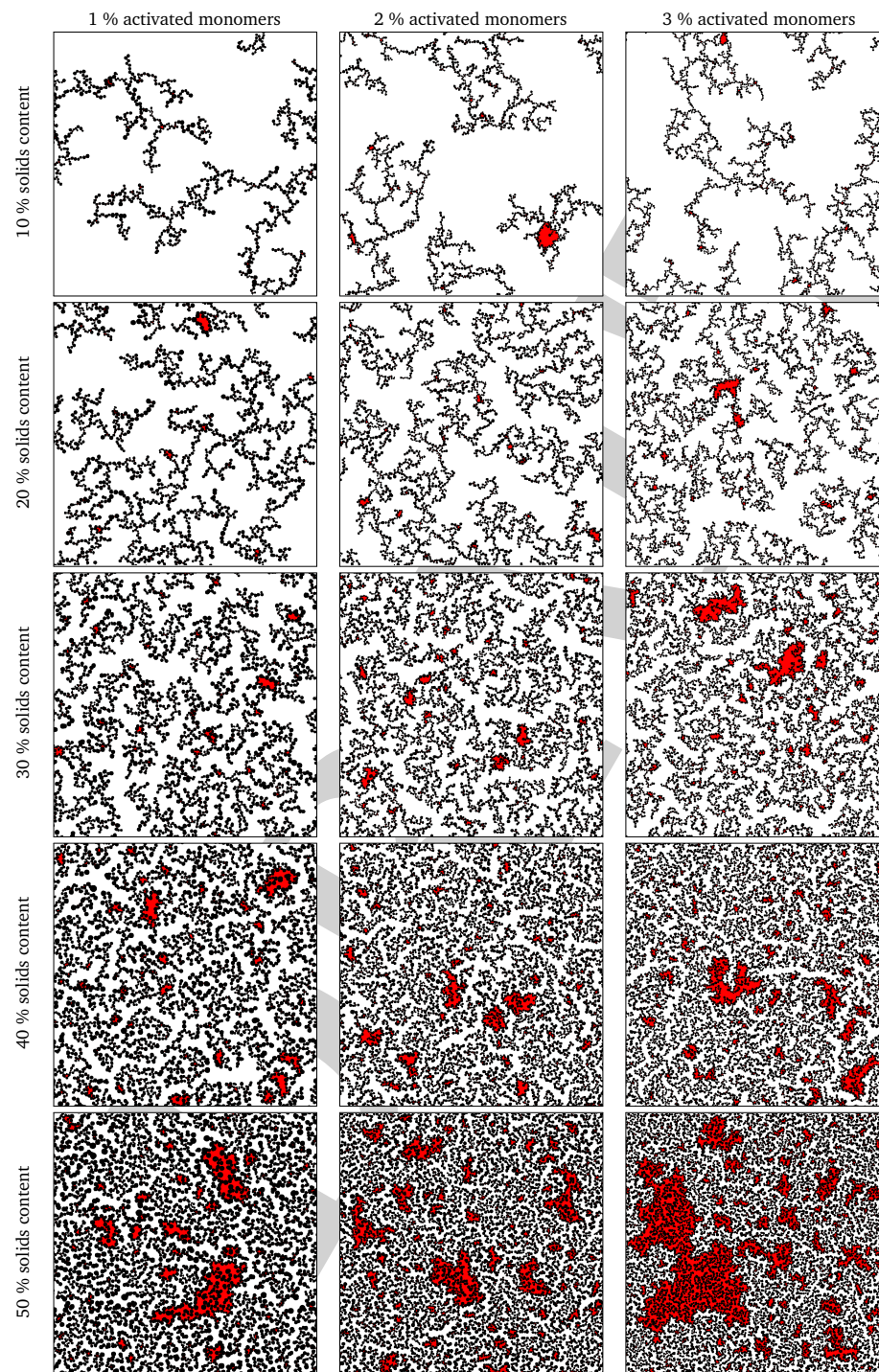


Fig. 4 Model of cluster growth of RF gels, with increasing percentage of activated monomers (left to right) and increasing solids content (top to bottom). Areas of inaccessible pore spaces are highlighted in red. The lattice used is 1000×1000 .

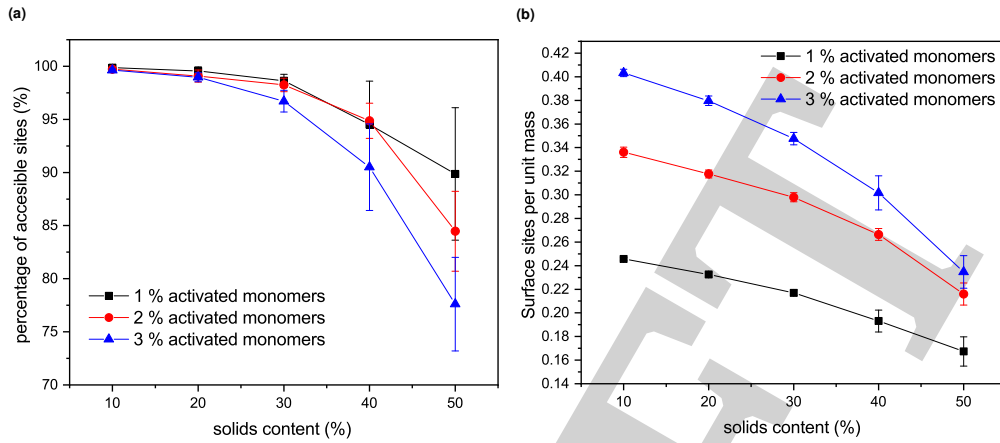


Fig. 5 (a) Percentage of accessible sites (relative to all unoccupied sites on the lattice) vs solids content for three percentages of activated monomers and (b) accessible surface area (in number of lattice sites) vs solids content for three percentages of activated monomers. Error bars represent standard deviation of values for 10 independent runs for each set of conditions, and lines connecting the data points provide a visual guide only.

ing:

$$C_r = \frac{1}{N(N-1)} \sum_{i=1}^N \sum_{j=1; j \neq i}^N \theta(r - |X_i - X_j|) \quad (1)$$

where N is the total number of clusters in the structure, θ is the Heaviside function, r is the radius of a circle centred on each sampled cluster i , and X_i and X_j are the coordinates of the centres of clusters i and j . The correlation sum is calculated for increasing values of r around all clusters and the Heaviside function takes on a value of 1 when the value of $r - |X_i - X_j|$ is positive, meaning clusters i and j are within the selected r , and a value of 0 when the two clusters are further apart than the selected r , leading to a negative value of $r - |X_i - X_j|$. This effectively allows counting of the number of clusters found within different distances from selected clusters, taking periodic boundaries into account. An example schematic is presented in Figure 6, where the chosen cluster is shown in red, and circles with increasing radii centred around it are used to evaluate the Heaviside function, as shown in dashed lines ($r_1 < r_2 < r_3$). It can be seen that as the radius of the circle increases, so does the number of clusters included within the radius. Once the radius is large enough to cover all clusters present on the lattice, the correlation sum does not change its value with increasing the radius further.

The correlation dimension of the system is obtained using a log-log scale plot of correlation sum vs radius. For small values of r ($\log(r)$ below 1), there are effects due to the discrete nature of the lattice, while the plateau at large r ($\log(r)$ around 3 and above) is due to the large-scale effects of the periodic boundary conditions mentioned above (recall the lattice size is 1000×1000). Between these sections is the scaling region, the slope of which is equal to the correlation dimension. Example plots for structures with 1% activated monomers and solids content 10, 20, and 30%, are shown in Figure 7.

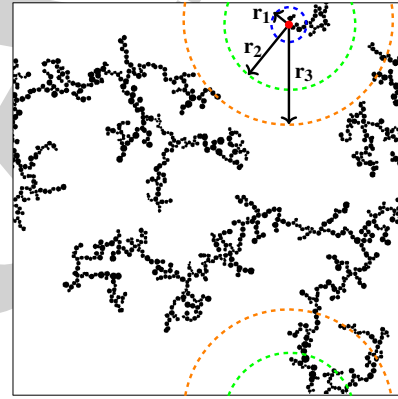


Fig. 6 Schematic of increasing radii of separation for correlation sum calculation.

Values of correlation dimensions for the solids contents and percentages of activated monomers studied here are shown in Figure 8. The values obtained vary in the range ~ 1.5 to ~ 2.0 , increasing with increasing values of S_C and C_C . The lower limit is in line with expectations for cluster-cluster aggregation in dilute systems⁵² while the upper limit is expected for dense media in two dimensions. This means that the aggregates fill space more completely as these parameters increase, as expected. At higher solids contents (50% and above), the correlation dimension plateaus at a value of 2.0 for all percentages of activated monomers. The most substantial increase in correlation dimension can be observed between 10 and 20% solids content, where, as can be seen in Figure 4, the structures differ most significantly

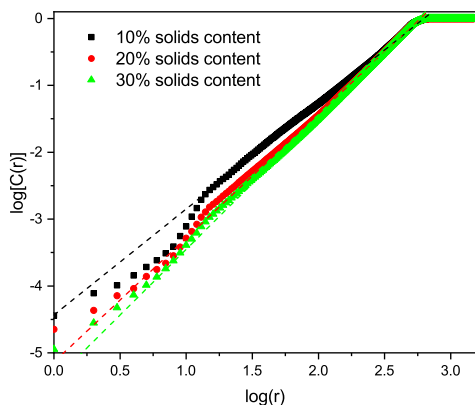


Fig. 7 Example plots as used to calculate the correlation dimension for 1 % activated monomers and 10, 20, and 30 % solids content. The slope of the linear portion (indicated by the dashed lines) is equal to the correlation dimension.

even visually.

An experimental study by Huber *et al.*⁵³ used dynamic light scattering measurements to quantify the fractal dimensions of particles formed during RF gelation. They observed an increase in fractal dimension with catalyst concentration, which agrees with the trend observed here.

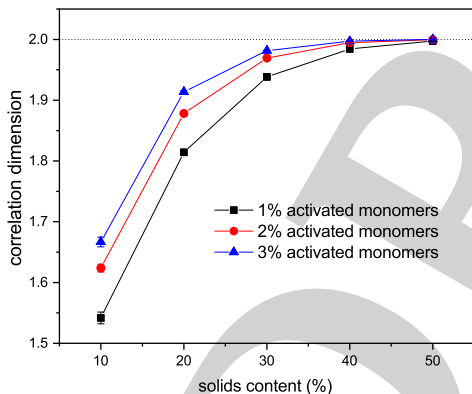


Fig. 8 Correlation dimension vs solids content for three percentages of activated monomers, the dotted line indicates a correlation dimension value of 2.0. Error bars represent standard deviation of values for 10 independent runs for each set of conditions, and lines connecting the data points provide a visual guide only.

4.2 Hurst exponent

Hurst exponent values of accessible pores within the cluster structures, obtained using the model presented here, were calculated using a random walker with only percolated porous structures considered. The inaccessible pores excluded from analysis are

coloured red in Figure 4. As mentioned above, and as seen from Figure 5a, increasing both values of S_C and C_C leads to more closed porosity in the system, which will have an effect on the values of the Hurst exponent as well.

For each simulation, the random walker was placed within the percolated pore structure and allowed to freely diffuse for 10 million steps (ten times the number of lattice sites). This was repeated for 1000 randomly distributed accessible positions on the lattice. Random walker traces in both x and y directions were then analysed for average displacement from the origin with varying time window size. This is shown in Figure 9, where traces of a random walker, in both x and y directions, are shown along with absolute displacements in both directions (ΔB_x and ΔB_y) for a selected time window (T_S). The time window slides along the time axis, and an average value of displacement in both directions is calculated for varying size of time windows. For a random walker, there is a relationship between the average displacement ($\overline{|\Delta B|}$) and time window size (T_S):

$$\overline{|\Delta B|} \propto T_S^H \quad (2)$$

Thus, calculating the slope of $\log(\overline{|\Delta B|})$ versus $\log(T_S)$ provides the value of the Hurst exponent (H). In this work, 11 time window sizes were used, starting at 100 steps and increasing exponentially up to 102400 steps. It is important that the highest time window size is significantly smaller than the total number of steps, to ensure sufficient points for the average displacement calculation, as the time window slides along the time axis.

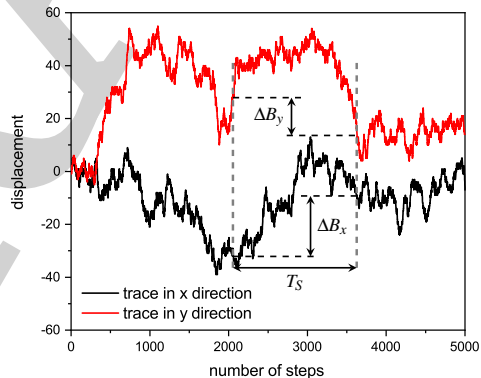


Fig. 9 Example traces in x and y directions for a random walker.

The values for the Hurst exponent, for a random walker diffusing in the percolated pore structures described above, are shown in Figure 10. It can be seen that increasing values of both S_C and C_C causes a decrease in the Hurst exponent (H) values. As mentioned in the introduction, a random walker diffusing on an empty lattice has a value of $H = 1/2$, exhibiting a random Brownian trace in both x and y dimensions. Deviation of the Hurst exponent from the value of $1/2$ towards $1/3$ suggests a more anti-persistent character of the walker trace. By increasing solids content, the obstacles encountered by the walker also increase and

the pore structure becomes more tortuous with more constricted pores, this limits the free diffusion of the walker, leading to a decrease of its Hurst exponent value.

Increased tortuosity of accessible pore structures can be observed in Figure 11, where cluster structures with two different values of solids content (S_C) are presented. The colours in Figure 11 represent the number of diffusion steps required to reach various points on the lattice starting from the indicated point. With increased S_C , the more constricted pores are increasingly difficult to access, as can be seen by the increased number of steps needed to reach these points. This is then reflected in the value of the Hurst exponent, as mentioned above.

An increase in number of activated sites increases the number of clusters in the structure, causing the structures to spread throughout the reaction space, again leading to a more complex pore structure and a higher ratio of closed porosity, in agreement with the trends observed for correlation dimension of the cluster structures, as discussed above.

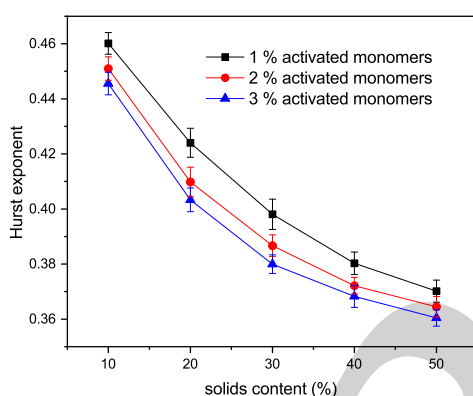


Fig. 10 Hurst exponent vs solids content for three percentages of activated monomers. Error bars represent standard deviation of values for 10 independent runs for each set of conditions and lines connecting the data points provide a visual guide only.

5 Summary and conclusions

This work presents a novel approach to modelling resorcinol-formaldehyde gel growth, along with the characterization of the fractal and structural properties of model structures. The cluster growth and aggregation model produces structures that are similar to those observed experimentally. The current version of the model could also capture the gelation of different gelling materials, if they are made by formation and subsequent cross-linking of spherical particles. It should be noted that even though the presented model has been developed with colloidal cluster aggregation mechanism, due to the nature of the model it could represent structures formed via microphase separation mechanism as well. Microphase separation theory suggests that after reaching a critical size, the growing clusters are not soluble in the reaction mixture, resulting in de-mixing. This would, however, not dramatically affect the way the model represents the cluster growth

and aggregation beyond the initial cluster size formed by the microphase separation. We will explore the impact of this in future work.

With increasing solids content and catalyst concentration, the final observed structures fill space more completely, which is reflected in their fractal properties, expressed here in the form of the correlation dimension for cluster structures and Hurst exponent for diffusion within the accessible pores. It was observed that the correlation dimension increased with both solids content and amount of activated monomers, plateauing at a value of ~ 2.0 at 50 % solids content, suggesting little structural change at higher solids contents, independent of catalyst concentration. It was also shown that increasing the solids content and percentage of activated monomers led to a decrease in Hurst exponent, which agrees with structures containing smaller and more restricted pores. These structural constrictions, reflected by the values of Hurst exponent, lead to pore voids that are more difficult to access externally, which affects kinetics of diffusional processes in RF gels, such as solvent exchange or gas adsorption. Materials exhibiting lower values of Hurst exponent (more restricted pores), could find uses in applications such as drug delivery systems, where a gradual emptying of the pore voids is preferential to a rapid discharge of substances from a more open pore structure.

The approach taken in this work allows a natural exploration of the range of solids content that is of experimental interest, showing the systematic trends in fractal properties, in contrast to previous models³⁰, developed for silica materials, where the simulation design does not attempt to follow growth from the earliest stages.

As explained above, this work presents findings using a two-dimensional version of the model developed to explore the structural consequences of the growth conditions. We intend to implement the methodology using three dimensions in our future work. This will allow for a better representation of the real materials and provide more direct predictive capabilities.

Better understanding of RF gel formation can help tailor their properties for particular applications. Due to the wide range of applications for these materials, the required characteristics vary significantly as well. For adsorption we require high accessible surface area with Brownian-like diffusion, indicating low solids concentration with high catalyst concentration. However, for drug release, we might require low catalyst concentration and high solids concentration to reduce the out-diffusion of the drug. Therefore, our work to link the properties of the gel structure to its manufacture paves the way for an intelligent design of porous materials that can be tailored to the application.

Conflicts of interest

There are no conflicts to declare.

Acknowledgements

Martin Prostredny thanks the University of Strathclyde and the Department of Chemical and Process Engineering for financial support.

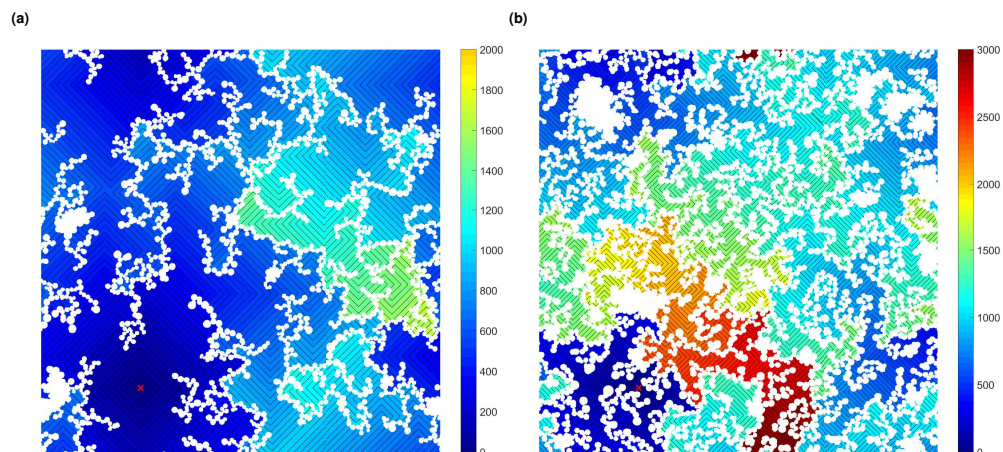


Fig. 11 Diffusion maps of selected cluster structures with 1 % activated monomers and (a) 20 % solids content and (b) 40 % solids content. Colours represent number of diffusion steps needed to reach a point from a selected origin (marked with red cross) with lower step values shown in blue and higher step values shown in red. Cluster points and inaccessible pore areas are shown in white.

References

- 1 J. Feng, C. Zhang and J. Feng, *Materials letters*, 2012, **67**, 266–268.
- 2 D. M. Smith, A. Maskara and U. Boes, *Journal of non-crystalline solids*, 1998, **225**, 254–259.
- 3 H.-H. Jung, S.-W. Hwang, S.-H. Hyun, K.-H. Lee and G.-T. Kim, *Desalination*, 2007, **216**, 377–385.
- 4 J. Li, X. Y. Wang, Q. H. Huang, S. Gamboa and P. J. Sebastian, *Journal of Power Sources*, 2006, **158**, 784–788.
- 5 Z. Wu, H. Joo and K. Lee, *Chemical Engineering Journal*, 2005, **112**, 227–236.
- 6 S. Álvarez, R. S. Ribeiro, H. T. Gomes, J. L. Sotelo and J. García, *Chemical Engineering Research and Design*, 2015, **95**, 229–238.
- 7 N. Job, F. Panariello, J. Marien, M. Crine, J.-P. Pirard and A. Léonard, *Journal of Non-Crystalline Solids*, 2006, **352**, 24–34.
- 8 N. Rey-Raap, E. G. Calvo, J. A. Menéndez and A. Arenillas, *Microporous and Mesoporous Materials*, 2017, **244**, 50–54.
- 9 M. Prostedný, M. Abduljalil, P. Mulheran and A. Fletcher, *Gels*, 2018, **4**, 36.
- 10 S. J. Taylor, M. D. Haw, J. Sefcik and A. J. Fletcher, *Langmuir*, 2014, **30**, 10231–10240.
- 11 R. W. Pekala, *Journal of Materials Science*, 1989, **24**, 3221–3227.
- 12 S. A. Al-Muhtaseb and J. A. Ritter, *Advanced Materials*, 2003, **15**, 101–114.
- 13 K. Z. Gaca, J. A. Parkinson and J. Sefcik, *Polymer*, 2017, **110**, 62–73.
- 14 D. W. Schaefer, R. Pekala and G. Beaucage, *Journal of Non-Crystalline Solids*, 1995, **186**, 159–167.
- 15 T. Yamamoto, T. Nishimura, T. Suzuki and H. Tamon, *Journal of Non-Crystalline Solids*, 2001, **288**, 46–55.
- 16 C. J. Gommès and A. P. Roberts, *Physical Review E - Statistical, Nonlinear, and Soft Matter Physics*, 2008, **77**, 041409.
- 17 A. Allahbakhsh and A. R. Bahramian, *Nanoscale*, 2015, **7**, 14139–14158.
- 18 M. Alshrah, M.-P. Tran, P. Gong, H. E. Naguib and C. B. Park, *Journal of Colloid and Interface Science*, 2017, **485**, 65–74.
- 19 I. Yang, S.-G. Kim, S. H. Kwon, M.-S. Kim and J. C. Jung, *Electrochimica Acta*, 2017, **223**, 21–30.
- 20 Y. Yan, M. Shi, Y. Wei, C. Zhao, L. Chen, C. Fan, R. Yang and Y. Xu, *Journal of Nanoparticle Research*, 2018, **20**, 260.
- 21 M. Alshrah, H. E. Naguib and C. B. Park, *Materials & Design*, 2018, **151**, 154–163.
- 22 E. Kinnertová and V. Slovák, *Journal of Thermal Analysis and Calorimetry*, 2018, **134**, 1215–1222.
- 23 P. Meakin, *Physical Review Letters*, 1983, **51**, 1119–1122.
- 24 M. Kolb, R. Botet and R. Jullien, *Physical Review Letters*, 1983, **51**, 1123–1126.
- 25 P. Meakin and R. Jullien, *The Journal of Chemical Physics*, 1988, **89**, 246–250.
- 26 S. Gavalda, K. Kaneko, K. T. Thomson and K. E. Gubbins, *Colloids and Surfaces A: Physicochemical and Engineering Aspects*, 2001, **187**, 531–538.
- 27 S. Gavalda, K. E. Gubbins, Y. Hanzawa, K. Kaneko and K. T. Thomson, *Langmuir*, 2002, **18**, 2141–2151.
- 28 V. Morales-Flórez, N. D. L. Rosa-Fox, M. Piñero and L. Esquivias, *Journal of Sol-Gel Science and Technology*, 2005, **35**, 203–210.
- 29 V. Morales-Flórez, M. Piñero, N. de la Rosa-Fox, L. Esquivias, J. A. Anta and J. Primera, *Journal of Non-Crystalline Solids*, 2008, **354**, 193–198.

- 30 C. A. Ferreira-Rangel and L. D. Gelb, *The Journal of Physical Chemistry B*, 2013, **117**, 7095–7105.
- 31 R. W. Pekala, C. T. Alviso, F. M. Kong and S. S. Hulse, *Journal of Non-Crystalline Solids*, 1992, **145**, 90–98.
- 32 H. Tamon and H. Ishizaka, *Journal of Colloid and Interface Science*, 1998, **206**, 577–582.
- 33 V. A. Emelichev and V. G. Ovchinnikov, *Cybernetics*, 1985, **21**, 216–221.
- 34 C. S. Sharma, M. M. Kulkarni, A. Sharma and M. Madou, *Chemical Engineering Science*, 2009, **64**, 1536–1543.
- 35 M. Alshrah, L. H. Mark, C. Zhao, H. E. Naguib and C. B. Park, *Nanoscale*, 2018, **10**, 10564–10575.
- 36 H. S. Ma, J. H. Prévost and G. W. Scherer, *International Journal of Solids and Structures*, 2002, **39**, 4605–4614.
- 37 P. Grassberger and I. Procaccia, *Physica D: Nonlinear Phenomena*, 1983, **9**, 189–208.
- 38 B. B. Mandelbrot, *Physica Scripta*, 1985, **32**, 257–260.
- 39 T. Gneiting and M. Schlather, *Society for Industrial and Applied Mathematics*, 2001, **46**, 269–282.
- 40 D. Stauffer and A. Aharony, *Introduction to percolation theory*, Taylor & Francis, London, 2nd edn, 1994, p. 181.
- 41 L. Anderson, *PhD thesis*, University of Strathclyde, 2013.
- 42 S. J. Taylor, *PhD thesis*, University of Strathclyde, 2014.
- 43 C. Lin and J. A. Ritter, *Carbon*, 1997, **35**, 1271–1278.
- 44 D. Fairén-Jiménez, F. Carrasco-Marín and C. Moreno-Castilla, *Carbon*, 2006, **44**, 2301–2307.
- 45 T. Yamamoto, T. Nishimura, T. Suzuki and H. Tamon, *Drying Technology*, 2001, **19**, 1319–1333.
- 46 A. Awadallah-F, A. M. Elkhatat and S. A. Al-Muhtaseb, *Journal of Materials Science*, 2011, **46**, 7760–7769.
- 47 V. G. Pol, L. K. Shrestha and K. Ariga, *ACS Applied Materials and Interfaces*, 2014, **6**, 10649–10655.
- 48 O. Tange, *The USENIX Magazine*, 2011, **36**, 42–47.
- 49 V. Bock, A. Emmerling and J. Fricke, *Journal of Non-Crystalline Solids*, 1998, **225**, 69–73.
- 50 N. Job, C. J. Gommès, R. Pirard and J. P. Pirard, *Journal of Non-Crystalline Solids*, 2008, **354**, 4698–4701.
- 51 P. Grassberger and I. Procaccia, *Physical review letters*, 1983, **50**, 346.
- 52 T. Vicsek, *Fractal growth phenomena*, World Scientific, 1st edn, 1989, p. 355.
- 53 M. M. Huber, H. Klein and L. Ratke, *Particle & Particle Systems Characterization: Measurement and Description of Particle Properties and Behavior in Powders and Other Disperse Systems*, 2003, **20**, 379–381.

Appendix E

Computational codes

E.1 Visual Basic for Application macros used for nitrogen sorption data analysis

E.1.1 BET surface area calculation

```
1 Option Explicit
2 'Macro to evaluate BET accessible area using nitrogen adsorption isotherm
   data exported from Micromeritics ASAP 2420 surface area and porosity
   analyser software
3 Sub Rouquerol()
4 'Used variables are declared in the beginning
5 Dim i, n, warning, i_max, i_min, p_min, p_max As Integer 'i=dummy variable;
   n=number of points for linear regression; answer=used for message box
6 Dim nitrogen_area As Double, molar_volume As Double, avogadros_number As
   Double 'nitrogen_area=cross-sectional area of nitrogen molecule;
   molar_volume=molar volume of nitrogen; avogadros_number=value of
   Avogadro's number
7 Dim P() As Double, Q() As Double 'P=pressure values; Q=amount of nitrogen
   asorbed
8 Dim y(), x() As Double 'y = (P/Po)/(Q*(1-(P/Po))); x = Q*(1-P/Po)
9 Dim intercept, slope, i_error, s_error As Double 'intercept and slope for
   linear regression and their corresponding error values
10 Dim C, Vm, S As Double 'values of C constant, monolayer volume and calculated
   BET surface area
11 Dim checkC, checkP As String 'strings for final report to check validity of
   correction
12 Dim temp() As Variant 'dummy variable
13
14 'values of constants used for calculations
15 nitrogen_area = 0.162 / (10 ^ 18)
16 molar_volume = 22.41
17 avogadros_number = 6.022 * 10 ^ 23
18
19 'read isotherm data
20 ReDim P(1 To 100)
21 C = 1 'C is used as a loop counter here
22 Do While Worksheets(1).Cells(29 + C, 12).Value <> ""
23     P(C) = Worksheets(1).Cells(29 + C, 12).Value
24     C = C + 1
25 Loop
26 C = C - 1
27 ReDim Preserve P(1 To C)
28
29 'find pressure range 0.01-0.65
30 For i = 1 To C
31     If P(i) > 0.01 Then
32         p_min = i
```

```

33     Exit For
34   End If
35 Next i
36
37 For i = C To 1 Step -1
38   If P(i) < 0.65 Then
39     p_max = i
40     Exit For
41   End If
42 Next i
43
44 'resize P array to include only points within the range and read values of Q
45 If p_min = 1 Then
46   ReDim Preserve P(1 To p_max)
47   For i = 1 To p_max
48     Q(i) = Worksheets(1).Cells(28 + i, 8).Value
49   Next i
50 Else
51   ReDim temp(p_min To p_max)
52   For i = p_min To p_max
53     temp(i) = P(i)
54   Next i
55   ReDim P(1 To (p_max - p_min + 1))
56   For i = 1 To (p_max - p_min + 1)
57     P(i) = temp(p_min - i + 1)
58   Next i
59   ReDim Q(1 To (p_max - p_min + 1))
60   For i = 1 To (p_max - p_min + 1)
61     Q(i) = Worksheets(1).Cells(27 + p_min + i, 8).Value
62   Next i
63 End If
64
65 'calculate values of x and y
66 ReDim y(1 To p_max - p_min + 1)
67 ReDim x(1 To p_max - p_min + 1)
68 For i = 1 To (p_max - p_min + 1)
69   x(i) = Q(i) * (1 - P(i))
70   y(i) = P(i) / (Q(i) * (1 - P(i)))
71 Next i
72
73 'find range where x increases with increasing relative pressure
74 If x(1) < x(2) Then 'positive slope in the beginning
75   i_min = 1
76 Else 'negative slope in the beginning
77   For i = 1 To (p_max - p_min)
78     If x(i) < x(i + 1) Then
79       i_min = i
80     Exit For
81   End If
82 Next i
83 End If
84
85 If x(p_max - p_min + 1) > x(p_max - p_min) Then 'positive slope in the end
86   i_max = p_max - p_min + 1
87 Else 'negative slope in the end
88   For i = (p_max - p_min + 1) To i_min Step -1
89     If x(i) > x(i - 1) Then
90       i_max = i
91     Exit For
92   End If
93 Next i
94 End If
95
96 'calculate y in pressure range obtained for x above
97 If i_max > (i_min + 1) Then
98 'resize array y to contain only elements in range where x keeps increasing
99 If i_min = 1 Then
100   ReDim Preserve y(1 To i_max)
101 Else
102   ReDim temp(p_min To p_max)
103   For i = p_min To p_max
104     temp(i) = P(i)

```

```

105     Next i
106     ReDim P(1 To (p_max - p_min + 1))
107     For i = 1 To (p_max - p_min + 1)
108         P(i) = temp(p_min - 1 + i)
109     Next i
110 End If
111 ReDim Preserve y(i_min To i_max)
112 ReDim Preserve P(i_min To i_max)
113
114 'calculate values of slope and intercept of the BET plot using linear
    regression
115 intercept = Application.WorksheetFunction.intercept(y, P)
116 slope = Application.WorksheetFunction.slope(y, P)
117 i_error = Application.WorksheetFunction.Index(Application.WorksheetFunction.
    LinEst(y, P, 1, 1), 2, 2)
118 s_error = Application.WorksheetFunction.Index(Application.WorksheetFunction.
    LinEst(y, P, 1, 1), 2, 1)
119
120 'calculate value of C constant
121 C = 1 + slope / intercept
122 'calculate value of monolayer coverage
123 Vm = 1 / (intercept * C)
124 'calculate BET surface area
125 S = (Vm / 1000) * avogadros_number * nitrogen_area / molar_volume
126 Else 'if the x values do not increase, set all values to zero
127     slope = 0
128     intercept = 0
129     C = 0
130     Vm = 0
131     S = 0
132 End If
133
134 'write output into Sheet 2
135 Worksheets(2).Cells.Clear
136 Worksheets(2).Cells(2, 3).Value = "Rouquerol Correction Results"
137 Worksheets(2).Cells(2, 3).Font.Underline = xlUnderlineStyleSingle
138 Worksheets(2).Cells(3, 4).Value = "Corrected BET Surface Area:"
139 Worksheets(2).Cells(4, 4).Value = "C value:"
140 Worksheets(2).Cells(5, 4).Value = "Monolayer volume:"
141 Worksheets(2).Cells(3, 5).Value = S
142 Worksheets(2).Cells(4, 5).Value = C
143 Worksheets(2).Cells(5, 5).Value = Vm
144 Range(Worksheets(2).Cells(3, 4), Worksheets(2).Cells(5,
    4)).HorizontalAlignment = xlRight
145 Worksheets(2).Cells(2, 6).Value = "Error"
146 If slope > 0 Then
147     Worksheets(2).Cells(3, 6).Value = S * s_error / slope
148 Else
149     Worksheets(2).Cells(3, 6).Value = "-"
150 End If
151 Worksheets(2).Cells(2, 8).Value = "Data used for Rouquerol correction"
152 Worksheets(2).Cells(2, 8).Font.Underline = xlUnderlineStyleSingle
153 Worksheets(2).Cells(3, 8).Value = "P/Po"
154 Worksheets(2).Cells(3, 9).Value = "Volume adsorbed (Q)"
155 Worksheets(2).Cells(3, 10).Value = "Q*(1-P/Po)"
156 Worksheets(2).Cells(3, 11).Value = "(P/Po)/(Q*(1-(P/Po)))"
157 If i_max > 1 Then
158     For i = 1 To i_max
159         Worksheets(2).Cells(3 + i, 8).Value = P(i)
160         Worksheets(2).Cells(3 + i, 9).Value = Q(i)
161         Worksheets(2).Cells(3 + i, 10).Value = x(i)
162         Worksheets(2).Cells(3 + i, 11).Value = y(i)
163     Next i
164 End If
165 Worksheets(2).Cells(2, 14).Value = "Linear regression"
166 Worksheets(2).Cells(2, 14).Font.Underline = xlUnderlineStyleSingle
167 Worksheets(2).Cells(3, 14).Value = "Slope"
168 Worksheets(2).Cells(4, 14).Value = "Intercept"
169 Worksheets(2).Cells(3, 15).Value = slope
170 Worksheets(2).Cells(4, 15).Value = intercept
171 Worksheets(2).Cells(2, 16).Value = "Errors"

```

```

172 Worksheets(2).Cells(3, 16).Value = s_error
173 Worksheets(2).Cells(4, 16).Value = i_error
174
175 'check if the value of C constant is positive and the monolayer volume is
      within the range
176 warning = 0
177 If C > 0 Then
178     checkC = "Value of C constant is positive."
179 Else
180     checkC = "WARNING! Value of C constant is NOT positive!"
181     warning = 1
182 End If
183
184 If Vm > Q(1) And Vm < Q(10) Then
185     checkP = "Monolayer capacity is within the used range."
186 Else
187     checkP = "WARNING! Monolayer capacity is NOT within the used range!"
188     warning = 1
189 End If
190
191 'set the cell colour with BET surface area value to green if both checks
      above are positive, otherwise change the colour to red
192 If warning = 0 Then
193     Worksheets(2).Range(Worksheets(2).Cells(2,2),
194         Worksheets(2).Cells(5,5)).Interior.ColorIndex = 43
195 Else
196     Worksheets(2).Range(Worksheets(2).Cells(2,2),
197         Worksheets(2).Cells(5,5)).Interior.ColorIndex = 3
198 End If
199
200 'switch to Sheet 2
201 Worksheets(2).Activate
202
203 'inform user that the correction is finished and show the results
204 If warning = 0 Then
205     MsgBox "Corrected value of BET Surface Area: " & Round(S, 1) & " m2/g" &
206         vbNewLine & _
207         "Value of corrected C constant: " & Round(C, 0) & vbNewLine & vbNewLine
208         & _
209         "Correction validity check:" & vbNewLine & _
210         checkC & vbNewLine & _
211         checkP & vbNewLine & vbNewLine & _
212         "-----"
213         & vbNewLine & _
214         "Results of the correction can be found in the worksheet Rouquerol
215         correction (should be the second worksheet)" & vbNewLine & _
216         "-----",
217         vbInformation, "Rouquerol correction finished!"
218 Else
219     MsgBox "Corrected value of BET Surface Area: " & Round(S, 1) & " m2/g" &
220         vbNewLine & _
221         "Value of corrected C constant: " & Round(C, 0) & vbNewLine & vbNewLine
222         & _
223         "Correction validity check:" & vbNewLine & _
224         checkC & vbNewLine & _
225         checkP & vbNewLine & vbNewLine & _
226         "-----"
227         & vbNewLine & _
228         "Results of the correction can be found in the worksheet Rouquerol
229         correction (should be the second worksheet)" & vbNewLine & _
230         "-----",
231         vbExclamation, "Rouquerol correction finished!"
232 End If
233 End Sub

```

E.1.2 t-plot method calculation

```
1 Option Explicit
```

```

2 'macro for evaluating micropore volume and external surface area using
  nitrogen sorption exported from Micromeritics ASAP 2420 surface area and
  porosity analyser software
3 Sub tplot()
4 'declare used variables
5 Dim P(1 To 15) As Double 'P is the relative pressure P/Po from isotherm
6 Dim Q(1 To 15) As Double 'Q is the volume adsorbed from isotherm
7 Dim P_slope(1 To 13) As Double 'P_slope is the 3 point slope for finding
  linear section of isotherm
8 Dim R(1 To 13) As Double 'R is the R^2 value for 3 point linear regression
9 Dim Ptemp() As Double, Qtemp() As Double 'arrays for passing arguments to 3
  point linear regression
10 Dim upper_P_slope As Double, lower_P_slope As Double 'upper and lower
  boundary of values within 10% of slope at R^2 = 1
11 Dim Pmin As Double, Pmax As Double 'upper and lower relative pressure limit
  for linear part
12 Dim i_min As Integer, i_max As Integer, count As Integer 'i values for Pmin
  and Pmax
13 Dim t() As Double 'array for calculating statistical thickness using ASTM
  standard D-6556-01
14 Dim intercept As Double, slope, i_error, s_error As Double 'intercept and
  slope for linear fitting of statistical thickness vs pressure
15 Dim external_SA As Double, mpore_volume As Double, mpore_area As Double,
  BET_SA 'external surface area [m^2/g], microporous volume [cm^3],
  microporous surface area [m^2/g], and BET surface area after Rouquerol
  correction, respectively
16 Dim i As Integer, j As Integer 'dummy variables
17 Dim linear As Variant
18 Dim warning As Integer 'used for final report to check validity of correction
19 Dim checkI As String 'used for final report to check validity of correction
20
21 'read values of P/Po and Q from table
22 For i = 1 To 15
23   P(i) = Worksheets(1).Cells(28 + i, 6).Value
24   Q(i) = Worksheets(1).Cells(28 + i, 8).Value
25 Next i
26
27 'calculate 3 point linear regression and values of P_slope and R^2
28 ReDim Ptemp(1 To 3)
29 ReDim Qtemp(1 To 3)
30 For i = 1 To 13
31   For j = 1 To 3
32     Ptemp(j) = P(j + i - 1)
33     Qtemp(j) = Q(j + i - 1)
34   Next j
35   linear = Application.WorksheetFunction.LinEst(Qtemp, Ptemp, True, True)
36   P_slope(i) = linear(1, 1)
37   R(i) = linear(3, 1)
38 Next i
39
40 'find the highest value of R^2
41 j = 1
42 For i = 1 To 13
43   If R(i) > R(j) Then
44     j = i
45   End If
46 Next i
47
48 'get 10% limits of P_slope around the highest value of R^2
49 lower_P_slope = 0.9 * P_slope(j)
50 upper_P_slope = 1.1 * P_slope(j)
51
52 'find linear range on isotherm within 10% P_slope deviation
53 Pmin = 1
54 Pmax = 0
55 For i = 1 To 13
56   If P_slope(i) > lower_P_slope And P_slope(i) < upper_P_slope Then
57     If P(i + 2) < Pmin Then
58       Pmin = P(i + 2)
59       i_min = i + 2
60     End If
61     If P(i + 2) > Pmax Then

```

```

62     Pmax = P(i + 2)
63     i_max = i + 2
64     End If
65 End If
66 Next i
67
68 'calculate statistical thickness of adsorbed gas layer
69 ReDim t(i_min To i_max)
70 ReDim Ptemp(i_min To i_max)
71 ReDim Qtemp(i_min To i_max)
72 For i = i_min To i_max
73     t(i) = 0.88 * (P(i)) ^ 2 + 6.45 * P(i) + 2.98
74     Ptemp(i) = P(i)
75     Qtemp(i) = Q(i)
76 Next i
77 count = i_max - i_min + 1
78
79 'calculate values of slope and intercept from linear regression
80 If count > 1 Then
81     slope = WorksheetFunction.slope(Qtemp, t)
82     intercept = WorksheetFunction.intercept(Qtemp, t)
83     i_error = Application.WorksheetFunction.Index(Application.WorksheetFunction.
84         LinEst(Qtemp, t, 1, 1), 2, 2)
85     s_error = Application.WorksheetFunction.Index(Application.WorksheetFunction.
86         LinEst(Qtemp, t, 1, 1), 2, 1)
87 Else
88     slope = 0
89     intercept = 0
90     s_error = 0
91     i_error = 0
92 End If
93
94 'read value of BET surface area evaluated using Sub Rouquerol()
95 BET_SA = Worksheets(2).Cells(3, 5).Value
96
97 'calculate external surface area, micropore volume and micropore surface area
98 external_SA = slope * 15.47
99 mpore_volume = intercept * 0.001547
100 mpore_area = BET_SA - external_SA
101
102 'write output into Sheet 3
103 Worksheets(3).Cells.Clear
104 Worksheets(3).Cells(2, 3).Value = "t-plot Correction Results"
105 Worksheets(3).Cells(2, 3).Font.Underline = xlUnderlineStyleSingle
106 Worksheets(3).Cells(3, 4).Value = "Micropore Volume:"
107 Worksheets(3).Cells(4, 4).Value = "External Surface Area:"
108 Worksheets(3).Cells(5, 4).Value = "Micropore Surface Area:"
109 Range(Worksheets(3).Cells(3, 4), Worksheets(3).Cells(5,
110     4)).HorizontalAlignment = xlRight
111 Worksheets(3).Cells(3, 5).Value = mpore_volume
112 Worksheets(3).Cells(4, 5).Value = external_SA
113 Worksheets(3).Cells(5, 5).Value = mpore_area
114 Worksheets(3).Cells(2, 6).Value = "Errors"
115 If intercept > 0 Then
116     Worksheets(3).Cells(3, 6).Value = mpore_volume * i_error / intercept
117 Else
118     Worksheets(3).Cells(3, 6).Value = "-"
119 End If
120 If slope > 0 Then
121     Worksheets(3).Cells(4, 6).Value = external_SA * s_error / slope
122 Else
123     Worksheets(3).Cells(4, 6).Value = "-"
124 End If
125
126 Worksheets(3).Cells(2, 8).Value = "Data used for t-plot correction"
127 Worksheets(3).Cells(2, 8).Font.Underline = xlUnderlineStyleSingle
128 Worksheets(3).Cells(3, 8).Value = "P/Po"
129 Worksheets(3).Cells(3, 9).Value = "Statistical Thickness [A]"
130 Worksheets(3).Cells(3, 12).Value = "Quantity adsorbed [cm3/g STP]"
131 j = 1
132 For i = i_min To i_max
133     Worksheets(3).Cells(3 + j, 8).Value = P(i)

```

```

131 Worksheets(3).Cells(3 + j, 9).Value = t(i)
132 Worksheets(3).Cells(3 + j, 12).Value = Q(i)
133 j = j + 1
134 Next i
135 Worksheets(3).Cells(14, 8).Value = "Linear regression"
136 Worksheets(3).Cells(14, 8).Font.Underline = xlUnderlineStyleSingle
137 Worksheets(3).Cells(15, 8).Value = "Slope"
138 Worksheets(3).Cells(16, 8).Value = "Intercept"
139 Worksheets(3).Cells(15, 9).Value = slope
140 Worksheets(3).Cells(16, 9).Value = intercept
141 Worksheets(3).Cells(14, 10).Value = "Errors"
142 Worksheets(3).Cells(15, 10).Value = s_error
143 Worksheets(3).Cells(16, 10).Value = i_error
144
145 'check if the value of intercept is positive and not too low (below 0.1)
146 warning = 0
147 If intercept > 0.1 Then
148     checkI = "Value of intercept is positive."
149 ElseIf intercept < 0 Then
150     checkI = "WARNING! Value of intercept is NOT positive!"
151     warning = 1
152 Else
153     checkI = "WARNING! Value of intercept is very low (less than 0.1)! This
154             means very low micropore volume!"
155     warning = 1
156 End If
157
158 'set the cell colour with micropore volume value to green if intercept check
159 'above is positive, otherwise change the colour to red
160 If warning = 0 Then
161     Worksheets(3).Range(Worksheets(3).Cells(2, 2), Worksheets(3).Cells(5,
162     5)).Interior.ColorIndex = 43
163 Else
164     Worksheets(3).Range(Worksheets(3).Cells(2, 2), Worksheets(3).Cells(5,
165     5)).Interior.ColorIndex = 3
166 End If
167
168 'switch to Sheet 3
169 Worksheets(3).Activate
170
171 'inform the user that the correction is finished and show the results
172 If warning = 0 Then
173 MsgBox "Corrected value of Micropore volume: " & Round(mpore_volume, 5) & "
174 cm^3" & vbNewLine & _
175     "Value of corrected External Surface Area: " & Round(external_SA, 1) &
176     " m^2/g" & vbNewLine & _
177     "Value of corrected Micropore Surface Area: " & Round(mpore_area, 1) &
178     " m^2/g" & vbNewLine & vbNewLine & _
179     "Correction validity check:" & vbNewLine & _
180     checkI & vbNewLine & vbNewLine & _
181     "-----"
182     & vbNewLine & _
183     "Results of the correction can be found in the worksheet t-plot
184     correction (should be the third worksheet)" & vbNewLine & vbNewLine
185     & _
186     "In order to see the linear range used for t-plot correction, press
187     'Plot isotherm' button" & vbNewLine & _
188     "-----",
189     vbInformation, "t-plot correction finished!"
190 Else
191 MsgBox "Corrected value of Micropore volume: " & Round(mpore_volume, 5) & "
192 cm^3" & vbNewLine & _
193     "Value of corrected External Surface Area: " & Round(external_SA, 1) &
194     " m^2/g" & vbNewLine & _
195     "Value of corrected Micropore Surface Area: " & Round(mpore_area, 1) &
196     " m^2/g" & vbNewLine & vbNewLine & _
197     "Correction validity check:" & vbNewLine & _
198     checkI & vbNewLine & vbNewLine & _
199     "-----"
200     & vbNewLine & _

```

```

186      "Results of the correction can be found in the worksheet t-plot
      correction (should be the third worksheet)" & vbNewLine & vbNewLine
      & _
187      "In order to see the linear range used for t-plot correction, press
      'Plot isotherm' button" & vbNewLine & _
188      "-----",
189      vbExclamation, "t-plot correction finished!"
190 End If
191 End Sub

```

E.2 Fortran codes

E.2.1 Cluster growth code

```

1 PROGRAM cluster
2   IMPLICIT NONE
3   !program that places activated and non-activated monomers on a lattice,
   !allows both monomers and clusters to diffuse using kinetic Monte Carlo
   !(kMC) algorithm, probability of diffusion is reversly proportional to
   !entity size, cluster links are stored in SuperCluster lattice, size of
   !individual clusters is stored in ClusterSize and size of aggregates in
   !FinalSize
4   INTEGER, PARAMETER :: Nlat=1000, dp=selected_real_kind(15, 307)
   !Nlat=size of lattice; dp=precision for real numbers
5   INTEGER :: Nmax, Nact, Nmon !Nmax=number of all species ; Nact=number of
   !activated monomers (clusters); Nmon=number of monomers
6   REAL :: solid, percentage !solid=solids content; percentage=percentage of
   !activated monomers;
7   INTEGER, ALLOCATABLE :: iCluster(:,,:), jCluster(:,,:), iMonomer(:,),
   !jMonomer(:,), Monomer(:,,:), Cluster(:,,:) !iCluster,jCluster=cluster
   !sites coordinates with elements as (Cluster ID, position);
   !iMonomer,jMonomer=monomer coordinates as for clusters; Monomer=monomer
   !distribution lattice; Cluster=cluster distribution lattice
8   INTEGER, ALLOCATABLE :: ClusterSize(:,), ClusterCounter(:,), FinalSize(:,),
   !SuperCluster(:,,:) !ClusterSize=size of each cluster;
   !ClusterCounter=position counter for drawing clusters; FinalSize=size
   !of cluster aggregates; SuperCluster=cluster links
9   REAL(KIND=dp), ALLOCATABLE :: MCSum(:) !sums for kMC algorithm
10  INTEGER :: MonDiff, FreeMon, i,j, k, ios, ClusterSum, MonomerSum,
   !SizeSum, s, p, r, No, current !MonDiff=monomer to diffuse;
   !FreeMon=number of remaining monomers; i,j=lattice coordinates; k=dummy
   !integer; ios=integer for status during opening files; ClusterSum=sum
   !of positions occupied by clusters on lattice; MonomerSum=sum of
   !monomers on the lattice in the beginning of a run; SizeSum=sum of
   !cluster sizes; s,p,r=solid, percentage, run integer values; No,
   !current=dummy variables
11  INTEGER :: rnd(1:8), WorkMon, WorkCluster, MonAbs, iList(Nlat*Nlat),
   !jList(Nlat*Nlat), move, ID, Clusters !rnd=for random number generator;
   !WorkMon,WorkCluster=monomer/cluster currently working with;
   !MonAbs=monomers being absorbed; iList,jList=i and j coordinates for
   !cluster drawing; move=integer used for diffusion; ID=Cluster ID;
   !Clusters=number of remaining clusters
12  INTEGER, DIMENSION(12) :: seed !seed=for random number generator
13  REAL(KIND=dp) :: ireal, jreal, MCmove, time !ireal, jreal=for random
   !number generator; MCmove=used for kMC algorithm; time=kMC time
14  CHARACTER(LEN=30) :: ClusterFile, SizeFile, iFile, jFile, TimeFile,
   !FinalFile, SummaryFile !file names
15  LOGICAL :: coalesce, last !used to recalculate MCSum only when it changes
   !due to a coalescent event; last=used as switch for output
16
17  WRITE(*,*) '----- Program started -----'
18  !inform user the program has started
19
20  CALL list(Nlat, iList, jList)
   !create list of positions for drawing clusters
21
22
23  r = 1 !run number from a range 1-10
24  seed = r*100 !seed for random number generator

```

```

25
26 s = 1 !solids content integer value form a range 1-5
27 solid = 1.0*s/10 !solids content real value
28
29 p = 1 !percentage of activated monomers integer value from a range 1-3
30 percentage = (1.0*p)/100 !percentage of activated monomers real value
31
32 !calculate number of species in simulation
33 Nmax = NINT(solid*Nlat*Nlat)
34 Nact = NINT(percentage*Nmax)
35 FreeMon = Nmax-Nact
36 Nmon = FreeMon
37
38 !allocate dynamic arrays
39 ios = 0
40 ALLOCATE( iCluster(Nact,Nlat), jCluster(Nact,Nlat),iMonomer(FreeMon),
41           jMonomer(FreeMon),&
42           Monomer(Nlat,Nlat), Cluster(Nlat,Nlat), ClusterSize(Nact),
43           ClusterCounter(Nact),&
44           SuperCluster(Nact,Nact), FinalSize(Nact), MCSum(Nmax), STAT=ios )
45 !if there is an issue allocating arrays, inform user and stop execution
46 IF (ios/=0) THEN
47   WRITE(*,*) 'Error allocating arrays'
48   STOP
49 END IF
50
51 !create file names
52 IF (r.LT.10) THEN
53   WRITE(ClusterFile,'(A8,F3.1,A1,F4.2,A1,I1,A4)') 'Cluster_', solid,
54     percentage, '_', r, '.dat'
55   WRITE(SizeFile,'(A5,F3.1,A1,F4.2,A1,I1,A4)') 'Size_', solid, '_',
56     percentage, '_', r, '.dat'
57   WRITE(iFile,'(A5,F3.1,A1,F4.2,A1,I1,A4)') 'iPos_', solid, '_',
58     percentage, '_', r, '.dat'
59   WRITE(jFile,'(A5,F3.1,A1,F4.2,A1,I1,A4)') 'jPos_', solid, '_',
60     percentage, '_', r, '.dat'
61   WRITE(TimeFile,'(A5,F3.1,A1,F4.2,A1,I1,A4)') 'Time_', solid, '_',
62     percentage, '_', r, '.dat'
63   WRITE(FinalFile,'(A6,F3.1,A1,F4.2,A1,I1,A4)') 'Final_', solid, '_',
64     percentage, '_', r, '.dat'
65   WRITE(SummaryFile,'(A4,F3.1,A1,F4.2,A1,I1,A4)') 'DEL_', solid, '_',
66     percentage, '_', r, '.dat'
67 ELSEIF ((r.GE.10) .AND. (r.LT.100)) THEN
68   WRITE(ClusterFile,'(A8,F3.1,A1,F4.2,A1,I2,A4)') 'Cluster_', solid,
69     percentage, '_', r, '.dat'
70   WRITE(SizeFile,'(A5,F3.1,A1,F4.2,A1,I2,A4)') 'Size_', solid, '_',
71     percentage, '_', r, '.dat'
72   WRITE(iFile,'(A5,F3.1,A1,F4.2,A1,I2,A4)') 'iPos_', solid, '_',
73     percentage, '_', r, '.dat'
74   WRITE(jFile,'(A5,F3.1,A1,F4.2,A1,I2,A4)') 'jPos_', solid, '_',
75     percentage, '_', r, '.dat'
76   WRITE(TimeFile,'(A5,F3.1,A1,F4.2,A1,I2,A4)') 'Time_', solid, '_',
77     percentage, '_', r, '.dat'
78   WRITE(FinalFile,'(A6,F3.1,A1,F4.2,A1,I2,A4)') 'Final_', solid, '_',
79     percentage, '_', r, '.dat'
80   WRITE(SummaryFile,'(A4,F3.1,A1,F4.2,A1,I2,A4)') 'DEL_', solid, '_',
81     percentage, '_', r, '.dat'
82 END IF
83
84 !open file for output during execution, if there is an issue opening the
85 file inform the user and stop execution
86 ios = 0
87 OPEN(14, FILE=TimeFile, STATUS='REPLACE', IOSTAT=ios)
88 IF (ios/=0) THEN
89   WRITE(*,*) 'Error opening file Time.dat', ios
90   STOP
91 END IF
92
93 !reset and initialise monomer and cluster density distribution lattices
94 and relevant arrays
95 Monomer = 0
96 Cluster = 0

```

```

79   ClusterCounter = 1
80   current = 0
81   SuperCluster = 0
82   DO i=1,Nact
83       SuperCluster(i,i) = 1
84   END DO
85   FinalSize = 1
86   iCluster = 0
87   jCluster = 0
88   MCSum(1) = 1
89   DO i=2,Nmax !calculate initial MCSum at for kMC algorithm
90       MCSum(i) = MCSum(i-1) + 1
91   END DO
92   time = 0 !initialise kMC time
93
94   !write headers for output file
95   WRITE(14,'(5A20)') 'Time elapsed', 'Remaining monomers', 'Number of
      clusters', 'No', 'current'
96
97   !initialise random number generator
98   CALL RANDOM_SEED(PUT=seed)
99
100  !distribute activated monomers on lattice
101  WorkMon = Nact
102  DO WHILE (WorkMon > 0)
103      !get a random position on lattice
104      CALL RANDOM_NUMBER(ireal)
105      CALL RANDOM_NUMBER(jreal)
106      iCluster(WorkMon,1) = INT(Nlat*ireal)+1
107      jCluster(WorkMon,1) = INT(Nlat*jreal)+1
108
109      !if the selected position is empty, place the monomer and move on to
      next monomer
110      IF (Cluster(iCluster(WorkMon,1),jCluster(WorkMon,1))==0) THEN
111          Cluster(iCluster(WorkMon,1),jCluster(WorkMon,1)) = WorkMon !put
      cluster number on lattice
112          ClusterSize(WorkMon) = 1 !set cluster size to 1
113          WorkMon = WorkMon - 1 !move on
114      END IF
115  END DO
116
117  !distribute monomers on lattice
118  WorkMon = FreeMon
119  DO WHILE (WorkMon > 0)
120      !get a random position on lattice
121      CALL RANDOM_NUMBER(ireal)
122      CALL RANDOM_NUMBER(jreal)
123      iMonomer(WorkMon) = INT(Nlat*ireal)+1
124      jMonomer(WorkMon) = INT(Nlat*jreal)+1
125
126      !if the selected position is empty, place the monomer and move on to
      next monomer
127      IF ((Cluster(iMonomer(WorkMon),jMonomer(WorkMon))==0) .AND.
      (Monomer(iMonomer(WorkMon),jMonomer(WorkMon))==0)) THEN
128          Monomer(iMonomer(WorkMon),jMonomer(WorkMon)) =
      Monomer(iMonomer(WorkMon),jMonomer(WorkMon)) + 1
129          WorkMon = WorkMon - 1
130      END IF
131  END DO
132
133  !check if any cluster seeds are adjacent to each other and if there are,
      link them into a cluster aggregate before initiating diffusion
134  DO i=1,Nact
135      CALL HK_scan(i, Nact, Nlat, Cluster, ClusterSize, iCluster, jCluster, &
      SuperCluster, coalesce, FinalSize)
136  END DO
137
138  coalesce = .TRUE. !set to true, so that in the first loop iteration
      cluster sum is calculated
140  No = 1 !initialise counters
141  current = Nact
142  last = .TRUE. !variable set to FALSE when 20 cluster aggregates remain

```

```

143
144 !loop until there is only one cluster aggregate left
145 mainloop: DO
146     !if a coalesce event occurred, recalculate number of remaining cluster
        aggregates
147     IF (coalesce) THEN
148         Clusters = 0
149         endloop: DO i=1,Nact
150             IF (FinalSize(i)>0) THEN
151                 Clusters = Clusters + 1
152             END IF
153         END DO endloop
154
155     !if there are 20 aggregates remaining
156     IF ((Clusters==20) .AND. (last)) THEN
157         current = 20
158         last = .FALSE.
159         !uncomment next line to switch on output to terminal during
            execution
160         !WRITE(*,*) 'Clusters remaining: ', Clusters, 'Percentage
            remaining: ', 1.0*Clusters/Nact*100
161     END IF
162
163     !every time number of aggregates remaining reduces by Nact/100
        write output
164     IF ((Clusters .LE. current) .AND. (Clusters>20)) THEN
165         WRITE(14,'(F20.2,4I20)') time, FreeMon, Clusters, No, current
166         CALL FLUSH(14)
167         !uncomment next 2 lines to switch on output to terminal during
            execution
168         !WRITE(*, '(F20.2,4I20)') time, FreeMon, Clusters, No, current
169         !WRITE(*,*) 'Clusters remaining: ', Clusters, 'Percentage
            remaining: ', 1.0*Clusters/Nact*100
170
171         !uncomment next line to write output for creating gif of
            structure formation
172         !CALL plotgif(Cluster,r,s,p,No,Nlat)
173
174         !increment counters
175         current = current - Nact/100
176         No = No + 1
177
178     !when there are only 20 and less aggregates remaining write ouput
        every time two aggregates merge
179     ELSEIF ((Clusters .LE. current) .AND. (Clusters .LE. 20)) THEN
180         WRITE(14,'(F20.2,4I20)') time, FreeMon, Clusters, No, current
181         CALL FLUSH(14)
182         !uncomment next 2 lines to switch on output to terminal during
            execution
183         !WRITE(*, '(F20.2,4I20)') time, FreeMon, Clusters, No, current
184         !WRITE(*,*) 'Clusters remaining: ', Clusters, 'Percentage
            remaining: ', 1.0*Clusters/Nact*100
185
186         !uncomment next line to write output for creating gif of
            structure formation
187         !CALL plotgif(Cluster,r,s,p,No,Nlat)
188
189         !increment counters
190         current = current - 1
191         No = No + 1
192     END IF
193 END IF
194
195     !check if there's only one aggregate left and no free monomers; if
        yes, exit the main loop and finalise the run
196     IF ((Clusters==1) .AND. (FreeMon<1)) EXIT mainloop
197
198     !reset coalesce variable
199     coalesce = .FALSE.
200
201     !get a random number within MCSum
202     CALL RANDOM_NUMBER(ireal)

```

```

203     MCmove = ireal * MCSum(Nmax)
204
205     !find which monomer/cluster is going to move
206     MCfind: DO i=1,Nmax
207         IF (MCSum(i)>MCmove) EXIT MCfind
208     END DO MCfind
209
210     IF (i .LE. Nact) THEN !if a cluster was selected
211         WorkCluster = i
212         !move the cluster one lattice site in a random direction
213         CALL diffuse_cluster(Cluster, Nlat, Nact, WorkCluster, iCluster,
214                             jCluster, SuperCluster, ClusterSize)
215
216         !check if the cluster/aggregate is adjacent to another
217         !cluster/aggregate
218         DO j=1,Nact
219             IF (SuperCluster(WorkCluster,j)==1) THEN
220                 CALL HK_scan(j, Nact, Nlat, Cluster, ClusterSize, iCluster,
221                             jCluster, &
222                             SuperCluster, coalesce, FinalSize)
223             END IF
224         END DO
225     ELSE !if a monomer was selected
226         WorkMon = i - Nact
227         !attempt to move the monomer one lattice site in a random direction
228         CALL diffuse_monomer(Monomer, Nlat, Nmon, iMonomer, jMonomer,
229                             WorkMon)
230
231         !if there is a cluster at the new position, use attach subroutine
232         !to add the monomer to the cluster
233         IF (Cluster(iMonomer(WorkMon),jMonomer(WorkMon))/=0) THEN
234             CALL attach(iMonomer(WorkMon), jMonomer(WorkMon), Nlat, Nact,
235                       iCluster, jCluster, Cluster, &
236                       ClusterSize, ClusterCounter, iList, jList, FinalSize)
237
238             !remove the absorbed monomer from the lattice
239             Monomer(iMonomer(WorkMon),jMonomer(WorkMon)) = 0
240
241             !set coalesce to TRUE to recalculate kMC sum
242             coalesce = .TRUE.
243
244             !see if the grown cluster/aggregate is adjacent to another
245             !cluster/aggregate
246             WorkCluster = Cluster(iMonomer(WorkMon),jMonomer(WorkMon))
247             CALL HK_scan(WorkCluster, Nact, Nlat, Cluster, ClusterSize,
248                       iCluster, jCluster, SuperCluster, &
249                       coalesce, FinalSize)
250
251             !set the absorbed monomer coordinates to 0
252             iMonomer(WorkMon) = 0
253             jMonomer(WorkMon) = 0
254
255             !reduce the number of remaining free monomers
256             FreeMon = FreeMon - 1
257         END IF
258     END IF
259
260     !advance the simulation clock
261     CALL RANDOM_NUMBER(ireal)
262     time = time - (LOG(ireal)/MCSum(Nmax))
263
264     !record time when all monomers were absorbed and set FreeMon to -1 so
265     !the time is not overwritten
266     IF (FreeMon==0) THEN
267         time_monomer = time
268         FreeMon = -1
269     END IF
270
271     !calculate kMC sum to get probabilities of cluster/monomer move when a
272     !coalescent event has occurred
273     IF (coalesce) THEN
274         DO i=1,Nmax

```

```

265         !set the probability for first cluster depending on its size
266         IF (i==1) THEN
267             !if the first cluster is pointing to another one within the
                aggregate, set its probability to 0
268             IF (FinalSize(1)>0) THEN
269                 MCSum(i) = 1/(REAL(FinalSize(i)))
270             ELSE
271                 MCSum(i) = 0
272             END IF
273             !set probabilities for the rest of clusters/aggregates
274             ELSEIF ((i .LE. Nact) .AND. (i>1)) THEN
275                 IF (FinalSize(i)>0) THEN
276                     MCSum(i) = MCSum(i-1) + 1/(REAL(FinalSize(i)))
277                 ELSE
278                     MCSum(i) = MCSum(i-1)
279                 END IF
280             !set probabilities for monomers
281             ELSE
282                 IF (iMonomer(i-Nact)/=0) THEN
283                     MCSum(i) = MCSum(i-1) + 1
284                 ELSE
285                     MCSum(i) = MCSum(i-1)
286                 END IF
287             END IF
288         END DO
289     END IF
290
291     END DO mainloop
292
293     !calculate the number of species on lattice to ensure no mass loss occurred
294     k = 0
295     DO i=1,Nlat
296         DO j=1,Nlat
297             IF (Cluster(i,j)/=0) k = k + 1
298         END DO
299     END DO
300
301     !write output
302     WRITE(14,*)
303     WRITE(14,'(5A20)') 'Lattice Sum', 'Solids content', 'Number of species',
                'Number of clusters', 'Number of monomers'
304     WRITE(14,'(5I20)') k, Nlat*Nlat/10*s, Nmax, Nact, Nmon
305
306     !open file for writing cluster distribution lattice
307     ios = 0
308     OPEN(8, FILE=ClusterFile, STATUS='REPLACE', IOSTAT=ios)
309     IF (ios/=0) THEN
310         WRITE(*,*) 'Error opening file Cluster.dat', ios
311         STOP
312     END IF
313
314     !write out cluster distribution lattice
315     CALL plotcluster(Cluster,Nlat, FreeMon)
316
317     !close the file
318     CLOSE(8)
319
320     !record final simulation time
321     time_final = time
322
323     !open file for writing cluster size distribution
324     ios = 0
325     OPEN(11, FILE=SizeFile, STATUS='REPLACE', IOSTAT=ios)
326     IF (ios/=0) THEN
327         WRITE(*,*) 'Error opening file Size.dat', ios
328         STOP
329     END IF
330
331     !write out cluster size distribution
332     WRITE(11,'(X,1000I6)') (ClusterSize(i), i=1,Nact)
333
334     !open file for writing cluster centre coordinates

```

```

335   ios = 0
336   OPEN(12, FILE=iFile, STATUS='REPLACE', IOSTAT=ios)
337   IF (ios/=0) THEN
338     WRITE(*,*) 'Error opening file iPos.dat', ios
339     STOP
340   END IF
341
342   !write out cluster number and cluster centre coordinates
343   DO i=1,Nact
344     WRITE(12,'(X,1000I6)') i, iCluster(i,1), jCluster(i,1)
345   END DO
346
347   !close files
348   DO i=11,12
349     CLOSE(i)
350   END DO
351
352   !deallocate dynamic arrays
353   ios = 0
354   DEALLOCATE( iCluster, jCluster, iMonomer, jMonomer, Monomer, Cluster,
355             ClusterSize, &
356             ClusterCounter, SuperCluster, FinalSize, MCSum, STAT=ios )
357   IF (ios/=0) THEN
358     WRITE(*,*) 'Error deallocating arrays'
359     STOP
360   END IF
361
362   !inform user the program has finished
363   WRITE(*,*) '----- Program finished -----'
364
365   !subroutines used by the main program
366   CONTAINS
367   SUBROUTINE diffuse_monomer(Monomer, Nlat, Nmon, iMonomer, jMonomer,
368     MonDiff)
369     !subroutine for monomer diffusion
370     IMPLICIT NONE
371     INTEGER, INTENT(IN) :: Nlat, Nmon, MonDiff !Nlat=lattice size;
372     Nmax=total number of monomers; MonDiff=monomer to diffuse
373     INTEGER, INTENT(INOUT) :: iMonomer(Nmon), jMonomer(Nmon),
374     Monomer(Nlat,Nlat) !iMonomer,jMonomer=monomer coordinate arrays;
375     Monomer=monomer distribution lattice
376     INTEGER :: i, j, move !local integer variables
377
378     !transfer monomer position into local variables
379     i = iMonomer(MonDiff)
380     j = jMonomer(MonDiff)
381
382     !make a random step up/down/left/right
383     move=INT(4*RAND())+1
384     SELECT CASE (move)
385     CASE (1)
386       i = i + 1
387     CASE (2)
388       i = i - 1
389     CASE (3)
390       j = j + 1
391     CASE (4)
392       j = j - 1
393     END SELECT
394
395     !apply periodic boundary conditions
396     IF (i > Nlat) i = i - Nlat
397     IF (i < 1) i = i + Nlat
398     IF (j > Nlat) j = j - Nlat
399     IF (j < 1) j = j + Nlat
400
401     !check if the new position is not occupied by another monomer
402     IF (Monomer(i,j)==0) THEN
403       !if the selected site is available, remove the monomer from the
404       original position
405       Monomer(iMonomer(MonDiff),jMonomer(MonDiff)) =
406         Monomer(iMonomer(MonDiff),jMonomer(MonDiff)) - 1

```

```

400
401      !place the monomer on the new position
402      Monomer(i,j) = Monomer(i,j) + 1
403
404      !set the monomer coordinates to the new position
405      iMonomer(MonDiff) = i
406      jMonomer(MonDiff) = j
407  END IF
408  END SUBROUTINE diffuse_monomer
409
410  SUBROUTINE diffuse_cluster(Cluster, Nlat, Nact, ClusterDiff, iCluster,
411      jCluster, SuperCluster, ClusterSize)
412      !subroutine for cluster diffusion
413      IMPLICIT NONE
414      INTEGER, INTENT(IN) :: Nlat, Nact, ClusterDiff !Nlat=lattice size;
415      Nact=total number of clusters; ClusterDiff=cluster to diffuse
416      INTEGER, INTENT(IN) :: SuperCluster(Nact,Nact), ClusterSize(Nact)
417      !SuperCluster=cluster links; ClusterSize=cluster size distribution
418      INTEGER, INTENT(INOUT) :: Cluster(Nlat,Nlat), iCluster(Nact,Nlat),
419      jCluster(Nact,Nlat) !iCluster,jCluster=cluster coordinates;
420      Cluster=cluster distribution lattice
421      INTEGER :: i, j, move, ios, ClusterNo !local variables
422
423      !remove cluster/aggregate from lattice
424      DO i=1,Nact
425        IF (SuperCluster(ClusterDiff,i)==1) THEN
426          DO j=1,ClusterSize(i)
427            Cluster(iCluster(i,j),jCluster(i,j)) = 0
428          END DO
429        END IF
430      END DO
431
432      !make a random step up/down/left/right
433      move=INT(4*RAND())+1
434      SELECT CASE (move)
435      CASE (1)
436        outer1: DO i=1,Nact !loop through all clusters
437          IF (SuperCluster(ClusterDiff,i)==1) THEN
438            !for clusters within the same aggregate
439            inner1: DO j=1,Nlat !loop through sites occupied by
440              current cluster
441              !loop until all the positions have been changed
442              IF (iCluster(i,j)==0) EXIT inner1
443              !update cluster coordinates
444              iCluster(i,j) = iCluster(i,j) + 1
445              !apply periodic boundary conditions
446              IF (iCluster(i,j) > Nlat) iCluster(i,j) =
447                iCluster(i,j) - Nlat
448              !put cluster back on lattice
449              Cluster(iCluster(i,j),jCluster(i,j)) = i
450            END DO inner1
451          END IF
452        END DO outer1
453      CASE (2)
454        outer2: DO i=1,Nact !loop through all clusters
455          IF (SuperCluster(ClusterDiff,i)==1) THEN
456            !for clusters within the same aggregate
457            inner2: DO j=1,Nlat !loop through sites occupied by
458              current cluster
459              !loop until all the positions have been changed
460              IF (iCluster(i,j)==0) EXIT inner2
461              !update cluster coordinates
462              iCluster(i,j) = iCluster(i,j) - 1
463              !apply periodic boundary conditions
464              IF (iCluster(i,j) < 1) iCluster(i,j) =
465                iCluster(i,j) + Nlat
466              !put cluster back on lattice
467              Cluster(iCluster(i,j),jCluster(i,j)) = i
468            END DO inner2
469          END IF
470        END DO outer2
471      CASE (3)

```

```

463         outer3: DO i=1,Nact !loop through all clusters
464             IF (SuperCluster(ClusterDiff,i)==1) THEN
465                 !for clusters within the same aggregate
466                 inner3: DO j=1,Nlat !loop through sites occupied by
467                     current cluster
468                     !loop until all the positions have been changed
469                     IF (jCluster(i,j)==0) EXIT inner3
470                     !update cluster coordinates
471                     jCluster(i,j) = jCluster(i,j) + 1
472                     !apply periodic boundary conditions
473                     IF (jCluster(i,j) > Nlat) jCluster(i,j) =
474                         jCluster(i,j) - Nlat
475                     !put cluster back on lattice
476                     Cluster(iCluster(i,j),jCluster(i,j)) = i
477                 END DO inner3
478             END IF
479         END DO outer3
480     CASE (4)
481     outer4: DO i=1,Nact !loop through all clusters
482         IF (SuperCluster(ClusterDiff,i)==1) THEN
483             !for clusters within the same aggregate
484             inner4: DO j=1,Nlat !loop through all positions
485                 occupied by current cluster
486                 !loop until all the positions have been changed
487                 IF (jCluster(i,j)==0) EXIT inner4
488                 !update cluster coordinates
489                 jCluster(i,j) = jCluster(i,j) - 1
490                 !apply periodic boundary conditions
491                 IF (jCluster(i,j) < 1) jCluster(i,j) =
492                     jCluster(i,j) + Nlat
493                 !put cluster back on lattice
494                 Cluster(iCluster(i,j),jCluster(i,j)) = i
495             END DO inner4
496         END IF
497     END DO outer4
498 END SELECT
499 END SUBROUTINE diffuse_cluster
500
501 SUBROUTINE attach(i, j, Nlat, Nact, iCluster, jCluster, Cluster,
502 ClusterSize, ClusterCounter, iList, jList, &
503 FinalSize)
504 !subroutine for monomer absorption by a cluster
505 IMPLICIT NONE
506 INTEGER, INTENT(IN) :: i, j, Nlat, Nact !i,j=coordinates; Nlat=lattice
507 size; Nact=number of clusters
508 INTEGER, INTENT(IN) :: iList(Nlat*Nlat), jList(Nlat*Nlat)
509 !iList,jList=coordinates for drawing clusters
510 INTEGER, INTENT(INOUT) :: iCluster(Nact,Nlat), jCluster(Nact,Nlat),
511 FinalSize(Nact) !iCluster,jCluster=cluster coordinates;
512 FinalSize=aggregate sizes
513 INTEGER, INTENT(INOUT) :: Cluster(Nlat,Nlat), ClusterSize(Nact),
514 ClusterCounter(Nact) !Cluster=cluster distribution lattice;
515 ClusterSize=cluster size distribution; ClusterCounter=counter for
516 drawing clusters
517 INTEGER :: ClusterNo, iC, jC, iPos, jPos, ID !local variables
518
519 !get cluster number at the location of monomer being absorbed
520 ClusterNo = Cluster(i,j)
521 !increase the corresponding cluster size
522 ClusterSize(ClusterNo) = ClusterSize(ClusterNo) + 1
523
524 !if cluster size is too large, inform the user and stop the execution
525 IF (ClusterSize(ClusterNo)>Nlat) THEN
526     WRITE(*,*) 'Cluster size is larger than i/jCluster array! Need to
527         increase array size!'
528     STOP
529 END IF
530
531 !increase the size of aggregate containing the cluster
532 IF (FinalSize(ClusterNo)>0) THEN
533     FinalSize(ClusterNo) = FinalSize(ClusterNo) + 1
534 ELSE

```

```

522         ID = -(FinalSize(ClusterNo))
523         FinalSize(ID) = FinalSize(ID) + 1
524     END IF
525
526     !get cluster centre coordinates
527     iC = iCluster(ClusterNo,1)
528     jC = jCluster(ClusterNo,1)
529
530     !draw the additional cluster site on lattice
531     check:DO
532         !find next position for drawing
533         iPos = iC + iList(ClusterCounter(ClusterNo))
534         jPos = jC + jList(ClusterCounter(ClusterNo))
535
536         !apply periodic boundary conditions
537         IF (iPos > Nlat) iPos = iPos - Nlat
538         IF (iPos < 1)   iPos = iPos + Nlat
539         IF (jPos > Nlat) jPos = jPos - Nlat
540         IF (jPos < 1)   jPos = jPos + Nlat
541
542         !if the position is not occupied by a cluster
543         IF (Cluster(iPos,jPos)==0) THEN
544             !add cluster site on lattice
545             Cluster(iPos,jPos) = ClusterNo
546             !add the new site coordinates to corresponding arrays
547             iCluster(ClusterNo,ClusterSize(ClusterNo)) = iPos
548             jCluster(ClusterNo,ClusterSize(ClusterNo)) = jPos
549             !increase the cluster counter
550             ClusterCounter(ClusterNo) = ClusterCounter(ClusterNo) + 1
551             EXIT check
552         ELSE
553             !if the selected position is occupied by a cluster, increment
554             !the cluster counter and move to the next site
555             ClusterCounter(ClusterNo) = ClusterCounter(ClusterNo) + 1
556         END IF
557     END DO check
558 END SUBROUTINE attach
559
560 SUBROUTINE HK_scan(WorkCluster,Nact,Nlat,Cluster,ClusterSize,iCluster,
561                  jCluster,SuperCluster,coalesce,FinalSize)
562     !subroutine to scan perimeter of a cluster for adjacent clusters
563     IMPLICIT NONE
564     INTEGER, INTENT(IN) :: Nact, Nlat !Nlat=lattice size; Nact=number of
565     !clusters
566     INTEGER, INTENT(IN) :: Cluster(Nlat,Nlat), ClusterSize(Nact),
567     !iCluster(Nact,Nlat), jCluster(Nact,Nlat) !Cluster=cluster
568     !distribution lattice; ClusterSize=cluster size distribution;
569     !iCluster,jCluster=cluster coordinates
570     INTEGER, INTENT(IN) :: WorkCluster !WorkCluster=current cluster
571     INTEGER, INTENT(INOUT):: SuperCluster(Nact,Nact), FinalSize(Nact)
572     !SuperCluster=cluster links; FinalSize=aggregate sizes
573     LOGICAL, INTENT(OUT) :: coalesce
574     !local variables
575     INTEGER :: i, j, k, iPos, jPos, CheckCluster
576     INTEGER :: neighbourUp, neighbourDown, neighbourLeft, neighbourRight
577     INTEGER :: left, right, up, down
578     LOGICAL :: perimeter, touch, linked
579
580     !loop backwards through the list of positions
581     inner: DO i=ClusterSize(WorkCluster),1,-1
582         !set default logical values of perimeter and touch in the
583         !beginning of loop and reset local variables
584         perimeter = .TRUE.
585         touch = .FALSE.
586         neighbourUp = 0
587         neighbourDown = 0
588         neighbourLeft = 0
589         neighbourRight = 0
590
591         !get the current position from list
592         iPos = iCluster(WorkCluster,i)
593         jPos = jCluster(WorkCluster,i)

```

```

586
587      !apply periodic boundary conditions
588      IF (iPos > Nlat) iPos = iPos - Nlat
589      IF (iPos < 1)   iPos = iPos + Nlat
590      IF (jPos > Nlat) jPos = jPos - Nlat
591      IF (jPos < 1)   jPos = jPos + Nlat
592
593      !evaluate neighbour coordinates applying periodic boundary
594      conditions
595      left = iPos - 1
596      IF (left > Nlat) left = left - Nlat
597      IF (left < 1)   left = left + Nlat
598      right = iPos + 1
599      IF (right > Nlat) right = right - Nlat
600      IF (right < 1) right = right + Nlat
601      down = jPos - 1
602      IF (down > Nlat) down = down - Nlat
603      IF (down < 1)   down = down + Nlat
604      up = jPos + 1
605      IF (up > Nlat)   up = up - Nlat
606      IF (up < 1)     up = up + Nlat
607
608      !if the position is on perimeter, check if there is another
609      cluster adjacent
610      IF (perimeter) THEN
611          IF ((Cluster(right,jPos)/=WorkCluster) .AND.
612              (Cluster(right,jPos)/=0)) THEN
613              touch = .TRUE.
614              neighbourRight = Cluster(right,jPos)
615          END IF
616          IF ((Cluster(left,jPos)/=WorkCluster) .AND.
617              (Cluster(left,jPos)/=0)) THEN
618              touch = .TRUE.
619              neighbourLeft = Cluster(left,jPos)
620          END IF
621          IF ((Cluster(iPos,up)/=WorkCluster) .AND.
622              (Cluster(iPos,up)/=0)) THEN
623              touch = .TRUE.
624              neighbourDown = Cluster(iPos,up)
625          END IF
626          IF ((Cluster(iPos,down)/=WorkCluster) .AND.
627              (Cluster(iPos,down)/=0)) THEN
628              touch = .TRUE.
629              neighbourUp = Cluster(iPos,down)
630          END IF
631
632      !if there's another cluster adjacent, link the clusters
633      IF (touch) THEN
634          coalesce = .TRUE.
635          IF (neighbourUp/=0) THEN !if there's a neighbour above,
636              link it
637              IF (SuperCluster(WorkCluster,neighbourUp)/=1) THEN
638                  CALL link_clusters(neighbourUp, Nact, SuperCluster,
639                      WorkCluster, FinalSize)
640              END IF
641          END IF
642          IF (neighbourDown/=0) THEN !if there's a neighbour below,
643              link it
644              IF (SuperCluster(WorkCluster,neighbourDown)/=1) THEN
645                  CALL link_clusters(neighbourDown, Nact,
646                      SuperCluster, WorkCluster, FinalSize)
647              END IF
648          END IF
649          IF (neighbourLeft/=0) THEN !if there's a neighbour to left,
650              link it
651              IF (SuperCluster(WorkCluster,neighbourLeft)/=1) THEN
652                  CALL link_clusters(neighbourLeft, Nact,
653                      SuperCluster, WorkCluster, FinalSize)
654              END IF
655          END IF
656      END IF

```

```

644         IF (neighbourRight/=0) THEN !if there's a neighbour to
645             right, link it
646             IF (SuperCluster(WorkCluster,neighbourRight)/=1) THEN
647                 CALL link_clusters(neighbourRight, Nact,
648                     SuperCluster, WorkCluster, FinalSize)
649             END IF
650         END IF
651     ELSE
652         EXIT inner
653     END IF
654 END DO inner
655 END SUBROUTINE HK_scan
656
657 SUBROUTINE link_clusters(neighbour, Nact, SuperCluster, WorkCluster,
658     FinalSize)
659     !subroutine for linking two adjacent clusters/aggregates
660     IMPLICIT NONE
661     INTEGER, INTENT(IN) :: Nact, WorkCluster, neighbour !Nact=number of
662         clusters; WorkCluster,neighbour=cluster IDs to be linked
663     INTEGER, INTENT(INOUT) :: SuperCluster(Nact,Nact), FinalSize(Nact)
664         !SuperCluster=cluster links; FinalSize=aggregate sizes
665     INTEGER :: i, ID1, ID2 !local variables
666     INTEGER :: CopyRow(Nact) !CopyRow=row from SuperCluster array that is
667         combination of links of both WorkCluster and neighbour and is
668         copied to all linked clusters
669
670     !if the clusters are already linked, return back
671     IF (SuperCluster(WorkCluster,neighbour)==1) RETURN
672
673     !add up the two corresponding rows of SuperCluster array to combine
674     cluster links
675     CopyRow = SuperCluster(WorkCluster,:) + SuperCluster(neighbour,:)
676     WHERE (CopyRow > 1) CopyRow = 1
677
678     !get IDs of both clusters/aggregates
679     IF (FinalSize(WorkCluster)>0) THEN
680         ID1 = WorkCluster
681     ELSE
682         ID1 = -(FinalSize(WorkCluster))
683     END IF
684     IF (FinalSize(neighbour)>0) THEN
685         ID2 = neighbour
686     ELSE
687         ID2 = -(FinalSize(neighbour))
688     END IF
689
690     !compare the ID labels and use the lower one, making the last
691     aggregate have ID=1
692     IF (ID1<ID2) THEN
693         WHERE (FinalSize==(-ID2)) FinalSize = -ID1
694         FinalSize(ID1) = FinalSize(ID1) + FinalSize(ID2)
695         FinalSize(ID2) = -ID1
696     ELSE
697         WHERE (FinalSize==(-ID1)) FinalSize = -ID2
698         FinalSize(ID2) = FinalSize(ID2) + FinalSize(ID1)
699         FinalSize(ID1) = -ID2
700     END IF
701
702     !link the two clusters and their linked clusters
703     DO i = 1,Nact
704         IF (CopyRow(i)/=0) THEN
705             SuperCluster(i,:) = CopyRow
706         END IF
707     END DO
708 END SUBROUTINE link_clusters
709
710 SUBROUTINE list(Nlat, iList, jList)
711     !subroutine for creating a list of positions for cluster drawing
712     IMPLICIT NONE
713     INTEGER, INTENT(IN) :: Nlat !Nlat=lattice size

```

```

707     INTEGER, INTENT(INOUT) :: iList(Nlat*Nlat), jList(Nlat*Nlat)
708         !iList,jList=coordinates for drawing clusters
709     INTEGER :: radius, size, Lattice(Nlat,Nlat), No !local variables
710
711     !initialise local variables
712     Lattice = 0
713     Lattice(Nlat/2,Nlat/2) = 1
714     No = 1
715     size = 1
716     iList = 0
717     jList = 0
718     radius = 1
719
720     !draw until the cluster diameter is equal to lattice size
721     DO WHILE (radius<Nlat/2)
722         !draw the cluster on lattice
723         CALL draw_list(Nlat, radius, Lattice)
724
725         !add new sites to the list
726         CALL scan_list(Nlat, radius, Lattice, No, iList, jList)
727
728         !increase cluster radius
729         radius = radius + 1
730     END DO
731 END SUBROUTINE list
732
733 SUBROUTINE draw_list(Nlat, radius, Lattice)
734     !subroutine for drawing clusters on lattice, used by list subroutine
735     IMPLICIT NONE
736     INTEGER, INTENT(IN) :: Nlat, radius !Nlat=lattice size; radius=cluster
737         radius
738     INTEGER, INTENT(INOUT) :: Lattice(Nlat,Nlat) !Lattice=cluster drawing
739         lattice
740     INTEGER :: iC, jC, m, mi, n, nj, jradius !local variables
741
742     !put cluster centre in the middle of lattice
743     iC = Nlat/2
744     jC = Nlat/2
745
746     DO m = (iC-radius),(iC+radius),1 !loop through i direction
747         mi = m !local variable used for periodic boundary conditions
748
749         !apply periodic boundary conditions
750         IF (mi > Nlat) mi = mi - Nlat
751         IF (mi < 1) mi = mi + Nlat
752
753         !calculate radius in j direction
754         jradius = INT(SQRT(1.0*(radius)**(2)-1.0*(m-iC)**(2)))
755
756         DO n = (jC-jradius),(jC+jradius),1 !loop through j direction
757             nj = n !local variable used for periodic boundary conditions
758
759             !apply periodic boundary conditions
760             IF (nj > Nlat) nj = nj - Nlat
761             IF (nj < 1) nj = nj + Nlat
762
763             !add value of 1 to each cluster site, leading to perimeter
764             sites being equal to 1
765             Lattice(mi,nj) = Lattice(mi,nj) + 1
766         END DO
767     END DO
768 END SUBROUTINE draw_list
769
770 SUBROUTINE scan_list(Nlat, radius, Lattice, No, iList, jList)
771     !subroutine for adding new sites to list, used by list subroutine
772     IMPLICIT NONE
773     INTEGER, INTENT(IN) :: Nlat, radius !Nlat=lattice size; radius=cluster
774         radius
775     INTEGER, INTENT(INOUT) :: Lattice(Nlat,Nlat), No, iList(Nlat*Nlat),
776         jList(Nlat*Nlat) !Lattice=cluster drawing lattice; No=site
777         counter; iList,jList=cluster drawing coordinates relative to
778         cluster centre
779     INTEGER :: iC, jC, m, mi, n, nj, jradius !local variables

```

```

772
773      !put cluster centre in the middle of lattice
774      iC = Nlat/2
775      jC = Nlat/2
776
777      DO m = (iC-radius),(iC+radius),1 !loop through i direction
778          mi = m !local variable used for periodic boundary conditions
779
780          !apply periodic boundary conditions
781          IF (mi > Nlat) mi = mi - Nlat
782          IF (mi < 1)    mi = mi + Nlat
783
784          !calculate radius in j direction
785          jradius = INT(SQRT(1.0*(radius)**(2)-1.0*(m-iC)**(2)))
786
787      DO n = (jC-jradius),(jC+jradius),1 !loop through j direction
788          nj = n !local variable used for periodic boundary conditions
789
790          !apply periodic boundary conditions
791          IF (nj > Nlat) nj = nj - Nlat
792          IF (nj < 1)    nj = nj + Nlat
793
794          !add perimeter sites to the list, using coordinates relative to
795          !cluster centre
796          IF (Lattice(mi,nj)==1) THEN
797              No = No + 1
798              iList(No) = mi - iC
799              jList(No) = nj - jC
800          END IF
801      END DO
802  END SUBROUTINE scan_list
803
804  SUBROUTINE plotcluster(Cluster, Nlat, FreeMon)
805      !subroutine for cluster distribution output to a file
806      IMPLICIT NONE
807      INTEGER, INTENT(IN) :: Nlat !lattice size
808      INTEGER, INTENT(IN) :: Cluster(Nlat,Nlat) !cluster distribution lattice
809      INTEGER, INTENT(IN) :: FreeMon !free monomers remaining
810      INTEGER :: i,j !local variables
811
812      !write cluster distribution into file
813      DO i=1,Nlat,1
814          WRITE(8,'(X,1000I6)') (Cluster(i,j), j=1,Nlat,1)
815          !note, format of writing is lattice size dependent
816      END DO
817
818      !insert blank line after lattice, in case multiple images are included
819      !in a single file
820      WRITE(8,*)
821  END SUBROUTINE plotcluster
822
823  SUBROUTINE plotgif(Cluster,r,s,p,No,Nlat)
824      !subroutine for writing cluster distribution lattice in order to
825      !create a gif image
826      IMPLICIT NONE
827      INTEGER, INTENT(IN) :: Nlat, r, s, p, No !Nlat=lattice size; r=run
828      !number; s=solids content; p=percentage of activated monomers;
829      !No=file counter
830      INTEGER, INTENT(IN) :: Cluster(Nlat,Nlat) !Cluster=cluster
831      !distribution lattice
832      INTEGER :: ios, i, j, l !local variables
833      CHARACTER(LEN=30) :: Name !local variable for file name
834
835      !create file name
836      IF (No<10) THEN
837          WRITE(Name,'(A4,3(I1,A1),I1,A4)') 'Gif_', r, '_', s, '_', p, '_',
838          No, '.dat'
839      ELSEIF ((No>9) .AND. (No<100)) THEN
840          WRITE(Name,'(A4,3(I1,A1),I2,A4)') 'Gif_', r, '_', s, '_', p, '_',
841          No, '.dat'
842      ELSEIF ((No>99) .AND. (No<1000)) THEN

```

```

836         WRITE(Name,'(A4,3(I1,A1),I3,A4)') 'Gif_', r, '_', s, '_', p, '_',
           No, '.dat'
837     ELSEIF ((No>999) .AND. (No<10000)) THEN
838         WRITE(Name,'(A4,3(I1,A1),I4,A4)') 'Gif_', r, '_', s, '_', p, '_',
           No, '.dat'
839     END IF
840
841     !open file for writing cluster size distribution
842     ios = 0
843     OPEN(17, FILE=Name, STATUS='REPLACE', IOSTAT=ios)
844     IF (ios/=0) THEN
845         WRITE(*,*) 'Error opening dat file in plotgif subroutine', ios
846         STOP
847     END IF
848
849     !write cluster distribution into file
850     DO i=1,Nlat,1
851         WRITE(17,'(X,1000I6)') (Cluster(i,j), j=1,Nlat,1)
852         !note, format of writing is lattice size dependent
853     END DO
854
855     !close the file
856     CLOSE(17)
857
858     END SUBROUTINE plotgif
859 END PROGRAM cluster

```

E.2.2 Percolation module

```

1  MODULE percolation
2  IMPLICIT NONE
3  !module used for accessible sites analysis
4  CONTAINS
5  SUBROUTINE accessible_sites(accessible,Cluster,Nlat)
6  !subroutine for evaluating pore structure accessible from all edges of
   the lattice
7  IMPLICIT NONE
8  INTEGER, INTENT(IN) :: Nlat, Cluster(Nlat,Nlat) !Nlat=lattice size;
   Cluster=cluster distribution lattice
9  INTEGER, INTENT(OUT) :: accessible(Nlat,Nlat) !accessible=accessible
   pore structure lattice
10  INTEGER :: iC, jC, ios, ClusterBorder(Nlat+2,Nlat+2), i, j,
   lattice(Nlat+2,Nlat+2) !local variables
11  INTEGER, ALLOCATABLE :: SuperLattice(:, :)
12  REAL :: ireal
13
14  !copy cluster structure into a lattice including a border on all sides
15  ClusterBorder = 0
16  DO i=1,Nlat
17     DO j=1,Nlat
18         ClusterBorder(i+1,j+1) = Cluster(i,j)
19     END DO
20  END DO
21
22  !initialise the analysis
23  iC = 1
24  jC = 1
25  accessible = 0
26  lattice = 0
27
28  !evaluate accessible pore structure
29  CALL eff_diff(iC,jC,Nlat+2,lattice,ClusterBorder)
30
31  !set initial point as accessible
32  lattice(iC,jC) = 1
33
34  !copy accessible structure without borders
35  DO i=1,Nlat
36     DO j=1,Nlat
37         accessible(i,j) = lattice(i+1,j+1)
38     END DO

```

```

39     END DO
40
41     !set all accessible sites to the value of 1
42     WHERE(accessible>0) accessible = 1
43 END SUBROUTINE accessible_sites
44
45 SUBROUTINE eff_diff(iC, jC, Nlat, Lattice, Cluster)
46 !subroutine for calculating diffusion on lattice
47 IMPLICIT NONE
48 INTEGER, INTENT(IN) :: Nlat, iC, jC !Nlat=lattice size;
49     iC,jC=coordinates of initial position
49 INTEGER, INTENT(IN) :: Cluster(Nlat,Nlat) !cluster distribution lattice
50 INTEGER, INTENT(OUT) :: Lattice(Nlat,Nlat) !accessible sites lattice
51 INTEGER :: steps, No, i, j, counterNext, counterTemp, u, d, l, r
52     !local variables
53 INTEGER :: iNext(Nlat*Nlat), jNext(Nlat*Nlat), iTemp(Nlat*Nlat),
54     jTemp(Nlat*Nlat)
55
56 !reset variables
57 Lattice = 0
58 Lattice(iC,jC) = -1
59 No = 1
60 steps = 1
61 counterNext = 1
62 counterTemp = 1
63 iNext = 0
64 jNext = 0
65 iTemp = 0
66 jTemp = 0
67
68 !if the initial site is occupied by a cluster, inform user and stop
69 execution
70 IF (Cluster(iC,jC)/=0) THEN
71     WRITE(*,*) 'First position occupied by a cluster!'
72     STOP
73 END IF
74
75 !check initial first 4 neighbouring sites
76 CALL scan_neighbours(iC, jC, steps, Nlat, Cluster, counterTemp, iTemp,
77     jTemp, Lattice)
78 CALL temp_next(Nlat, iNext, jNext, iTemp, jTemp)
79 steps = steps + 1
80
81 !analyse the lattice until all available sites have been covered
82 DO
83     !move to the next layer of accessible sites
84     CALL advance(steps, Nlat, Cluster, counterNext, iNext, jNext,
85         iTemp, jTemp, Lattice)
86
87     !if there are no more positions in Next arrays, all the accessible
88     lattice has been covered
89     IF (iTemp(1)==0) EXIT
90
91     !copy data from temporary arrays to next arrays
92     CALL temp_next(Nlat, iNext, jNext, iTemp, jTemp)
93
94     !increment the step counter
95     steps = steps + 1
96 END DO
97 END SUBROUTINE eff_diff
98
99 SUBROUTINE advance(steps, Nlat, Cluster, counterNext, iNext, jNext,
100     iTemp, jTemp, Lattice)
101 !subroutine for advancing to the next layer of accessible sites
102 IMPLICIT NONE
103 INTEGER, INTENT(IN) :: Nlat, Cluster(Nlat,Nlat), steps !Nlat=lattice
104     size; Cluster=cluster distribution lattice; steps=step counter
105 INTEGER, INTENT(INOUT) :: iNext(Nlat*Nlat), jNext(Nlat*Nlat)
106     !iNext,jNext=coordinates of the next layer of accessible sites
107 INTEGER, INTENT(INOUT) :: Lattice(Nlat,Nlat), iTemp(Nlat*Nlat),
108     jTemp(Nlat*Nlat) !Lattice=accessible sites lattice;
109     iTemp,jTemp=arrays temporary storing coordinates of next layer of
110     accessible sites

```

```

99     INTEGER :: counterNext, counterTemp !local variables
100
101     !initialise counters for Next and Temp arrays
102     counterNext = 1
103     counterTemp = 1
104
105     DO !loop until all sites in the next layer of accessible sites have
        been covered
106         IF (iNext(counterNext)==0) EXIT
107
108         !analyse sites adjacent to the current layer of accessible sites
109         CALL scan_neighbours(iNext(counterNext), jNext(counterNext),
            steps, Nlat, Cluster, &
110             counterTemp, iTemp, jTemp, Lattice)
111
112         !increase counter for Next arrays
113         counterNext = counterNext + 1
114     END DO
115 END SUBROUTINE advance
116
117 SUBROUTINE scan_neighbours(iC, jC, steps, Nlat, Cluster, counterTemp,
    iTemp, jTemp, Lattice)
118 !subroutine to analyse adjacent sites (up, down, left, right) for
    accessibility
119 IMPLICIT NONE
120 INTEGER, INTENT(IN) :: Nlat, Cluster(Nlat,Nlat), iC, jC, steps
    !Nlat=lattice size; Cluster=cluster distribution lattice;
    iC,jC=coordinates of analysed site; steps=step counter
121 INTEGER, INTENT(INOUT) :: counterTemp, iTemp(Nlat*Nlat),
    jTemp(Nlat*Nlat) !counterTemp=counter for Temp arrays;
    iTemp,jTemp=arrays temporary storing coordinates of next layer of
    accessible sites
122 INTEGER, INTENT(INOUT) :: Lattice(Nlat,Nlat) !Lattice=accessible sites
    lattice
123 INTEGER :: i, j, k !local variables
124 INTEGER :: u, d, l, r
125
126 !analyse first adjacent site for accessibility
127 i=iC
128 j=jC-1
129 !apply periodic boundary conditions
130 CALL periodic_boundary(j,Nlat)
131 !if the site is accessible and was not analysed previously
132 IF ((Cluster(i,j)==0) .AND. (Lattice(i,j)==0)) THEN
133     !set the site to the current step counter value
134     Lattice(i,j)=steps
135     !add the site coordinates to Temp arrays in order to be analysed
        in the next iteration
136     iTemp(counterTemp) = i
137     jTemp(counterTemp) = j
138     !increment counter for Temp arrays
139     counterTemp = counterTemp + 1
140 END IF
141
142 !analyse second adjacent site for accessibility
143 j=jC+1
144 !apply periodic boundary conditions
145 CALL periodic_boundary(j,Nlat)
146 !if the site is accessible and was not analysed previously
147 IF ((Cluster(i,j)==0) .AND. (Lattice(i,j)==0)) THEN
148     !set the site to the current step counter value
149     Lattice(i,j)=steps
150     !add the site coordinates to Temp arrays in order to be analysed
        in the next iteration
151     iTemp(counterTemp) = i
152     jTemp(counterTemp) = j
153     !increment counter for Temp arrays
154     counterTemp = counterTemp + 1
155 END IF
156
157 !analyse third adjacent site for accessibility
158 i=iC-1
159 j=jC

```

```

160      !apply periodic boundary conditions
161      CALL periodic_boundary(i,Nlat)
162      !if the site is accessible and was not analysed previously
163      IF ((Cluster(i,j)==0) .AND. (Lattice(i,j)==0)) THEN
164          !set the site to the current step counter value
165          Lattice(i,j)=steps
166          !add the site coordinates to Temp arrays in order to be analysed
           in the next iteration
167          iTemp(counterTemp) = i
168          jTemp(counterTemp) = j
169          !increment counter for Temp arrays
170          counterTemp = counterTemp + 1
171      END IF
172
173      !analyse fourth adjacent site for accessibility
174      i=iC+1
175      !apply periodic boundary conditions
176      CALL periodic_boundary(i,Nlat)
177      !if the site is accessible and was not analysed previously
178      IF ((Cluster(i,j)==0) .AND. (Lattice(i,j)==0)) THEN
179          !set the site to the current step counter value
180          Lattice(i,j)=steps
181          !add the site coordinates to Temp arrays in order to be analysed
           in the next iteration
182          iTemp(counterTemp) = i
183          jTemp(counterTemp) = j
184          !increment counter for Temp arrays
185          counterTemp = counterTemp + 1
186      END IF
187      END SUBROUTINE scan_neighbours
188
189      SUBROUTINE periodic_boundary(i,Nlat)
190          !subroutine for applying periodic boundary conditions
191          IMPLICIT NONE
192          INTEGER, INTENT(IN) :: Nlat !lattice size
193          INTEGER, INTENT(INOUT) :: i !lattice coordinate
194          !if i is larger than the lattice size, subtract lattice size (move to
           the lower end of the lattice)
195          IF (i > Nlat) i = i - Nlat
196          !if i is smaller than the first lattice coordinate, add lattice size
           (move to the higher end of the lattice)
197          IF (i < 1) i = i + Nlat
198      END SUBROUTINE periodic_boundary
199
200      SUBROUTINE temp_next(Nlat, iNext, jNext, iTemp, jTemp)
201          !subroutine to copy Temp arrays into Next arrays and reset Temp arrays
202          IMPLICIT NONE
203          INTEGER, INTENT(IN) :: Nlat !lattice size
204          INTEGER, INTENT(INOUT) :: iNext(Nlat*Nlat), jNext(Nlat*Nlat)
           !coordinates of the next layer of accessible sites
205          INTEGER, INTENT(INOUT) :: iTemp(Nlat*Nlat), jTemp(Nlat*Nlat) !arrays
           temporary storing coordinates of next layer of accessible sites
206
207          !copy values from Temp arrays to Next arrays
208          iNext = iTemp
209          jNext = jTemp
210
211          !reset Temp arrays
212          iTemp = 0
213          jTemp = 0
214      END SUBROUTINE temp_next
215      END MODULE percolation

```

E.2.3 Surface area analysis code

```

1  PROGRAM surface_area
2      USE percolation
3      IMPLICIT NONE
4      INTEGER, PARAMETER :: Nlat=1000 !lattice size

```

```

5  INTEGER :: Cluster(Nlat,Nlat), lattice(Nlat,Nlat), out(Nlat+2,Nlat+2)
      !Cluster=cluster distribution lattice; lattice=accessible sites
      !lattice=lattice with an additional layer around lattice edges
6  INTEGER :: i, j, ios, s, p, r, SA_outside, SA_periodic, SA_lattice, up,
      down, left, right, accessible !i,j=loop counters; ios=variable used
      when opening files; s,p,r=integer values of solids content, percentage
      of activated monomers, and run number; SA_outside=surface area
      accessible from outside; SA_periodic=surface area accessible within
      periodic boundary conditions; SA_lattice=surface area accessible
      within the lattice; up,down,left,right=coordinates of adjacent sites;
      accessible=accessible pore structure lattice
7  CHARACTER(LEN=30) :: fname !file name variable
8
9  !open file for writing out surface area data
10 ios = 0
11 OPEN(2, FILE='surface_area.dat', STATUS='REPLACE', IOSTAT=ios)
12 !if there is an issue opening the file, inform user and stop execution
13 IF (ios/=0) THEN
14     WRITE(14,*) 'Error opening file input.dat', ios
15     STOP
16 END IF
17
18 !write out headers to the file
19 WRITE(2,'(7A20)') 'solid', 'percentage', 'run', 'SA_lattice',
      'SA_periodic', 'SA_outside', 'accessible_sites'
20
21 !loop through values of solids contents, percentage of activated
      monomers, and run numbers
22 DO s=1,5
23     DO p=1,3
24         DO r=1,10
25             !create file name of a file containing cluster structure
26             IF (r.LT.10) THEN
27                 WRITE(fname,'(A10,I1,A4,I1,A1,I1,A4)') 'Cluster_0.', s,
                    '_0.0', p, '_', r, '.dat'
28             ELSE
29                 WRITE(fname,'(A10,I1,A4,I1,A1,I2,A4)') 'Cluster_0.', s,
                    '_0.0', p, '_', r, '.dat'
30             END IF
31
32             !open file containing cluster structure
33             ios = 0
34             OPEN(3, FILE=fname, STATUS='OLD', IOSTAT=ios)
35             IF (ios/=0) THEN
36                 WRITE(14,*) 'Error opening file input.dat', ios
37                 STOP
38             END IF
39
40             !read in the cluster distribution lattice from file
41             DO i=1,Nlat
42                 READ(3,'(X,1000I6)') (Cluster(i,j),j=1,Nlat)
43             END DO
44             CLOSE(3)
45
46             !analyse structure for accessible pore structure
47             CALL accessible_sites(lattice,Cluster,Nlat)
48
49             !reset variables
50             SA_outside = 0
51             SA_periodic = 0
52             SA_lattice = 0
53             accessible = 0
54
55             !loop through all lattice sites
56             DO i=1,Nlat
57                 DO j=1,Nlat
58                     !if the selected lattice site is accessible
59                     IF (lattice(i,j)==1) THEN
60                         !increment counter of accessible sites
61                         accessible = accessible + 1
62
63                         !find adjacent sites
64                         CALL neighbours(i,j,Nlat,up,down,left,right)

```

```

65
66         !if any of the adjacent sites is occupied by a
67         !cluster, this is a surface site
68         IF ((Cluster(up,j)/=0).OR.(Cluster(down,j)/=0).OR.
69         (Cluster(i,left)/=0).OR.(Cluster(i,right)/=0))
70         THEN
71         !increment counter for surface area within
72         !periodic boundary conditions
73         SA_periodic = SA_periodic + 1
74         !if the adjacent cluster site is within the
75         !lattice, increment the corresponding surface
76         !area counter
77         IF ((Cluster(up,j)/=0).AND.(up==i-1)) THEN
78         SA_lattice = SA_lattice + 1
79         CYCLE
80         ELSE IF ((Cluster(down,j)/=0).AND.(down==i+1))
81         THEN
82         SA_lattice = SA_lattice + 1
83         CYCLE
84         ELSE IF ((Cluster(i,left)/=0).AND.(left==j-1))
85         THEN
86         SA_lattice = SA_lattice + 1
87         CYCLE
88         ELSE IF ((Cluster(i,right)/=0).AND.(right==j+1))
89         THEN
90         SA_lattice = SA_lattice + 1
91         CYCLE
92         END IF
93         END IF
94         END DO
95         END DO
96
97         !set surface area accessible from outside to the value of
98         !lattice surface area
99         SA_outside = SA_lattice
100        !copy cluster structure to lattice with external borders of
101        !empty sites
102        out = 0
103        DO i=1,Nlat
104        DO j=1,Nlat
105        out(i+1,j+1)=Cluster(i,j)
106        END DO
107        END DO
108
109        !analyse additional border sites for surface sites
110        DO i=1,Nlat
111        IF (Cluster(i,1)/=0) SA_outside = SA_outside + 1
112        IF (Cluster(i,Nlat)/=0) SA_outside = SA_outside + 1
113        END DO
114
115        DO j=2,Nlat-1
116        IF(Cluster(1,j)/=0) SA_outside = SA_outside + 1
117        IF(Cluster(Nlat,j)/=0) SA_outside = SA_outside + 1
118        END DO
119
120        !write obtained values to the file
121        WRITE(2,'(7I20)') s*10, p, r, SA_lattice, SA_periodic,
122        SA_outside, accessible
123        END DO
124        END DO
125        END DO
126
127        !close the output file
128        CLOSE(2)
129
130        !subroutine used by the main program
131        CONTAINS
132        SUBROUTINE neighbours(i,j,Nlat,u,d,l,r)
133        !subroutine for evaluating coordinates of adjacent sites using
134        !periodic boundary conditions
135        IMPLICIT NONE

```

```

124     INTEGER, INTENT(IN) :: i,j,Nlat !i,j=site coordinates; Nlat=lattice
        size
125     INTEGER, INTENT(OUT) :: u,d,l,r !coordinates of adjacent sites
126
127     !evaluate coordinates of adjacent sites applying periodic boundary
        conditions
128     u = i - 1
129     CALL periodic_boundary(u,Nlat)
130     d = i + 1
131     CALL periodic_boundary(d,Nlat)
132     l = j - 1
133     CALL periodic_boundary(l,Nlat)
134     r = j + 1
135     CALL periodic_boundary(r,Nlat)
136     END SUBROUTINE neighbours
137 END PROGRAM surface_area

```

E.2.4 Correlation dimension analysis

```

1 PROGRAM fractal
2 IMPLICIT NONE
3 INTEGER, PARAMETER :: Nlat=1000, dp=selected_real_kind(15, 307)
    !Nlat=lattice size; dp=precision for real numbers
4 INTEGER :: Nmax, Nact !Nmax=number of all species ; Nact=number of
    activated monomers (clusters)
5 REAL :: solid, percentage, d !solid=solids content; percentage=percentage
    of activated monomers; d=distance between two cluster centres
6 REAL(KIND=dp) :: C(1500) !correlation sum
7 INTEGER, ALLOCATABLE :: iCluster(:), jCluster(:), Cluster(:, :)
    !iCluster,jCluster=cluster site coordinates; Cluster=cluster
    distribution lattice
8 INTEGER :: i,j,k, ios, s, p, r, distance !i,j,k=loop counters;
    ios=integer for status during opening files; s,p,r=integer values of
    solids content, percentage of activated monomer, and run number;
    distance=integer value of distance between two cluster centres
9 CHARACTER(LEN=26) :: ClusterFile, iFile, CFile !file names
10
11 !loop through run numbers, solids contents, and percentage of activated
    monomers
12 DO r=1,10
13     DO s=1,5
14         solid = 1.0*s/10
15         DO p=1,3
16             percentage = (1.0*p)/100
17
18             !calculate total number of species and clusters
19             Nmax = NINT(solid*Nlat*Nlat)
20             Nact = NINT(percentage*Nmax)
21
22             !create file names
23             IF (r.LT.10) THEN
24                 WRITE(ClusterFile,'(A8,F3.1,A1,F4.2,A1,I1,A4)') 'Cluster_',
                    solid, '_', percentage, '_', r, '.dat'
25                 WRITE(iFile,'(A5,F3.1,A1,F4.2,A1,I1,A4)') 'iPos_', solid,
                    '_', percentage, '_', r, '.dat'
26                 WRITE(jFile,'(A5,F3.1,A1,F4.2,A1,I1,A4)') 'jPos_', solid,
                    '_', percentage, '_', r, '.dat'
27                 WRITE(CFile,'(A2,F3.1,A1,F4.2,A1,I1,A4)') 'C_', solid, '_',
                    percentage, '_', r, '.dat'
28             ELSE IF ((r.GE.10).AND.(r.LT.100)) THEN
29                 WRITE(ClusterFile,'(A8,F3.1,A1,F4.2,A1,I2,A4)') 'Cluster_',
                    solid, '_', percentage, '_', r, '.dat'
30                 WRITE(iFile,'(A5,F3.1,A1,F4.2,A1,I2,A4)') 'iPos_', solid,
                    '_', percentage, '_', r, '.dat'
31                 WRITE(jFile,'(A5,F3.1,A1,F4.2,A1,I2,A4)') 'jPos_', solid,
                    '_', percentage, '_', r, '.dat'
32                 WRITE(CFile,'(A2,F3.1,A1,F4.2,A1,I2,A4)') 'C_', solid, '_',
                    percentage, '_', r, '.dat'
33             END IF
34
35             !allocate dynamic arrays

```

```

36      ios = 0
37      ALLOCATE( iCluster(Nact), jCluster(Nact), Cluster(Nlat,Nlat),
38              STAT=ios )
39      IF (ios/=0) THEN
40          WRITE(*,*) 'Error allocating arrays'
41          STOP
42      END IF
43
44      !open file containing cluster centre coordinates
45      ios = 0
46      OPEN(12, FILE=iFile, STATUS='OLD', ACTION='READ', IOSTAT=ios)
47      IF (ios/=0) THEN
48          WRITE(*,*) 'Error opening file iPos.dat', ios
49          STOP
50      END IF
51
52      !open file for data output
53      ios = 0
54      OPEN(14, FILE=CFile, STATUS='REPLACE', ACTION='WRITE',
55          IOSTAT=ios)
56      IF (ios/=0) THEN
57          WRITE(*,*) 'Error opening file C.dat', ios
58          STOP
59      END IF
60
61      !reset correlation sum
62      C = 0
63
64      !read in cluster centre coordinates
65      DO i=1,Nact
66          READ(12,'(X,1000I6)') j, iCluster(i), jCluster(i)
67      END DO
68
69      !loop through all cluster pairs
70      iloop: DO i=1,Nact
71          jloop: DO j=1,Nact
72              !do not count the pairs of the same clusters
73              IF (i==j) CYCLE jloop
74              !calculate the closest distance between the cluster
75              !centres applying periodic boundary conditions
76              CALL dist(i, j, d, Nlat, Nact, iCluster, jCluster)
77              !round the distance value up to the nearest integer
78              distance = CEILING(d)
79              !update the correlation sum with the current cluster
80              !pair data
81              kloop: DO k=distance,1500
82                  C(k) = C(k) + 1.0/Nact
83              END DO kloop
84          END DO jloop
85      END DO iloop
86
87      !scale correlation sum with the number of clusters
88      C = C/(1.0*(Nact-1))
89
90      !write output data into file
91      DO i=1,1500
92          WRITE(14,'(X,I6,X,F15.12,X,F15.12,X,F15.12)') i, C(i),
93              LOG10(1.0*i), LOG10(1.0*C(i))
94      END DO
95
96      !close all open files
97      DO i=12,14
98          CLOSE(i)
99      END DO
100
101      !deallocate dyanmic arrays
102      ios = 0
103      DEALLOCATE( iCluster, jCluster, Cluster, STAT=ios )
104      IF (ios/=0) THEN
105          WRITE(*,*) 'Error deallocating arrays'
106          STOP
107      END IF
108  END DO

```

```

104     END DO
105     END DO
106
107     !subroutine used by the main program
108     CONTAINS
109     SUBROUTINE dist(Cluster1, Cluster2, distance, Nlat, Nact, iCluster,
110                   jCluster)
111     !subroutine for evaluating closest distance between two points on a
112     !lattice, including periodic images of the lattice
113     IMPLICIT NONE
114     INTEGER, INTENT(IN) :: Cluster1, Cluster2, Nact, Nlat
115     !Cluster1,Cluster2=cluster numbers; Nact=total number of clusters;
116     !Nlat=lattice size
117     INTEGER, INTENT(IN) :: iCluster(Nact), jCluster(Nact)
118     !iCluster,jCluster=cluster centre coordinates
119     REAL, INTENT(OUT) :: distance !closest distance between two points
120     !including periodic boundary conditions
121     INTEGER :: i1, j1, i2, j2 !local variables
122     REAL :: d(9) !array containing distances within the lattice and with
123     !all periodic images of the lattice
124
125     !get values of cluster centre coordinates
126     i1 = iCluster(Cluster1)
127     j1 = jCluster(Cluster1)
128     i2 = iCluster(Cluster2)
129     j2 = jCluster(Cluster2)
130
131     !calculate 9 values of distance between the two analysed points
132     d(1) = SQRT(1.0*((i2-Nlat)-i1)**2 + 1.0*((j2-Nlat)-j1)**2)
133     d(2) = SQRT(1.0*(i2-i1)**2 + 1.0*((j2-Nlat)-j1)**2)
134     d(3) = SQRT(1.0*((i2+Nlat)-i1)**2 + 1.0*((j2-Nlat)-j1)**2)
135     d(4) = SQRT(1.0*((i2-Nlat)-i1)**2 + 1.0*(j2-j1)**2)
136     d(5) = SQRT(1.0*(i2-i1)**2 + 1.0*(j2-j1)**2)
137     d(6) = SQRT(1.0*((i2+Nlat)-i1)**2 + 1.0*(j2-j1)**2)
138     d(7) = SQRT(1.0*((i2-Nlat)-i1)**2 + 1.0*((j2+Nlat)-j1)**2)
139     d(8) = SQRT(1.0*(i2-i1)**2 + 1.0*((j2+Nlat)-j1)**2)
140     d(9) = SQRT(1.0*((i2+Nlat)-i1)**2 + 1.0*((j2+Nlat)-j1)**2)
141
142     !minimum value of the distance
143     distance = MINVAL(d)
144     END SUBROUTINE dist
145 END PROGRAM fractal

```

E.2.5 Hurst exponent analysis

```

1 PROGRAM brownian
2 IMPLICIT NONE
3 INTEGER, PARAMETER :: Nlat=1000, dp=selected_real_kind(15, 307)
4 !Nlat=lattice size; dp=precision for real numbers
5 INTEGER :: Nsteps, Npositions, position, TimeWindows, pos_counter
6 !Nsteps=number of diffusion steps; Npositions=number of starting
7 !positions; position=loop counter; TimeWindows=number of time windows;
8 !pos_counter=counter for number of attempts to find percolated pore
9 !structure
10 REAL :: solid, percentage, ireal !solid=solids content;
11 !percentage=percentage of activated monomers; ireal=used for random
12 !number generator
13 INTEGER, ALLOCATABLE :: X(:), Y(:), Bx(:), By(:), SuperLattice(:, :),
14 !dT(:) !X,Y=walker coordinates; Bx,By=walker displacement;
15 !SuperLattice=9 periodic images of Cluster lattice; dT=time window sizes
16 INTEGER :: i, j, k, ios, s, p, r, iC, jC, Cluster(Nlat, Nlat),
17 !Walk(Nlat, Nlat) !i, j, k=loop counters; ios=integer for status during
18 !opening files; s, p, r=integer values of solids content, percentage of
19 !activated monomer, and run number; iC, jC=lattice coordinates;
20 !Cluster=cluster distribution lattice; Walk=lattice containing sites
21 !visited by a walker
22 CHARACTER(LEN=26) :: ClusterFile, Xfile !file names
23 INTEGER, DIMENSION(12) :: seed !seed=for random number generator
24 REAL(KIND=dp) :: average, stdev !average and standard deviation

```

```

11 REAL(KIND=dp), ALLOCATABLE :: Xaverage(:), Yaverage(:), Xstdev(:),
    Ystdev(:) !average and standard deviation values of displacement in x
    and y directions
12 LOGICAL :: percolated !for percolation subroutine
13
14 r = 1 !set run number
15 s = 1 !set solids content
16 solid = 1.0*s/10
17 p = 1 !set percentage of activated monomers
18 percentage = (1.0*p)/100
19
20 Nsteps = 10*Nlat*Nlat !set number of walker steps
21 Npositions = Nlat !set number of starting positions
22 TimeWindows = 11 !set number of time windows
23 pos_counter = 1 !reset counter
24 seed = 100 !seed the random number generator
25 CALL RANDOM_SEED(PUT=seed)
26
27 !allocate dynamic arrays
28 ios = 0
29 ALLOCATE( X(Nsteps), Y(Nsteps), Bx(Nsteps), By(Nsteps), dT(TimeWindows),
    Xaverage(TimeWindows), &
30 Yaverage(TimeWindows), Xstdev(TimeWindows), Ystdev(TimeWindows),
    STAT=ios )
31 IF (ios/=0) THEN
32 WRITE(*,*) 'Error allocating arrays'
33 STOP
34 END IF
35
36 !set values of time windows for calculating the Hurst exponent
37 dT(1) = 100
38 DO i=2,TimeWindows
39 dT(i) = 2*dT(i-1)
40 END DO
41
42 !create file names
43 IF (r.LT.10) THEN
44 WRITE(ClusterFile,'(A8,F3.1,A1,F4.2,A1,I1,A4)') 'Cluster_', solid,
    ' ', percentage, ' ', r, '.dat'
45 WRITE(Xfile,'(A3,F5.3,A1,F4.2,A1,I1,A4)') 'XY_', solid, ' ',
    percentage, ' ', r, '.dat'
46 ELSE IF ((r.GE.10).AND.(r.LT.100)) THEN
47 WRITE(ClusterFile,'(A8,F3.1,A1,F4.2,A1,I2,A4)') 'Cluster_', solid,
    ' ', percentage, ' ', r, '.dat'
48 WRITE(Xfile,'(A3,F5.3,A1,F4.2,A1,I2,A4)') 'XY_', solid, ' ',
    percentage, ' ', r, '.dat'
49 END IF
50
51 !open file containing cluster structure
52 ios = 0
53 OPEN(12, FILE=ClusterFile, STATUS='OLD', ACTION='READ', IOSTAT=ios)
54 IF (ios/=0) THEN
55 WRITE(*,*) 'Error opening file Cluster.dat', ios
56 STOP
57 END IF
58
59 !open file for data output
60 ios = 0
61 OPEN(13, FILE=Xfile, STATUS='REPLACE', ACTION='WRITE', IOSTAT=ios)
62 IF (ios/=0) THEN
63 WRITE(*,*) 'Error opening file X.dat', ios
64 STOP
65 END IF
66
67 !read in cluster distribution lattice and close the file
68 DO i=1,Nlat,1
69 READ(12,'(X,1000I6)') (Cluster(i,j), j=1,Nlat,1)
70 END DO
71 CLOSE(12)
72
73 !reset variables
74 Xaverage = 0

```

```

75     Yaverage = 0
76     Xstdev = 0
77     Ystdev = 0
78
79     !loop through the number of starting positions
80     DO position = 1,Npositions
81         !inform user about simulation progress
82         WRITE(*,*) position, ' of ', Npositions
83
84         !reset position counter
85         pos_counter = 1
86         pos_loop: DO
87             !get a random position on the lattice
88             CALL RANDOM_NUMBER(ireal)
89             iC = INT(Nlat*ireal)+1
90             CALL RANDOM_NUMBER(ireal)
91             jC = INT(Nlat*ireal)+1
92
93             !if it is a pore site
94             IF (Cluster(iC,jC)==0) THEN
95
96                 !allocate dynamic array
97                 ios = 0
98                 ALLOCATE( SuperLattice(3*Nlat,3*Nlat), STAT=ios )
99                 IF (ios/=0) THEN
100                     WRITE(*,*) 'Error allocating SuperLattice array'
101                     STOP
102                 END IF
103
104                 !create periodic images of the cluster distribution lattice
105                 CALL copy_SuperLattice(iC, jC, Nlat, Cluster, SuperLattice)
106
107                 !analyse the lattice for percolated pore structure
108                 CALL percolate(iC, jC, Nlat, SuperLattice, percolated)
109
110                 !deallocate dynamic array to free up allocated memory
111                 ios = 0
112                 DEALLOCATE( SuperLattice, STAT=ios )
113                 IF (ios/=0) THEN
114                     WRITE(*,*) 'Error deallocating SuperLattice array'
115                     STOP
116                 END IF
117
118                 !if the selected position is within percolated pore structure
119                 IF (percolated) THEN
120                     !exit the loop and continue with further calculations
121                     EXIT pos_loop
122                 ELSE
123                     !if the selected position is not within percolated pore
124                     !structure
125                     IF (pos_counter.GT.NINT(0.01*Nlat*Nlat)) THEN
126                         !if more than a set number of sites was analysed
127                         !without finding percolated pore structure inform
128                         !user and cancel execution
129                         WRITE(*,*) '*****could not find percolated
130                         structure*****'
131                         STOP
132                     ELSE
133                         !otherwise increment position counter and try another
134                         !position
135                         pos_counter = pos_counter + 1
136                         CYCLE pos_loop
137                     END IF
138                 END IF
139             END DO pos_loop
140
141         !reset arrays
142         X = 0
143         Y = 0
144         Walk = 0
145
146         !set starting position coordinates

```

```

143     X(1) = iC
144     Y(1) = jC
145
146     !loop through all diffusion steps
147     DO k=2,Nsteps
148         CALL diffuse(k,Nlat,Cluster,X,Y, Walk)
149     END DO
150
151     !loop through time window sizes
152     DO k=1,TimeWindows
153         !reset arrays
154         Bx = 0
155         By = 0
156         !calculate displacement for current tme window size
157         DO i=(dT(k)+1),Nsteps
158             Bx(i) = ABS(X(i) - X(i-dT(k)))
159             By(i) = ABS(Y(i) - Y(i-dT(k)))
160         END DO
161         !evaluate relevant statistical values
162         CALL stat(Bx(dT(k)+1:),average,stdev)
163         Xaverage(k) = Xaverage(k) + average
164         Xstdev(k) = Xstdev(k) + stdev
165         CALL stat(By(dT(k)+1:),average,stdev)
166         Yaverage(k) = Yaverage(k) + average
167         Ystdev(k) = Ystdev(k) + stdev
168     END DO
169 END DO
170
171 !finalise calculations
172 Xaverage = Xaverage/Npositions
173 Yaverage = Yaverage/Npositions
174 Xstdev = Xstdev/Npositions
175 Ystdev = Ystdev/Npositions
176
177 !write headers for output data
178 WRITE(13,'(8A15)') 't', 'Xaverage', 'Yaverage', 'Xstdev', 'Ystdev',
179     'log(t)', 'log(|X|^2)', &
180     'log(|Y|^2)'
181
182 !write output data into file
183 DO k=1,TimeWindows
184     WRITE(13,'(I15,7F15.3)') dT(k), Xaverage(k), Yaverage(k), Xstdev(k),
185         Ystdev(k), &
186         LOG10(1.0*dT(k)), LOG10(Xaverage(k)), LOG10(Yaverage(k))
187 END DO
188
189 !deallocate dynamic arrays
190 ios = 0
191 DEALLOCATE( X, Y, Bx, By, dT, Xaverage, Yaverage, Xstdev, Ystdev,
192     STAT=ios )
193 IF (ios/=0) THEN
194     WRITE(*,*) 'Error deallocating arrays'
195 STOP
196 END IF
197
198 !close output file
199 CLOSE(13)
200
201 !subroutines used by the main program
202 CONTAINS
203 SUBROUTINE diffuse(No, Nlat, Cluster, X, Y, Walk)
204     !subroutine for walker diffusion
205     IMPLICIT NONE
206     INTEGER, INTENT(IN) :: Nlat, No !Nlat=lattice size ;No=diffusion steps
207     counter
208     INTEGER, INTENT(IN) :: Cluster(Nlat,Nlat) !cluster distribution lattice
209     INTEGER, INTENT(INOUT) :: X(:), Y(:) !arrays to store i and j
210     coordinates
211     INTEGER, INTENT(INOUT) :: Walk(:, :) !sites visited previously by the
212     walker
213     INTEGER :: i, j, move !local variables

```

```

209      !transfer walker coordinates from the previous diffusion step into
        local variables
210      i = X(No-1)
211      j = Y(No-1)
212
213      !apply periodic boundary conditions
214      CALL periodic_boundary(i,Nlat)
215      CALL periodic_boundary(j,Nlat)
216
217      !attempt a random diffusion step up/down/left/right
218      move=INT(4*RAND())+1
219      SELECT CASE (move)
220      CASE (1)
221          i = i + 1
222      CASE (2)
223          i = i - 1
224      CASE (3)
225          j = j + 1
226      CASE (4)
227          j = j - 1
228      END SELECT
229
230      !apply periodic boundary conditions
231      CALL periodic_boundary(i,Nlat)
232      CALL periodic_boundary(j,Nlat)
233
234      !check if the new position is empty
235      IF (Cluster(i,j)==0) THEN
236          !if the site wasn't visited by the walker previously, mark it as
            visited
237          IF (Walk(i,j)==0) Walk(i,j) = 100
238          !record the new coordinates to the corresponding arrays, without
            applying periodic boundary conditions
239          SELECT CASE (move)
240          CASE (1)
241              X(No) = X(No-1) + 1
242              Y(No) = Y(No-1)
243          CASE (2)
244              X(No) = X(No-1) - 1
245              Y(No) = Y(No-1)
246          CASE (3)
247              Y(No) = Y(No-1) + 1
248              X(No) = X(No-1)
249          CASE (4)
250              Y(No) = Y(No-1) - 1
251              X(No) = X(No-1)
252          END SELECT
253      ELSE
254          !if the new site is occupied by a cluster, remain in the same
            position and record it
255          X(No) = X(No-1)
256          Y(No) = Y(No-1)
257      END IF
258      END SUBROUTINE diffuse
259
260      SUBROUTINE periodic_boundary(i,Nlat)
261          !subroutine for applying periodic boundary conditions
262          IMPLICIT NONE
263          INTEGER, INTENT(IN) :: Nlat !lattice size
264          INTEGER, INTENT(INOUT) :: i !coordinate value
265
266          !loop until the value is within lattice coordinates
267          DO
268              IF (i > Nlat) i = i - Nlat
269              IF (i < 1) i = i + Nlat
270              IF ((i .GE. 1) .AND. (i .LE. Nlat)) EXIT
271          END DO
272      END SUBROUTINE periodic_boundary
273
274      SUBROUTINE stat(data,ave,sdev)

```

```

275      !subroutine for calculating average and standard deviation for set of
276      data (adapted from Numerical Recipes in Fortran 90)
277      IMPLICIT NONE
278      REAL(KIND=dp), INTENT(OUT) :: ave, sdev !average value and standard
279      deviation
280      INTEGER, INTENT(IN) :: data(:) !data set for analysis
281      INTEGER :: n !number of values in the data set
282      REAL :: ep, var !local variables
283      REAL, DIMENSION(SIZE(data)) :: p,s !local variables
284
285      !calculate average and standard deviation for the data set
286      n = size(data)
287      ave = SUM(REAL(data))/n
288      s = data - ave
289      ep = SUM(s)
290      p = s*s
291      var = SUM(p)
292      p = p*s
293      var = (var-ep**2/n)/(n-1)
294      sdev = SQRT(var)
295      END SUBROUTINE stat
296
297      SUBROUTINE percolate(iC, jC, Nlat, SuperLattice, percolated)
298      !subroutine for evaluating percolated pore structure
299      IMPLICIT NONE
300      INTEGER, INTENT(IN) :: Nlat, iC, jC !Nlat=lattice size;
301      iC,jC=evaluated position coordinates
302      INTEGER, INTENT(INOUT) :: SuperLattice(:, :) !periodic images of
303      cluster distribution lattice
304      INTEGER :: steps, No, i, j, counterNext, counterTemp, u, d, l, r
305      !local variables
306      INTEGER :: iNext(Nlat*Nlat), jNext(Nlat*Nlat), iTemp(Nlat*Nlat),
307      jTemp(Nlat*Nlat)
308      LOGICAL, INTENT(OUT) :: percolated
309
310      !transfer coordinates to local variables
311      i = iC + Nlat
312      j = jC + Nlat
313
314      !reset local variables
315      No = 1
316      steps = 1
317      counterNext = 1
318      counterTemp = 1
319      iNext = 0
320      jNext = 0
321      iTemp = 0
322      jTemp = 0
323      percolated = .FALSE.
324
325      !check initial first 4 neighbouring sites
326      CALL scan_neighbours_percolate(i, j, steps, counterTemp, iTemp, jTemp,
327      percolated, SuperLattice)
328      CALL temp_next(Nlat, iNext, jNext, iTemp, jTemp)
329      steps = steps + 1
330
331      !continue through the lattice until all available sites have been
332      covered
333      DO
334      CALL advance_percolate(steps, Nlat, counterNext, iNext, jNext,
335      iTemp, jTemp, &
336      SuperLattice, percolated)
337
338      !if the structure is percolated or all sites have been covered,
339      return
340      IF (percolated) EXIT
341      IF (iTemp(1)==0) EXIT
342
343      !copy data from temporary arrays to next arrays
344      CALL temp_next(Nlat, iNext, jNext, iTemp, jTemp)
345
346

```

```

337         !increment steps counter
338         steps = steps + 1
339     END DO
340 END SUBROUTINE percolate
341
342 SUBROUTINE scan_neighbours_percolate(iC, jC, steps, counterTemp, iTemp,
343     jTemp, percolated, SuperLattice)
344     !subroutine to analyse adjacent sites (up, down, left, right) for
345     !accessibility
346     IMPLICIT NONE
347     INTEGER, INTENT(IN) :: iC, jC, steps !iC,jC=coordinates of analysed
348     !site; steps=step counter
349     INTEGER, INTENT(INOUT) :: counterTemp, iTemp(Nlat*Nlat),
350     jTemp(Nlat*Nlat), SuperLattice(:, :) !!counterTemp=counter for Temp
351     !arrays; iTemp,jTemp=arrays temporary storing coordinates of next
352     !layer of accessible sites; SuperLattice=periodic images of cluster
353     !distribution lattice
354     LOGICAL, INTENT(INOUT) :: percolated !switch for finding percolated
355     !structure
356     INTEGER :: i, j !local variables
357
358     !analyse first adjacent site for accessibility
359     i=iC
360     j=jC-1
361     !if the site is within the lattice
362     IF (j .GE. 1) THEN
363         !if the site is not occupied by a cluster and hasn't been analysed
364         !previously
365         IF (SuperLattice(i,j)==0) THEN
366             !set the site to the current step counter value
367             SuperLattice(i,j)=steps
368             !add the site coordinates to Temp arrays in order to be
369             !analysed in the next iteration
370             iTemp(counterTemp) = i
371             jTemp(counterTemp) = j
372             !increment counter for Temp arrays
373             counterTemp = counterTemp + 1
374             !if a periodic image of the starting point was reached, percolated
375             !structure was found
376             ELSEIF (SuperLattice(i,j)<0) THEN
377                 percolated = .TRUE.
378                 RETURN
379             END IF
380         END IF
381     END IF
382
383     !analyse second adjacent site for accessibility
384     j=jC+1
385     IF (j .LE. 3*Nlat) THEN
386         IF (SuperLattice(i,j)==0) THEN
387             SuperLattice(i,j)=steps
388             iTemp(counterTemp) = i
389             jTemp(counterTemp) = j
390             counterTemp = counterTemp + 1
391             ELSEIF (SuperLattice(i,j)<0) THEN
392                 percolated = .TRUE.
393                 RETURN
394             END IF
395         END IF
396     END IF
397
398     !analyse third adjacent site for accessibility
399     i=iC-1
400     j=jC
401     IF (i .GE. 1) THEN
402         IF (SuperLattice(i,j)==0) THEN
403             SuperLattice(i,j)=steps
404             iTemp(counterTemp) = i
405             jTemp(counterTemp) = j
406             counterTemp = counterTemp + 1
407             ELSEIF (SuperLattice(i,j)<0) THEN
408                 percolated = .TRUE.
409                 RETURN
410             END IF
411         END IF
412     END IF

```

```

398     END IF
399
400     !analyse fourth adjacent site for accessibility
401     i=iC+1
402     IF (i .LE. 3*Nlat) THEN
403         IF (SuperLattice(i,j)==0) THEN
404             SuperLattice(i,j)=steps
405             iTemp(counterTemp) = i
406             jTemp(counterTemp) = j
407             counterTemp = counterTemp + 1
408         ELSEIF (SuperLattice(i,j)<0) THEN
409             percolated = .TRUE.
410             RETURN
411         END IF
412     END IF
413 END SUBROUTINE scan_neighbours_percolate
414
415 SUBROUTINE advance_percolate(steps, Nlat, counterNext, iNext, jNext,
416     iTemp, jTemp, &
417     SuperLattice, percolated)
418     !subroutine for advancing to the next layer of accessible sites
419     IMPLICIT NONE
420     INTEGER, INTENT(IN) :: Nlat, steps !Nlat=lattice size; steps=step
421     counter
422     INTEGER, INTENT(INOUT) :: iNext(Nlat*Nlat), jNext(Nlat*Nlat)
423     !iNext,jNext=coordinates of the next layer of accessible sites
424     INTEGER, INTENT(INOUT) :: SuperLattice(:,:), iTemp(Nlat*Nlat),
425     jTemp(Nlat*Nlat) !SuperLattice=periodic images of cluster
426     distribution lattice; iTemp,jTemp=arrays temporary storing
427     coordinates of next layer of accessible sites
428     LOGICAL, INTENT(INOUT) :: percolated !switch for finding percolated
429     structure
430     INTEGER :: counterNext, counterTemp !local counters
431
432     !initialise counters for next and temp arrays
433     counterNext = 1
434     counterTemp = 1
435
436     !loop until all the sites have been covered
437     DO
438         IF (iNext(counterNext)==0) EXIT
439         IF (percolated) EXIT
440
441         !check neighbouring sites
442         CALL scan_neighbours_percolate(iNext(counterNext),
443             jNext(counterNext),steps, counterTemp, &
444             iTemp, jTemp, percolated, SuperLattice)
445
446         !increment counter for next arrays
447         counterNext = counterNext + 1
448     END DO
449 END SUBROUTINE advance_percolate
450
451 SUBROUTINE temp_next(Nlat, iNext, jNext, iTemp, jTemp)
452     !subroutine to copy Temp arrays into Next arrays and reset Temp arrays
453     IMPLICIT NONE
454     INTEGER, INTENT(IN) :: Nlat !lattice size
455     INTEGER, INTENT(INOUT) :: iNext(Nlat*Nlat), jNext(Nlat*Nlat)
456     !iNext,jNext=coordinates of the next layer of accessible sites
457     INTEGER, INTENT(INOUT) :: iTemp(Nlat*Nlat), jTemp(Nlat*Nlat)
458     !iTemp,jTemp=arrays temporary storing coordinates of next layer of
459     accessible sites
460
461     !copy values from Temp arrays to Next arrays
462     iNext = iTemp
463     jNext = jTemp
464
465     !reset Temp arrays
466     iTemp = 0
467     jTemp = 0
468 END SUBROUTINE temp_next
469
470 SUBROUTINE copy_SuperLattice(i, j, Nlat, Cluster, SuperLattice)

```

```

460 !subroutine for creating periodic images of cluster distribution lattice
461 IMPLICIT NONE
462 INTEGER, INTENT(IN) :: Nlat, Cluster(Nlat,Nlat), i, j !Nlat=lattice
      size; Cluster=cluster distribution lattice; i,j=coordinates
463 INTEGER, INTENT(OUT):: SuperLattice(:, :) !periodic images of cluster
      distribution lattice
464
465 !reset lattice
466 SuperLattice = 0
467
468 !create 9 copies of cluster lattice
469 SuperLattice(1:Nlat, 1:Nlat) = Cluster(1:Nlat,1:Nlat)
470 SuperLattice(Nlat+1:2*Nlat, 1:Nlat) = Cluster(1:Nlat,1:Nlat)
471 SuperLattice(2*Nlat+1:3*Nlat, 1:Nlat) = Cluster(1:Nlat,1:Nlat)
472 SuperLattice(1:Nlat, Nlat+1:2*Nlat) = Cluster(1:Nlat,1:Nlat)
473 SuperLattice(Nlat+1:2*Nlat, Nlat+1:2*Nlat) = Cluster(1:Nlat,1:Nlat)
474 SuperLattice(2*Nlat+1:3*Nlat, Nlat+1:2*Nlat) = Cluster(1:Nlat,1:Nlat)
475 SuperLattice(1:Nlat, 2*Nlat+1:3*Nlat) = Cluster(1:Nlat,1:Nlat)
476 SuperLattice(Nlat+1:2*Nlat, 2*Nlat+1:3*Nlat) = Cluster(1:Nlat,1:Nlat)
477 SuperLattice(2*Nlat+1:3*Nlat, 2*Nlat+1:3*Nlat) = Cluster(1:Nlat,1:Nlat)
478
479 !put in 8 copies of the initial point to the 8 surrounding lattices
480 SuperLattice(i,j) = -1
481 SuperLattice(i+Nlat,j) = -1
482 SuperLattice(i+2*Nlat,j) = -1
483 SuperLattice(i,j+Nlat) = -1
484 SuperLattice(i+Nlat,j+Nlat) = 0 !this is the central initial starting
      point
485 SuperLattice(i+2*Nlat,j+Nlat) = -1
486 SuperLattice(i,j+2*Nlat) = -1
487 SuperLattice(i+Nlat,j+2*Nlat) = -1
488 SuperLattice(i+2*Nlat,j+2*Nlat) = -1
489 END SUBROUTINE copy_SuperLattice
490 END PROGRAM brownian

```

E.2.6 Solvent exchange simulation

```

1 PROGRAM solvent_exchange
2 USE percolation
3 IMPLICIT NONE
4 INTEGER, PARAMETER :: Nlat=1000 !lattice size
5 INTEGER :: i, j, iPos, jPos, swap, c, temp, ios !i,j=loop counters;
      iPos,jPos=lattice coordinates; swap=used to determine adjacent site to
      attempt swap with; c=file name counter; temp=used for swapping species;
      ios=integer for status during opening files
6 INTEGER :: Cluster(Nlat,Nlat), poresites, s, p, r, outsites
      !Cluster=cluster distribution lattice; poresites=number of accessible
      sites; s,p,r=integer values of solids content, percentage of activated
      monomers, and run number; outsites=number of external sites
7 INTEGER, ALLOCATABLE :: lattice(:, :), count(:) !lattice=accessible sites
      lattice; count=number of accessible sites in rows perpendicular to
      lattice edge
8 INTEGER, DIMENSION(12) :: seed !seed=for random number generator
9 REAL :: ireal, jreal !real dummy variables
10 REAL(KIND=8) :: out, in !out=external concentration; in=lattice
      concentration
11 REAL(KIND=16) :: time, dt !time=simulation time; dt=used for data output
12 LOGICAL :: image !if set to TRUE, lattice snapshots are part of output
13 CHARACTER(LEN=30) :: fname, fmt !fname=file name variable; fmt=output
      format
14
15 !set to true to allow lattice snapshots output
16 image = .TRUE.
17
18 !set values of solids content, percentage of activated monomers, and run
      number
19 s = 1
20 p = 1
21 r = 1
22

```

```

23      !create file names
24      IF (r.LT.10) THEN
25          WRITE(fname,'(A6,I1,A4,I1,A1,I1)') 'out_0.', s, '_0.0', p, '_', r
26      ELSE
27          WRITE(fname,'(A6,I1,A4,I1,A1,I2)') 'out_0.', s, '_0.0', p, '_', r
28      END IF
29
30      !open file for progress output
31      OPEN(14,FILE=fname)
32
33      IF (r.LT.10) THEN
34          WRITE(fname,'(A10,I1,A4,I1,A1,I1,A4)') 'Cluster_0.', s, '_0.0', p,
35              '_', r, '.dat'
36      ELSE
37          WRITE(fname,'(A10,I1,A4,I1,A1,I2,A4)') 'Cluster_0.', s, '_0.0', p,
38              '_', r, '.dat'
39      END IF
40
41      !open file containing cluster distribution lattice
42      ios = 0
43      OPEN(3, FILE=fname, STATUS='OLD', IOSTAT=ios)
44      IF (ios/=0) THEN
45          WRITE(14,*) 'Error opening file input.dat', ios
46          STOP
47      END IF
48
49      !read cluster distribution lattice and close the file
50      DO i=1,Nlat
51          READ(3,'(X,1000I6)') (Cluster(i,j),j=1,Nlat)
52      END DO
53      CLOSE(3)
54
55      !allocate dynamic arrays
56      ios = 0
57      ALLOCATE( lattice(Nlat,Nlat), count(Nlat), STAT=ios )
58      IF (ios/=0) THEN
59          WRITE(14,*) 'Error allocating dynamic arrays'
60          STOP
61      END IF
62
63      !evaluate accessible pore sites on the cluster distribution lattice
64      CALL accessible_sites(lattice,Cluster,Nlat)
65
66      !initialise concentration values
67      in = 1.0
68      out = 0.0
69
70      !count the number of accessible sites
71      poresites = 0
72      DO i=1,Nlat
73          DO j=1,Nlat
74              IF (lattice(i,j)/=0) poresites = poresites + 1
75          END DO
76      END DO
77
78      WHERE(lattice>1) lattice = 1 !make all accesible sites equal to 1
79      WHERE(lattice==0) lattice = -1 !make all inaccessible sites equal to -1
80
81      !count the number of accessible sites in rows perpendicular to the
82      lattice edge
83      count = 0
84      DO j=1,Nlat
85          DO i=1,Nlat
86              IF (lattice(i,j)==1) count(j) = count(j) + 1
87          END DO
88      END DO
89
90      !set the number of external sites
91      outsites = poresites
92
93      !start the random number generator using a seed value
94      seed = 100

```

```

93 CALL RANDOM_SEED(PUT=seed)
94
95 !reset simulation time
96 time = 0.0
97
98 !create file name and open file for data output
99 IF (r.LT.10) THEN
100   WRITE(fname,'(A7,I1,A4,I1,A1,I1,A4)') 'time_0.', s, '_0.0', p, '_', r,
      '.dat'
101 ELSE
102   WRITE(fname,'(A7,I1,A4,I1,A1,I2,A4)') 'time_0.', s, '_0.0', p, '_', r,
      '.dat'
103 END IF
104 ios = 0
105 OPEN(2, FILE=fname, STATUS='REPLACE', IOSTAT=ios)
106 IF (ios/=0) THEN
107   WRITE(14,*) 'Error opening file time.dat', ios
108   STOP
109 END IF
110
111 !initialise file number counter
112 c = 1
113
114 !if additional output is switched on
115 IF (image) THEN
116   !create file name and open file for lattice snapshot
117   ios = 0
118   CALL namef(c,fname)
119   OPEN(3, FILE=fname, STATUS='REPLACE', IOSTAT=ios)
120   IF (ios/=0) THEN
121     WRITE(14,*) 'Error opening file lattice.dat', ios
122     STOP
123   END IF
124
125   !set output data format and write data into file and close the file
126   WRITE(fmt,'(A1,I4,A3)') '(, Nlat, 'I3)'
127   DO i=1,Nlat
128     WRITE(3,fmt) (lattice(i,j),j=1,Nlat)
129   END DO
130   CLOSE(3)
131
132   !create file name and open file for concentration profile data output
133   IF (r.LT.10) THEN
134     WRITE(fname,'(A10,I1,A4,I1,A1,I1,A4)') 'profile_0.', s, '_0.0', p,
      '_', r, '.dat'
135   ELSE
136     WRITE(fname,'(A10,I1,A4,I1,A1,I2,A4)') 'profile_0.', s, '_0.0', p,
      '_', r, '.dat'
137   END IF
138   OPEN(12, FILE=fname, STATUS='REPLACE', IOSTAT=ios)
139   IF (ios/=0) THEN
140     WRITE(*,*) 'Error opening file profile.dat', ios
141     STOP
142   END IF
143
144   !create header for concentration profile output
145   WRITE(12,'(1000I6)') (i,i=1,Nlat)
146   !write concentration profile data into file
147   CALL profile(lattice,Nlat,count)
148 END IF
149
150 !create headers and write output data into file
151 WRITE(2,'((A20,X),2(A10,X))') 'time/(Nlat^4)', 'in', 'out'
152 WRITE(2,'((F20.8,X),2(F10.8,X))') time/(Nlat**2), in, out
153 WRITE(14,'(F10.6,2F10.4)') time/(Nlat**2), in, out
154 CALL FLUSH(14)
155
156 !increment file number counter
157 c = c + 1
158
159 !diffusion loop until selected lattice concentration was reached
160 mainloop: DO

```

```

161      !get a random position on the lattice
162      CALL RANDOM_NUMBER(ireal)
163      CALL RANDOM_NUMBER(jreal)
164      iPos = INT(Nlat*ireal) + 1
165      jPos = INT(Nlat*jreal) + 1
166
167      !if the lattice concentration reached selected final value
168      IF (in.LE.0.65) THEN
169          !write final data output into file
170          WRITE(2,'(F20.8,X,2(F10.8,X))') time/(Nlat**2), in, out
171
172          !if additional output is switched on
173          IF (image) THEN
174              !write concentration profile into file
175              CALL profile(lattice,Nlat,count)
176
177              !write lattice snapshot into file
178              ios = 0
179              CALL namef(c,fname)
180              OPEN(3, FILE=fname, STATUS='REPLACE', IOSTAT=ios)
181              IF (ios/=0) THEN
182                  WRITE(14,*) 'Error opening file lattice.dat', ios
183                  STOP
184              END IF
185              WRITE(fmt,'(A1,I4,A3)') '( ', Nlat, 'I3)'
186              DO i=1,Nlat
187                  WRITE(3,fmt) (lattice(i,j),j=1,Nlat)
188              END DO
189              CLOSE(3)
190          END IF
191          !exit the diffusion loop and finalise execution
192          EXIT mainloop
193      END IF
194
195      time = time + (1.0/(Nlat**2)) !increment simulation time
196
197      !write data output every time concentration changes by 1%
198      dt = out*100
199      IF ((c-1)==INT(dt)) THEN
200          WRITE(2,'(F20.8,X,2(F10.8,X))') time/(Nlat**2), in, out
201          WRITE(14,'(F10.6,2F10.4)') time/(Nlat**2), in, out
202          CALL FLUSH(14)
203          IF (image) THEN
204              ios = 0
205              CALL namef(c,fname)
206              OPEN(3, FILE=fname, STATUS='REPLACE', IOSTAT=ios)
207              IF (ios/=0) THEN
208                  WRITE(14,*) 'Error opening file lattice.dat', ios
209                  STOP
210              END IF
211              WRITE(fmt,'(A1,I4,A3)') '( ', Nlat, 'I3)'
212              DO i=1,Nlat
213                  WRITE(3,fmt) (lattice(i,j),j=1,Nlat)
214              END DO
215              CLOSE(3)
216              CALL profile(lattice,Nlat,count)
217          END IF
218          c = c + 1
219      END IF
220
221      !choose a random adjacent position for swap
222      CALL RANDOM_NUMBER(ireal)
223      swap=INT(4*ireal)+1
224      i = iPos
225      j = jPos
226      SELECT CASE (swap)
227          CASE (1)
228              i = i + 1
229          CASE (2)
230              i = i - 1
231          CASE (3)
232              j = j + 1

```

```

233         CASE (4)
234             j = j - 1
235     END SELECT
236
237     IF ((j<1).OR.(j>Nlat)) THEN
238         !if the position is on the edge of the box and swap is with a site
                outside the box
239         CALL RANDOM_NUMBER(ireal)
240         !use a random number to determine whether the swap will happen,
                using outside concentration
241         IF (ireal>out) THEN
242             IF (lattice(iPos,jPos)==1) THEN
243                 !update the concentration inside and outside the lattice
244                 in = in - 1.0/poresites
245                 out = out + 1.0/poresites
246                 !swap with species 0
247                 lattice(iPos,jPos) = 0
248             END IF
249         ELSE
250             !swap with species 1
251             IF (lattice(iPos,jPos)==0) THEN
252                 !update the concentration inside and outside the box
253                 in = in + 1.0/poresites
254                 out = out - 1.0/poresites
255                 lattice(iPos,jPos) = 1
256             END IF
257         END IF
258     ELSE IF ((i<1).OR.(i>Nlat)) THEN
259         !if the swap is within the periodic boundaries of the box
260         CALL periodic_boundary(i,Nlat)
261         IF ((lattice(i,j)).NE.(lattice(iPos,jPos)).AND.
                (lattice(i,j).GE.0).AND.(lattice(iPos,jPos).GE.0)) THEN
262             !if the positions are occupied by different species and are
                accessible sites swap them
263             temp = lattice(iPos,jPos)
264             lattice(iPos,jPos) = lattice(i,j)
265             lattice(i,j) = temp
266         END IF
267     ELSE
268         !if the swap is with a site within the box
269         IF ((lattice(i,j)).NE.(lattice(iPos,jPos)).AND.
                (lattice(i,j).GE.0).AND.(lattice(iPos,jPos).GE.0)) THEN
270             !if the positions are occupied by different species and are
                accessible sites swap them
271             temp = lattice(iPos,jPos)
272             lattice(iPos,jPos) = lattice(i,j)
273             lattice(i,j) = temp
274         END IF
275     END IF
276 END DO mainloop
277
278 !close opened files
279 CLOSE(2)
280 IF (image) CLOSE(12)
281
282 !deallocate dynamic arrays
283 ios = 0
284 DEALLOCATE( lattice, STAT=ios )
285 IF (ios/=0) THEN
286     WRITE(14,*) 'Error deallocating arrays'
287     STOP
288 END IF
289
290 IF (image) CLOSE(3)
291 WRITE(14,*) '----- PROGRAM FINISHED -----'
292 CLOSE(14)
293
294 !subroutines used by the main program
295 CONTAINS
296     SUBROUTINE namef(i,fname)
297         !subroutine for creating file name for lattice snapshots output
298         INTEGER, INTENT(IN) :: i !file number counter

```

```

299     CHARACTER(LEN=30), INTENT(OUT) :: fname !file name
300
301     !create file name
302     IF(i.LT.10) THEN
303         WRITE(fname,'(A10,I1,A4,I1,A1,I1,A4,I1,A4)') 'lattice_0.', s,
304             '_0.0', p, '_', r, '_000',c, '.dat'
305     ELSE IF(i.LT.100) THEN
306         WRITE(fname,'(A10,I1,A4,I1,A1,I1,A3,I2,A4)') 'lattice_0.', s,
307             '_0.0', p, '_', r, '_00',c, '.dat'
308     ELSE IF(i.LT.1000) THEN
309         WRITE(fname,'(A10,I1,A4,I1,A1,I1,A2,I3,A4)') 'lattice_0.', s,
310             '_0.0', p, '_', r, '_0',c, '.dat'
311     ELSE IF(i.LT.10000) THEN
312         WRITE(fname,'(A10,I1,A4,I1,A1,I1,A1,I4,A4)') 'lattice_0.', s,
313             '_0.0', p, '_', r, '_',c, '.dat'
314     ELSE
315         !if the file counter is too high, inform user and stop execution
316         WRITE(*,*) 'File number above 10 000, not enough space for
317             lattice.dat file name!'
318         STOP
319     ENDIF
320     RETURN
321 END SUBROUTINE namef
322
323 SUBROUTINE profile(lattice,Nlat,count)
324 !subroutine for concentration profile data output
325 IMPLICIT NONE
326 INTEGER, INTENT(IN) :: Nlat, lattice(:,:) !Nlat=lattice
327 size; lattice=simulation lattice; count=number of accessible
328 lattice sites in each row perpendicular to the lattice edge
329 REAL :: conc(Nlat) !concentration profile
330 INTEGER :: i, j !loop counters
331 CHARACTER(LEN=30):: fmt !data output format
332
333 !reset concentration profile array
334 conc = 0
335 !calculate concentration profile
336 DO j=1,Nlat
337     DO i=1,Nlat
338         IF (lattice(i,j)==1) conc(j) = conc(j) + 1
339     END DO
340     conc(j) = conc(j)/count(j)
341 END DO
342
343 !create data output format
344 IF (Nlat.LT.1000) THEN
345     WRITE(fmt,'(A1,I3,A5)') '(', Nlat, 'F6.3)'
346 ELSE
347     WRITE(fmt,'(A1,I4,A5)') '(', Nlat, 'F6.3)'
348 END IF
349
350 !write concentration profile into file
351 WRITE(12,fmt) (conc(i),i=1,Nlat)
352 END SUBROUTINE profile
353 END PROGRAM solvent_exchange

```

E.2.7 Gas sorption simulation

```

1 PROGRAM mft_slit
2 IMPLICIT NONE
3 !program based on a code by Peter A. Monson, original code introduction:
4 Solution of the mean field equations for a 3D lattice gas model in
5 finite length slit pore with nearest neighbor interactions.
6 Calculations take advantage of the 2D symmetry of the slit. Simple
7 cubic lattice. Peter A. Monson (February 2007)
8 !this version is for a slit pore with both ends open
9 INTEGER :: nsite, mx, mz, l, ios, ncp, nx, i, j, ifile, iads, ides,
10 maxit, icp, iter, nporesites !nsite=total number of lattice gas sites;
11 mx,mz=lattice dimensions; l=pore length; ios=integer for status during
12 opening files; ncp,nx=number of steps for chemical potential/relative
13 activity increase; i,j=loop counters; ifile=file number counter;

```

```

        iads,ides=loop counters; maxit=maximum number of iterations; icp=loop
        counter; iter=iteration counter; nporesites=number of sites within the
        pore
6  INTEGER, ALLOCATABLE :: ieta(:,:) !ieta=pore structure lattice
7  REAL :: y, tstar !y=ratio of fluid-solid to fluid-fluid interactions;
        tstar=temperature term
8  REAL(KIND=8) :: snn, error, dcp, rhog, cp, cp0, x0, dx, x !snn=density
        sum of nearest neighbours; error=convergence criterion value;
        dcp=chemical potential increment; rhog=initial bulk gas density;
        cp=chemical potential; cp0=initial value of chemical potential;
        x0=initial value of relative activity; dx=relative activity increment;
        x=relative activity
9  REAL(KIND=8) :: rhoav, gp !rhoav=average density; gp=grand potential
10 REAL(KIND=8), ALLOCATABLE :: phi(:,:), rhoold(:,:), rhonew(:,:)
        !phi=external field lattice; rhoold,rhonew=previous and updated
        density distribution lattice
11 CHARACTER(LEN=30) :: fname1, fname2, fmt !file names and output format
12
13 !inform user calculation started
14 WRITE(*,*) '----- Program started -----'
15
16 !open file containing parameter values
17 OPEN(1,FILE='mft_slit.dat',STATUS='OLD', IOSTAT=ios)
18 !check if there was an issue opening the file
19 CALL ios_check(ios, 'opening file mft_slit.dat')
20
21 !read values of parameters from file with example values presented for
        reference in comments
22 READ(1,*) y, mz, l !y=3.0; mz=12; l=40
23 READ (1,*) tstar, ncp, cp0, dcp, nx, x0, dx, ides, rhog !tstar=1.0;
        ncp=3201; cp0=-8.0; dcp=0.0025; nx=2001; x0=0.0; dx=0.0005; ides=2;
        rhog=0.00001
24 READ(1,*) maxit, error !maxit=100000; error=1.0e-8
25
26 CLOSE(1) !close the file
27
28 !calculate lattice length based on pore length and bulk gas sites
29 mx = l + 20
30
31 !inform user about pore dimension
32 WRITE(*,*) 'Pore width: ', mz-2, 'Pore length: ', l
33
34 !create output file name and open the file
35 WRITE(fname1, '(A11,I2,A4)') 'open_width ', mz-2, '.dat'
36 OPEN(4,FILE=fname1, STATUS='REPLACE', IOSTAT=ios)
37 CALL ios_check(ios, 'opening file' // fname1)
38
39 !write data output headers (header format is for OriginPro)
40 WRITE(4,'(4(A20,X))') '\g(1)/\g(1)\-(0)', '\g(r)', '\g(m)', '\g(W)'
41
42 !allocate dynamic arrays
43 ios = 0
44 ALLOCATE( rhoold(mx,mz), rhonew(mx,mz), ieta(mx,mz), phi(mx,mz),STAT=ios )
45 CALL ios_check(ios, 'allocating arrays')
46
47 ifile = 0 !reset file number counter
48
49 !inform user about lattice dimensions
50 WRITE(*,*) 'Box length: ', mx, 'Box width: ', mz, 'Pore length: ', l
51
52 !set values for pore structure lattice (gas sites are equal to 1 and wall
        sites are equal to 0)
53 ieta = 1
54 DO i=((mx-1)/2)+1,(mx+1)/2
55     ieta(i,1) = 0 !top wall within the pore set to 0
56     ieta(i,mz) = 0 !bottom wall within the pore set 0
57 END DO
58
59 !count total number of gas sites and number of gas sites within the pore
60 nporesites = 0
61 nsite = 0
62 DO i=1,mx

```

```

63     DO j=1,mz
64         IF (ieta(i,j)/=0) THEN
65             nsite = nsite + 1
66             IF ((i.GE.11).AND.(i.LE.(mx-10))) nporesites = nporesites + 1
67         END IF
68     END DO
69 END DO
70
71 !initialize density distribution and external field lattices
72 phi = REAL(0)
73 rhoold = rhog
74 rhonew = REAL(0)
75 DO i=1,mx
76     DO j=1,mz
77         IF(ieta(i,j).EQ.1) THEN
78             !this excludes the wall sites
79             IF((i.GT.10).AND.(i.LE.(mx-10))) THEN
80                 !this restrains it to the sites within the pore
81                 IF (i/=1) phi(i,j) = phi(i,j) - (1.0-REAL(ieta(i-1,j)))*y
82                 IF (i/=mx) phi(i,j) = phi(i,j) - (1.0-REAL(ieta(i+1,j)))*y
83                 IF (j/=1) phi(i,j) = phi(i,j) - (1.0-REAL(ieta(i,j-1)))*y
84                 IF (j/=mz) phi(i,j) = phi(i,j) - (1.0-REAL(ieta(i,j+1)))*y
85                 !calculate external fields for sites within the pore
86             END IF
87         END IF
88     END DO
89 END DO
90
91 !perform sorption calculations
92 WRITE(*,*) 'Calculating adsorption with linear increase in relative
93           activity...'
94 !loop over adsorption and desorption
95 DO iads=1,ides
96     !loop over relative activity
97     DO icp = 1,nx
98         !calculate value of relative activity
99         x = x0 + (icp - 1)*dx
100        !calculate value of chemical potential
101        cp = Tstar*LOG(x) - 3
102
103        !for positive values of relative activity
104        IF (x.GT.0) THEN
105            !perform calculations
106            CALL calculate(cp, error, ieta, l, maxit, mx, mz, nsite, phi,
107                          tstar, rhoav, gp, rhonew, rhoold)
108
109            !increment file number counter
110            ifile = ifile + 1
111
112            !write output data into file
113            WRITE(4, '(2(ES20.12,X),F7.3,X,ES20.12,X)')
114                exp((cp+3.0d0)/tstar), rhoav, cp, gp
115        END IF
116    END DO
117
118    !switch to desorption
119    x0 = x-dx
120    dx = -dx
121    nx = nx-1
122 END DO
123
124 CLOSE(4) !close output file
125
126 !deallocate dynamic arrays
127 ios = 0
128 DEALLOCATE( rhoold, rhonew, ieta, phi, STAT=ios )
129 CALL ios_check(ios, 'deallocating arrays')
130
131 !inform user execution finished
132 WRITE(*,*) '----- Program finished -----'
133
134 !subroutines used by the main program
135 CONTAINS

```

```

133 SUBROUTINE namef(i, fname1, fname2)
134 !subroutine for creating file names
135 INTEGER, INTENT(IN) :: i !file name counter
136 CHARACTER(LEN=12), INTENT(OUT) :: fname1, fname2 !file names
137
138 IF(i.LT.10) THEN
139     WRITE(fname1, '(A7,I1,A4)') 'rho_000', i, '.dat'
140     WRITE(fname2, '(A7,I1,A4)') 'rho_000', i, '.gif'
141 ELSE IF(i.LT.100) THEN
142     WRITE(fname1, '(A6,I2,A4)') 'rho_00', i, '.dat'
143     WRITE(fname2, '(A6,I2,A4)') 'rho_00', i, '.gif'
144 ELSE IF(i.LT.1000) THEN
145     WRITE(fname1, '(A5,I3,A4)') 'rho_0', i, '.dat'
146     WRITE(fname2, '(A5,I3,A4)') 'rho_0', i, '.gif'
147 ELSE
148     WRITE(fname1, '(A4,I4,A4)') 'rho_', i, '.dat'
149     WRITE(fname2, '(A4,I4,A4)') 'rho_', i, '.gif'
150 ENDIF
151
152 RETURN
153 END SUBROUTINE namef
154
155 SUBROUTINE ios_check(ios, string)
156 !subroutine for checking status of in input/output action
157 IMPLICIT NONE
158 INTEGER, INTENT(IN) :: ios !value of input/output status integer
159 CHARACTER, INTENT(IN) :: string !string including information about
    the action
160
161 !if ios is not equal to 0, an issue occurred
162 IF (ios/=0) THEN
163     !inform user about the issue and stop execution
164     WRITE(*,*) 'Error ', string, ios
165     STOP
166 END IF
167 END SUBROUTINE ios_check
168
169 SUBROUTINE calculate(cp, error, ieta, l, maxit, mx, mz, nsite, phi,
    tstar, rhoav, gp, rhonew, rhoold)
170 !subroutine performing gas sorption calculations
171 IMPLICIT NONE
172 INTEGER, INTENT(IN) :: l, maxit, mx, mz, nsite !l=pore length;
    maxit=maximum number of iterations; mx,mz=lattice dimensions;
    nsite=total number of lattice gas sites;
173 INTEGER, INTENT(IN) :: ieta(mx,mz) !ieta=pore structure lattice
174 REAL, INTENT(IN) :: tstar !tstar=temperature term
175 REAL(KIND=8), INTENT(IN) :: cp, phi(mx,mz), error !cp=chemical
    potential; phi=external field lattice; error=convergence criterion
    value
176 REAL(KIND=8), INTENT(OUT) :: rhoav, gp !rhoav=average density;
    gp=grand potential
177 REAL(KIND=8), INTENT(INOUT) :: rhonew(:, :), rhoold(:, :)
    !rhoold, rhonew=previous and updated density distribution lattice
178 INTEGER :: i, j, iter !i,j=loop counters; iter=iteration counter
179 REAL(KIND=8) :: snn, sumgp, sumh0, sumrho, sumsq, xi !snn=density sum
    of nearest neighbours; sumgp=grand potential sum; sumh0=sum used
    for grand potential calculation; sumrho=density sum; sumsq=density
    difference sum; xi=term used for density calculation
180
181 !start the iteration loop
182 iter = 0
183 iterloop: DO
184     !increment iteration counter
185     iter = iter + 1
186
187     !if the number of iterations exceeds the maximum set value, inform
    user and stop execution
188 IF(iter.GT.maxit) THEN
189     WRITE(*,*) '-----'
190     WRITE(*,*) 'Maximum number of iterations exceeded!'
191     WRITE(*, '(A,I2,A,F10.7)') 'iads = ', iads, ' chemical potential
    = ', cp

```

```

192         STOP
193     END IF
194
195     !reset sum values
196     sumsq = 0.0
197     sumrho = 0.0
198     sumh0 = 0.0
199     sumgp = 0.0
200
201     !loop through all lattice sites
202     DO i=1,mx
203         DO j=1,mz
204             !perform calculations only for gas sites
205             IF(ieta(i,j).EQ.1) THEN
206                 !calculate nearest neighbor density sum
207                 snn=2.0*rhoold(i,j) !include sites in orthogonal
                periodic dimension
208                 IF (i/=1) THEN
209                     IF (ieta(i-1,j).EQ.1) snn = snn + rhoold(i-1,j)
210                 END IF
211                 IF (i/=mx) THEN
212                     IF (ieta(i+1,j).EQ.1) snn = snn + rhoold(i+1,j)
213                 END IF
214                 IF (j/=1) THEN
215                     IF (ieta(i,j-1).EQ.1) snn = snn + rhoold(i,j-1)
216                 END IF
217                 IF (j/=mz) THEN
218                     IF (ieta(i,j+1).EQ.1) snn = snn + rhoold(i,j+1)
219                 END IF
220
221                 !calculate value of xi, used for density calculation
222                 xi = (snn-phi(i,j)+cp)/tstar
223
224                 !calculate new density value
225                 rhonew(i,j) = 1.0/(1.0+EXP(-xi))
226
227                 !calculate desnity difference
228                 sumsq = sumsq + (rhonew(i,j) - rhoold(i,j))*2
229
230                 !for sites within the pore calculate sum values
231                 IF((i.GT.10).AND.(i.LE.(mx-10))) THEN
232                     sumrho = sumrho + rhonew(i,j)
233                     sumgp = sumgp - ieta(i,j)*tstar*LOG(1.0+EXP(xi))
234                     sumh0 = sumh0 + rhonew(i,j)*snn
235                 END IF
236             ENDIF
237         END DO
238     END DO
239
240     !transfer new value of density from rhonew to rhoold
241     DO i = 1,mx
242         DO j = 1,mz
243             IF(ieta(i,j).EQ.1) THEN
244                 rhoold(i,j) = rhonew(i,j)
245             END IF
246         END DO
247     END DO
248
249     !normalise sums with number of sites
250     sumsq = sumsq/nsite
251     rhoav = sumrho/nporesites
252     sumgp = sumgp/nporesites
253     sumh0 = sumh0/2.0/nporesites
254     gp = sumgp + sumh0
255
256     !if the density difference is lower than selected threshold value,
257     move to the next sorption point
258     IF (sumsq.LT.error) EXIT iterloop
259 END DO iterloop
260 END SUBROUTINE
END PROGRAM mft_slit

```